

Investigation of novel electrical and magnetic properties of perovskite oxides

Thesis submitted for the degree of
Doctor of Philosophy (Science)

in

Physics (Experimental)

by

Rajib Nath

Department of Physics
University of Calcutta
January 2015

To my Parents.....

Acknowledgments

It has been a long and eventful journey and at the end of this journey, I would like to thank all who has made this journey successful and wonderful.

First of all, I express my sincere respect and gratitude to my supervisor Prof. Arup Kumar Raychaudhuri. It was his guidance, wisdom and continuous enthusiasm which helped me to complete this dissertation. His approach to science always inspired me to become a good researcher. I always appreciated his all-around knowledge on science, society, entertainment, and politics. He always motivated us to become a knowledgeable person rather than an informative one. I learned from him how to frame and find a scientific question and the ways to solve it. It has been a pleasure and an honour to work with you which I will cherish for my whole life. I would also like to thank Prof. Dipten Bhattacharya, late Prof. Ya. M. Mukovskii, Prof. Pravat Mandal, Prof. Valdimir Chichkov for their valuable suggestions, discussions and active collaboration which helped me a lot in my research. I also acknowledge my M.Sc. project supervisor Dr. Tanmoy Banerjee (at The University of Burdwan) who motivated me to involve in scientific research. I acknowledge the help and suggestions of Dr. Barnali Ghosh and all the technical cell members (especially Shakti Da, Surajit Da and Dipankar) in our centre for their unconditional support and help whenever I needed.

I appreciate the financial support from the Council of Scientific and Industrial Research (CSIR), India and S. N. Bose National centre for Basic Sciences, Kolkata.

During initial days of my Ph.D. tenure, I was fortunate enough to have unconditional love, support and help from my seniors like Dr. Manoranjan Ghosh, Dr. M Venkat Kamlakar, Dr. Sudeshna Samanta, Dr. Soma Das, Dr. Tapati Sarkar and Dr. Rajesh Kr. Neogy. Venkat Da and Sudeshna Di helped me a lot to learn different experimental techniques and interface programming. Sudeshna Di also helped me in making contact on my samples as my resolution was always limited to "mm" region. I shared a very special relation with Rajesh da and Tandrima Di. They always treated me as their younger brother and motivated me to do better and better in my life. Rajesh Da and I worked together in some research projects and my first publication was with him. I also acknowledge the academic support from Dr. Parthasarathi Mondal (from CGCRI, Kolkata). I started to work on my first thesis problem with him. Partha Da had been always with me whenever I needed some help in academic as well as in personal matters. In addition to my seniors, the other two most important people were Dr. Kaustuv Das and Dr. Kuntal Chakrabarty. Kaustuv Da was my "tea-mate" (along with Rajesh Da) throughout my Ph.D. tenure. We used to discuss many things over a small cup of tea at kaka and Dulal da's tea stall. Those small "teatime" short breaks helped me to break monotony and get rejuvenated. He also aided me with his experimental and academic knowledge whenever it's required. Kuntal Da is a fun & food loving person and I always enjoyed every bit of moment with him. He introduced me to every nook and corner of Kolkata and each time it looks beautiful through his eyes. We had delicious foods at some great restaurants in Kolkata and with him I always felt alive. Those experiences were very precious to me.

I had the pleasure to work with some of the most vibrant group-mates and friends without whom this journey would never be the same. First of all, I acknowledge the help and support of my friends, batchmates & labmates Manotosh and Shahnewaz. They are wonderful people having diagonally opposite characteristics. However, one thing was common that both of them were very good in their

experiments and scientific knowledge. I was always benefited working with them and every time they helped me to improve. When I joined as a fresh Ph.D. student, both of them helped me to learn many experimental techniques as well as software programmings. Manotosh was my longest (4 yrs) room partner in my student life and I always astonished how a man can be so cool irrespective of any situations. I think it is his nature which made me stronger to deal with any situation. On the contrary, I had always some friendly fights and debates with Shahnewaz in issues like academics, politics, history and entertainment. However, I learned a lot from these debates and I will always appreciate him for that. Apart from my labmates, I spent wonderful times with Sandeep (Agru), Singh Ji, Tanumay, Abhijit, Debmalya, JenaJi, Tanmoy, Wasim, Saikat and PandeJi (sincere apologies if I forgot to mention anyone). They always supported me, loved me and helped me. Whenever I got frustrated, I used to go to Sandeep and he always acted as a sink or frustration absorber (though sometimes he himself became radiator). Tanmoy (TG) is my junior from my university days and without him it would be very difficult for me to spend last few months of my Ph.D tenure. He also helped in proof reading of my thesis. I also want to thank my university friends Saibal, Anindita, Samu, Ayan, Arup and Astik Da for their constant encouragement to do better in life. It would be unfair if I do not mention the name of my college friends Partha, Ushnish, Bidtyut and Pravakar. They were always with me in any situations.

I also acknowledge the support and love from my juniors Rabaya, Putul, Sabyasachi, RishiJi, Ravindra, Shaili and Vibhuti. Whenever I asked for any help, they were always there for me. Thanks to Ravindra, Shaili and Rishi Ji for making my birthdays so special. I also thank Rishi Ji for guiding me to explore his beautiful country Nepal (my first visit to a foreign country) and hope to do more in future. Their faith in me that I can do well in my carrier always pushes me to go for that extra mile.

At the end, I am thankful to my family members (Ma, Baba, Didi, TapasDa, PutkuDi, BabuDa, Pintu, my two sweet angels Bubun&Bulan) for their support, unconditional love and affection which always strengthen my confidence. They never forced me to do something which I don't like and always supported my decisions. I am also very thankful to Puspita without her I would not be able to complete this long journey. She always believed me and stood by my side. She enjoyed my success more than me and always patted me on the back even for very small achievements. I think they dreamed my journey, I have just completed it. My only prayer is that I can always make them happy.

Finally, I thank everyone for this amazing journey.....

RajibNath
S. N. Bose National Centre for Basic Sciences
Kolkata, India
January, 2015

List of Publications

1. **Rajib Nath**, A. K. Raychaudhuri, Ya. M. Mukovskii, N. Andreev and Vladimir Chichkov, *Room temperature resistive switching with hysteresis in $GdMnO_3$ thin film with low threshold voltage*, **App. Phys. Lett.** **104**, 183508 (2014)*
2. **Rajib Nath** and A. K. Raychaudhuri, *Electric Double Layer gate controlled non-linear transport in a nanostructured functional perovskite oxide film*, **App. Phys. Lett.** **104**, 083515 (2014)*
3. **Rajib Nath**, A. K. Raychaudhuri, Ya. M. Mukovskii, Parthasarathi Mondal, Dipten Bhattacharya and P. Mandal, *Electric field driven destabilization of the insulating state in nominally pure $LaMnO_3$* , **J. Phys.: Condens. Matter.** **25**, 155605 (2013)*
4. **Rajib Nath** and A. K. Raychaudhuri, *Control of co-existing phases and charge transport in a nanostructured manganite film by field effect with electric double layer as gate dielectric*, **submitted in Phys. Rev. B.** *
5. **Rajib Nath**, A. K. Raychaudhuri, Sandeep Agarwal, P. K. Mukhopadhyay, Ya M Mukovskii and P. Mandal, *Large magneto-resistance in the low temperature insulating state of nominally pure $LaMnO_3$ single crystal*, **to be submitted** *
6. Rajesh Kumar Neogy and **Rajib Nath**, *Dielectric Constant Enhancement of Ethylene Glycol by Au NanoNetworks*, **Nanoscience and Nanotechnology Letters** **4**, 409 (2012)
7. Rajesh Kumar Neogy and **Rajib Nath**, *Synthesis of Micron Sized Gold Network Structure by Assembling Individual Gold Nanoparticles by Laser Assisted PEGylation Method*, **Micro and Nanosystems** **3**, 319-325 (2011)
8. Rajesh Kumar Neogy, **Rajib Nath** and A. K. Raychaudhuri, *Morphology dependent thermal transport in Gold Nanofluids*, **submitted in Appl. Phys. Lett.**

List of Abbreviations

CMR:	Colossal magnetoresistance	MR:	Magnetoresistance
COO:	Charge and Orbital order	RP:	Ruddlesden-Popper (RP) phase
JT:	Jahn-Teller	t_G :	Goldschmidt tolerance factor
AFM:	Antiferromagnetic/Antiferromagnetism	FM:	Ferromagnetic/Ferromagnetism
PM:	Paramagnetic/Paramagnetism	PI/PMI:	Paramagnetic Insulating
FMM:	Ferromagnetic Metallic	FI/FMI:	Ferromagnetic insulating
HRS:	High Resistive State	LRS:	Low Resistive State
PLD:	Pulsed Laser Deposition	EDL:	Electric double Layer
FET:	Field Effect Transistor	CT:	Charge Transfer
CD:	Charge Disproportionation	E_a :	Activation Energy
V :	Applied Bias	I :	Current
V:	Volt	s:	sec
K:	Kelvin	Ω :	Ohm
A:	Ampere	nm:	nanometer
R_L :	Load Resistor	R :	sample Resistance
ρ :	Resistivity	R_S :	Resistance between +I & -I
f :	Metallic volume fraction	f_c :	Volume fraction for percolation
T :	Temperature	T:	Tesla
T_R :	Structural transition temperature	R_L :	Load Resistor
V_S :	Sample Voltage	ρ_{ms} :	Resistivity of HRS
ρ_m :	Resistivity of LRS	f :	frequency (in chapter 4)
M :	Magnetic Moment	H :	Magnetic field
T_{CL} :	Cluster Formation temperature	V_{DS} :	Source-Drain Voltage
I_{DS} :	Source-Drain Current	V_G :	Gate Voltage
I_G :	Gate Current	λ_D :	Debye Length
GB:	Grain Boundary	ϕ_{GB} :	Grain Boundary Potential
$T_{OO'}$:	$O - O'$ transition temperature	T_{FI} :	Onset of the FMI state
UHV:	Ultra high vacuum	STM:	Scanning Tunneling Microscope
DOS:	Density of states	LCMAP:	Local Conduction Mapping
e_{\parallel} :	In-plane strain	e_{\perp} :	Out of plane strain
e_{Eff} :	effective strain	I_t :	Tunneling current

Contents

Table of Contents	vii
List of Figures	x
List of Tables	xx
1 Introduction	1
1.1 Motivation	2
1.2 Crystal structure of perovskites	3
1.3 Cationic Disorder	5
1.4 Electronic structure of perovskite manganites	5
1.5 Magnetic interactions in manganites	7
1.6 Magnetization due to divalent atom doping	11
1.7 Resistive switching in perovskites	12
1.8 Phenomena of phase separation in manganites	14
1.9 Magnetoresistance in manganites	17
1.10 Carrier modulation in perovskite using electrostatic electric double layer gate	20
1.11 Overview of the thesis	24
2 Sample preparation, characterisation and measurement techniques	27
2.1 Introduction	28
2.2 Preparation of manganite single crystals	30
2.2.1 Floating zone technique	30
2.2.2 Growth of LaMnO_3 and $\text{La}_{0.9}\text{Sr}_{0.1}\text{MnO}_3$ single crystal	32
2.2.3 Manganite single crystals used in the experiment	35
2.3 Thin film deposition techniques	35
2.3.1 Pulsed laser deposition	36
2.3.1.1 Components of a PLD set up	36
2.3.1.2 Pulsed laser deposition technique	38
2.3.1.3 Making and Characterisation of PLD target	41
2.3.2 RF Magnetron sputtering	42
2.4 Making of EDL -FET device	44
2.5 Brief description to characterisation techniques	44
2.5.1 XRD, High Temperature XRD and Rocking curve	45

2.5.2	Scanning electron microscope	47
2.5.3	Energy dispersive X-ray Analysis	50
2.5.4	Electron energy loss spectroscopy	52
2.5.5	X-ray photo electron spectroscopy	55
2.5.6	Atomic force Microscopy	57
2.5.7	Thickness of the thin film by ellipsometry	60
2.6	Magnetisation measurements	63
2.6.1	D.C. Magnetisation in Vibrating sample magnetometer	64
2.6.2	A.C. susceptibility measurement	65
2.7	Electrical and magneto transport measurement	66
2.7.1	Electrical measurement in constant current and voltage method	67
2.7.2	Measurement-set up for transport and magneto transport	70
2.8	Local tunneling conductance measurement using UHV-STM	74
3	Effect of electric field on the insulating state of undoped LaMnO₃ and GdMnO₃	80
3.1	Introduction	81
3.2	Polaronic insulating state in LaMnO ₃ , La _{0.9} Sr _{0.1} MnO ₃ and GdMnO ₃	83
3.3	Effect of electric field on the polaronic insulating state of LaMnO ₃ single crystals and GdMnO ₃ thin film	86
3.3.1	Temperature dependent $I - V$ data and bias induced destabilization of the polaronic state in LaMnO ₃	88
3.3.2	$I - V$ data for hole doped La _{0.9} Sr _{0.1} MnO ₃	91
3.3.3	$I - V$ data of GdMnO ₃ thin film	93
3.4	Temperature dependence of switched state in LaMnO ₃ and GdMnO ₃	95
3.5	A phenomenological model for the transition	99
3.6	Microscopic scenarios for the phenomenological model	104
3.7	Issue of Joule heating	107
3.8	Conclusion	109
4	Magnetoresistance of nominally pure LaMnO₃ single crystals.	110
4.1	Introduction	111
4.2	Investigation of presence of Mn ⁴⁺ in the three LaMnO ₃ single crystals	113
4.2.1	High temperature XRD of LaMnO ₃ single crystals and variation of structural transition	113
4.2.2	XPS and EELS Analysis to check the mix valency of Mn	114
4.3	D.C. Magnetisation in the three LaMnO ₃ samples	116
4.4	A.C. susceptibility of the three LaMnO ₃ samples	122
4.5	Magneto-transport measurements	125
4.5.1	Temperature dependent Magnetoresistance of the three LaMnO ₃ single crystals	126
4.5.2	Field dependence of MR	127
4.5.3	Phenomenological model for MR in LaMnO ₃	129
4.5.4	Role of D(H) in the three LaMnO ₃ samples	133
4.6	Conclusion	135

5	Electrostatic EDL gate effect on the electrical transport of $\text{La}_{0.85}\text{Ca}_{0.15}\text{MnO}_3$	137
5.1	Introduction	138
5.2	Modulation of GB controlled non-linear transport in nano-structured film	139
5.2.1	Making of EDL-FET device and formation of electric double layer	140
5.2.2	Static and dynamic characteristics of the channel	143
5.2.3	Modulation of the Grain boundary conductance by the EDL gate dielectric	145
5.2.4	Transient response of the EDL-FET device and characteristics of the gate dielectric	149
5.3	Control of Electronic phases in manganites using EDL-FET	151
5.3.1	Gate bias modulated temperature dependent channel resistance with coexisting electronic phases	151
5.3.2	The Field effect and induced charge in channel	155
5.3.3	Quantitative comparison of gate dielectric induced carrier modulation with that achieved by chemical doping(x)	156
5.3.4	Dependence of the activation energy of transport on the gate bias.	158
5.3.5	Control of coexisting electronic phases by the electrostatic gate	159
5.4	Conclusion	163
6	Strain and Phase separation effect on the transport in ferromagnetic insulating manganite	165
6.1	Introduction	166
6.2	Substrate induced strain in the film of $\text{La}_{0.85}\text{Ca}_{0.15}\text{MnO}_3$	169
6.3	Determination of the Scale of inhomogeneity present in the three thin films by local conduction mapping	172
6.4	Differences in tunnelling conductivities in $\text{La}_{0.85}\text{Ca}_{0.15}\text{MnO}_3$ films grown on NGO and STO substrates	178
6.5	Effect of strain and inhomogeneity on the electronic transport of the $\text{La}_{0.85}\text{Ca}_{0.15}\text{MnO}_3$ film grown on different substrates	180
6.6	Discussion	183
6.7	Conclusion	185
7	Conclusion and future outlook	186
7.1	Conclusion	186
7.2	Future outlook	188
A	Appendix	190
A.1	Increase of temperature due to applied bias in LaMnO_3	190
A.2	Magnetoresistance of the $\text{La}_{0.85}\text{Ca}_{0.15}\text{MnO}_3$ film grown on single crystal substrates of NGO, LAO and STO	192
A.3	The C++ code for pulse voltage measurement in LaMnO_3	193
A.4	The C++ code for $\rho - T$ measurement in cryogen free VTI system	199
	Bibliography	202

List of Figures

1.1	(a) Ideal cubic structure of perovskite oxides. (b) Distorted orthorhombic structure from ideal cubic structure. Image from [12].	3
1.2	Schematic diagram of (a) the crystal field splitting (Δ_{cf}) of Mn d levels into e_g and t_{2g} levels. Further splitting of e_g levels occurs due to JT splitting (Δ_{JT}) and (b) JT distortion of the MnO_6 octahedra. Image from [16].	6
1.3	Schematic diagram of spins and orbitals arrangement in superexchange. The orbitals involved are Mn e_g and O 2p. The dashed arrows represent the virtual transfer of the electron between these orbitals. This means that the electron is located on the oxygen ion for the majority of the time but can be found in the manganese orbital indicated by the arrow. The three panels result in an (a) AFM, (b) AFM, and (c) FM arrangement of the core manganese spins respectively. Image from [19].	8
1.4	Schematic diagram of the double exchange mechanism. Image from [19].	9
1.5	Schematic diagram of hopping of electron from Mn^{3+} to Mn^{4+} site. Image from [26].	10
1.6	Schematic diagram of (a) unipolar and (b) bipolar resistive switching.	12
1.7	Switching of resistance states (HR: High Resistivity, LR: Low Resistivity) for single crystal $Pr_{0.7}Ca_{0.3}MnO_3$ in the COI state at temperature $T = 20$ K, as a function of applied voltage. Image from Asamitsu et al. [35].	13

- 1.8 Phase diagram of $\text{La}_{1-x}\text{Ca}_x\text{MnO}_3$. PMI: Paramagnetic Insulator, FMM: Ferromagnetic Metal, FMI: Ferromagnetic Insulator, AFI: Antiferromagnetic Insulator, CAF: Canted AF and CO: Charge/Orbital Ordering. Filled and open circles indicate Neel (T_N) and Curie (T_C) temperatures respectively. Stars indicate the orbitally ordered Orthorhombic (O) to orbitally disordered pseudo-Orthorhombic (O*) phase structural transition temperature. Image from [1, 2, 7]. . . . 15
- 1.9 Generic spectroscopic images ($0.61\mu\text{m} \times 0.61\mu\text{m}$; scale bar: 100 nm) of the local electronic structure of $\text{La}_{0.73}\text{Ca}_{0.27}\text{MnO}_3$ thin film taken just below T_C in magnetic fields of 0, 0.3, 1, 3, 5, and 9 T (from left to right and top to bottom). Parts of the surface are insulating (light colors), whereas others are metallic (dark colors) or in an intermediate state. Image from [59]. . . . 17
- 1.10 Magnetic field dependence of resistivity of $\text{La}_{0.67}\text{Ca}_{0.33}\text{MnO}_3$ thin film at different temperatures. Image from [64]. . . . 18
- 1.11 (a) Temperature dependence of (a) resistance and (b) volume fraction of FM for $\text{La}_{5/8}\text{Ca}_{3/8}\text{MnO}_3$ film in 0, 1, 2, 3, 5, 8, and 10 T. The solid red lines in panel (a) are the fitting results using Eqn. (1.3). (c) Magnetic field dependence of f_{FM} at different temperatures. Image from [77]. . . . 19
- 1.12 Illustration of the zero-temperature behaviour of various correlated materials as a function of sheet charge density (n_{2D}). Silicon is shown as a reference. The examples for high T_C superconductors and for colossal magnetoresistive (CMR) manganites reflect $\text{YBa}_2\text{Cu}_3\text{O}_{7-\delta}$ and $(\text{La,Sr})\text{MnO}_3$, respectively. The top bar has been drawn to illustrate schematically the richness of materials available for field-effect tuning and the spectrum of their phases. AF: antiferromagnetic; FM: ferromagnetic; I: insulator; M: metal; SC: superconductor; FQHE: fractional quantum Hall effect; Wigner: Wigner crystal. Image from [80]. . . . 21
- 1.13 Cross-section of a typical sample geometry used for field-effect studies. S, source; G, gate; D, drain. Image from [80]. . . . 21

1.14	The temperature (T) dependence of the sheet resistance (R_s) at gate voltage (V_G) of 0 and ± 3 V. The positive and negative V_G correspond to electron and hole doping, respectively. The inset shows gate voltage dependence of both T_C (Curie temperature) and T_{MI} (metal to insulator transition temperature) defined as the temperature where $d(\ln R_s)/dT = 0$ on cooling. Right side image shows $R_s - T$ curves of the device at the magnetic field (B) of 5 T for $V_G = 0$ and ± 3 V. Image from [85].	23
2.1	(a) Schematic diagram of the floating Zone melting apparatus. 1,7 represents ellipsoidal reflectors, 2 is the feeding rod, 3 is the crystal, 4 is the heater, 5 represents light flux regulator and 6 is the xenon lamp. (b) Design of the crystallization chamber: (1) Insulator, (2) RF coil, (3) eddy current concentrator, (4) annealing furnace, (5) siloxane rubber packing, (6) quartz container. Image is from Balbashov et. al. [101].	31
2.2	Single crystal of $(La_{0.7}Ca_{0.3})_{0.93}MnO_3$ made by floating zone technique. scale is in cm. From Shulyatev et al. [100].	33
2.3	Binary phase diagram of La_2O_3 - Mn_2O_3 in air. From Roosmalen et al. [102].	34
2.4	PLD set up in our lab.	37
2.5	(a) Rotating target holder inside the chamber. (b) Substrate holder.	38
2.6	Schematic diagram of the PLD technique.	39
2.7	(a) Area of the focussed laser spot at the target place. (b) Intense area of the laser plume at the substrate place.	40
2.8	SEM image of the target pellet heated at (a) 1100°C, (b) 1400°C and (c) 1600°C.	41
2.9	(a) XRD of the powder taken from the $La_{0.85}Ca_{0.15}MnO_3$ target. (b) EDAX analysis of the target pellet.	42
2.10	Schematic diagram of (a) X-ray diffraction from the crystal planes. (b) XRD measurement technique.	45
2.11	Schematic diagram of the SEM imaging technique (courtesy: Ref. [114]).	48

2.12	(a) SEM image of one of the PLD grown $\text{La}_{0.85}\text{Ca}_{0.15}\text{MnO}_3$ film on NGO. Image shows a smooth surface with lower concentration of particulates. (b) Approximate thickness of a $\text{La}_{0.85}\text{Ca}_{0.15}\text{MnO}_3$ film grown on Si substrate with 4000 laser shots in PLD using cross-sectional SEM.	49
2.13	Schematic diagram of (a) interaction of sample surface with energetic electron beam (from Ref. [115]) and (b) emission of characteristic X-rays form the element.	50
2.14	EDAX data of LaMnO_3 -1	52
2.15	Energy-loss spectrum of LaMnO_3 -1 nano particle in the low loss region.	53
2.16	Energy-loss spectrum of LaMnO_3 -1 nano particle	54
2.17	Schematic diagram of the XPS measurement procedure.	55
2.18	Core level XPS spectra of LaMnO_3 -1.	56
2.19	Schematic diagram of the AFM measurement procedure.	57
2.20	AFM image of the $\text{La}_{0.85}\text{Ca}_{0.15}\text{MnO}_3$ thin film deposited with different laser shots on SiO_2/Si in PLD . Color code representing the height variation on the surface.	59
2.21	AFM image of the $\text{La}_{0.85}\text{Ca}_{0.15}\text{MnO}_3$ thin film deposited with 1000 laser shots in PLD on (a) NGO, (b) LAO and (c) STO substrates. Dotted lines are showing the preferred pattern of the the films.	60
2.22	(a) Measurement of the vertical distance of the etched $\text{La}_{0.85}\text{Ca}_{0.15}\text{MnO}_3$ film on SiO_2/Si substrate in AFM. (b) Height profile at 1, 2, and 3 (green, red and blue) lines and corresponding vertical heights (from the zero reference level) are given in the below table.	61
2.23	Schematic diagram of the ellipsometry method	62
2.24	Ellipsometry data of $\text{La}_{0.85}\text{Ca}_{0.15}\text{MnO}_3$ thin film grown on SiO_2/Si , NGO, STO and LAO substrates by PLD with 1000 shots	63
2.25	Schematic diagram of the set up coils in the a.c. susceptibility measurement. Image from Ref. [120].	66

2.26	Schematic diagram of four probe measurement method for electrical measurement with (a) constant current source and voltmeter and (b) constant voltage source with current-meter and voltmeter	68
2.27	Sample Resistance (R) versus applied bias voltage (V) with corresponding values of variable resistor (R_L) in the circuit.	69
2.28	(a) Image of the measurement set up. (b) Schematic diagram of the sample stick connected with different measurement set-up. SM: Sourcemeater, TC: Temperature controller.	71
2.29	Schematic diagram of the VTI operation. Image from Ref. [121].	72
2.30	Schematic diagram of overlap of electronic weave functions of sample and tip. Image from Ref. [123].	74
2.31	Schematic diagram of the tunneling phenomenon in different biasing conditions. Image form Ref. [123].	75
2.32	Image of the RHK-UHV 350 STM system in our lab.	76
2.33	(a) Schematic diagram of to detect the tunnel current. (b) Schematic diagram of the electronic circuit for imaging in constant current mode [124].	77
2.34	Image of the Scan-head of an UHV-STM system with the schematic view of the sample holder [127].	79
3.1	Temperature dependent resistivities (ρ) of (a) LaMnO_3 -1, LaMnO_3 -2 and LaMnO_3 -3 single crystals, (b) $\text{La}_{0.9}\text{Sr}_{0.1}\text{MnO}_3$ single crystal and (c) GdMnO_3 thin film.	84
3.2	Adiabatic polaronic fit of $\rho - T$ for (a) LaMnO_3 -1, LaMnO_3 -2 and LaMnO_3 -3 single crystals, (b) $\text{La}_{0.9}\text{Sr}_{0.1}\text{MnO}_3$ single crystal and (c) GdMnO_3 thin film.	86
3.3	Circuit configuration to measure bias voltage (V) versus sample current(I) for (a) LaMnO_3 single crystals and $\text{La}_{0.9}\text{Sr}_{0.1}\text{MnO}_3$ single crystal. R_L is the variable resistor to limit the current through the sample and (b) GdMnO_3 thin film. Due to the high resistance of the film R_L was not used in the circuit.	87

3.4	Temperature dependent $I-V$ data for (a) LaMnO_3 -1, (b) LaMnO_3 -2 and (c) LaMnO_3 -3 single crystals.	88
3.5	Power law dependence of $I-V$ curve before and after switching at 180K for LaMnO_3 -1.	89
3.6	(a) Sample voltage (V_S) versus bias voltage (V) at different temperatures, (b) Typical threshold voltage V_{Th} at which the sample voltage jumps to a lower value and (c) Variation of the threshold field E_{th} for the three different LaMnO_3 crystals used.	90
3.7	(a) Sample resistance (R) vs. applied bias voltage (V) for LaMnO_3 -1 and (b) Percentage of change in resistivity with temperature for the three LaMnO_3 samples used at the resistive state transition.	91
3.8	(a) $I-V$ characteristics of $\text{La}_{0.9}\text{Sr}_{0.1}\text{MnO}_3$ at different temperatures. Inset shows the data at higher temperatures $T > 160\text{K}$ and (b) Sample voltage versus bias voltage at different temperatures in the range $10\text{K} < T < 240\text{K}$. Inset shows the jump of sample voltage at the resistive state transition below 50K.	92
3.9	(a) $I-V$ curve of the GdMnO_3 film with positive and negative bias; green arrows showing the threshold voltage for switching to LRS and blue arrows showing the threshold voltage for switching to HRS. (b) Power dependence of the $I-V$ curve.	93
3.10	$\rho-T$ curves for a LaMnO_3 single crystal measured at different constant bias from 1V to 310V in four probe configuration. The transition in resistivity from LRS to HRS on cooling at different bias can be seen.	96
3.11	$\rho-T$ measurement in GdMnO_3 with different bias showing the temperature dependent resistivities in the two states.	97
3.12	Linear fit to $\rho-T$ curve in LRS for GdMnO_3	98
3.13	(a) Two phase model below $E < E_{th}$; f represents the metallic phase (the dark circles) and $(1-f)$ is the polaronic insulating phase. (b) Formation of the parallel conducting channel (ρ_m) above $E > E_{th}$ when f becomes equal to a critical concentration f_c	100
3.14	(a) Variation of the fraction f with the applied field E for LaMnO_3 -1. (b) Activated temperature variation of the fraction f for LaMnO_3 -1.	101

3.15	Variation of metallic fraction f vs. electric field E in increasing and decreasing field sequence. f vs. E fitted with an activated dependence on E	102
3.16	Resistivities of LaMnO_3 , GdMnO_3 and $\text{La}_{0.9}\text{Sr}_{0.1}\text{MnO}_3$ in HRS in comparison to the ρ_m of the LRS as deduced from the experiment.	103
3.17	Schematic diagram of the adiabatic potentials for (a) without charge transfer and (b) with charge transfer. Q is related to the lattice degrees of freedom and U is the charge disproportion energy. Image is reproduced from [89] with author's permission.	106
3.18	Time dependent current measurement on application of a switching voltage for (a) LaMnO_3 -2 and (b) GdMnO_3 thin film.	107
4.1	"A" type AFM structure of perovskite unite cell. Spins of Mn atoms are represented by upward and downward arrows.	111
4.2	(a), (b) and (c) High temperature XRD of three LaMnO_3 single crystals.	114
4.3	(a) XPS spectra of Mn $2p_{3/2}$ peak for LaMnO_3 -1. (b) Mn EELS peak for LaMnO_3 -1 (c) Mn EELS peak for LaMnO_3 -2 and (d) Mn EELS peak for LaMnO_3 -3.	115
4.4	Calibration of Mn valence from the intensity ratio of L_3 and L_2 lines of different known Mn valence oxide compounds. Image form [165]	116
4.5	Zero field cooled $M - T$ data of the three LaMnO_3 samples with 20 Oersted field.	117
4.6	(a) $M - H$ curve for all the three LaMnO_3 samples below T_N . Inset shows the $M - H$ curve at 300K). Ferromagnetic hysteresis loop at lower field for (b) LaMnO_3 -1, (c) LaMnO_3 -2 and (d) LaMnO_3 -3.	118
4.7	$M - T$ curves in the presence of different applied magnetic field (a) for LaMnO_3 -1 ,(b) for LaMnO_3 -2, and (c) for LaMnO_3 -3.	119
4.8	Determination of T_{CL} with different applied field (50 Oe, 100 Oe, 500 Oe and 1000 Oe) for LaMnO_3 -1.	120
4.9	Determination of T_{CL} with different applied field (50 Oe, 100 Oe, 500 Oe and 1000 Oe) for LaMnO_3 -2.	120

4.10	$\frac{1}{\chi}$ vs. T plot with different applied field (50 Oe, 100 Oe, 500 Oe and 1000 Oe) for LaMnO ₃ -3.	121
4.11	Variation of T_{CL} with applied field.	121
4.12	Frequency dependent real part of linear a.c susceptibility (χ_1) (a) for LaMnO ₃ -1 ,(b) for LaMnO ₃ -2, (c) for LaMnO ₃ -3. (d) Activated fit of relaxation time (τ).	123
4.13	Fitting of Vogel-Fulcher equation for (a) LaMnO ₃ -1, (b) LaMnO ₃ -2 and (c) LaMnO ₃ -3.	125
4.14	$\rho - T$ curve in the presence of magnetic field (a) for LaMnO ₃ -1, (b) for LaMnO ₃ -2, (c) for LaMnO ₃ -3. (d) Temperature dependent MR for the three samples at 8T field.	126
4.15	(a) $R - H$ curve for LaMnO ₃ -1 at $T < T_N$. Inset shows $R - H$ curve at $T > T_N$. (b) $R - H$ curve for LaMnO ₃ -2 at $T < T_N$. Inset shows $R - H$ curve at $T > T_N$. (c) $R - H$ curve for LaMnO ₃ -3 at $T < T_N$.	128
4.16	Magnetic field dependent MR for (a) LaMnO ₃ -1, (b) LaMnO ₃ -2 and (c) LaMnO ₃ -3.	128
4.17	Fitting of FM cluster model (Eqn. 4.10) to MR vs. T curve for all the three LaMnO ₃ samples at 8T field.	130
4.18	((a) MR vs. T data of LaMnO ₃ -1 at 8T and 14T. Red curve shows the fitted curve with Eqn. 4.10. (b) Theoretically calculated curve using the Eqn. 4.10 with the fitting parameters form experimental curve.	132
4.19	Dependence of $D(H)$ on H and fitted with $D(H) = 1 + pH + qH^2$.	132
4.20	Magnetic field dependent MR for (a) LaMnO ₃ -1,(b) LaMnO ₃ -2 and (c) LaMnO ₃ -3. Red curve is the fitted curve with eqn. 4.10.	134
4.21	Variation of $\frac{D(H) - 1}{H}$ vs. H for three LaMnO ₃ samples.	134
5.1	(a) Surface topography of the La _{0.85} Ca _{0.15} MnO ₃ film taken by AFM. (b) Grain size distribution of the film.	141
5.2	Schematic diagram of the EDL-FET device for measuring gate bias (V_G) dependent $I_{DS} - V_{DS}$ curves. (b) Biasing arrangement of the EDL-FET device for measuring $\rho - T$ curves with different V_G .	142
5.3	$I - V$ curve of the device with La _{0.85} Ca _{0.15} MnO ₃ channel without any gate bias.	143

5.4	Static Characteristic of the EDL–FET device with nano-structured $\text{La}_{0.85}\text{Ca}_{0.15}\text{MnO}_3$ channel.	144
5.5	Dynamic Characteristic of the EDL-FET device with nano-structured $\text{La}_{0.85}\text{Ca}_{0.15}\text{MnO}_3$ channel. Black arrow is showing gate current I_G form $V_G = +4\text{V}$ to -10V and green arrow is showing I_G form $V_G = -10\text{V}$ to $+4\text{V}$.	144
5.6	The conductance $G(V_{DS}) = dI_{DS}/dV_{DS}$ of the channel as a function of V_{DS} for different applied gate bias.	145
5.7	The conductance $G(V_{DS}) = dI_{DS}/dV_{DS}$ of the channel as a function of V_{DS} for different applied gate bias. The lines through the data are fit to the equation $G = G_0 + G_2V^{4/3}$.	147
5.8	Dependence of (a) G_0 and (b) G_2 on gate bias V_G .	148
5.9	Top panel shows the step change in the voltage V_G . Middle panel shows the transient response of the normalised (I_{DS}/I_{max}) drain current I_{DS} at fixed $V_{DS} = 0.4\text{V}$ and bottom panel shows the transient response of gate current I_G .	149
5.10	$R - T$ curves of the channel with different gate bias.	152
5.11	(a) $\text{La}_{1-x}\text{Ca}_x\text{MnO}_3$ phase diagram for chemical doping (x) vs. temperature (T) plane. Different phases are PI: Paramagnetic Insulator, FM: Ferromagnetic Metal, FI: Ferromagnetic Insulator, AF: Antiferromagnetic Insulator, CAF: Canted AF and CO: Charge/Orbital Ordering. "O" represents the Jahn-Teller distorted orthorhombic structure and O* represents octahedra rotated structure. Image from [1,2,7,50,51,139]. (b) $\rho - T$ data of $\text{La}_{0.82}\text{Ca}_{0.18}\text{MnO}_3$ (LCMO18) and $\text{Nd}_{0.7}\text{Pb}_{0.3}\text{MnO}_3$ (NPMO30) single crystals showing existence of different electronic phases. T_C is the onset of PI to FM transition and T_{FMI} is the onset of FI state. Image is adopted from [194].	152
5.12	The characteristics temperature regions (I, II and III) of the LCMO channel as determined from transport data by plotting normalized $\frac{d(\ln RT^{-1})}{dT^{-1}}$ vs. T at $V_G = +4\text{V}$, 0V and -4V . Colour boundaries indicate different characteristic transition temperatures. Red arrow shows the position of T_C^* .	153
5.13	Variation of $T_{OO'}$, T_C^* and T_{FI} as a function of gate bias.	154

5.14	Schematic diagram of (a) the effect of $-V_G$ within the channel; s and d are source and drain electrodes. h, e, and GR represents holes, electrons and grains. Black and Red (lower) potential wells represent the GB barrier potential at $V_G = 0V$ & at $-V_G$, and (b) the effect of $+V_G$ within the channel. Black and Red (higher) potential wells represent the GB barrier potential at $V_G = 0V$ and at $+V_G$	156
5.15	Variation of δx and δx_e with different V_G calculated from induced charge due to field effect (δx_e) and from the change in $T_{OO'}$ (δx).	158
5.16	Variation of E_a with V_G . Inset shows the polaronic fit to $R - T$ data for $V_G = +4V, 0V$ and $-4V$	159
5.17	Temperature dependence of f with different V_G	161
5.18	The field dependence of the scaled $f(V, T)/f_0$ with V_G/V_0 . The inset shows the T dependence of $V_0(T)$	162
6.1	Rocking curve of the $\text{La}_{0.85}\text{Ca}_{0.15}\text{MnO}_3$ film on (a) LAO (1 0 0) (b) NGO (2 0 0) and (c) STO (2 0 0). Films were grown in the same deposition process using same deposition condition.	169
6.2	Schematic diagram of the nature of substrate induced strain due to lattice mismatch when (a) $a_{Sub} < a_{bulk}$ and (b) $a_{Sub} > a_{bulk}$	171
6.3	AFM image of the $\text{La}_{0.85}\text{Ca}_{0.15}\text{MnO}_3$ thin film deposited with 1000 laser shots in PLD on (a) NGO, (b) LAO and (c) STO substrates. Dotted lines are showing the preferred pattern of the the films.	172
6.4	Topographic image of the $\text{La}_{0.85}\text{Ca}_{0.15}\text{MnO}_3$ film on NGO substrate in $500\text{nm} \times 500\text{nm}$ area. Green dots represents the points in a matrix from where $\frac{dI}{dV}$ spectra were taken and green arrow represents the position of the STM tip.	175
6.5	Local conduction mapping (LCMAP) in a $500\text{nm} \times 500\text{nm}$ area for $\text{La}_{0.85}\text{Ca}_{0.15}\text{MnO}_3$ film on NGO at (a) 300K and (b) 110K at 0.5V. Colour code (from blue to red) represents lower conductive region to higher conductive regions.	176

6.6	Local conduction mapping(LCMAP) in a $500\text{nm} \times 500\text{nm}$ area for $\text{La}_{0.85}\text{Ca}_{0.15}\text{MnO}_3$ film on STO at (a) 300K and (b)110K. Colour code (from blue to red) represents lower conductive region to higher conductive regions.	177
6.7	$G - V$ curve in the phase-I & phase-II (blue and red coloured regions in LCMAP) in $\text{La}_{0.85}\text{Ca}_{0.15}\text{MnO}_3$ film on NGO at 110K.	179
6.8	$G - V$ curve in the phase-I & phase-II regions (blue and red coloured regions in LCMAP) in $\text{La}_{0.85}\text{Ca}_{0.15}\text{MnO}_3$ film on STO at 110K.	180
6.9	(a) $\rho - T$ curves of the film on LAO, NGO and STO (b) Adibatic polaronic fit to the $\rho - T$ curves.	181
6.10	$\frac{d(\ln\rho T^{-1})}{d(T^{-1})}$ vs. T for film on LAO, STO and NGO. Region I, II and III represents different coexisting electronic phases.	182
A.1	(a) Temperature rise and fall (ΔT) for each ON and OFF pulses from 10 to 190 V and (b) from 200 to 340V. Total increment in temperature is calculated by adding the ΔT for each ON and OFF pulses	191
A.2	$\rho - T$ curve of the $\text{La}_{0.85}\text{Ca}_{0.15}\text{MnO}_3$ films at different applied magnetic field H are shown in a, b and c. In d, e, and f, we have shown the variation of MR with T at different H	192

List of Tables

2.1	Dimension (Diameter "D" and thickness "t") of the different single crystals used in various experiments.	35
2.2	Some excimer lasers with their corresponding wavelengths (λ).	37
2.3	EDAX quantification of compositional elements in $\text{La}_{0.85}\text{Ca}_{0.15}\text{MnO}_3$ target.	43
2.4	B.E values of different element form the XPS spectra.	56
2.5	Thickness (estimated from the different measurements) of the $\text{La}_{0.85}\text{Ca}_{0.15}\text{MnO}_3$ films grown on different substrates with 1000 laser shots.	63
2.6	Different electrical and magnetotransport measurements. R , ρ , I , V , T , I_{DS} , V_{DS} , I_G and V_G represents resistance, resistivity, current, voltage, temperature, source to drain current, source to drain voltage, gate current and gate voltage respectively.	67
3.1	Comparison of resistive switching in the LaMnO_3 single crystals and GdMnO_3 thin film.	95
4.1	Determination of δ in the three LaMnO_3 samples	116
4.2	Coercive and exchange fields for three LaMnO_3 samples from Fig. 4.6.	118
4.3	M in μ_B/Mn for the three LaMnO_3 samples at $T < T_N$ and $T > T_N$	122
4.4	Fitting parameters from VogelFulcher equation.	125
4.5	Fitting parameters from MR vs T data fitted with equation 4.10 for $H = 8\text{T}$	131
4.6	Fitting parameters from equation 4.10 for LaMnO_3 -1.	132
4.7	Variation of $D(H)$ for three LaMnO_3 single crystals.	134

4.8	Comparison of C , $\frac{D(H)-1}{H}$, E_{τ} (eV), T_0 , T_R and $J(0)$ in the three LaMnO_3 samples.	135
6.1	Orthorhombic and pseudocubic lattice constants and lattice spacing of bulk $\text{La}_{0.85}\text{Ca}_{0.15}\text{MnO}_3$ and NGO, LAO and STO substrates from ICDD data base and MTI corporation.	170
6.2	Values of e_{\parallel} , e_{\perp} along in plane and out of plane directions in the $\text{La}_{0.85}\text{Ca}_{0.15}\text{MnO}_3$ film and the effective strain in the film.	171
6.3	Values of E_a for $\text{La}_{0.85}\text{Ca}_{0.15}\text{MnO}_3$ film on LAO, NGO and STO.	181

Chapter 1

Introduction

In this chapter, we will give a basic introduction to perovskite in the context of manganites. We will discuss the physical properties of manganite in undoped and lightly hole doped regions and the underlying physics that makes these system interesting. A brief review will be given on some novel and interesting electronic and magnetic properties associated with perovskite manganites. An overview of the thesis will be presented to highlight the main studies made in this thesis.

1.1 Motivation

Perovskite oxides, in particular manganites, show a fascinating range of electronic transport, magnetic and dielectric phenomena which include effects such as colossal magnetoresistance (CMR), charge and orbital ordering (COO), ferroelectricity, multiferroicity and a number of related phenomena due to their complicated as well as adaptive structure. The physical properties of perovskites are strongly dependent on its structure, chemical composition, orbital & charge ordering, and spin distribution [1, 2]. "Perovskites" is the generic name for any oxides which have the same crystal structure as calcium titanate (CaTiO_3) or ABO_3 , where "A" stands for rare-earth elements like La, Pr, Nd, Gd, "B" represents a transition metal ion like Mn, Ti, Co and O is the oxygen. The ABO_3 structure is the special case of Ruddlesden-Popper (RP) phases ($\text{A}_{n+1}\text{B}_n\text{O}_{3n+1}$) which crystallize in $I4/mmm$ or $Fmmm$ space group with tetragonal or orthorhombic unit cell. RP phase can also be written as $\text{A}_{1+1/n}\text{BO}_{3+1/n}$ and when $n \rightarrow \infty$, it gives ABO_3 . There are hundreds of different oxides which have this structure and shows various electronic and magnetic properties like insulating, antiferromagnetic (AFM), ferromagnetic (FM), ferroelectric, piezoelectric, thermoelectric, semiconducting, conducting and probably most famous superconducting [3, 4]. These oxides have been investigated for a long time due to this wide spectrum of electronic, magnetic and structural properties.

In our work, we deal with perovskites having $\text{A}_{1-x}\text{C}_x\text{MnO}_3$ (where $\text{A} = \text{La, Gd}$, $\text{C} = \text{Ca, Sr}$ and x varies from 0 to 0.15) composition. The manganites exhibit a rich phase diagram having various electronic and magnetic properties. The study on these electronic and magnetic phases helps us to gain more insight in correlated electron systems and explore the possibilities of these material for technical applications. In these strongly correlated oxides, electronic states are localized due to strong electron-phonon coupling mediated by the Jahn-Teller (JT) distortion leading to the formation of polarons. Below a certain temperature (T_{JT}), cooperative JT distortions set in and one obtains a polaronic insulating state accompanied by a orthorhombic distortion of the lattice [5–8]. The orthorhombic polaronic insulating state can be destabilized by hole doping (x) using divalent substitution (like Ca, Sr) at the rare-earth site. This leads to insulator-metal transition with long range FM order which triggers

certain phenomena like CMR, COO and electronic phase separation. These form the complete gamut of phenomena that make the field of manganites so interesting. The effect of external stimulations that perturb the ground states of these samples have been an important research interest over the last two decades [1, 2] and researchers have studied the effect of external stimulations like pressure [9], very high magnetic field [10] as well as high electric field close to T_{JT} in these electronic states [11]. There still remains some unexplored areas in electrical and magnetic transport properties of the parent and as well as hole doped perovskites which needs detail understanding.

1.2 Crystal structure of perovskites

As mentioned earlier, perovskite has ABO_3 structure where BO_6 octahedra ("B" is at the centre of the octahedra) situated at the body center position of the cube with "A" at the corner positions of the cube. The ideal perovskite structure is shown in Fig. 1.1. The BO_6 octahedra plays a crucial role in the

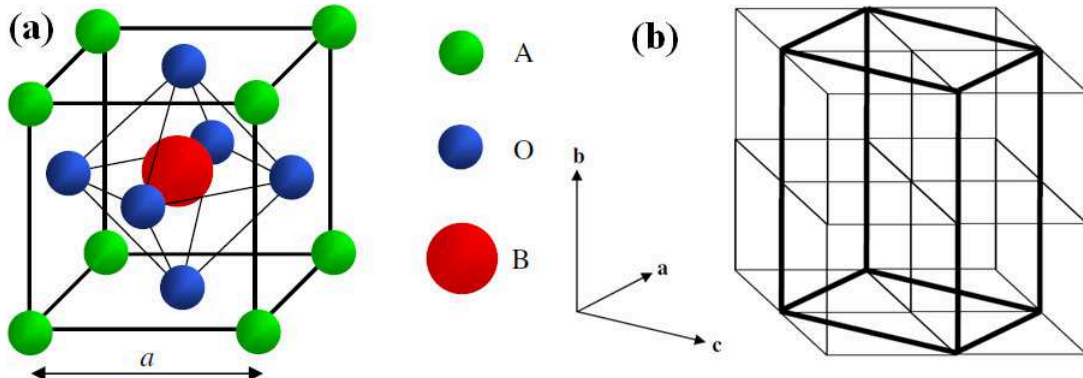


Figure 1.1 (a) Ideal cubic structure of perovskite oxides. (b) Distorted orthorhombic structure from ideal cubic structure. Image from [12].

ABO_3 structure. The octahedra can be tilted or distorted depending on the chemical composition of "B" atom and B–O bond length. To maintain the ideal cubic structure, the compositional ions must satisfy the relation $(r_A+r_O)\approx\sqrt{2}(r_B+r_O)$, where r_A , r_B and r_O are ionic radii of the A, B and oxygen ions respectively. The tolerance factor t_G (introduced by Goldschmidt) can be defined to distinguish the effects of different chemical compositions, having atoms of different size with different doping

levels, on the unit cell structure and it is expressed as $t_G = \frac{r_A + r_O}{\sqrt{2}(r_B + r_O)}$ [13]. For an ideal perovskite structure, $t_G \approx 1$ and a small deviation (depending on the ionic radii of compositional atoms) from this value leads to a considerable amount of stress. This stress leads to the displacement of atoms from their ideal positions to minimize the free energy and a distorted perovskite structure is formed. The perovskite structures are stable within the range $0.89 < t_G < 1.02$ in oxides. The oxygen stoichiometry of these ABO_3 compounds depend on the synthesis conditions. Most of the perovskite manganites ($A_{1-x}C_xMnO_3$) are of cubic structure with $t_G = 1$. The cubic structure is distorted by cation concentration, cation size mismatch and JT effect. This distortion results two most frequent structures like orthorhombic ($t_G < 0.96$) and rhombohedral ($0.96 < t_G < 1$). For example, parent $LaMnO_3$ has a distorted orthorhombic structure ($t_G \approx 0.89$) below 750K having $pnma$ space group. The crystal structure of the manganites depends on the level of doping (x), the A-site cation size as well as the temperature. The cubic structure shown in Fig. 1.1 is realized only at a very high temperature. The average size of the A-site cations plays a strong role in determining the physical properties. This is due to the fact that the A-site cations are relatively small, such that the surrounding MnO_6 octahedra are tilted. The presence of single valence electron in a degenerate level leads to the JT distortions of these octahedra which also has significant effects on the physical properties. Due to the reduction of radius of the A site, BO_6 octahedra rotate and tilt, resulting in a decrease of the B–O–B bond angle (θ) from 180° . The hopping amplitude for carriers to move from one Mn site to the next also decreases as θ reduces from 180° (for a 90° bond, the hopping involving a p orbital at the oxygen is zero). As the tolerance factor decreases, the tendencies to charge localization increase due to a reduction in the carrier mobility. The relevance of the crystal structure arises from the fact that in the manganites the three degrees of freedom (charge, spin and lattice) are coupled to each other. Thus, a change in the structure (lattice) is reflected in a change in the magnetic state (spin degree of freedom) or electronic state (charge degree of freedom) of the system. In addition, extrinsic and intrinsic strain also plays a significant role and due to that single crystals, epitaxial films and polycrystalline sample of manganites are often found to behave quite differently.

1.3 Cationic Disorder

The cationic radius $\langle r_A \rangle$ plays an important role to determine the physical properties of the manganites or perovskites. When two or more different cations placed on the rare earth element (A) lattice site at random, disorder is introduced in the crystal structure. The cationic disorder σ^2 (quantified by the variance of the A site cation radius distribution) and the average A site radius $\langle r_A \rangle$ are expressed as:

$$\sigma^2 = \sum_i (x_i r_{Ai}^2) - \langle r_A \rangle^2 \quad (1.1)$$

, where $\langle r_A \rangle = \sum_i x_i r_{Ai}$ is the average ionic radii of the ions "i" with fractional doping levels x_i and radii r_{Ai} , occupying the A site [14]. For an example, in $\text{La}_{1-x}\text{Ca}_x\text{MnO}_3$ system, the doping level x of divalent cation Ca controls the valence of Mn ions and the average radius of the cations (both divalent Ca and trivalent La) can be expressed as:

$$\langle r_A \rangle = (1-x)r_{La}^{3+} + xr_{Ca}^{2+} \quad (1.2)$$

The variation in radius introduces the distortion in lattice. We have mentioned in the earlier section that transfer integral of an e_g electron between two neighbouring Mn sites is mediated by the O 2p orbitals and hence the hybridization between Mn 3d orbitals and O 2p orbitals is sensitive to the lattice distortion and tilting of the MnO_6 octahedra. The distortion increases with the decrease of $\langle r_A \rangle$ which causes the narrowing of e_g band. This will localize the itinerant electron and the system will become more insulating.

1.4 Electronic structure of perovskite manganites

The physical properties of the parent and doped perovskite manganite system strongly depend on the electronic structure of the transition metal ion. The transition metal ion Mn in isolation has an active d shell with five degenerate levels. In the case of manganites, each Mn ion in the perovskite structure is surrounded by an oxygen octahedra. These degenerate levels get affected by the crystal field of the surrounding oxygen ions. The degenerate Mn-3d orbitals, placed in such an octahedral coordination,

get separated into lower lying t_{2g} states and higher lying e_g states [15]. The splitting of the degenerate d levels are shown in Fig. 1.2(a). This crystal field splitting (Δ_{cf}) between the t_{2g} and e_g states is about 1–2 eV. The Mn ion in manganites can be in its 2+, 3+, and 4+ ionization state corresponding

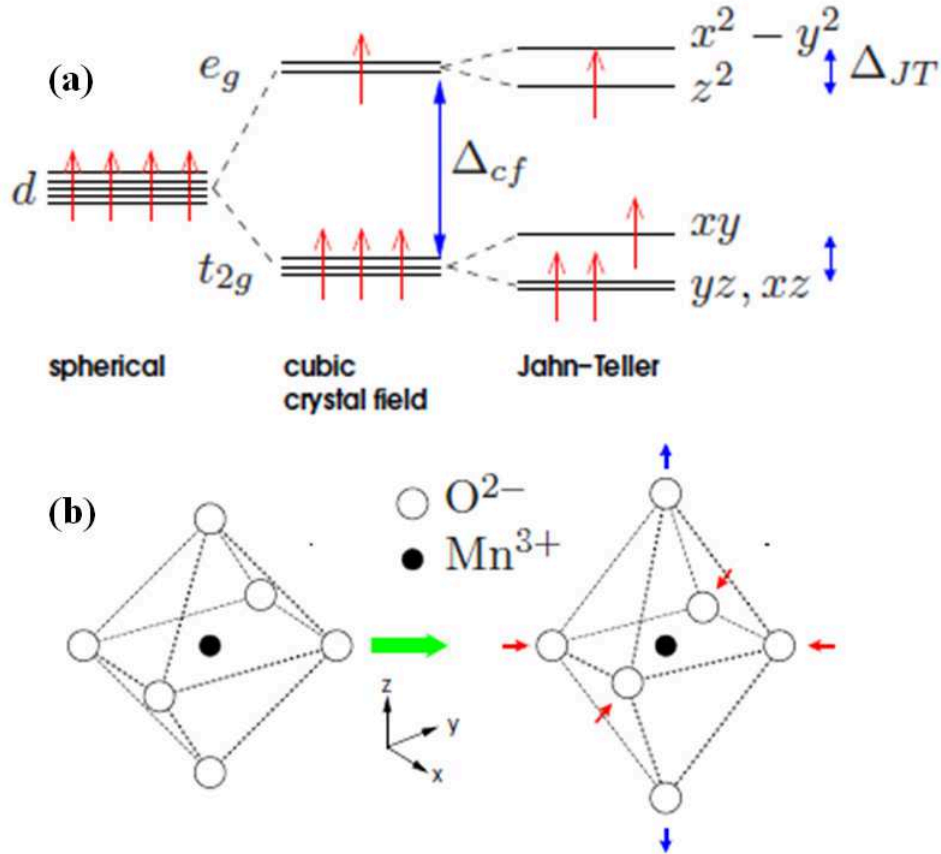


Figure 1.2 Schematic diagram of (a) the crystal field splitting (Δ_{cf}) of Mn d levels into e_g and t_{2g} levels. Further splitting of e_g levels occurs due to JT splitting (Δ_{JT}) and (b) JT distortion of the MnO_6 octahedra. Image from [16].

to 5, 4, and 3 electrons in the 3d level respectively. The electrons in the t_{2g} levels form a localized core spin of magnitude $3/2 \mu_B$, where μ_B is the Bohr Magnetron. Any remaining electrons occupy the e_g levels and may be localized or delocalized/itinerant. Delocalization of the Mn e_g electrons occurs via the intervening oxygen O 2p levels. If there is a single electron occupancy (for Mn^{3+}) at e_g level, the electron suffers a JahnTeller (JT) distortion which causes a deformation of the oxygen octahedra surrounding Mn^{3+} . This distortion lifts the degeneracy of the e_g levels, which in turn results in the lowering of energy of the electron (shown in Fig. 1.2(a)). Elongation of the octahedron along the axis

through the apical oxygens favours occupation of the $3z^2 - r^2$ orbitals, while compression along the said axis favours occupation of the $x^2 - y^2$ orbitals, of the Mn. The JT effect therefore mediates a coupling between the electrons and lattice (phonon) [17] in manganites. Typical range of JT splitting energy $\delta_{JT} \approx 0.25-1.5\text{eV}$. JT distortions can also lead to the localization of otherwise itinerant e_g electrons by forming lattice polarons with them. In the case of the parent compound LaMnO_3 , Mn atom has one e_g electron which get localized due to strong JT distortion and the Fermi level lies in the gap opened in the conduction band. Strong JT distortion along with onsite Coulomb repulsion (U) as well as charge transfer energy plays a crucial role to make the system like LaMnO_3 insulating. In the insulating state, the e_g electron carries the distortion as it hops from site to site creating a JT polaron. When electron vacancies or holes are created (due to the presence of Mn^{4+}) in the e_g orbital states by divalent atom substitution, the e_g electrons can be itinerant due to the lowering of JT effect. Thus it can play the role of conduction electron. This hole-doping (x) process thus corresponds to the creation of mobile Mn^{4+} species on the Mn sites and increases the conductivity of the system.

1.5 Magnetic interactions in manganites

The transition metal ion in perovskite oxides plays an important role for determining the magnetic structure as the direct exchange interaction between the cation is not possible due to the intervening oxygen. In case of manganites, magnetic interaction depends on the exchange interaction between the Mn ions. Wollan and Koehler (1955) published an extensive neutron diffraction study of the series of $\text{La}_{1-x}\text{Ca}_x\text{MnO}_3$ identifying the type of magnetic order displayed by the end compounds and built the first magnetic structure based phase diagram for the manganites. These interactions are relatively large between the two Mn spins separated by an O atom and are controlled by the overlap between the Mn d orbitals and the O p orbitals. Goodenough and Kanamori proposed some rules with rigorous mathematical insight for different magnetic interactions occurs in manganites [18]. They suggested that if neighbouring Mn ions point their empty orbitals towards O_2 then Mn-Mn separation is small and coupling between Mn ions is AFM or the interaction is superexchange. Superexchange is a very

common interaction in most of the oxides mainly in insulating magnetic oxides where the magnetic interaction between adjacent ions is mediated by intermediate nonmagnetic ion with a closed shell. The intermediate ion is O^{2-} in superexchange. If two orbitals on adjacent ions point towards each other, with one orbital fully occupied and the other orbital having a vacancy, then the electron will spend part of its time in the empty orbital on the other ion. For the case of the manganites, the orbitals involved are the vacant Mn e_g orbital and the occupied O 2p orbital, and so it is the O 2p electron that is "shared" between the two ions. This virtual transfer of the electron is what characterises superexchange. This mechanism leads either to a FM or an AFM alignment of the spins, depending on the occupancy of the Mn orbitals as depicted in Fig. 1.3. There is strong Hund's coupling between the core Mn t_{2g}

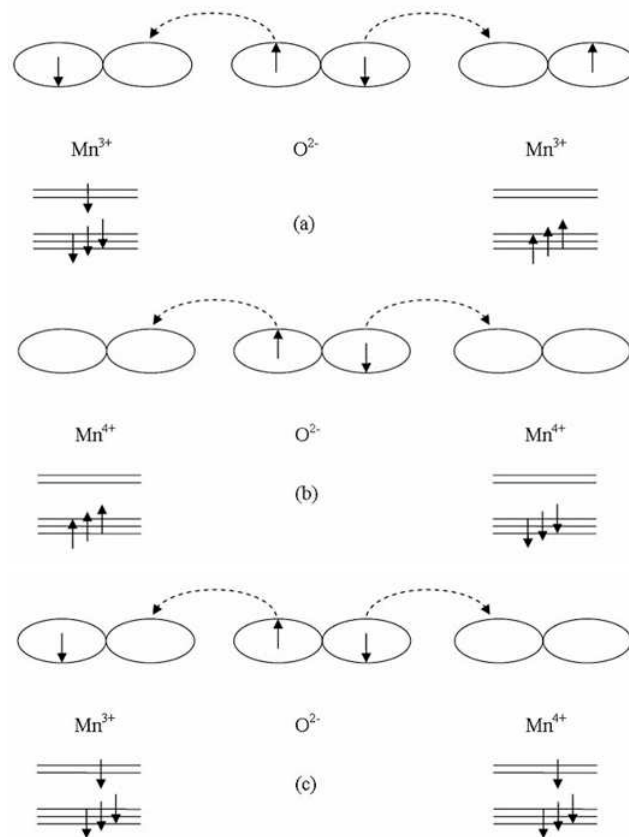


Figure 1.3 Schematic diagram of spins and orbitals arrangement in superexchange. The orbitals involved are Mn e_g and O 2p. The dashed arrows represent the virtual transfer of the electron between these orbitals. This means that the electron is located on the oxygen ion for the majority of the time but can be found in the manganese orbital indicated by the arrow. The three panels result in an (a) AFM, (b) AFM, and (c) FM arrangement of the core manganese spins respectively. Image from [19].

spins and any e_g electron(s). There are two cases to consider, namely when the Mn e_g orbital has one permanent electron (Mn^{3+}) and occasionally the virtual electron, or only the virtual electron (Mn^{4+}). For Mn^{4+} , the t_{2g} and permanent e_g electron will be spin aligned (Hund's rules), so that spin of the transferred electron has to have the opposite sign, as required by the Pauli exclusion Principle. For Mn^{4+} , the electrons in the Mn t_{2g} orbitals align with the virtual electron from the oxygen ion. By applying these two rules and noting that the two electrons from the O 2p orbital have opposite spins and the two adjacent empty Mn orbitals or two half-full orbitals will lead to AFM order, whereas an empty Mn orbital pointing towards a half-full one will lead to a FM alignment of the core Mn spins. Superexchange always results in an insulating state. Depending on the types of orbitals involved, the

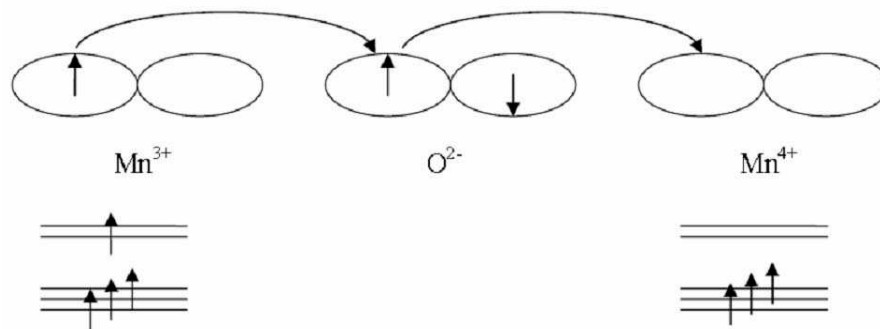


Figure 1.4 Schematic diagram of the double exchange mechanism. Image from [19].

interaction could be AFM or FM. For an example: $\text{Mn}^{3+}-\text{O}-\text{Mn}^{3+}$ interaction is AFM type whereas, $\text{Mn}^{3+}-\text{O}-\text{Mn}^{4+}$ may be AFM or FM type. LaMnO_3 has all the Mn ions at 3+ states, its ground state is AFM.

In addition to super exchange magnetic coupling in these manganites can also be double exchange. The strong correlation between ferromagnetism and metallic conductivity in doped manganites, Zener (in 1951) offered an explanation to understand the correlation between magnetism and conductivity of the magnetic oxides [20, 21]. Zener noted that, in doped manganese oxides, the two configurations $\phi_1: \text{Mn}^{3+}-\text{O}_2-\text{Mn}^{4+}$ and $\phi_2: \text{Mn}^{4+}-\text{O}_2-\text{Mn}^{3+}$ are degenerate and are connected by so-called double-exchange matrix element. This matrix element arises via the transfer of an electron from Mn^{3+} to the central O_2^- simultaneous with transfer from O_2^- to Mn^{4+} (shown in Fig. 1.4). Zener points

out that the degeneracy of ϕ_1 and ϕ_2 , a consequence of the two valencies of the Mn ions, makes this process fundamentally different from conventional superexchange. Because of strong Hund's coupling, the transfer-matrix (t) element has a finite value only when the core spins of the Mn ions are aligned ferromagnetically, again distinguished from superexchange which favours antiferromagnetism. According to Zener, double exchange (DE) is a magnetic interaction mediated by itinerant spin polarized d electrons which coupled according to Hund's rule to localize magnetic moments. The hopping amplitude of electrons in the Mn–O–Mn bond can be expressed as: $t = t_0 \cos(\frac{\theta}{2})$, where t_0 is the transfer integral and θ is the relative angle between the adjacent Mn t_{2g} core spins (shown in Fig. 1.5). It is clear that " t " achieves its maximum possible value t_0 for $\theta = 0$, i.e. under the Zener dou-

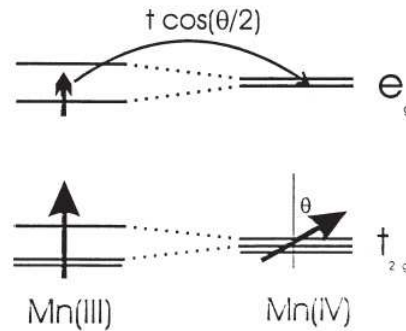


Figure 1.5 Schematic diagram of hopping of electron from Mn^{3+} to Mn^{4+} site. Image from [26].

ble exchange mechanism, a FM state is also a metallic state. Typical value of t is 0.2–0.5eV. Since the electron transfer depends on the angle between neighbouring magnetic moments, double exchange mechanism qualitatively explains the relationship between ferromagnetism and metallicity in mixed valence ($\text{La}_{1-x}\text{Ca}_x\text{MnO}_3$) manganites. But it cannot explain the observed metal insulator transition and CMR effect in hole doped manganites.

To explain the CMR effect and metal-insulator transition in manganites, T.V. Ramakrishnan et. al. [24] further proposed that the two fold degenerate e_g ($d_{x^2-y^2}$ and $d_{3z^2-r^2}$) orbitals of Mn are dynamically reorganized into a set of states "I" (which are localized with large local lattice distortion and have exponentially small intersite overlap) and "b" which form a broad band by the strong JT coupling between the e_g orbitals and lattice modes of vibration (of the oxygen octahedra surrounding the Mn ions). These "I" and "b" states can coexisted microscopically and can be influenced by doping (x),

temperature and local Coulomb repulsion (U). This model consider all the strong interactions occur in manganites [24, 25]. For example, Zener double exchange theory, consider solely the Hund's exchange coupling J_H . However, the theory by the Millis, Mueller and Shraiman [23] additionally includes the effect of the strong JT coupling of e_g electrons but they considered the local JT lattice distortion as a static disorder and neglected U . This theory also can not explain the observed metal– insulator transition in manganites. The proposed model [24, 25] by T.V Ramakrishnan has an unique feature that it consider the coexistence of JT distorted, localized "l" states and undistorted, broad band "b" states. The theory proposed that external stimuli or small perturbations change the physical properties of manganites because the "l" states, being localized and lattice distorted, are strongly influenced by local perturbations, which then affects delicate relative stability of the "l" and "b" states. The existence of this localized polaronic "l" states in the presence of large " U " and J_H give rise to a doping dependent ferromagnetic nearest neighbour exchange coupling J_F between the t_{2g} core spins [24, 25]. This arises due to virtual, fast hopping processes of the "l" electrons to neighbouring empty sites and back. The calculations by T. V. Ramakrishnan suggest that this virtual, correlated double exchange between the localized electrons is the dominant source of ferromagnetism and of the FM transition temperature T_C in the hole doped manganites. This ferromagnetism and the occurrence of T_C is not governed by the conventional double exchange due to mobile e_g electrons as previously believed [24, 25].

1.6 Magnetization due to divalent atom doping

In the previous section, we discuss that transfer of e_g electron from Mn^{3+} site to Mn^{4+} site depends on the angle between the neighbouring magnetic moments. Divalent atom doping (x) determines the concentration of Mn^{4+} present in a doped $La_{1-x}Ca_xMnO_3$ system. For $x = 0$, the material is anti-ferromagnetic. However, as x increases, the double exchange becomes the dominant interaction, and consequently the FM moment increases. The maximum value of moment is observed around $x = 0.33$ where the FM moment approaches the theoretical spin–only value for a FM mixture of Mn^{3+} and Mn^{4+} (calculated as $(1-x) \mu_B + 3x \mu_B$, where μ_B is the Bohr magneton). Ferromagnetic moment starts

to decrease when x is increased further. This is due to the direct overlap between t_{2g} orbitals, which leads to antiparallel exchange coupling because only the spin down states are empty. The competition between FM ($\text{Mn}^{3+} - \text{Mn}^{4+}$) double exchange coupling and the AFM ($\text{Mn}^{4+} - \text{Mn}^{4+}$) coupling exist in the doping level of $0.33 \leq x \leq 0.5$. For $x = 0.5$, AFM state becomes dominant due to superexchange, charge and orbital ordering becomes important for conduction process. When $x > 0.875$, the charge ordered state in $\text{La}_{1-x}\text{Ca}_x\text{MnO}_3$ disappears, and the low temperature state becomes antiferromagnetic again [18, 27].

1.7 Resistive switching in perovskites

Resistive switching with hysteresis in perovskite materials have been investigated for some time in pursuit of material that can make a Resistive Random Access Memory (RRAM). Such devices are in either a top-down [28–31] or a planar structures [32–34] with a semiconducting or insulating material coupled with two metal electrodes. The main feature of a resistive switching devices is that it has two resistive states of high and low resistances (HRS and LRS) with a particular threshold voltage V_{SET} . The Device switches from HRS to LRS on increment of bias $> V_{SET}$ and returns back to HRS (from LRS) at a reset bias of V_{RESET} . If the SET and RESET voltages have same polarity, it is called unipolar switching. The resistive switching is called bipolar if the SET and RESET voltages are of opposite polarity. The schematic diagram of unipolar and bipolar resistive switching is shown in Fig. 1.6. In recent

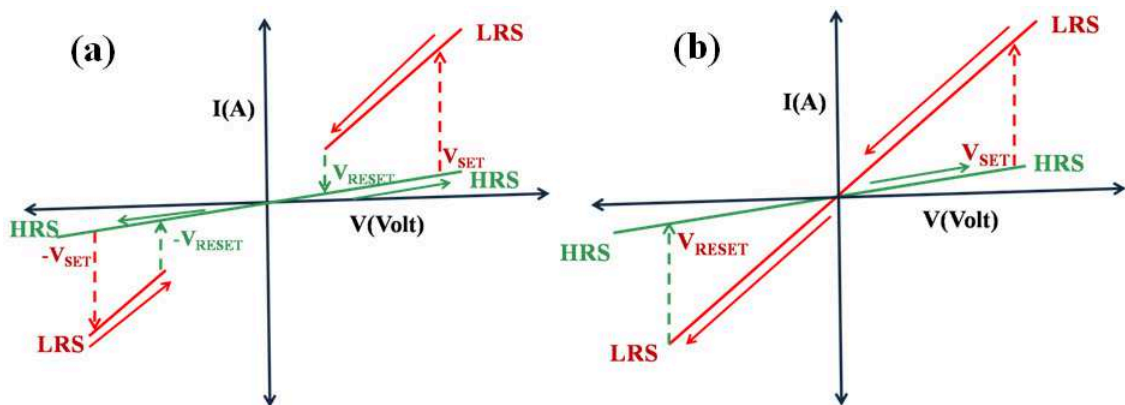


Figure 1.6 Schematic diagram of (a) unipolar and (b) bipolar resistive switching.

years, various perovskite materials have been successfully investigated for resistive switching effect, such as $\text{Pr}_{1-x}\text{Ca}_x\text{MnO}_3$ [31, 33–35], Cr-doped SrZrO_3 [36], SrTiO_3 [37], $\text{La}_{0.7}\text{Ca}_{0.3}\text{MnO}_3$ [29] and $\text{La}_{1-x}\text{Sr}_x\text{MnO}_3$ [38]. However, the switching phenomena can be different depending on the material. The mechanism behind this kind of switching are different for different materials but most celebrated are the formation of conducting filament due to oxygen vacancy migration [39–41], phase separation in transition metal oxides [35, 42–44] and Schottky barrier effect in metal semiconductor metal devices [45, 46]. In general, switching with hysteresis has been observed in manganites due to substantial mixed valency of Mn ions (Mn^{3+} and Mn^{4+}) and the oxygen vacancy which plays a crucial role to control the valence state. Modifications of oxygen vacancy by the applied field has been proposed as the cause of such switching [47–49]. In materials like SrTiO_3 the observed resistive switching needs much larger threshold field and the switching with memory was related to manipulation of oxygen vacancies by the applied field [37]. Most of the resistive switching effects that have been reported are for

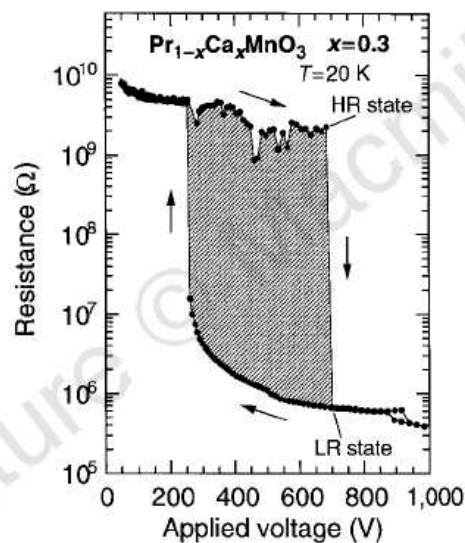


Figure 1.7 Switching of resistance states (HR: High Resistivity, LR: Low Resistivity) for single crystal $\text{Pr}_{0.7}\text{Ca}_{0.3}\text{MnO}_3$ in the COI state at temperature $T = 20$ K, as a function of applied voltage. Image from Asamitsu et al. [35].

compositions that show FMM and COI states. An electric field induced current switching of resistive states effect was first reported by Asamitsu et al. [35] in a single crystal of charge ordered insulating (COI) manganite $\text{Pr}_{0.7}\text{Ca}_{0.3}\text{MnO}_3$. They reported the existence of a threshold voltage (see figure 1.7)

above which the resistive state of the sample switched to a value lower than that observed for voltages below the threshold voltage. These observations amounted to a more than 3 orders of magnitude decrease in resistivity, when the low temperature COI state "melts" (at applied voltages higher than the threshold voltage) to a metallic state. The reason of the switching is generally due to the tuning of volume fraction of metallic phase (FMM) in comparison with insulating phase (COI). In our thesis we investigate the resistive switching in parent manganites which have different origin than the previously observed resistive switching in manganites or perovskites.

1.8 Phenomena of phase separation in manganites

Perovskite manganites have very interesting phase diagram which is rich with various kind of resistive, magnetic and structural phases. The electronic energy in manganites depends on the (i) kinetic energy of e_g electrons, (ii) Hund's on site magnetic coupling between e_g and t_{2g} electron spins, (iii) coupling between e_g electrons and distortion of MnO_6 octahedra (JT Effect), (iv) crystal field splitting in the octahedral coordination, (v) Heisenberg's magnetic coupling between nearest neighbour localized electron spins, and (vi) the Coulomb interaction between e_g electrons. The competition between these effects results in different electronic and magnetic ground states in manganite. For example, the phase diagram (different electronic and magnetic phases at various temperatures and concentrations) of $\text{La}_{1-x}\text{Ca}_x\text{MnO}_3$ (LCMO) is shown in Fig. 1.8 . The phase diagrams have been constructed from detail measurements of macroscopic physical quantities like resistivity, susceptibility and magnetization on single crystal and bulk ceramic samples. Even though the phase diagram is different at different compositions due to the difference in radii of the atoms involved, but they have some common features. LCMO is an intermediate bandwidth compound and is among the most studied compounds of the manganite family. Schiffer et. al. gave the first phase diagram of LCMO in 1995 [50] but the complete phase diagram was established by Cheong and Hwang [51]. The first phase coexistence has been seen in the system of $\text{Nd}_{0.25}\text{La}_{0.25}\text{Ca}_{0.5}\text{MnO}_3$ [52]. At low temperatures, LCMO undergoes the following transitions: the end compositions ($x = 0$ and $x = 1$) are insulators at all temperatures, and canted anti-

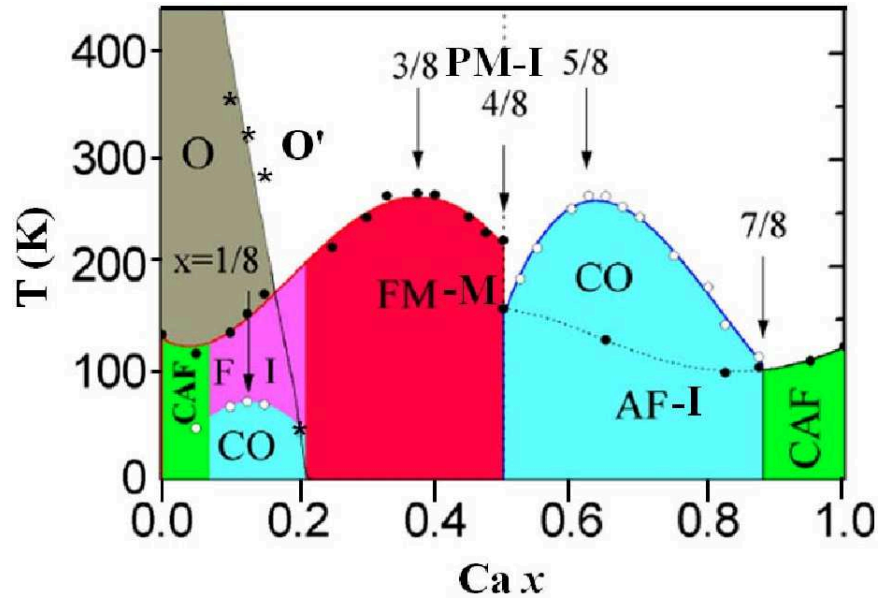


Figure 1.8 Phase diagram of $\text{La}_{1-x}\text{Ca}_x\text{MnO}_3$. PMI: Paramagnetic Insulator, FMM: Ferromagnetic Metal, FMI: Ferromagnetic Insulator, AFI: Antiferromagnetic Insulator, CAF: Canted AF and CO: Charge/Orbital Ordering. Filled and open circles indicate Neel (T_N) and Curie (T_C) temperatures respectively. Stars indicate the orbitally ordered Orthorhombic (O) to orbitally disordered pseudo-Orthorhombic (O^*) phase structural transition temperature. Image from [1, 2, 7].

ferromagnetic (CAF) at low temperatures. On increasing the Ca concentration, FMI phase occurs till $x = 0.22$. Between $x = 0.22$ and $x = 0.5$, we get a FMM state exhibiting the CMR effect. $x = 0.33$ is the optimal doping concentration yielding the highest ferromagnetic Curie temperature (T_C) = 270 K. At $x = 0.5$ where the $\text{Mn}^{3+} : \text{Mn}^{4+}$ is 1:1, a CO antiferromagnetic insulating phase starts to evolve at low temperatures. This phase continues till $x = 0.87$, beyond which we again get a CAF regime. At high temperatures, we get a paramagnetic insulating phase. Kim et. al. identified a tricritical point in the $\text{La}_{1-x}\text{Ca}_x\text{MnO}_3$ phase diagram for $x = 0.4$, thereby marking a boundary between the first order ($x < 0.4$) and second order ($x > 0.4$) phase transitions within the FM range ($0.22 < x < 0.5$) [199]. Recently, the point ($x_t = 0.25$, $T_t = 205$ K) on the (x , T) phase diagram of LCMO has also been identified as a tricritical point. If $T_C < T_t$, the FM to PM transition is second order, while at $T_C > T_t$, the transition is first order [54]. From the phase diagram of LCMO, it is clear that at some doping level x , there is a coexistence of different electronic and magnetic phases and the phase boundaries are not strictly clear as these phases always coexist and compete with each other. External stimuli like pressure, electric

field, magnetic field and strain also plays an important role to control these phases.

The physics of manganites appear to be dominated by states that are microscopically and intrinsically inhomogeneous. This is due to the several physical interactions such as spin, charge, lattice and/or orbital being simultaneously active. The results of theoretical calculations have led Dagotto et al. [55] to argue that phase separation and phase coexistence occurs on a wide range of length scales from nanometres to microns throughout the doping range and an appreciation of these tendencies towards phase separation is fundamental to the understanding of the properties of manganites. The type of phase separation occurs in manganites is not the result of chemical phase separation or structural inhomogeneities but is intrinsic and caused by the similar free energies of the competing ground states. Two types of phase separation are suggested. The first is driven by disorder induced by the random substitution of ions of different sizes on the "A" site of the crystal and leads to phase separation on a scale that can be as large as microns. It has been shown that the properties of manganites depend greatly on both the average size of the "A" site cations and also the standard deviation of the sizes of the substituted atoms [56]. The other type of phase separation suggested by Dagotto et al. [55] is electronic phase separation where nanometre sized patches with different electron densities coexist although the composition of the crystal is constant.

There are lots of experimental evidence for the inhomogeneous states in manganites [55, 213]. Among the most direct evidences of phase separation in manganites is the scanning tunnelling microscopy (STM) studies carried out at room temperature on $\text{Bi}_{0.24}\text{Ca}_{0.76}\text{MnO}_3$ by Renner et al. [58]. Another remarkable evidence of mixed-phase characteristics in manganites was observed in a thin film of $\text{La}_{0.73}\text{Ca}_{0.27}\text{MnO}_3$ using scanning tunnelling spectroscopy where a phase-separated state was observed below T_C [59]. There were clusters with metallic and insulating phases and the size of the clusters depends on the applied magnetic field (see figure 1.9). The coexisting clusters have typical sizes varying from tens to hundreds of nanometers. The metallic clusters can be seen to evolve upon application of a magnetic field. It has been argued that the observed T_C and associated MR behaviour are caused by a percolation process [59]. The presence of inhomogeneous states in manganites is widely accepted and there is a tremendous amount of ongoing research focussing on unravelling the

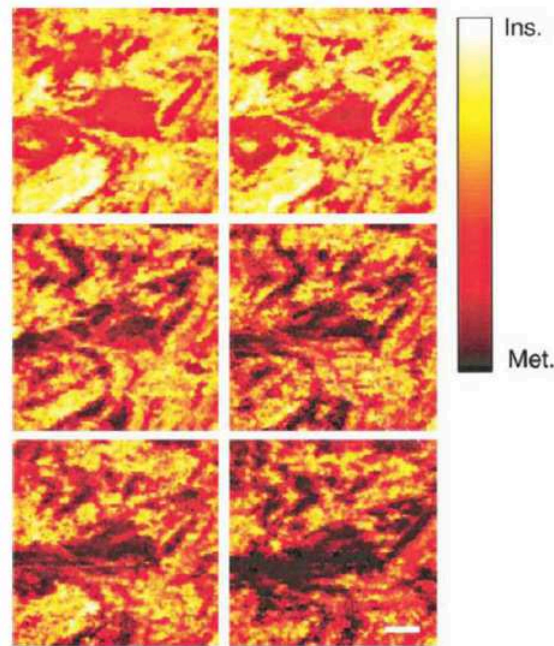


Figure 1.9 Generic spectroscopic images ($0.61\mu\text{m} \times 0.61\mu\text{m}$; scale bar: 100 nm) of the local electronic structure of $\text{La}_{0.73}\text{Ca}_{0.27}\text{MnO}_3$ thin film taken just below T_C in magnetic fields of 0, 0.3, 1, 3, 5, and 9 T (from left to right and top to bottom). Parts of the surface are insulating (light colors), whereas others are metallic (dark colors) or in an intermediate state. Image from [59].

role of these inhomogeneities and the effect of these inhomogeneities on the electrical and magnetic transport of perovskites or manganites.

1.9 Magnetoresistance in manganites

Magnetoresistance (MR) is defined as the change (increase or decrease) in resistance due to the externally applied magnetic field. The MR becomes CMR if the change in resistance is huge due to the applied magnetic field. MR is expressed as $\pm MR\% = \frac{\rho(H) - \rho(0)}{\rho(0)}$, where $\rho(H)$, $\rho(0)$ are the resistivities of the material with and without field while \pm indicates the positive and negative MR. Perovskite oxides can show both positive and negative MR depending on the elements present in the material as well as disorder in oxygen stoichiometry. But it is the CMR behaviour in hole doped perovskite manganites $\text{Re}_{1-x}\text{A}_x\text{MnO}_3$, where Re is a trivalent rare-earth (La, Pr, Sm, etc.) and A is a divalent ion (Ca, Sr, Ba), which has aroused tremendous interest due to their rich fundamental physics and great

potential application in spintronics [1, 2, 60, 61]. MR investigation as well as a phenomenological analysis was reported for $\text{La}_{1-x}\text{Pb}_x\text{MnO}_3$ crystals in 1969 [62]. CMR effect was discovered in thin film of $\text{La}_{0.67}\text{Ca}_{0.33}\text{MnO}_3$ having thousand fold change in resistance at 77K with 6T magnetic field in mid 1990's [63]. Magnetic field dependence of the resistivity for epitaxial $\text{La}_{0.67}\text{Ca}_{0.33}\text{MnO}_3$ thin films at different temperatures is shown in Fig. 1.10. It is generally believed that the underlying origin of CMR

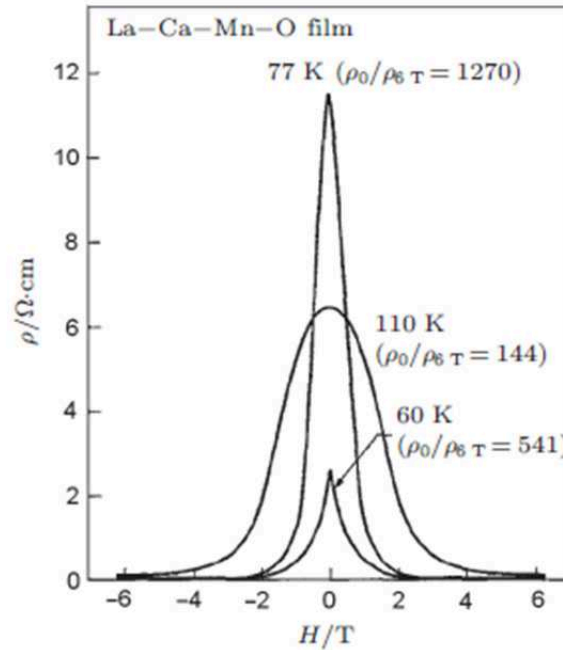


Figure 1.10 Magnetic field dependence of resistivity of $\text{La}_{0.67}\text{Ca}_{0.33}\text{MnO}_3$ thin film at different temperatures. Image from [64].

is closely related to the nature of CMR manganites which are strongly correlated electron systems with interplay among the lattice, spin, charge, and orbital degrees of freedom, such as double exchange interaction, JT effect, electronic phase separation, and charge ordering. The CMR effect is closely related to the field-sensitive complex electron–electron and electron–lattice effects in manganites, which will result in tremendous conductivity variation in magnetic fields. In addition, the insulating/metallic phase separation is another field-dependent factor critical for the observed CMR effects. Both experimental and theoretical studies have shown that typical length scale for phase-separation in manganites is from several nanometers to submicrometer scale, depending on the material and the dopant level [65–70]. A phenomenological model was proposed to describe the relationship between the phase separation and

CMR in manganites [71, 72]. For example, in a FMM/PI phase-separated system, the total resistance can be considered as a linear combination of the resistance of the coexisting phases and written as:

$$R = f_{FM}R_{FM} + (1 - f_{FM})R_{PI} \quad (1.3)$$

, where f_{FM} and $(1-f_{FM})$ are the volume fractions, and R_{FM} and R_{PI} are the resistances of the FM metallic and PI phases, respectively [71, 73]. The metallic resistance R_{FM} is related to the single magnon's scattering (AT^2) and electron phonon interaction (BT^5) [74, 75]. The resistance R_{PI} can be described as $R_{PI} = C \exp\left(\frac{E_a}{\kappa_B T}\right)$ in terms of the magnetic polaron picture. The constants A, B, and activation energy E_a are magnetic field-dependent and become smaller due to the suppression of single-magnon scattering in FM metallic regions and the formation of magnetic polarons in PM insulating regions under a magnetic field [76]. Thus, resistivity decreases and CMR appears. Liu et al. have employed this model to analyze the magnetic transport data of $\text{La}_{5/8}\text{Ca}_{3/8}\text{MnO}_3$ film [77]. Magnetic field dependent transport data of $\text{La}_{5/8}\text{Ca}_{3/8}\text{MnO}_3$ is shown in Fig. 1.11. It implies that the competition

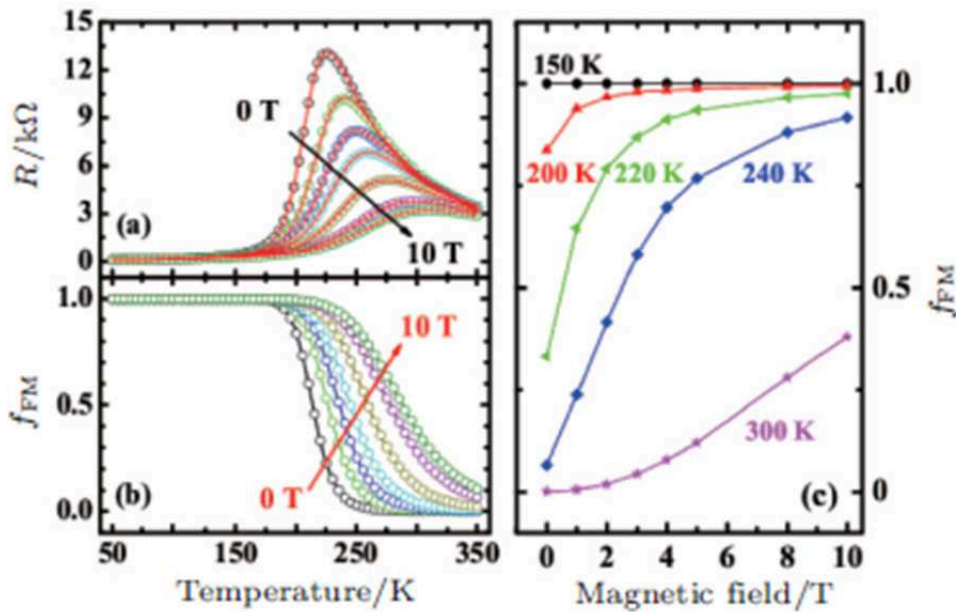


Figure 1.11 (a) Temperature dependence of (a) resistance and (b) volume fraction of FM for $\text{La}_{5/8}\text{Ca}_{3/8}\text{MnO}_3$ film in 0, 1, 2, 3, 5, 8, and 10 T. The solid red lines in panel (a) are the fitting results using Eqn. (1.3). (c) Magnetic field dependence of f_{FM} at different temperatures. Image from [77].

between the FM metallic and PM insulating phases plays an important role in the CMR effect. It is well

known that the hole doped manganites (e.g. $\text{La}_{1-x}\text{Ca}_x\text{MnO}_3$ with $0.5 \leq x \leq 0.9$) become insulating below the charge ordered transition temperature T_{CO} , because e_g electrons accompanied by their JT distortions freeze in a static order followed by a long-range AFM spin order at Neel temperature $T_N \leq T_{CO}$. However, the real-space order of e_g electrons can be destroyed by magnetic field, which will cause an insulator-metal transition below T_{CO} due to the strong spincharge coupling, thus leading to another kind of CMR effect [2, 73, 78]. It is found that most of the MR measurements were done in manganites in the hole doped region of $0.2 \leq x \leq 0.9$ due to the coexistence of different electronic phases or the coexistence of phase separated regions which plays an important role in MR. But there are few reports available on the MR behaviour of lightly doped or parent manganites in which the competition between Antiferromagnetic (AFM) and FM interaction can play a crucial role to determine the MR behaviour. In this thesis, we have studied the magneto transport behaviour in parent manganites ($x = 0$). In this region of interest, manganites have AFM ground state and the high temperature phase is paramagnetic insulating. But FM moments can appear in these systems due to the presence of slight Mn^{4+} . The presence of Mn^{4+} in parent manganites can be due to the intrinsic doping (which will be discussed in detail in chapter 3 & 4) which have a different microscopical origin than the conventional hole doping. These FM moments can play a crucial role to develop a noticeable MR effect in parent perovskites.

1.10 Carrier modulation in perovskite using electrostatic electric double layer gate

The electronic and magnetic properties of perovskites or manganites strongly depend on their carrier concentration. The several properties of the materials as a function of their sheet charge density is shown in Fig. 1.12 where silicon is shown as a reference [80]. The carrier concentration can be varied by external doping (x) which introduce disorder in the system. Another approach is to modulate the electrical charge carrier density by application of electric field in a field effect device configuration using the perovskite as a channel like Semiconductor MOSFET. As the carrier concentration is a crucial parameter which governs the properties of these systems, the electrostatic field effect approach is an

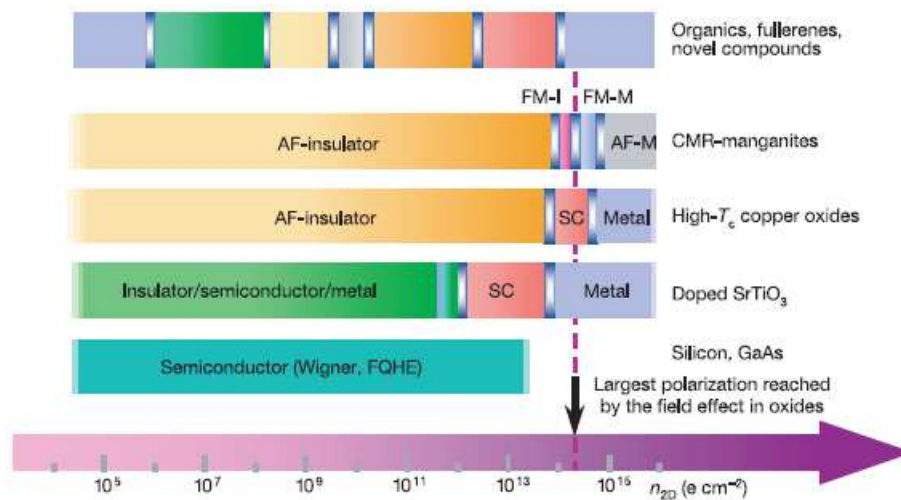


Figure 1.12 Illustration of the zero-temperature behaviour of various correlated materials as a function of sheet charge density (n_{2D}). Silicon is shown as a reference. The examples for high T_C superconductors and for colossal magnetoresistive (CMR) manganites reflect $\text{YBa}_2\text{Cu}_3\text{O}_{7-\delta}$ and $(\text{La,Sr})\text{MnO}_3$, respectively. The top bar has been drawn to illustrate schematically the richness of materials available for field-effect tuning and the spectrum of their phases. AF: antiferromagnetic; FM: ferromagnetic; I: insulator; M: metal; SC: superconductor; FQHE: fractional quantum Hall effect; Wigner: Wigner crystal. Image from [80].

ideal tool to investigate the physics of correlated electron systems, allowing controlled and reversible changes of the carrier concentration without altering the disorder [80]. The basic structure of the field effect transistor is shown in Fig. 1.13. The field is applied across a gate insulator using a gate electrode

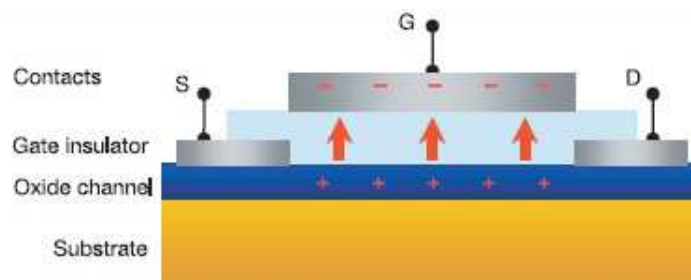


Figure 1.13 Cross-section of a typical sample geometry used for field-effect studies. S, source; G, gate; D, drain. Image from [80].

(G) and the change in conductivity is measured by the S and D electrodes. When we apply an electric field to a material through the gate dielectric, it attracts or repels charge carriers which creates a thin charge accumulation or depletion layer at the surface. This charge layer modifies the electrical con-

ductivity between the source (S) and drain (D) contact. The characteristic width of the accumulation or depletion layer is given by the Thomas-Fermi electrostatic screening length λ_{el} . In standard metallic systems, λ_{el} is extremely short, fraction of an atomic diameter, and thus negligible field effects are found. In low-carrier-density systems, larger screening lengths and field effects are expected, which are the reasons why standard transistors are made with semiconductors rather than metals. Many of the interesting physical properties of strongly correlated oxides or perovskites occur at carrier densities in the range of 10^{19} to 10^{22} carriers cm^{-3} as shown in Fig. 1.12. To achieve substantial carrier modulation at these densities, one have to use ultrathin (few nm thick) drain-source (DS) channels and high dielectric constant material for gate dielectric. The conventional gate dielectric used in semiconductor FET are generally solid state oxides and they need much higher voltages to get a noticeable carrier modulation in the perovskite channels. Recently, a different type of field effect device, the electric double-layer transistor (EDLT), was found to have the ability to induce sufficient carrier modulation in perovskite channel at much lower voltages than the conventional solid state dielectrics [81, 82]. Instead of solid gate dielectrics, the EDLT employs ionic conductors such as electrolytes or ionic liquids. At the oxide/electrolyte interface, an electric double layer, a self-organized capacitor with subnanoscale thicknesses, is formed [83]. The working mechanism of EDLT's nearly similar to that of solid gated MOSFET's. But the crucial difference is that the gate voltage (V_G) predominantly drops at the EDL interface and produce a huge electric field (10MV cm^{-1}) which results in a high density charge accumulation of nearly 10^{15} cm^{-2} [84]. This value is 12 orders of magnitude larger than that achieved in solid-gated MOSFET's, which are breakdown limited. The application of V_G induced insulator-to-metal transitions followed by superconductivity was first demonstrated in SrTiO_3 ($T_C = 0.45$ K) [81]. Electric double layer gate are now used vastly to change different electronic properties of perovskites. Hatano et. al. showed the electric double layer gate control on electronic phases in $\text{Pr}_{1-x}\text{Sr}_x\text{MnO}_3$ ($x = 0.5$) thin films [85]. The electric field effect on the transport properties of a 5 nm thick $\text{Pr}_{1-x}\text{Sr}_x\text{MnO}_3$ ($x = 0.5$) thin film is shown in Fig. 1.14. Electrostatic control of the metal-insulator transition in the typical correlated-electron material NdNiO_3 was also achieved through a large effective capacitance of the electric double layer at the electrolyte/ NdNiO_3 interface. The metal insulator transition tempera-

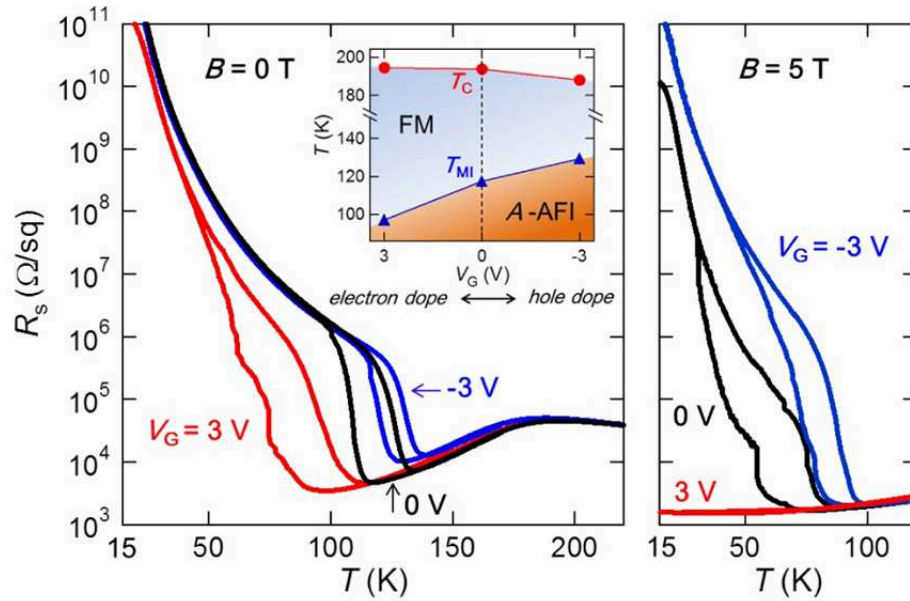


Figure 1.14 The temperature (T) dependence of the sheet resistance (R_s) at gate voltage (V_G) of 0 and ± 3 V. The positive and negative V_G correspond to electron and hole doping, respectively. The inset shows gate voltage dependence of both T_C (Curie temperature) and T_{MI} (metal to insulator transition temperature) defined as the temperature where $d(\ln R_s)/dT = 0$ on cooling. Right side image shows $R_s - T$ curves of the device at the magnetic field (B) of 5 T for $V_G = 0$ and ± 3 V. Image from [85].

ture T_{MI} of NdNiO_3 is found to decrease drastically by the application of gate voltage V_G [86]. Gating effect in perovskite insulators such KTaO_3 [87] have also been investigated in EDLT geometry. By using ionic liquid as gate electrolyte in EDLT, the accumulated electron density around 10^{21} cm^{-3} (\sim one order of magnitude larger than maximum chemical doping concentration) and superconductivity was observed in KTaO_3 . These results demonstrate the possibility of using EDL-FET structure to induce phase transitions in materials where chemical doping concentration is inadequate. In this thesis, we have studied the electrostatic gate effect on the electrical transport of low hole doped ($x = 0.15$) nanostructured manganite thin film using an EDL gate.

EDLT's have achieved the maximum accumulated carrier concentration than the conventional FET at a moderate gate voltage (1V-5V). They have been proven to be promising to be utilized to investigate electric field induced phenomena in a broad range of materials and probe correlated electron physics. However, there are still some technological challenges in ionic liquid gated EDLT's before they could be possibly applied outside basic scientific research. The foremost disadvantage of ionic

liquids or/electrolyte gated EDLT's is the liquid form of the gate, which will give rise to concerns on stability, scalability and integration. Another challenge is that one needs to go above the glass transition temperature of ionic liquid (IL) or electrolyte (EL) to make it possible to modulate carrier density modulation by gate voltage, which would cause difficulties in the dynamic control and fine tuning of the channel conductance at low temperatures [88]. IL/EL gated EDLT's usually have a significantly longer relaxation time compared with conventional oxide dielectric due to slow motion of the ions, which may hinder it for ultrafast switching applications. The microscopic mechanisms of slow relaxations require a more detailed understanding. The EDLT's may not be suitable for high-temperature operation because of IL's or EL's degraded chemical stability at elevated temperatures. The electrochemical reactions between IL/EL and channel material can affect the electrostatic carrier doping and one has to be careful while interpreting the data and it requires a deep understanding.

1.11 Overview of the thesis

In this thesis work we have investigated the electrical and magnetic transport properties of perovskite manganites on the application of external stimuli like electric field, magnetic field, charge induction due to electrolyte gating and substrate induced strain . The thesis mainly focussed on undoped (parent) LaMnO_3 or lightly doped with $x \leq 0.15$. In this composition range the manganite is still insulating but with different variants. Specifically, we looked at the following issues:

(a) Effect of electric field on the destabilization of the insulating state at low and room temperature in the single crystal of nominally pure LaMnO_3 [90] and thin film of GdMnO_3 . The observed reversible destabilization of the highly resistive insulating state to a lower resistance bad metallic state is explained by bias driven percolation type transition between two coexisting phases, where the majority phase is a charge and orbitally ordered polaronic insulating (PI) phase and the minority phase is a bad metallic phase. The important physics studied here is that bad metallic minority phase can co-exist with PI state due to charge transfer instability driven charge disproportionation which creates electron hole (E-H) pair ($\text{Mn}^{3+} + \text{Mn}^{3+} \rightarrow \text{Mn}^{2+} + \text{Mn}^{4+}$). These E-H pair is depinned by applied field and shows

an activated kinetics [89, 90]. This transition is distinct from the field induced resistance state change (both with memory and without memory) that have been seen in manganites with much higher level of hole doping (typically $x \geq 0.2$) [91–94].

(b) We have studied the effect of magnetic field on the electrical transport in single crystals of parent manganite LaMnO_3 . Interestingly except very early MR measurement on polycrystalline LaMnO_3 [96], there was no comprehensive study on single crystals of LaMnO_3 . We found that though the parent single crystal LaMnO_3 has an orthorhombic orbital ordered ground state with super exchange interaction in between Mn-O-Mn electrons, it shows typically small magneto-resistance (MR) at room temperature on cooling close to Neel temperature (T_N), the MR (negative) is nearly 70% at high magnetic field. Interestingly, the MR shows a field dependence that changes as T_N is approached. The important phenomena studied here is the MR behaviour in nominally pure LaMnO_3 due to the formation of FM cluster in an AFM matrix by the applied magnetic field. In particular, we have established a correlation between MR and the extent of FM cluster formation in nominally pure LaMnO_3 .

(c) The effect of electrostatic surface charge induction due to the formation of electrical double layer (EDL) by an electrolyte gate on the transport of hole doped functional perovskites like $\text{La}_{0.85}\text{Ca}_{0.15}\text{MnO}_3$ is another important research aspect in this thesis. In this work we have explored a bipolar nanoscopic control that can be obtained on the transport in such EDL–FET device at room temperature. The main motivation is to control the depletion region at the grain boundaries (GB) of a nanostructured films [95, 97, 98] and tune the electronic phases through electrostatic gate. We have also modulated the resistivity of the sample and change its characteristic electronic phase transition temperatures with applied gate bias without any chemical doping into the sample.

(d) We have also investigated the effect of strain / strain inhomogeneity in the phase separated region of FM insulator. We have studied the effect of strain (biaxial) as well as local strain inhomogeneity on phase separation and its effect on the electrical and magnetic transport of $x = 0.15$ doped manganite. We have tuned the strain in a controlled way by growing epitaxial thin films on different substrates whose lattice constants are close to the sample and thus investigated the effect of strain on phase separation. The effect of local electronic phase inhomogeneity on the conduction and its evo-

lution with temperature is studied by tunnelling conduction measurements done in ultra high vacuum using a scanning tunneling microscope (STM). We found that the increase or decrease of the energy gap at the density of states occurs with spatial inhomogeneity. We also tried to correlate how this gap effect the electrical as well as magnetic transport in these phase separated perovskites.

The thesis is made of following chapters:

Chapter 1: Introduction; **Chapter 2:** Sample preparation, characterisation, and measurement techniques; **Chapter 3:** Effect of electric field on the insulating state of undoped LaMnO_3 and GdMnO_3 ; **Chapter 4:** Effect of magnetic field on the transport of undoped LaMnO_3 ; **Chapter 5:** Electrostatic gate effect on the electrical transport of $\text{La}_{0.85}\text{Ca}_{0.15}\text{MnO}_3$; **Chapter 6:** Strain and Phase separation effect on the transport in ferromagnetic insulating manganite and **Chapter 7:** Conclusion and future outlook.

Chapter 2

Sample preparation, characterisation and measurement techniques

In this chapter, we will discuss sample preparation, characterisation, and measurement techniques which were used for different investigations. Bulk single crystals and thin films were used for different measurements. We will briefly discuss the single crystal growth procedure and different thin film deposition techniques. The samples were characterised by the measurements like XRD, SEM, EDAX, VSM, a.c. susceptibility, AFM, EELS, XPS and ellipsometry. For temperature dependent electrical and magneto transport measurement, we used a commercial cryogen free 10T VTI system. An UHV-STM was used to measure the local tunnelling conductance.

2.1 Introduction

In this thesis work, we have investigated the electrical and magnetic transport properties of manganites on the application of external stimuli like electric field, strain, charge induction due to electrolyte gating and magnetic field. For these investigations, most of the experiments in this thesis has been carried out on single crystals, epitaxial and nanostructured thin films. Three nominally undoped single crystals of LaMnO_3 (LaMnO_3 -1, LaMnO_3 -2 and LaMnO_3 -3) and one doped single crystal of $\text{La}_{0.9}\text{Sr}_{0.1}\text{MnO}_3$ were used in the resistive switching measurement to see the effect of electric field on their polaronic insulating state. Nominally pure LaMnO_3 single crystals were also used to observe the effect of magnetic field on the electronic transport i.e. for the MR measurement. In the next section, we will discuss about the growth techniques to grow these single crystals which were used in measurements in the present thesis. We have also used thin film of parent manganite (GdMnO_3) as well as low hole doped manganite like $\text{La}_{0.85}\text{Ca}_{0.15}\text{MnO}_3$ for our various measurements. GdMnO_3 thin film was used for the resistive switching measurement at room temperature. We have grown thin films of $\text{La}_{0.85}\text{Ca}_{0.15}\text{MnO}_3$ on three different single crystal substrates of NGO (2 0 0), STO (2 0 0), LAO (1 0 0) for studying the strain and electronic phase separation effect on the electrical transport. These films are highly oriented and are likely to be partly strain relaxed. The local tunnelling conductance measurement were done on these films. The nanostructured film of $\text{La}_{0.85}\text{Ca}_{0.15}\text{MnO}_3$ on SiO_2/Si were used to study the effect on the electronic transport due to the electrostatic surface charge induction by the formation of electrical double layer (EDL) using an electrolyte gate. One of the thin film (GdMnO_3) were grown by Radio frequency (RF) magnetron sputtering and rest of the films were grown by pulsed laser deposition techniques. These thin film deposition techniques will be discussed in the later sections.

We have performed different characterisation measurement in the samples to check the stoichiometry, phase formation, surface morphology, magnetisation and thickness. X-ray diffraction (XRD) and Rocking curve analysis were done in the single crystals and thin films to check the phase formation as well as to measure the strain in the thin films. High temperature XRD was done in the three LaMnO_3 single crystals to check the structural transition temperature (T_R) in the three samples. To check the

composition of the single crystal and thin films, we have done Energy dispersive analysis of x-ray (EDAX) which confirms the presence of different compositional elements. X-ray photo electron spectroscopy (XPS) and Electron energy loss spectroscopy (EELS) were done in the three LaMnO_3 single crystal to check the mix valency of transition metal ion Mn (that arise from deviation of stoichiometry from perfect 3+). To check the surface morphology of the samples (mainly the thin films), we have used Atomic force microscopy (AFM) and Scanning electron microscopy (SEM). The thickness of the films were measured using ellipsometry, cross-sectional SEM and AFM. Magnetisation and a.c. susceptibility of the three LaMnO_3 single crystals were measured using vibrating sample magnetometer (VSM) and a.c. susceptibility set up. All these characterisation techniques will be briefly discussed in this chapter

For our study, we have done electrical, magneto transport and local tunneling conductance measurement. In the electrical measurement, we have performed temperature dependent I-V and resistivity ($\rho - T$) measurements in single crystals and in thin films. Measurements were done using a commercial cryogen free (He gas based) low temperature ($\approx 1.5\text{K}$) variable temperature insert (VTI) set-up. For the magneto resistance measurement, we have measured $\rho - T$ data in the presence of magnetic field up to 10T using an commercial cryogen free superconducting magnet. We have automated the data acquisition in commercial resistivity measurement set up by interfacing it with a computer writing a C++ code. To study the effect of electrostatic gate effect on the electronic transport of low hole doped manganite, we fabricated an EDL-FET device using $\text{La}_{0.85}\text{Ca}_{0.15}\text{MnO}_3$ as a channel. We have taken the $I - V$ as well as $R - T$ characteristics of the channel in the presence of different gate voltages. Finally, to see the scale of inhomogeneity present in the thin films grown on different single crystal substrates, local tunneling conductance measurement was done using a commercial ultra high vacuum (UHV) scanning tunnelling microscopy (STM). In this chapter, we present a brief description of the measurement techniques of temperature dependent $I - V$ and resistivity. We also describe the apparatus in which the measurements were performed and the methodology used to perform the measurements.

2.2 Preparation of manganite single crystals

Manganites having the general formula $AMnO_3$, where A stands for rare-earth elements like La, Pr, Nd, Gd and Mn is a transition metal ion which shows a fascinating range of electronic and magnetic transports. The introduction or inclusion (doping) of divalent atom like Ca, Sr, Ba, Pb at rare earth element site A, creates a mix valency in Mn^{3+} site or develops Mn^{3+}/Mn^{4+} ratio. The electrical and magnetic properties of manganites are very sensitive to the Mn^{3+}/Mn^{4+} ratio [1, 2]. This ratio is also affected by oxygen nonstoichiometry or cation (A) nonstoichiometry. This is so because the crystal structure of manganites admits vacancies in the rare earth (A site) sublattice [99, 100]. To measure the physical properties in manganites, one needs to be very careful about the quality of the sample, as the grain boundaries (for polycrystalline sample) and the interface between the sample and substrate (for thin film) also play a crucial role to determine the electrical and magnetic properties. In this regard, single crystal samples are best choice to measure the electronic and magnetic transport in manganite. In this thesis, we have used four single crystals of parent and low doped manganite ($LaMnO_3$ and $La_{0.9}Sr_{0.1}MnO_3$) for the electrical and magnetic properties of perovskites.

In this section, we will discuss the growth of these single crystals. Generally two techniques are used for manganite single crystal growth; one is floating zone technique and another is flux growth technique. All the single crystals used in this thesis were made by floating zone technique at Moscow State and Alloys University (MSAV), Moscow, Russia and Saha Institute of Nuclear physics (SINP), Kolkata, India.

2.2.1 Floating zone technique

In the floating zone technique, radiative heating is used for the melting (without any crucible) using an image furnace [99, 101]. This technique is widely used for growing high quality single crystals of metal, semiconductor and insulators. The chance of contamination of the melt is avoided in this crucible less method. This method is generally useful for the following cases: i. The materials with very high melting point ($\approx 2500^\circ\text{C}$).

ii. The oxide materials which needs high pressure ($\approx 10\text{atm}$) and specific atmosphere (like oxygen) for growth to control the oxygen stoichiometry.

iii. For the doped material, solid solution with controlled chemical composition can be prepared. In this regard, this method is more useful as it avoids contamination for not using crucible for melting.

For the single crystal growth, it's desirable that growth rate should be in user control. It also requires a uniform heating in the radial direction of the growth zone. These requirements are generally fulfilled in a image furnace in floating zone technique. In Fig. 2.1, we have shown the schematic of the image furnace and the design of the crystallisation chamber which were used for manganite single crystal used in this thesis work [101]. The image furnace (in Fig. 2.1(a)) is made of a biellipsoidal mirror (1,7

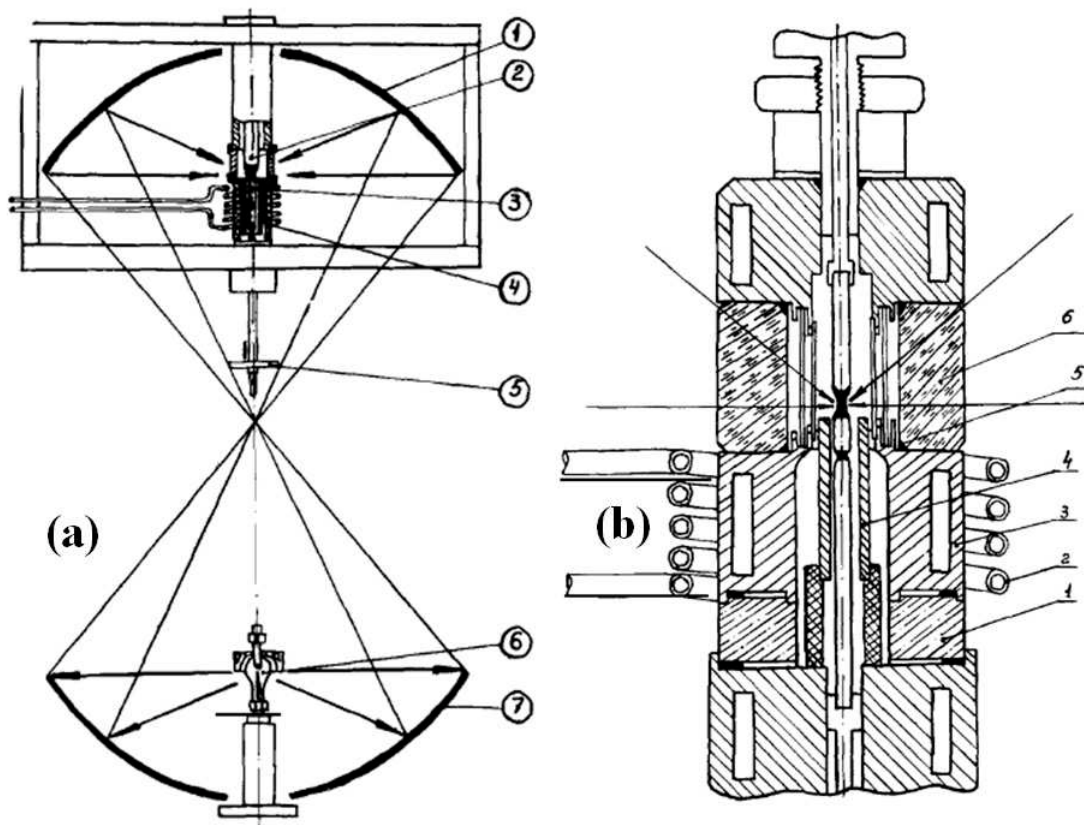


Figure 2.1 (a) Schematic diagram of the floating Zone melting apparatus. 1,7 represents ellipsoidal reflectors, 2 is the feeding rod, 3 is the crystal, 4 is the heater, 5 represents light flux regulator and 6 is the xenon lamp. (b) Design of the crystallization chamber: (1) Insulator, (2) RF coil, (3) eddy current concentrator, (4) annealing furnace, (5) siloxane rubber packing, (6) quartz container. Image is from Balbashov et. al. [101].

in Fig. 2.1(a)) with a vertical optical axis. A high power arc lamp (xenon lamp) is placed at the focus of one of the mirrors. The other mirror is kept in a position such that it can be moved along the optical axis. The feed rod (2 in Fig. 2.1(a)) is placed so that the focus of the movable mirror can be placed anywhere along the length of the feed rod (discussion on the feed rod will be made in next subsection). The design parameters of the particular furnace used for growing the present crystals can be obtained from Balbashov et al. [101].

The design of the growth chamber is shown in Fig. 2.1(b). The growth chamber has an optical grade quartz container with inner volume $\leq 0.5\text{L}$ having diameter $\approx 30\text{mm}$ and wall thickness $\approx 25\text{ mm}$. The pressure of nearly 100 bar can be maintained inside it and the temperature at the growth zone can be as high as 3000°C . During the growth process, materials may escape or evaporate from the feed rod and can damage and contaminate the inner wall. To protect the inner wall of the container, replaceable quartz tubes are incorporated into the container. Two annealing furnaces are provided among which the first uses a radio frequency (RF) heating scheme and achieves temperatures up to $\sim 1600^\circ\text{C}$. The second heater is cylindrical shaped and surrounds the cavity. This heater can achieve temperatures of up to 2000°C .

2.2.2 Growth of LaMnO_3 and $\text{La}_{0.9}\text{Sr}_{0.1}\text{MnO}_3$ single crystal

The general stoichiometric formula for manganite single crystal growth is $(\text{A}_{1-x}\text{B}_x)_y\text{MnO}_{3-\delta}$, where A is the rare earth element (like La), B is the divalent atom (like Ca, Sr) doping, y represents the A and /or B cation non-stoichiometry and δ is the oxygen non-stoichiometry. Single crystals of $(\text{A}_{1-x}\text{B}_x)_y\text{MnO}_{3-\delta}$ with $0 \leq x \leq 0.3$ and B=Ca, Sr, were made in floating zone technique from the starting material of La_2O_3 , MnCO_3 , SrCO_3 and CaCO_3 in high purity [99, 100]. For the preparation of LaMnO_3 single crystals (where $x=0$ and $y=1$), Mn_3O_4 (obtained from the calcination of MnCO_3 at 1000°C for 24hr) and dehydrated La_2O_3 (heated in air at 900°C for 10hr) were mixed in a desired ratio and pressed to tablet in a pressure of 0.6 to 0.8 ton/cm². The mixed tablet is then heated in air to 1000°C for 24hr. The Tablets were ground to make feed rods of size $8 \times 80\text{ mm}^3$ using a pressure of 1 ton/cm² and sintered in air at 1300°C for 24hr. The crystals were then grown in the URN 2 ZM image furnace using

radiative heating [101] from a water cooled xenon lamp. The Ar or air ambient is maintained to a pressure of 3–5 bar. The rate of crystallization was controlled between 10 to 20mm/h. A previously grown single crystal was used to seed the growth process. The seed and the feed rod were rotated in opposite directions at a rate of 50 r.p.m and 1 r.p.m respectively. In the similar manner doped $\text{La}_{0.9}\text{Sr}_{0.1}\text{MnO}_3$ feed rod was formed using the starting material of La_2O_3 , MnCO_3 , SrCO_3 in desired weight ratio. Chemical composition of the final crystals was obtained using an electron probe microanalyser and XRD [99]. In Fig. 2.2, we have shown a single crystal made in floating Zone melting technique [100]. Though floating zone melting technique is widely used in high purity manganite single crystal growth,

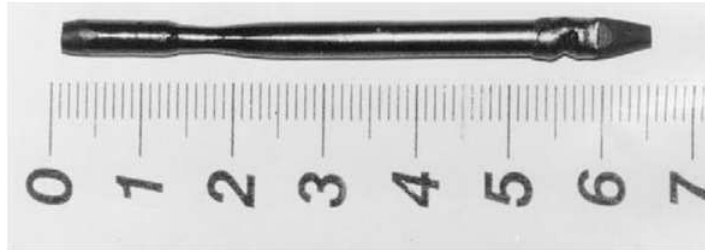


Figure 2.2 Single crystal of $(\text{La}_{0.7}\text{Ca}_{0.3})_{0.93}\text{MnO}_3$ made by floating zone technique. scale is in cm. From Shulyatev et al. [100].

still there are some problems found as given below, [99]

- i. different electronic and magnetic properties for the same nominal composition,
- ii. we do not have full information about the factors which controls cation ratio, homogeneity of element distribution and defect structure in the crystal.

The process of defect formation and elemental distribution in the crystal can be understood by the binary phase diagram in air [102] shown in Fig. 2.3. In this phase diagram, LaMnO_3 has a homogeneous region at $0.908 < \text{La}:\text{Mn} < 1.202$ at 1123K. The La:Mn ratio in growing single crystal generally depends on the non-stoichiometry of the feed rod and evaporation of Mn from the melt during the growth process in floating zone technique. The increased La:Mn ratio shifts the composition of the melting zone towards the eutectic point of $\text{La}_2\text{O}_3 - \text{LaMnO}_3$. In this region, the difference between T_{solid} and T_{liquid} is small ($\approx 100-150^\circ\text{C}$). Due to this small temperature difference, slight variation in temperature and concentration in diffusion layer can lead to crystallisation of La_2O_3 inclusions. The effective

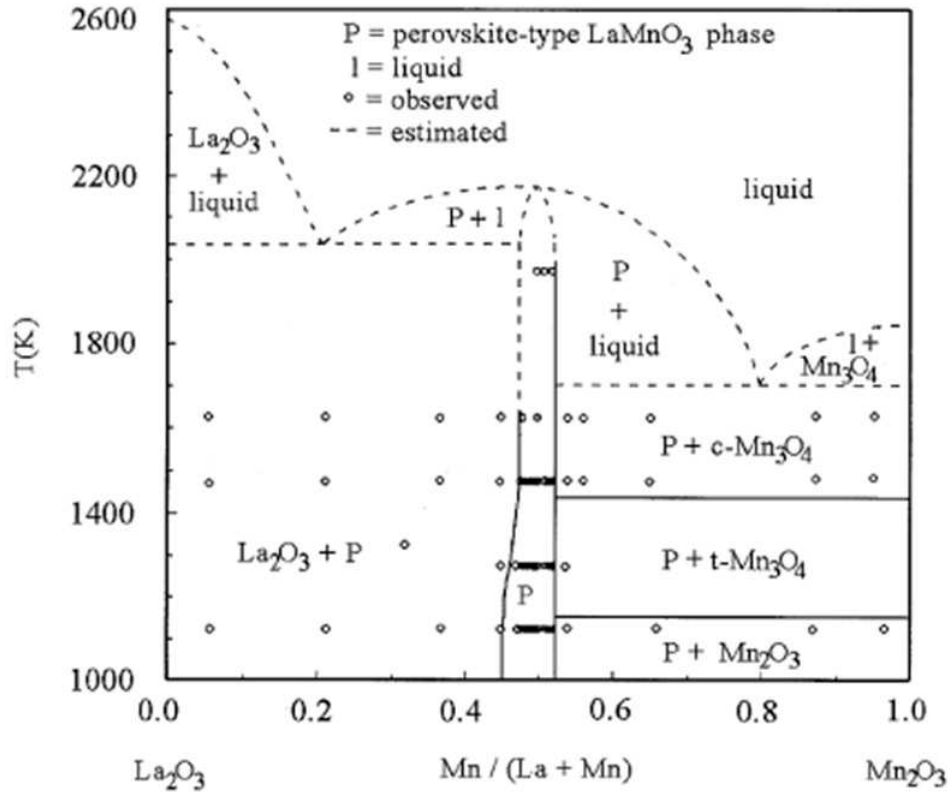


Figure 2.3 Binary phase diagram of La_2O_3 - Mn_2O_3 in air. From Roosmalen et al. [102].

distribution coefficient of Ca or Sr is expressed as $k_B = \frac{C_S}{C_L} (<1)$, where C_S and C_L are respectively the concentration of Ca/Sr in the grown–solid and in the melt/liquid zone. The C_S distribution is expressed as:

$$C_S = C_f \left(1 - (1 - k_B) \exp\left(-\frac{k_B z}{l}\right) \right), \quad (2.1)$$

where C_f is the concentration of the B-site element (A and/or B) in the feed rod, z is the current length, and l is the zone length. This causes the concentration of Ca to increase in the melt during the steady growth stage [103] causing the cation ratio $(\text{La}+\text{Ca}/\text{sr})/\text{Mn}$ in the melt to exceed unity. The ambient atmosphere has a noticeable effect on the distribution coefficient of Ca/Sr. For example, a reduced oxygen atmosphere can increase the distribution coefficient (k_B) [99]. One has to optimize different parameters to make a perfect stoichiometric single crystal.

2.2.3 Manganite single crystals used in the experiment

To investigate physical properties of perovskites, we have used three LaMnO_3 single crystals and on $\text{La}_{0.9}\text{Sr}_{0.1}\text{MnO}_3$ single crystals having different dimensions. Between the three LaMnO_3 single crystal, one was made in SINP, Kolkata, India and other two are made in Moscow [99, 100]. $\text{La}_{0.9}\text{Sr}_{0.1}\text{MnO}_3$ single crystal was also made in Moscow. In the following table, we have given the dimensions (diameter D and thickness t) & stoichiometry of different single crystals used in this thesis. As we discussed in

Table 2.1 Dimension (Diameter "D" and thickness "t") of the different single crystals used in various experiments.

Sample	Size of Crystal	Grown at
LaMnO_3 -1	D: 5mm, t: 1mm	SINP, Kolkata
LaMnO_3 -2	D: 4mm, t: 1mm	Moscow, Russia
LaMnO_3 -3	D: 3mm, t: 1mm	do
$\text{La}_{0.9}\text{Sr}_{0.1}\text{MnO}_3$	D: 4mm, t: 1mm	do

the earlier section that during single crystal growth La:Mn ratio may not be exactly equal due to the different melting point and vapour pressure of these two elements. Another factor which can effect this ratio is the stoichiometry at the oxygen site. Due to these factors and to maintain the neutrality of LaMnO_3 , Mn can have slight mix valency i.e. presence of Mn^{4+} . Although the concentration of Mn^{4+} is very very less than the hole doped LaMnO_3 . So two LaMnO_3 samples made by same method can have slightly different stoichiometry with different Mn^{4+} content. Here, LaMnO_3 -1, LaMnO_3 -2 and LaMnO_3 -3 have the dissimilar concentration of Mn^{4+} (which is shown in Chapter 4 in section 2). LaMnO_3 -3 is self doped with composition $\text{La}_{0.97}\text{MnO}_3$ to maintain La:Mn ratio to 1 [99, 103].

2.3 Thin film deposition techniques

In this section, we will discuss about the techniques for growing thin films of manganites which were used for various experiments. To get a good quality thin film, we have deposited the thin films by

pulsed laser deposition (in our lab) and RF magnetron sputtering (at Moscow). Mainly the thin films of $\text{La}_{0.85}\text{Ca}_{0.15}\text{MnO}_3$ were deposited on single crystal substrates of NdGaO_3 (NGO), SrTiO_3 (STO) and LaAlO_3 (LAO) in (2 0 0) and (1 0 0) direction. To investigate the modulation of grain boundary potential by electrostatic gate, we have grown the $\text{La}_{0.85}\text{Ca}_{0.15}\text{MnO}_3$ film on polycrystalline SiO_2/Si substrate. GdMnO_3 thin film, used for resistive switching measurement, was deposited by RF magnetron sputtering.

2.3.1 Pulsed laser deposition

Pulsed laser deposition (PLD) is widely used method for growing thin film of complex multicomponent inorganic materials. PLD method was first successfully utilised for depositing high T_C superconducting film of $\text{YBa}_2\text{Cu}_3\text{O}_{7-x}$ (x represents the oxygen vacancies) by T. Venkatesan and his co-workers [104]. By this method one can deposit a variety of material from metal to insulator via semiconductor [105, 106]. But the important use of it is to deposit complex material like perovskites with perfect stoichiometry [107, 108]. Another important aspect of this method is to control layer by layer deposition of different material with desired thickness [109].

2.3.1.1 Components of a PLD set up

The main component of the PLD set are a pulsed excimer laser, focussing arrangement (like lens) and a vacuum chamber. The PLD set up in our lab is shown in Fig. 2.4. The laser used in PLD falls in the category of the gas laser. The laser uses a mixture of a noble gas (Kr, Ar, Xe) and a reactive halogen gas (F, Cl) as an active medium. The wavelength of the laser depends on the mixture of these two gases. The term excimer is used for the laser which means excited dimer or excited diatomic molecule i.e. the molecules (active medium) which represent a bound state of their constituents only in the excited electronic state, but not in the electronic ground state. The wavelength of the excimer laser falls in the range of 126nm-400nm i.e. in the ultraviolet region (some excimer laser with their corresponding wavelengths shown in the table 2.2). For the deposition of the manganite thin films, we have used KrF excimer laser of wavelength 248 nm with pulse duration 10ns.



Figure 2.4 PLD set up in our lab.

Table 2.2 Some excimer lasers with their corresponding wavelengths (λ).

Laser	λ (nm)
XeCl	308
XeBr	282
KrF	248
ArF	193

The deposition chamber consists of the following components,

- i. laser focussing system (a biconvex UV transparent lens mounted on a movable scale),
- ii. few high quality quartz (for passing the laser into the chamber) and glass windows (for viewing),
- iii. rotating target holder (shown in Fig. 2.5(a)),
- iv. substrate holder with a heater (shown in Fig. 2.5(b)),
- v. pumping system for high vacuum
- vi. different gas (inert and O_2) lines for required ambient atmosphere during the deposition.

There is a gate valve between the pumping system and the chamber. Six targets can be mounted at a time inside the chamber on the target holder at an interval of angle 60° .

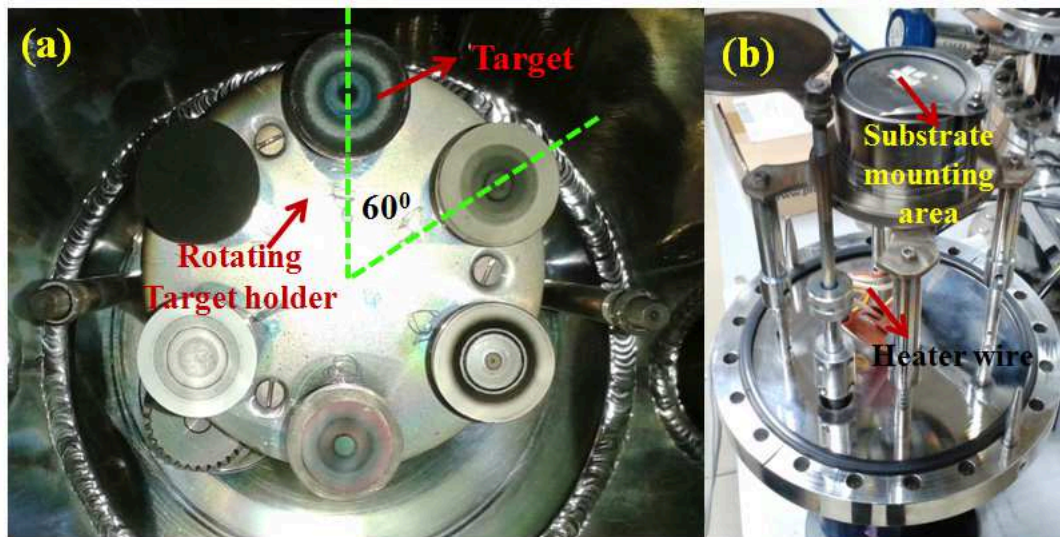


Figure 2.5 (a) Rotating target holder inside the chamber. (b) Substrate holder.

2.3.1.2 Pulsed laser deposition technique

PLD is actually a physical vapour deposition process carried out in vacuum or in the presence of inert/O₂ gas pressure. A high power pulsed laser (typically of the order of 10-100 MW/cm²) is focussed on a target material that is to be deposited. The high power laser pulse ablates the target material and make a plume of the material directed to the substrate. The plume of the target material is actually a plasma containing energetic species which may be atoms, ions, molecules and electrons which expands in a flow perpendicular to the surface and is collected on a suitable substrate. In Fig. 2.6, we have shown the schematic diagram of the deposition technique. In PLD, eximer laser evaporates the target material in a non equilibrium way where huge amount of heat is generated in a few ns in the thin surface layer of the target material. This way of laser ablation preserves the sample stoichiometry (whole compound material evaporates together at a time) in the substrate as the target material. In the equilibrium thermal evaporation process, generally it is difficult to maintain the stoichiometry of a complex material due to different thermal evaporation rate of building elements. During the deposition of the thin film, we rotate the target to get a uniform ablation on the target (other wise in course of time high intensity laser at same place can damage the target at that area). Also it can produce particulate (chunk of material) in the film which are undesirable for a good quality film. The factors which control the film growth in

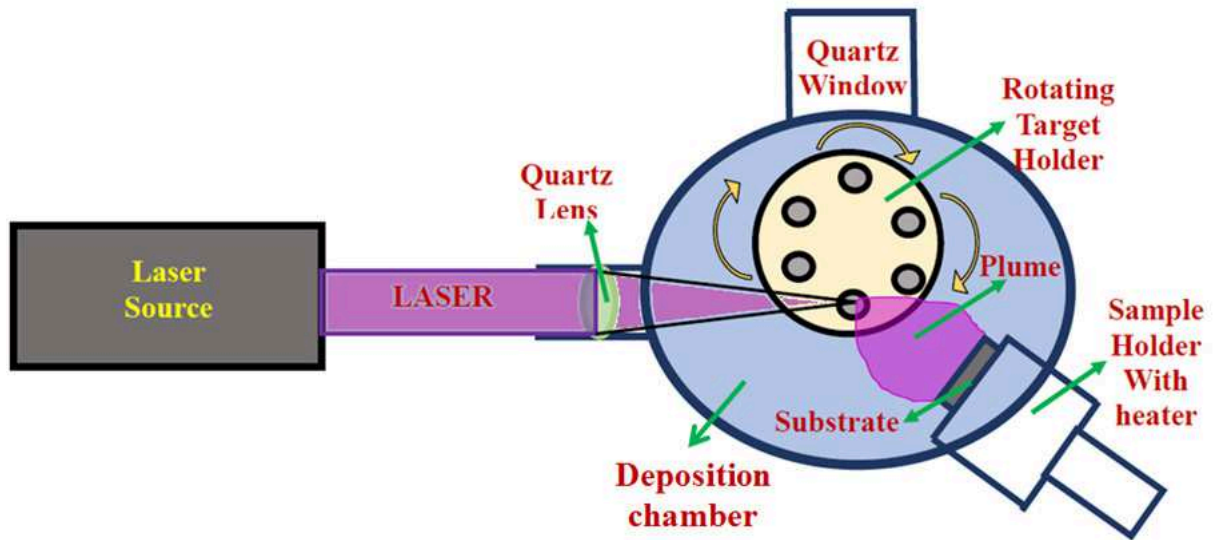


Figure 2.6 Schematic diagram of the PLD technique.

PLD are following,

- i. stoichiometric and compact target
- ii. fluence (i.e. energy/cm²) at the target,
- iii. no. of laser shots
- iv. repetition rate of the laser (i.e no. of pulse/sec),
- v. reactive gas (O₂ or N₂ or Ar) pressure or vacuum in the chamber,
- vi. chemically cleaned substrate,
- vii. substrate temperature at the time of deposition and
- viii. annealing time after deposition.

One has to optimise these parameters to get a good quality homogeneous film of desired composition. We have used 1 inch non-porous, stoichiometric target of La_{0.85}Ca_{0.15}MnO₃ (detail about the target is in next subsection) for the deposition of the thin films on different substrates. The fluence of the laser pulse is calculated by E/A where E is the laser energy (measured by a light meter at the laser window) and A is the area of the laser spot on the target (generally few mm²). Area of the laser spot is measured by keeping a laser sensitive paper at the target place and focussed laser makes a spot in the paper (shown in Fig. 2.7(a)). One can change the laser fluence by varying the area of the laser spot by moving the lens position. The required laser fluence will be different for different materials. We have optimised and used the laser fluence of 1-2 J/cm² for the deposition of La_{0.85}Ca_{0.15}MnO₃ film. The no. of laser shots, used for the deposition, determine the thickness of the film when the other controlling parameters are kept constant. But the thickness of the film can vary with similar no. of laser shots if the substrates or the target materials are different.

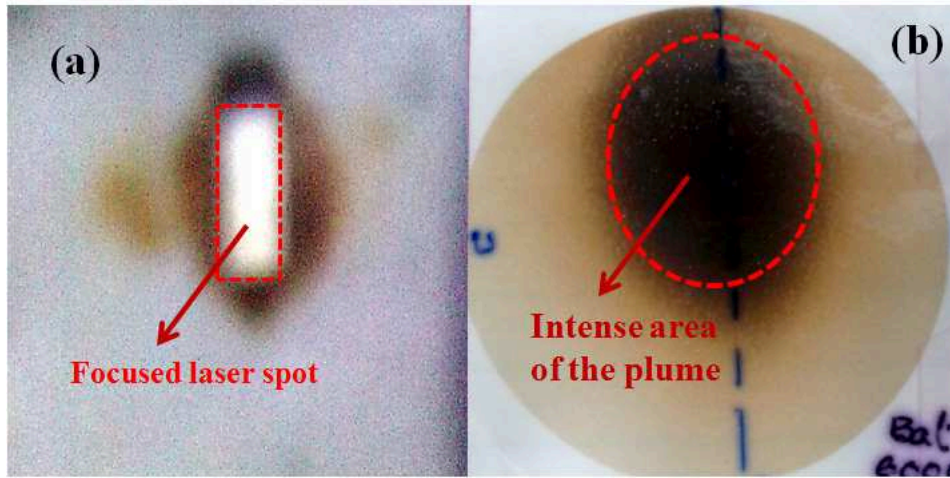


Figure 2.7 (a) Area of the focussed laser spot at the target place. (b) Intense area of the laser plume at the substrate place.

For the deposition of thin film of few nm, we have used 500-1500 laser shots for the deposition. All the $\text{La}_{0.85}\text{Ca}_{0.15}\text{MnO}_3$ thin films used for the investigation in this thesis are deposited with 1000 laser shots. The repetition rate of the laser pulse helps to deposit the film uniformly over the substrate or helps in the growth process of the film. High repetition rate can pile up the material on the substrate instead of layer by layer growth. We have used low repetition rate of 3Hz to deposit all the films. The thin films can be deposited in the presence of different gases in the chamber. For metal film deposition, high vacuum or inert gas atmosphere is required in the chamber. Oxygen is used in the chamber for depositing oxide samples and nitrogen is used for growing nitride films. Generally, the reactive gas (O_2 or N_2) pressure in the chamber plays a crucial role to maintain the stoichiometry of the oxide and nitride films. In our case, we have maintained the O_2 pressure of 10^{-3} mbar in the deposition chamber. The substrate on which the film will be deposited should be cleaned properly. We have cleaned the substrates using different chemicals like Tri-chloro Ethylene (T.C.E), Acetone, Methanol and mild acid and base solutions. To make a homogeneous film, one should expose the larger area of the plume to the substrate. The exposed area of the substrate to the plume can be varied by changing the distance of the substrate holder to the rotating target holder. Before putting the substrate into the substrate holder, we covered the area of the holder by a laser sensitive paper and got the intensity profile (Shown in Fig. 2.7(b)). We mounted the substrates in the middle of the highly intense area of the plume so that the

substrate is exposed to larger portion of the plume. Before the deposition, we heated the substrate up to 600°-700°C. Then we annealed the deposited film in O₂ ambient for few hours which helps to lower the film's roughness and maintain the oxygen stoichiometry in the deposited film.

2.3.1.3 Making and Characterisation of PLD target

As we mentioned in the earlier section that the target (the material which will be deposited on the substrate) in PLD plays an important role to determine the quality of the thin film. In this work, we have made a La_{0.85}Ca_{0.15}MnO₃ target by chemical synthesis route. We prepared a 10ml 0.4M solution of La(CH₃CO₂)₃, Ca(C₂H₃O₂)₂ and Mn(CH₃COO)₂ dissolved in 1:1 ratio of CH₃COOH and H₂O in desired proportion. Then the solution is heated and stirred at 150°C for overnight. After that, we kept and stirred the solution at 200°C for 6hr. Gradually the solution is heated at 350°C for 1.5hr, 450°C for 1.5hr and at 650°C to 1000°C for 6hrs (till the solution become nearly solid). Then we grind the solid material and pelletised it. Generally, the as grown pellet is not compact or it is porous. Due to that, we heated the pellet in a furnace at higher temperature (1000°C ≤ T ≤ 1600°C) for different times until the grains in the pellet developed in larger size and make it compact. In Fig. 2.8, we have shown the SEM image of the target pellet at different temperatures. From Fig. 2.8, we can see that

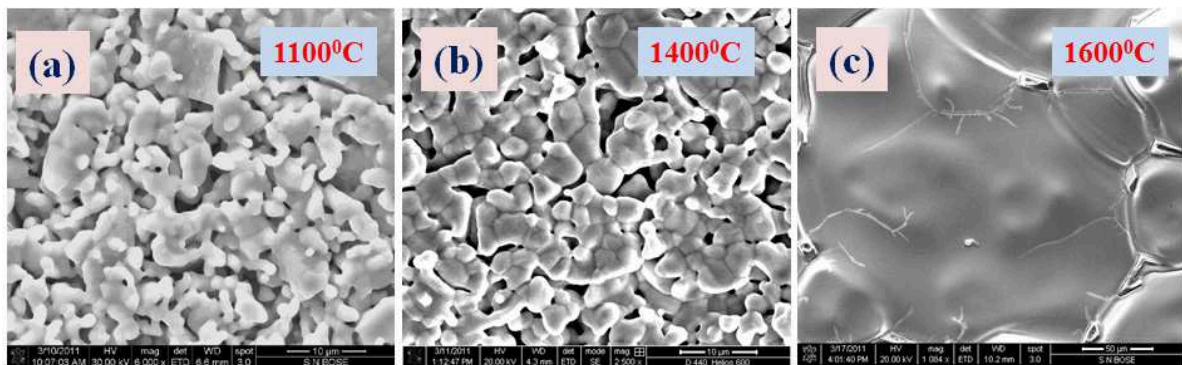


Figure 2.8 SEM image of the target pellet heated at (a) 1100°C, (b) 1400°C and (c) 1600°C.

the target pellet becomes more compact when we heated it to higher temperature. The grain size of the pellet become as large as hundreds of a micron. This type of compact target pellet is very useful for depositing particulate less high quality film.

To check the formation of the desired phase, we have performed XRD and EDAX (the detail about the procedures are in the next section) on the target pellet. In Fig. 2.9 (a), we have shown the x-ray diffraction peaks of the $\text{La}_{0.85}\text{Ca}_{0.15}\text{MnO}_3$ (in powder form taken from the target). We find that all the experimental XRD peaks are well matched with the standard ICDD peaks of $\text{La}_{0.85}\text{Ca}_{0.15}\text{MnO}_3$. We have also denoted the corresponding hkl value of all the peaks. XRD pattern of the $\text{La}_{0.85}\text{Ca}_{0.15}\text{MnO}_3$ powder confirms the formation of desired phase without any impurity. In Fig. 2.9(b), we have shown

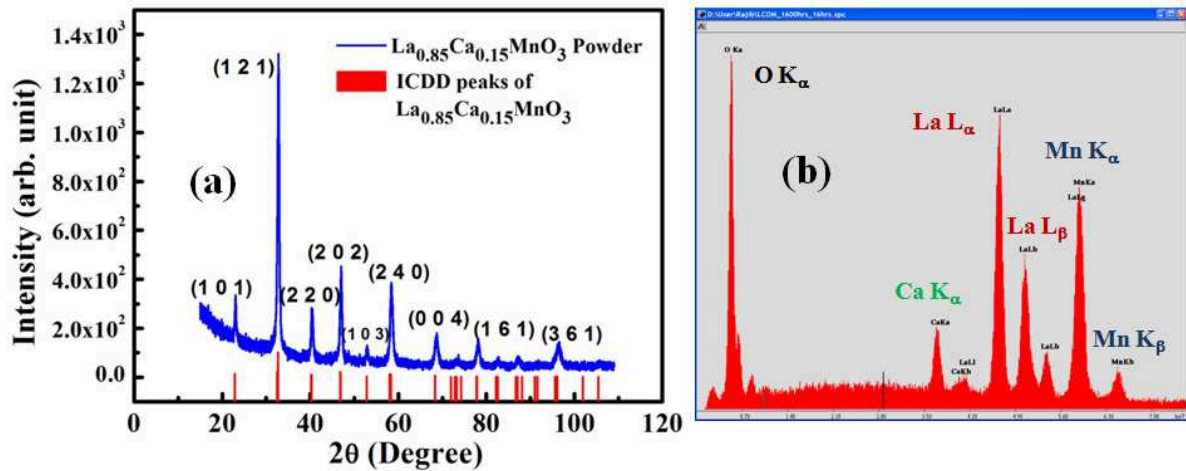


Figure 2.9 (a) XRD of the powder taken from the $\text{La}_{0.85}\text{Ca}_{0.15}\text{MnO}_3$ target. (b) EDAX analysis of the target pellet .

the EDAX analysis of the target pellet to check the presence of all compositional elements with the expected atomic ratio. From the EDAX analysis, we found presence of all the building elements for the target material like La, Ca, Mn and O with their corresponding L_α , L_β , K_α , K_β x-ray lines without any lines from impurity elements. In table 2.2, we have tabulated the atomic percentage of all the compositional elements. From table 2.2, we found that the $\text{La}_{0.85}\text{Ca}_{0.15}\text{MnO}_3$ target has nearly perfect stoichiometry with desired atomic ratios of La, Ca, Mn and O. Thus we have made a stoichiometric compact target of $\text{La}_{0.85}\text{Ca}_{0.15}\text{MnO}_3$ for thin film deposition in PLD.

2.3.2 RF Magnetron sputtering

In this section, we will discuss RF Magnetron sputtering method which is one of the common ways for deposition of thin film. Sputtering is also a physical vapour deposition (PVD) process like PLD

Table 2.3 EDAX quantification of compositional elements in $\text{La}_{0.85}\text{Ca}_{0.15}\text{MnO}_3$ target.

Elements	At%
La	16.4
Ca	2.98
Mn	19.01
O	61.04

which uses a plasma created from an inert gas (generally Ar). The energetic neutral atoms, ions of the inert gas collide with the target material and eject atoms from the target. These ejected atoms then travel some distance until they reach the substrate and start to condense into a film. The plasma is created in the vacuum chamber placing the inert gas at a pressure of 1 to 10 mTorr between a high d.c. voltage. The d.c. voltage is applied between the target (Cathode) and the substrate (Anode). This plasma is also known as a glow discharge due to the light emitted. The Argon ions in the plasma are now charged and are accelerated to the anode target. Their collision with the target ejects target atoms, which travel to the substrate and deposited. Electrons released during Argon ionization are accelerated to the anode substrate, subsequently colliding with additional Argon atoms, creating more ions and free electrons in the process, continuing the cycle. This process of sputtering method is also applicable in d.c. sputtering. But in RF magnetron sputtering, a strong magnetic field near the target area is used. Due to this magnetic field, electrons move in spiral direction along the magnetic flux lines near the target instead of being attracted towards the substrate. The advantage of this is that the plasma is confined to an area near the target, without causing damages to the thin film being formed. Also, electrons travel for a longer distance, increasing the probability of further ionizing Argon atoms. This tends to generate a stable plasma with high density of ions. More ions mean more ejected atoms from the target, which increases the efficiency of the sputtering process. The faster ejection rate, and hence deposition rate, minimizes impurities to form in the thin film. Also the increased distance between the plasma and substrate minimizes damage caused by stray electrons and Argon ions [110, 111].

The GdMnO_3 thin film used in this thesis is made by this method at "MiSiS", Moscow, Russia [112].

This scheme allows stoichiometric transfer of target material to a substrate. The GdMnO_3 target was made by solid-state synthesis using Gd_2O_3 and MnO_2 oxides powders. The films were deposited on orthorhombic (001) oriented NdGaO_3 (NGO) (space group Pbnm ; $a = 5.431 \text{ \AA}$, $b = 5.499 \text{ \AA}$, $c = 7.710 \text{ \AA}$). The substrate was heated to 650°C . The films were grown in an atmosphere consisting of a mixture of Ar and O_2 with pressure 1-2 mTorr. GdMnO_3 thin film has generally two types of crystal structure (orthorhombic and hexagonal) depending on the substrates on which the film was deposited. GdMnO_3 thin film has orthorhombic structure when it is grown on NGO [112].

2.4 Making of EDL -FET device

The electric double layer field effect transistor (EDL-FET) used for this work was fabricated with PLD deposited thin film channel of $\text{La}_{0.85}\text{Ca}_{0.15}\text{MnO}_3$. We made the channel length 2mm and width $300 \mu\text{m}$ by using a Si hard mask on top of the SiO_2/Si substrate. The source (s) and drain (d) contact pads were made by thermally evaporating Au/Ti. The source and drain pads were protected from the polymer electrolyte by a thick layer of e-beam resist (PMMA) baked for 3 min at 180°C . A window was opened in the resist layer on the channel for applying the gate. We used 10:1 mixture of PEO: LiClO_4 electrolyte as a gate dielectric. Electrolyte solution was made by dissolving PEO and LiClO_4 mixture in methanol and then stirring it till the methanol evaporated and the solution becomes a gel which was applied to the exposed region of the channel. A thin metal wire was used as the gate contact. The image of the device and corresponding electronic circuit is shown in chapter 5. The voltage V_{DS} and channel current I_{DS} between "s" and "d" is applied and measured by a 2400 Keithley Sourcemeter (SM). Another 2400 SM apply the gate voltage V_G and detect the gate current I_G in the circuit.

2.5 Brief description to characterisation techniques

In this section, we will discuss various sample characterisation methods which were used to check the phase formation, stoichiometry, valence state of an element, surface topography and thickness.

2.5.1 XRD, High Temperature XRD and Rocking curve

X-ray diffraction (XRD) technique is a non-destructive analytical technique widely used in material science for detail structural studies. This tool reveals information about the crystallographic structure, chemical composition, and physical properties of materials and thin films. X-ray diffraction is based on constructive interference of monochromatic X-rays scattered coherently from the atoms in a periodic lattice in a crystalline sample. X-rays are scattered by atoms (due to the interaction between surrounding electron cloud and the oscillating electric field of the light wave). Constructive interference occurs in specific directions given by Bragg's law: $2d_{hkl}\sin\theta = n\lambda$, where λ is the wavelength of the X-ray, d_{hkl} is the distance between two lattice planes, hkl represents the miller indices of a crystal plane, θ represents the angle between the incoming X-ray and the reflecting lattice plane, and n is the order of the reflection (shown in Fig. 2.10(a)). These diffracted X-rays are detected and counted. Normally X-ray powder diffraction (XRD) is primarily used for phase identification of a crystalline material and can provide information on unit cell dimensions using the Bragg's law. By scanning the sample through a range of 2θ angles, all possible diffraction directions of the lattice should be attained due to the random orientation of the powdered material. Conversion of the diffraction peaks to d-spacings allows identification of the material. X-ray diffractometers consist of three basic elements: an X-ray tube, a

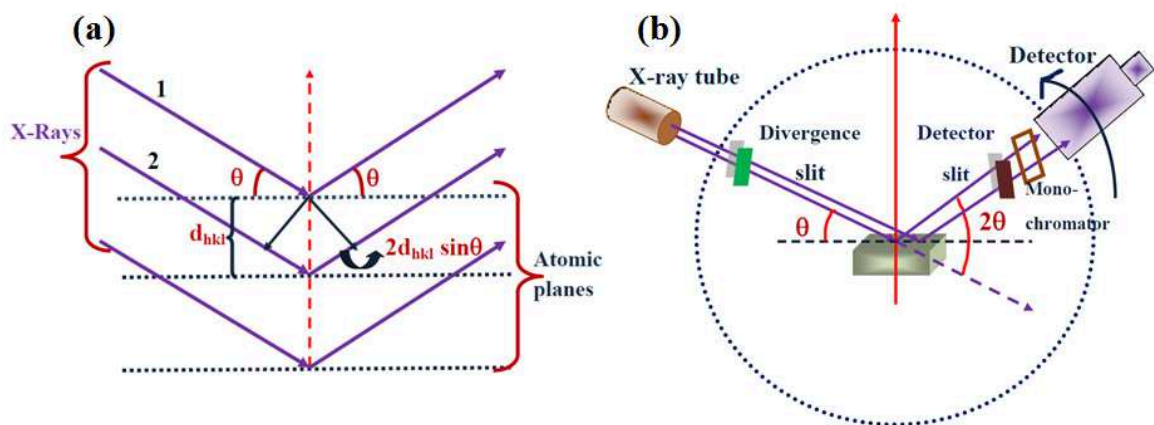


Figure 2.10 Schematic diagram of (a) X-ray diffraction from the crystal planes. (b) XRD measurement technique.

sample holder, and an X-ray detector (shown in Fig. 2.10(b)). X-rays are generated in a cathode ray

tube by heating a filament to produce electrons, accelerating the electrons toward a target by applying a voltage, and bombarding the target material with electrons. When electrons have sufficient energy to dislodge inner shell electrons of the target material, characteristic X-ray spectra are produced. These spectra consist of several components, the most common being K_{α} and K_{β} . To produce Monochromatic X-rays needed for diffraction, filtering of X-rays by foils or crystal monochromators is required. These X-rays are collimated and directed onto the sample. The sample or/and the detector are rotated and the intensity of the reflected X-rays is recorded. When the angle of the incident X-rays satisfies the Bragg condition, constructive interference occurs and a peak appears in intensity profile.

In our experiments XRD spectra were recorded using PANalytical X-PERT PRO diffractometer. The wavelength of the X-rays used is 1.54\AA corresponding to Cu K_{α} source. These X-rays have sufficient energy to penetrate the solids and permit to analyse their internal structures. The operating conditions are 45kV and 40 mA. Here the sample stage is fixed while both the source and the detectors are rotated. In the source side programmable divergence slit is used to automatically select the slit dimension while we use PIXEL detector for fast measurements with low signal to noise ratio. In Fig. 2.9(a), we have shown normal XRD data of $\text{La}_{0.85}\text{Ca}_{0.15}\text{MnO}_3$ powder. For a polycrystalline sample, Bragg peaks appear at different 2θ values due to the presence of different orientation of crystallite planes having dissimilar hkl values. One can identify the hkl values of different Bragg peaks by comparing them to the data base of International Center for Diffraction Data (ICDD).

High resolution X-ray diffraction (HRXRD) is an important technique for studying individual Bragg peaks of single-crystal and thin-film materials. The HRXRD technique requires a highly parallel X-ray beam (to ≈ 10 arc-seconds divergence) incident on the sample, which is achieved using very high quality mirror and monochromator combinations. Typical routine applications of HRXRD include reflectivity measurements, rocking curves and reciprocal space mapping. This allows for the precise measurement of layer thickness, layer composition analysis and diffuse scatter measurements to be performed. High-resolution x-ray rocking curves are used to analyse the thickness, composition, and strain of epitaxial single crystal films. In rocking curve, we usually measure scattered X-ray intensity as a function of θ and 2θ such that θ changes in a way that is linked to 2θ as $\theta = \frac{1}{2} 2\theta + \text{offset}$. It

is done by fixing the detector at the center of the expected Bragg reflection (from the substrate) and following the diffracted intensity as the sample is independently rotated (or "rocked"). The intensity of the diffracted X-rays is measured as a function of angle with respect to the sample surface (θ), in a step-wise manner. Rocking curve on a thin film is generally performed to check the epitaxial and oriented growth of the sample along the crystallographic direction of a single crystal substrate. The sample peak can be broadened depending on the inhomogeneity, strain present in the sample and one can estimate these parameters from the rocking curve data. We have done rocking curve of the $\text{La}_{0.85}\text{Ca}_{0.15}\text{MnO}_3$ film grown on single crystal substrates of NGO, LAO and STO to measure the variation of strain on these three films (detail discussion is in Chapter 6).

For dynamic monitoring of structural phase change X-ray diffraction measurements are performed with varying temperature. Here, we used high-temperature sample stage from Anton Paar (HTK 16N) for in-situ investigations of phase transitions. The attachment consists of a small chamber which can be evacuated by a oil-free pump. The sample is directly heated with a heating filament which can go up to 1500°C . The heating strip is platinum. The main applications of High-temperature XRD are: (a) in-situ crystallographic characterization of high-temperature materials (b) phase transformation studies, (c) structure determination of high-temperature phases, (d) determination of thermal expansion coefficients, and (e) investigation of chemical reactions. We have performed high temperature XRD in three LaMnO_3 single crystal to find out the structural transition (Orthorhombic to Rhombohedral) temperature T_R (discussed in detail in chapter 4).

2.5.2 Scanning electron microscope

A scanning electron microscope (SEM) is an electron microscope creating the image of a sample by scanning a focused electron beam over the sample surface and detecting the secondary electrons emitted from it. The electrons in the beam interact with the sample, producing various signals that can be used to obtain information about the surface topography and composition. The SEM produces images by scanning the sample with a high-energy beam of electrons. When the electron beam hits the surface of the sample, it penetrates the sample to a depth of a few microns, depending on the accelerating voltage

and the density of the sample. As the electrons interact with the sample, they produce secondary electrons, backscattered electrons and characteristic X-rays. These signals are collected by one or more detectors to form images, which are then displayed on the computer screen. The scattering of the electrons from the sample surface will depend on the available scattering cross section. It may differ in the different regions and produce an intensity profile of the scattered electrons which makes the contrast in the image of the material [113]. The schematic diagram of the different components in SEM for imaging is shown in Fig. 2.11. A regular SEM is mainly composed of electron source, condenser lens,

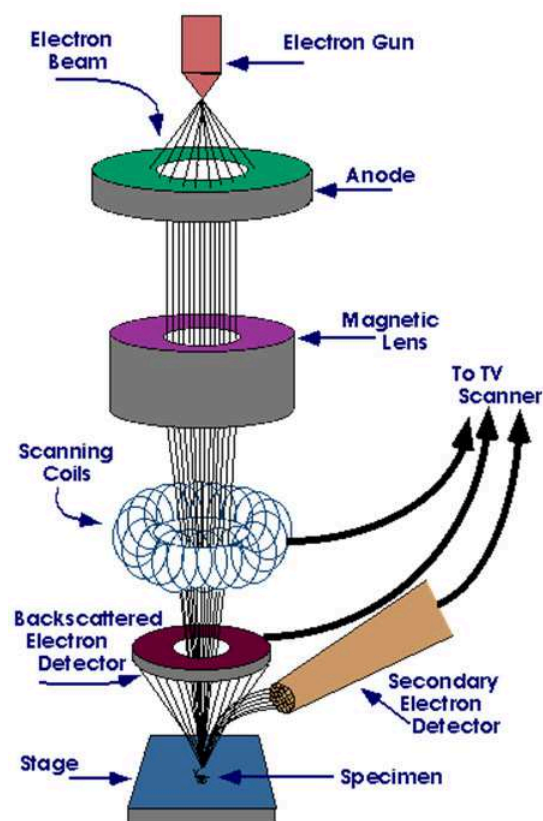


Figure 2.11 Schematic diagram of the SEM imaging technique (courtesy: Ref. [114]).

scanning coils, secondary electron detectors and vacuum chamber. There are three types of commonly used electron sources: 1. Tungsten filament 2. Solid state crystal (CeB_6 or LaB_6) and 3. Field emission gun (FEG). Electrons are produced at the source by thermionic heating. These electrons are then accelerated to a voltage between 1-30 kV and condensed into a narrow beam which is used for imaging

and analysis. A series of condenser lenses focus the electron beam as it moves from the source down the column. Narrower the beam, smaller will be the spot size in contact with the surface. After the beam is focused, scanning coils are used to deflect the beam in the X and Y axes so that it scans in a raster fashion over the surface of the sample. Samples are mounted and placed into a chamber that is evacuated. The sample chamber can include a translation stage, tilt and rotation devices, feed-throughs to the outside, temperature stages, optical cameras, and a variety of other devices to assist in imaging the sample. The detector collects the electrons coming from the sample. Two types of electrons are typically used for imaging: secondary electrons (SE) and backscattered electrons (BSE). Secondary electrons are low energy electrons produced when electrons are ejected from the k-orbitals of the sample atoms by the imaging beam. The most popular detector in SEMs is the Everhart-Thornley detector. It consists of a Faraday cage which accelerates the electrons towards a scintillator. This in turn produces a current, which is directed towards a photomultiplier, and the amplified signal is read on the monitor.

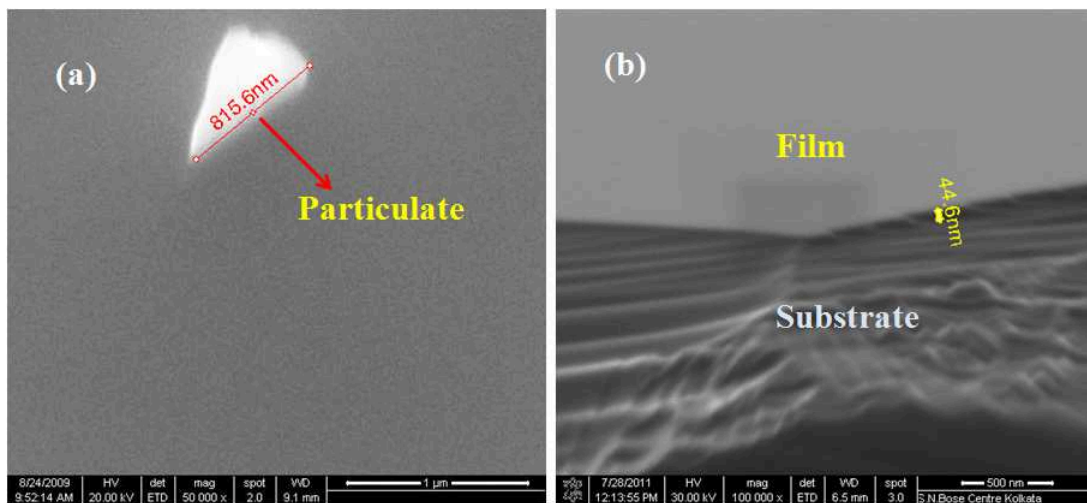


Figure 2.12 (a) SEM image of one of the PLD grown $\text{La}_{0.85}\text{Ca}_{0.15}\text{MnO}_3$ film on NGO. Image shows a smooth surface with lower concentration of particulates. (b) Approximate thickness of a $\text{La}_{0.85}\text{Ca}_{0.15}\text{MnO}_3$ film grown on Si substrate with 4000 laser shots in PLD using cross-sectional SEM.

The imaging can be done either in vacuum ($\leq 10^{-3}$ mbar) or in a desired ambient (depending on the sample). As it uses electron as an imaging tool, it has higher resolution than the optical imaging

techniques. To image a sample which has much lower dimension than the wavelength of the visible light, it is an useful and efficient technique. Mainly various types of inorganic and organic samples, having dimension in sub micron to nanometre range, are used for imaging in SEM. We have used SEM for imaging the growth of the grain size of $\text{La}_{0.85}\text{Ca}_{0.15}\text{MnO}_3$ target pellet with different temperatures (shown in Fig. 2.8) and to check the surface quality (concentration of particulates and the presence of grains on the film surface) of a deposited thin film (shown in Fig. 2.12(a)). We have also used cross sectional SEM imaging to measure the approximate thickness of the deposited thin films (shown in Fig. 2.12(b)).

2.5.3 Energy dispersive X-ray Analysis

Energy-dispersive X-ray analysis (EDAX) is an analytical technique used for the elemental analysis or chemical characterization of a sample. It is complementary to electron microscope, which enables us to determine the composition of the features imaged by the microscope. EDAX makes use of the X-ray spectrum emitted by a solid sample bombarded with a focused beam of electrons to obtain a localized chemical analysis. The principle of EDAX is that electron beam is incident on the sample

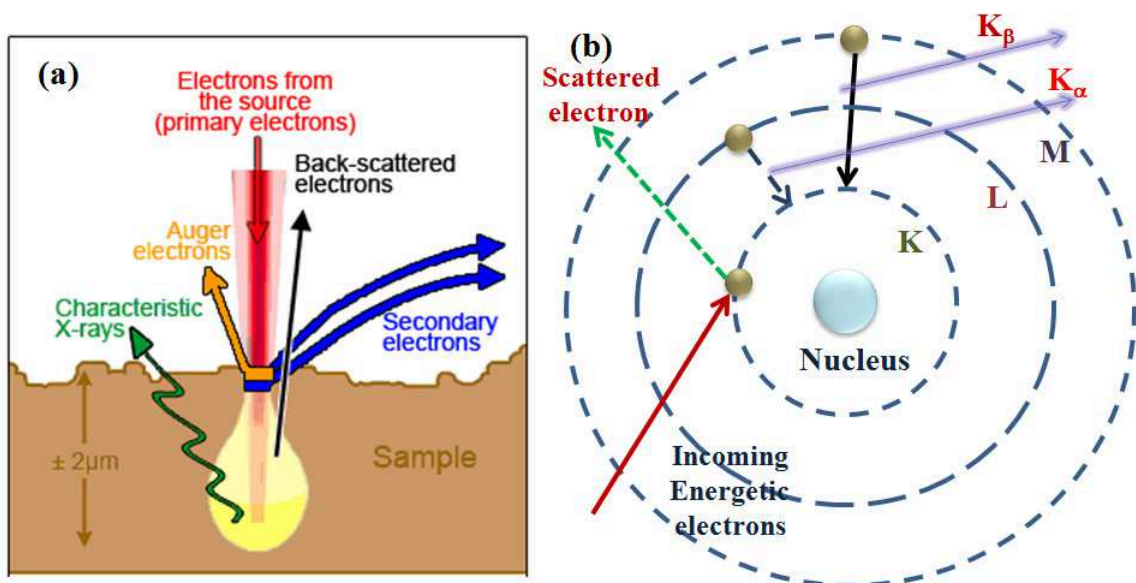


Figure 2.13 Schematic diagram of (a) interaction of sample surface with energetic electron beam (from Ref. [115]) and (b) emission of characteristic X-rays form the element.

surface to achieve X-rays having energies characteristics of the element. When the incident beam interacts with the sample creating secondary electrons leaving holes in the electron shells where the secondary electrons used to be. If these holes are in inner shells, the atoms are not in a stable state. To stabilize the atoms, electrons from outer shells will drop into the inner shells, losing some energy in the form of X-rays. Essentially, each element has characteristic X-ray line(s) that allow a sample's elemental composition to be identified by a nondestructive technique. The schematic diagram of the interaction of the sample with energetic electrons and emission of X-ray lines are shown in Fig. 2.13. Since the X-rays are formed by the electron beam interaction with the sample surface, what ever area of the sample being imaged is analysed. This allows the SEM to perform elemental analysis in very selected areas. The X-rays emitted from the sample atoms are characteristic in energy and wavelength not only to the element of the parent atom, but also to the shells from which electrons have been lost or replaced. The emitted X-rays are represented as K, L and M lines depending on the transition to the specific shell of K, L or M. Greek letter α and β subscribed to a X-ray line (K or L or M) to distinguish the transition from different high energy levels to a particular low energy levels like K, L and M. All elements from atomic number 4 (Be) to 92 (U) can be detected in principle as the energy of the characteristic x-ray from an element is proportion al square of the atomic no. Z i.e. $\nu \propto Z^2$. Qualitative analysis involves the identification of the lines in the spectrum and is fairly straightforward owing to the simplicity of X-ray spectra. Here, we have used environmental scanning electron microscope (ESEM) from FEI, Netherland (model Quanta 200) which can be operated both at High vacuum or at required environmental condition with a maximum operating voltage of 30 kV.

EDAX is used in this thesis for checking the presence of compositional elements and stoichiometry of the investigated materials like LaMnO_3 single crystals, $\text{La}_{0.85}\text{Ca}_{0.15}\text{MnO}_3$ target (shown in Fig. 2.9(b)) and all the thin films used for the different experiments. In Fig. 2.14 ,we have shown EDAX data of LaMnO_3 -1. It is confirmed form the EDAX data that all the compositional element of LaMnO_3 -1 are present in the sample without having any impurity elements (similar analysis were done in the other two LaMnO_3 single crystals). We also found that La:Mn ratio slightly deviates from 1:1 in the three LaMnO_3 single crystals due to the nominal mix valence at Mn site (discussed earlier in

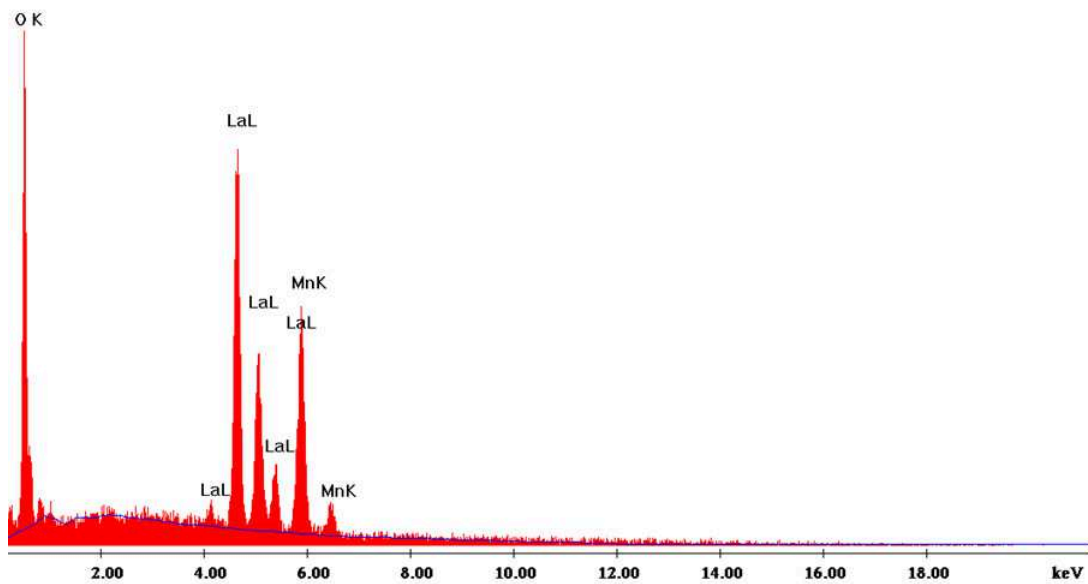


Figure 2.14 EDAX data of $\text{LaMnO}_3 - 1$.

section 2.1). But it is difficult to quantify this nominal mix valency (Mn^{3+} : Mn^{4+}) from EDAX as the difference in binding energy ($\approx 4\text{eV}$) of electrons in Mn^{3+} and Mn^{4+} are less than the resolution ($\approx 100\text{eV}$) of the EDAX. We have tried to find out the mix valency at Mn site from the spectroscopic measurements like EELS and XPS which will be discussed in the next sections.

2.5.4 Electron energy loss spectroscopy

Electron energy loss spectroscopy (EELS) is an useful and efficient technique for elemental characterisation of a material and to determine the valance state of an element in a compound [116, 117]. In EELS, we measure the energy distribution of electrons that have interacted with a specimen and lost energy due to inelastic scattering. EELS is generally carried out in high vacuum in a transmission electron microscopy (TEM) in which higher energy (100-300keV) electrons pass through the specimen (provided that the sample thickness is $\leq 1\mu\text{m}$). The high energetic electron beam is made to an imaging tool of smaller probe having diameter of few nm to produce a transmitted image of the specimen with a special resolution down to atomic scale. Thus EELS measured in TEM has very high spacial resolution. When a high energetic electron pass through a solid, it suffers collision with the atomic

nuclei of the constituent elements and with the electrons in the specimen due to electrostatic Coulomb force. These collisions can be elastic or inelastic. In an elastic collisions between the atomic nuclei and the fast electrons, there is no net transfer of energy or very small energy transfer which is hard to detect by the spectrometer. The transmitted electron beam is directed into a high-resolution electron spectrometer that separates the electrons according to their kinetic energy and produces an electron energy-loss spectrum showing the number of electrons (scattered intensity) as a function of their decrease in kinetic energy. EELS spectrum of a material which is measured up to a few tens of electron volts is called the low-loss region [117, 118]. In Fig. 2.15, we have shown the zero loss peak and the

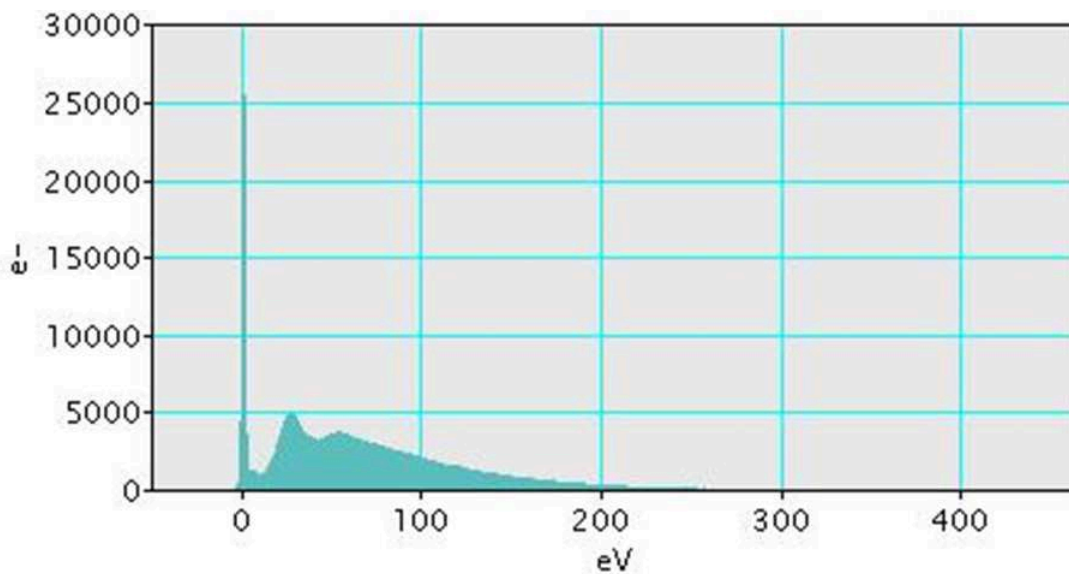


Figure 2.15 Energy-loss spectrum of LaMnO₃ -1 nano particle in the low loss region.

low loss region in the measurement of EELS in the nanoparticle of one of the LaMnO₃ single crystal. The most intense peak in the spectrum occurs at 0eV and is therefore called the zero loss peak. It represents electrons that did not undergo inelastic scattering (interaction with the electrons of the specimen) but which might have been scattered elastically (through interaction with atomic nuclei) with an energy loss too small to measure. The width of the zero-loss peak falls typically between 0.2–2eV which is mainly the energy distribution of the electron source. Other low-loss features can come from inelastic scattering by conduction or valence electrons. The energy loss is higher for the fast electrons when it collide with the inner shell electrons of the elements. Due to this collision, inner shell electrons make

an upward transition above the Fermi level if it absorbs an amount of energy similar to or greater than its original binding energy. The fast electron loses an equal amount of energy as the total energy is conserved at each collision. Due to this inner-shell scattering, the target atom will be in highly excited (or ionized) state and will quickly lose its excess energy. In the de-excitation process, an outer-shell electron (or an inner-shell electron of lower binding energy) undergoes a downward transition to the vacant place at the core level and the excess energy is liberated as electromagnetic radiation (x-rays) or as kinetic energy of another atomic electron (Auger emission). For inner shell excitations, electron intensity in EELS takes the form of edges instead of peaks. The inner-shell intensity rising rapidly and then falling more slowly with increasing energy loss. The sharp rise occurs at the ionization threshold whose energy-loss is approximately equal to the binding energy of the corresponding atomic shell. Since inner-shell binding energies depend on the atomic number of the scattering atom, the ionization edges present in an energy-loss spectrum reveal which elements are present within the specimen. Quantitative elemental analysis is possible by measuring an area under the appropriate ionization edge. Both the valence electron (low-loss) peaks and the ionization edges possess a fine structure that reflects the crystallographic or energy band structure of the specimen [116–118]. Even with an energy resolution of 2eV, it is possible to distinguish between different forms of an element. That is why EELS is an

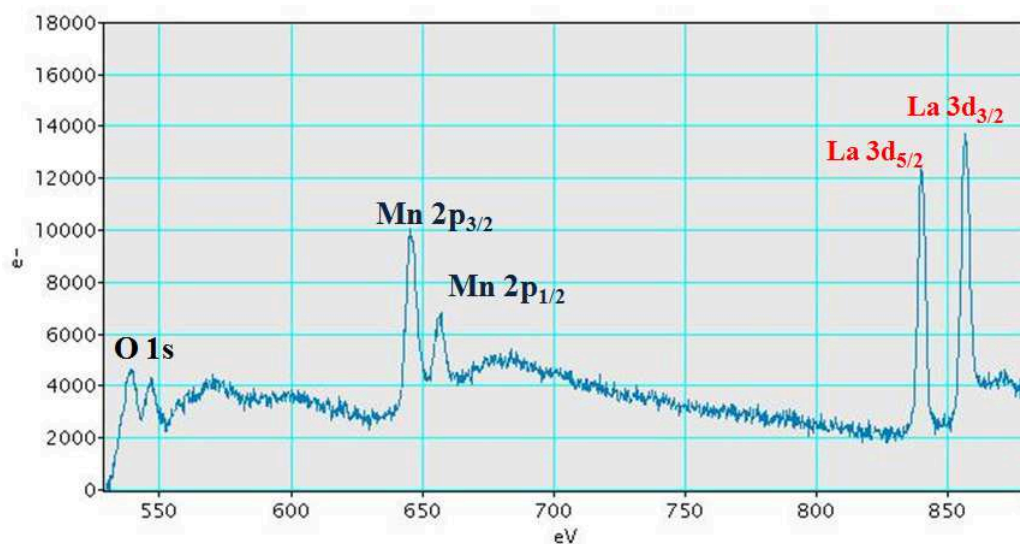


Figure 2.16 Energy-loss spectrum of LaMnO₃ -1 nano particle .

useful tool to measure the valence state of an element. We used EELS to find out the Mn valency in the three nominally pure LaMnO_3 single crystals (detail discussion in chapter 4). We prepare the sample for the EELS measurement by taking some powder samples from the three LaMnO_3 single crystals and mixed them in ethanol. Then, we make it a colloidal solution of LaMnO_3 particles and put few drops of the solution on a TEM Cu grid. The Cu grid was dried overnight and loaded to the TEM chamber. In Fig. 2.16, we have shown the EELS spectrum in nanoparticle of one of the LaMnO_3 single crystals which shows the K (inner shell excitations from 1s), L(inner shell excitations from 2p) and M (inner shell excitations from 3D) of O, Mn and La respectively.

2.5.5 X-ray photo electron spectroscopy

X-ray photo electron spectroscopy (XPS) is widely used analytical tool for surface analysis (within tenth of a nm) of a material which gives the minute details about the chemical and electronic states of the compositional elements, relative composition of the constituents in the surface region and the valence band structure. It is actually a photo electric effect where electrons come out of the material due to the interaction with high energetic X-rays. XPS and EELS generate nearly same information from a material. But in XPS, high energetic ($h\nu$) photons (instead of electrons) interact with the valence

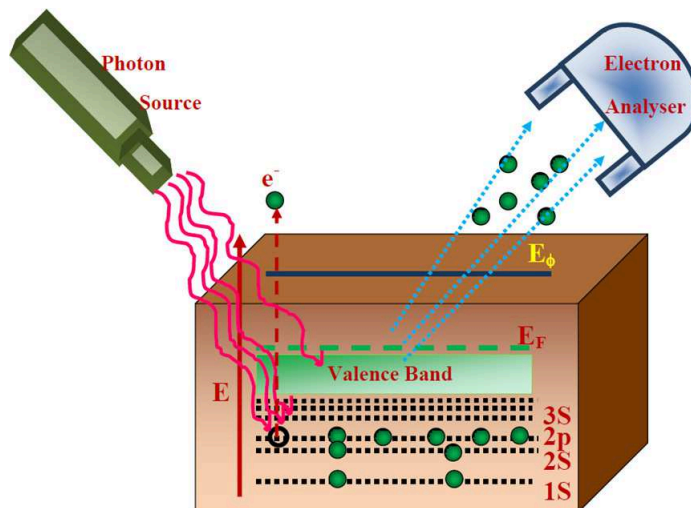


Figure 2.17 Schematic diagram of the XPS measurement procedure.

electrons and come out from the material if the binding energy (B.E.) of $E_B \geq h\nu$, where "h" is the

plank constant and ν is the frequency. These photo electrons are then collected in a spectrometer in ultra high vacuum ($\approx 10^{-10}$ mbar). The photoelectrons spectrum is generated by plotting the intensity of the photoelectrons with their kinetic energy (K.E.) or E_B following the equation $K.E = h\nu - (E_B + \phi)$, where ϕ is the work function of the material. In Fig. 2.17, we have shown the schematic digram of the XPS method. We have used XPS to check the valence state of Mn in LaMnO_3 -1 single crystal

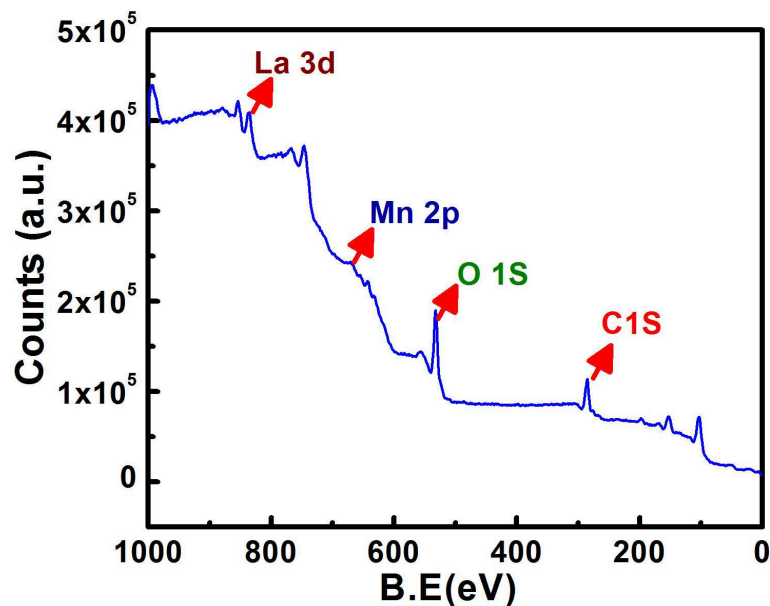


Figure 2.18 Core level XPS spectra of LaMnO_3 -1.

(detail discussion in chapter 4). Measurement was done using a commercial VG – microtech XPS instrument at I.O.P, Bhubaneswar, India. We have used $\text{MgK}\alpha$ (1253.6eV) radiation as the photon

Table 2.4 B.E values of different element form the XPS spectra.

Element	B.E (eV)
C(1s)	284.5
O(1s)	529.5, 532
Mn ($2p_{3/2,1/2}$)	641.9, 653.5
La ($3d_{5/2,3/2}$)	835, 851

source. We have done the core-level XPS spectra in LaMnO_3 -1 single crystal from which we get

peaks at different energy levels for different elements (Ls, Mn, O) due to the transition of electrons from various spin-orbit coupling states (shown in Fig. 2.18). The peak positions are assigned by taking C 1s signal as reference having B.E.= 284.5eV. We have tabulated (in table 2.4) the B.E values of the different elements from the XPS spectra (in Fig. 2.18) which matches well with the previously reported data [119].

2.5.6 Atomic force Microscopy

Atomic force microscopy (AFM) is an imaging tool to measure surface topography of a material from in sub-micron to atomic scale. Unlike optical and electron microscopes (which use photon and electrons for imaging), the imaging probe for an AFM system is a sharp tip (having dia $\approx 30\text{nm}$) made of Si or SiN mounted on a cantilever. To construct the image of the surface, mechanical interaction force (attractive or repulsive) between the atoms in the tip and surface is considered. Due to the undulation (height variation) on a specific surface, the force (ΔF) between the tip and the sample surface changes which deflects (Δx) the cantilever as $\Delta F = K\Delta x$, where K is the force or spring constant of the tip. The

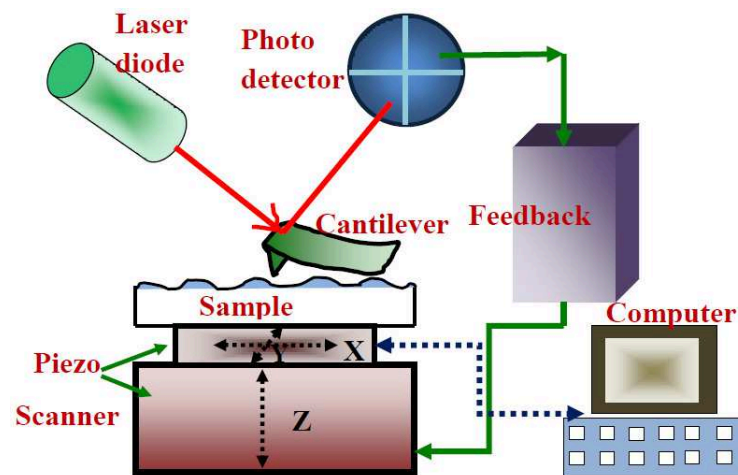


Figure 2.19 Schematic diagram of the AFM measurement procedure.

cantilever in an AFM system plays an important role for taking a surface topography. The cantilevers in AFM have spring constant (0.01-10 N/m) comparable or even less than the molecular spring constant ($\approx 1-10^2\text{N/m}$). This is why it can be sensitive to various atomic forces. The AFM tip scans the area

of a sample surface in a raster method. To detect the deflection of cantilever during the scanning of the sample surface in raster mode, a laser is focused on the head of the cantilever. The deflection of the laser beam is collected in quadrant photo detector and analysed. The height profile or the image of the surface is generated using a feedback loop. The deflection of the cantilever is used as input to a feedback circuit that moves the cantilever scanner up and down in z direction, responding to the surface topography by keeping the cantilever deflection constant. As the cantilever deflection is held constant, the total force applied to the sample is constant. Thus the image is generated from the piezoelectric scanner's z-motion with respect to X-Y motion. The scanning speed is thus limited by the response time of the feedback circuit. The detection scheme of the AFM is shown in Fig. 2.19. A vibration isolation system is attached to the AFM system so that the tip should not be perturbed by any external source.

The AFM can be operated in three modes: Contact, non- contact and tapping mode. The distance between the sample and tip should be a few angstroms in contact mode imaging. The tip should be in physical contact with the sample surface. Depending upon the topography of the sample surface, the repulsive force then bends the cantilever. In contact mode, the deflection of the cantilever is kept constant. However, in non-contact mode, the tip is oscillated at the resonance frequency and the amplitude of the oscillation is kept constant. Tapping mode is in between these two ways of imaging. Contact mode imaging is heavily influenced by frictional and adhesive forces and can damage samples and distort the acquired image. Non-contact imaging generally provides low resolution and can also be hampered by the contaminant like water layer which can interfere with oscillation. In tapping mode, frictional forces is eliminated by contacting the surface and oscillating with sufficient amplitude to prevent the tip from being trapped by adhesive meniscus forces from the contaminant layer. Depending on the nature of the sample surface (hard or soft) and quality (roughness), one has to wisely choose one of these three techniques. AFM has some advantages over optical and electron microscopes like as :

- (a) the resolution of the image in AFM is not diffraction limited (as electron or photons are not used),
- (b) image is free from aberration effects (as it is a lens less process),
- (c) AFM can measure the vertical dimension while optical and electron microscopes generates the 2D image of a surface and
- (d) imaging

can be done without vacuum.

We have used AFM in contact mode for imaging the thin films of $\text{La}_{0.85}\text{Ca}_{0.15}\text{MnO}_3$ grown on different substrates like NGO, STO, LAO and SiO_2/Si by PLD. From the AFM image of the films, we have extracted the informations like surface roughness, grain size distribution and height variation which determine the quality of the thin films. In Fig. 2.20, we have shown the images of three $\text{La}_{0.85}\text{Ca}_{0.15}\text{MnO}_3$ film deposited on SiO_2/Si with different no. of laser shots. From Fig. 2.20, we can

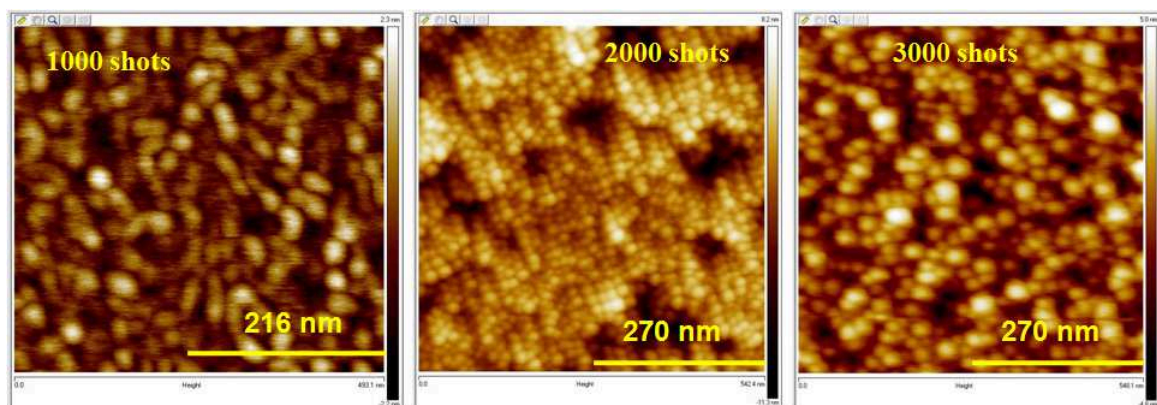


Figure 2.20 AFM image of the $\text{La}_{0.85}\text{Ca}_{0.15}\text{MnO}_3$ thin film deposited with different laser shots on SiO_2/Si in PLD . Color code representing the height variation on the surface.

see that the structure and size of the grains in the films are different with different laser shots. For higher laser shots (> 1000), surface of the film is covered with uniform spherical grains of tenth of a nm. We have used the $\text{La}_{0.85}\text{Ca}_{0.15}\text{MnO}_3$ film grown (with 1000 laser shots) on Si/SiO_2 substrate to study its electrical transport due to electrostatic carrier induction by an electric double layer (in chapter 5). AFM image of the $\text{La}_{0.85}\text{Ca}_{0.15}\text{MnO}_3$ film on single crystal substrates of NGO , LAO and STO are shown in Fig. 2.21. As expected, the surface of the film on single crystal substrates is quite different from the film on polycrystalline SiO_2/Si . Films on NGO, LAO and STO have preferential pattern (shown by the dotted line) and layer by layer growth (instead of clustering of spherical grains) in Fig. 2.21. However, there is no such preferential pattern present in the films on SiO_2/Si . The preferential growth pattern occurs due to terracing on single crystal surface when they get heated in the growth chamber before deposition. All the films has maximum r.m.s surface roughness of 1-2 nm which signifies the smoothness of the film. The unit cell dimension of manganites $\approx 0.8\text{nm}$. Thus the surface smoothness

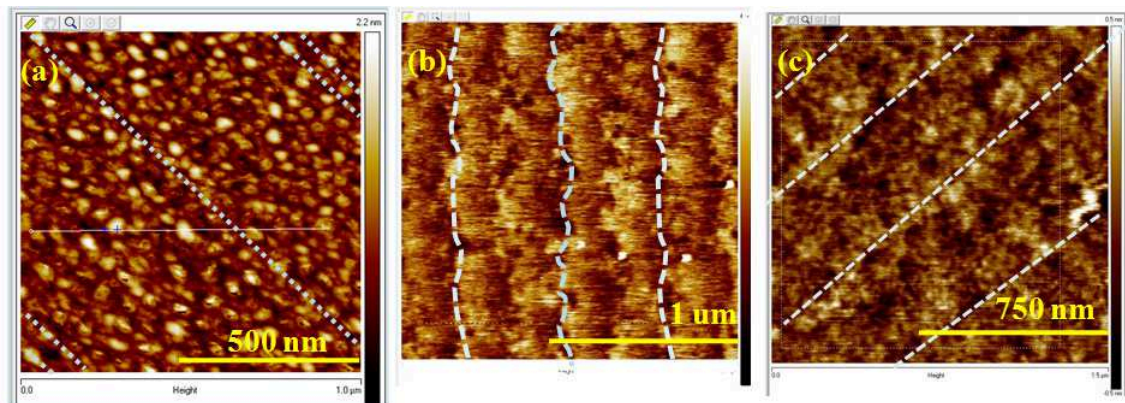


Figure 2.21 AFM image of the $\text{La}_{0.85}\text{Ca}_{0.15}\text{MnO}_3$ thin film deposited with 1000 laser shots in PLD on (a) NGO, (b) LAO and (c) STO substrates. Dotted lines are showing the preferred pattern of the films.

is around 1–2 unit cells. We have also used AFM to measure the approximate thickness of the film. We have deposited a $\text{La}_{0.85}\text{Ca}_{0.15}\text{MnO}_3$ film on SiO_2/Si substrate with 1500 laser shots in PLD. Then we covered the half of the film by a polymer resist and other half is etched by using citric acid solution (concentration 500 mg/ml) at 50°C for few minutes. Then we removed the photo resist from the other half by acetone. We have estimated the thickness of the film from the edge of the film to the etched region on the substance by measuring the vertical distance by AFM at three different positions (shown in Fig. 2.22). The average thickness comes out $\approx 17.33\text{ nm}$ for 1500 shots. On average a 10 nm film is grown by 1000 shots. The thickness of the film is again confirmed by ellipsometry (which will be discussed in later section).

2.5.7 Thickness of the thin film by ellipsometry

Ellipsometry is a technique to measure the thickness and optical constants (refractive index and extinction coefficient) of a material mainly in the thin film form using an elliptically polarised light. In Ellipsometry, we measure the change in polarization state of light reflected from the surface of a sample. When a beam of light is incident on a sample surface at some arbitrary angle of incidence θ_i , it suffers a reflection as well as refraction. The reflection from the surface change the polarisation state of the incoming light beam. The change in the polarisation state of the reflected light depends on the

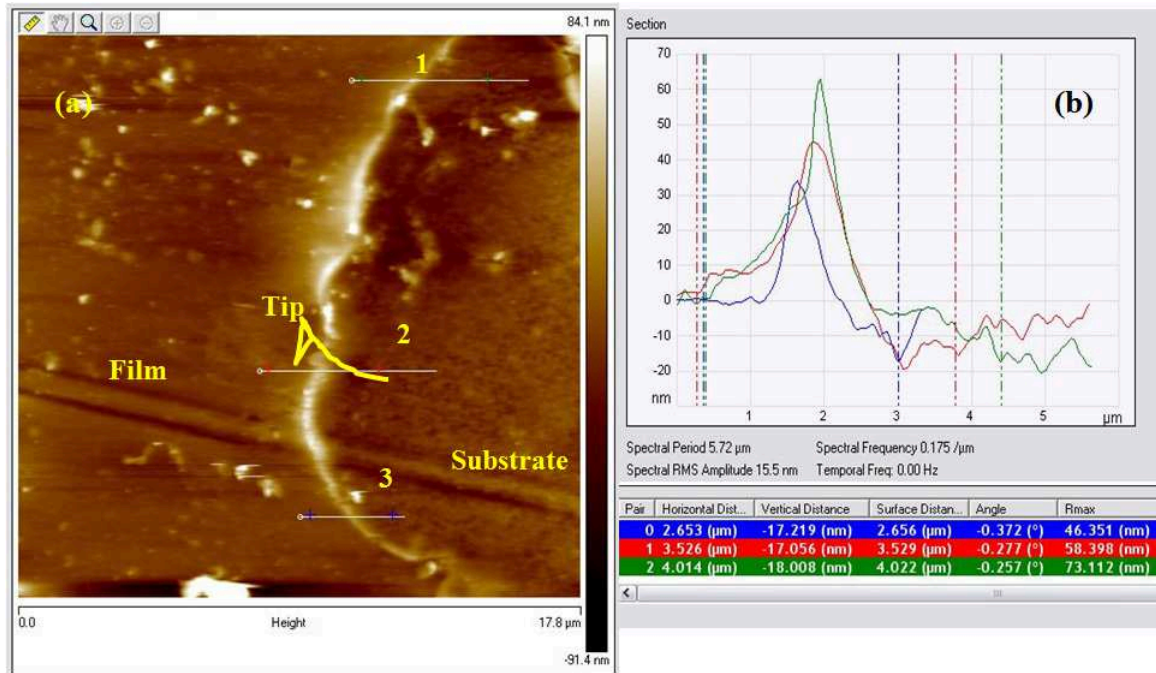


Figure 2.22 (a) Measurement of the vertical distance of the etched $\text{La}_{0.85}\text{Ca}_{0.15}\text{MnO}_3$ film on SiO_2/Si substrate in AFM. (b) Height profile at 1, 2, and 3 (green, red and blue) lines and corresponding vertical heights (from the zero reference level) are given in the below table.

sample thickness, dielectric constant and refractive index. The complex reflectance ratio ρ is related to the reflection amplitude ratio ψ and the phase difference Δ influenced by the reflection as: $\rho = \frac{R_p}{R_s} = \tan \psi \exp(i\Delta)$, where R_p and R_s are the Fresnel reflection coefficients for p (in which electric field vector is in the plane of incidence) and s (in which electric field vector is perpendicular to the plane of incidence) polarized light respectively. The ellipsometer measures ψ and Δ over a large wavelength range from which we extract the useful information. Since this technique involves the ratio of two quantities it is an accurate and sensitive method. The measurement scheme of an Ellipsometer is shown in Fig. 2.23. Ellipsometry is based on models on non-depolarizing surfaces with planar interfaces. For calculating ρ , we need the value of the dielectric constant as a function of wavelength. This can be obtained with the help of various models. In Ellipsometry, we measured the thickness of a film by the following procedures: measure ψ and $\Delta \rightarrow$ simulate data by considering appropriate model \rightarrow fitting the simulated data to the experimental data \rightarrow taking the thickness value at which error in fitting is least.

Ellipsometry measurements was done by a M 2000 Spectroscopic Ellipsometer (J.Woolam Co.,Inc)

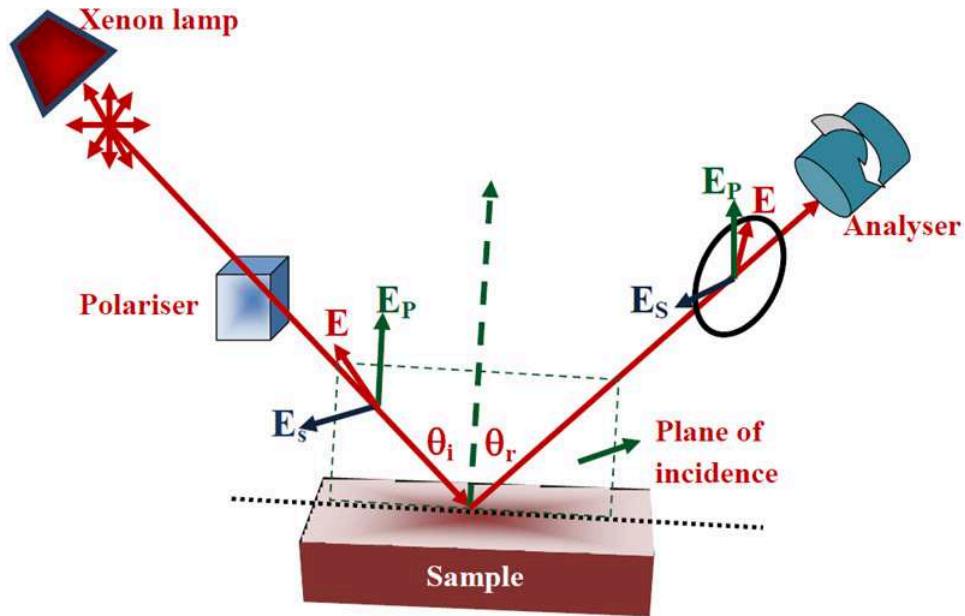


Figure 2.23 Schematic diagram of the ellipsometry method .

which is of rotating analyser type configuration. To analyse the change in ellipticity due to reflected polarized light from sample, an ellipsometer should have the following components: Light Source (Xenon lamp), Polariser (Calcite crystal), Compensator (Quarter wave plate), Phase modulator, Analyser (calcite crystal) and a Detector (Photo multiplier tube).

We have used ellipsometry to measure the thickness of the PLD grown films of $\text{La}_{0.85}\text{Ca}_{0.15}\text{MnO}_3$ on different substrates. In Fig. 2.24, we have shown the generated and experimental ellipsometry data for $\text{La}_{0.85}\text{Ca}_{0.15}\text{MnO}_3$ film on SiO_2/Si , NGO, STO and LAO substrates grown in PLD with 1000 laser shots. The thickness of the films comes out tenth of a nm from the fitting of experimental data (ψ vs. λ and Δ vs. λ) and the values are tabulated in table 2.5. The thickness of the films are comparable to the values found from SEM data (in Fig. 2.11(b)) and AFM data (in Fig. 2.21(b)). All the films used in the experiment have thickness around 10 nm.

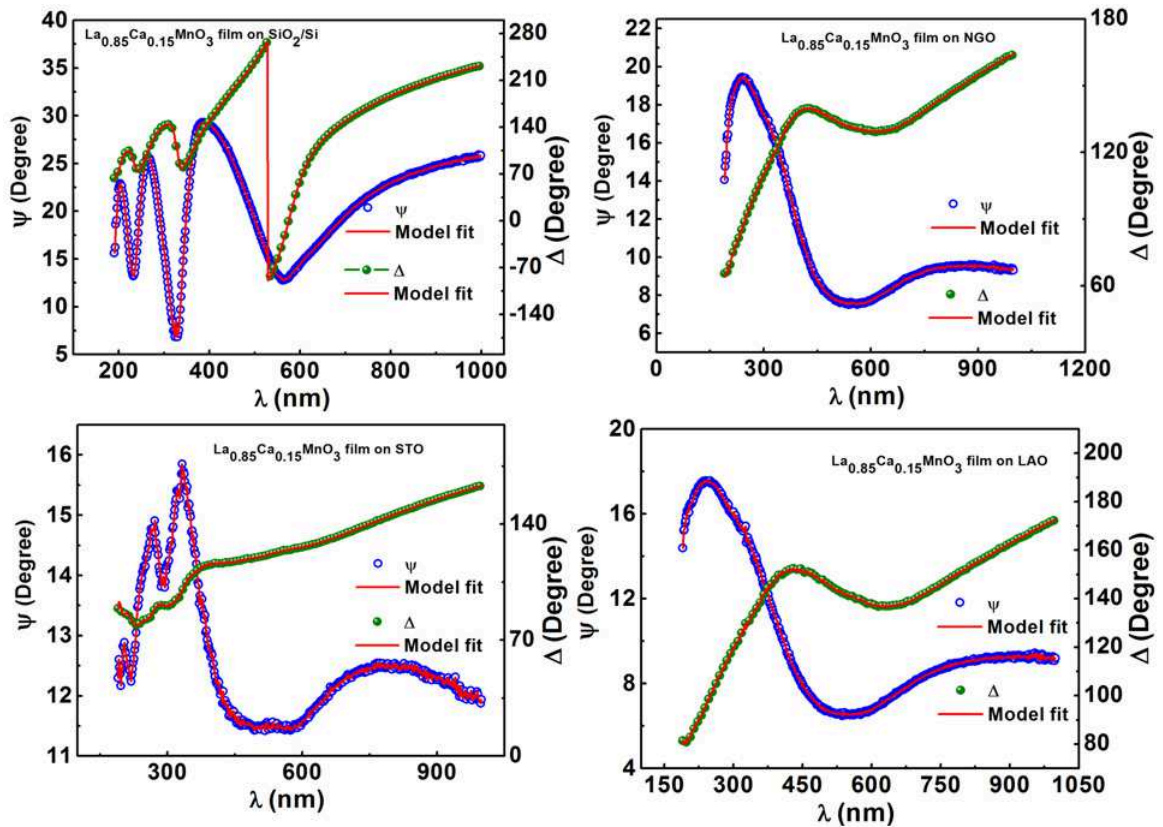


Figure 2.24 Ellipsometry data of $\text{La}_{0.85}\text{Ca}_{0.15}\text{MnO}_3$ thin film grown on SiO_2/Si , NGO , STO and LAO substrates by PLD with 1000 shots .

Table 2.5 Thickness (estimated from the different measurements) of the $\text{La}_{0.85}\text{Ca}_{0.15}\text{MnO}_3$ films grown on different substrates with 1000 laser shots.

Sample	Thickness (nm)
$\text{La}_{0.85}\text{Ca}_{0.15}\text{MnO}_3$ on SiO_2	11.32
$\text{La}_{0.85}\text{Ca}_{0.15}\text{MnO}_3$ on NGO	13.30
$\text{La}_{0.85}\text{Ca}_{0.15}\text{MnO}_3$ on LAO	12.32
$\text{La}_{0.85}\text{Ca}_{0.15}\text{MnO}_3$ on STO	12.90

2.6 Magnetisation measurements

In this section, we will briefly discuss the magnetisation measurement techniques used to investigate the presence of different magnetic phases in the three LaMnO_3 single crystals. Magnetisation (M) of a

material is defined as the magnetic moment per unit volume developed inside it due to the application of external applied field (H). M and H are related as $M = \chi H$, where χ is the magnetic susceptibility of the material. Magnetic susceptibility χ determines the behaviour of a material in an externally applied magnetic field. Depending on the magnitude and temperature (T) dependence of χ , we can distinguish material in three main classes as diamagnetic ($\chi \ll 0$ and independent of T), paramagnetic (χ is small but positive and $\propto \frac{1}{T}$), ferromagnetism ($\chi \gg 0$ and $= \frac{C}{T - \theta}$, C is the Curie constant and θ is Curie temperature) and antiferromagnetism ($\chi > 0$ and $= \frac{C}{T + \theta}$). By the magnetisation measurement, we can find out the magnetic nature of the sample. The measurement can be done in both d.c. and a.c. magnetic field. D.C. magnetisation measurement gives us the information about evaluation of the magnetic moments or magnetisation of a material depending on T and H or $M - T$ and $M - H$ curves of a material. D.C. magnetic measurements determine the equilibrium value of the magnetization in a sample. A.C. magnetisation deals with the evaluation of the magnetic spins with time or the magnetisation dynamics in the material. In the next subsections, we will discuss both these two techniques.

2.6.1 D.C. Magnetisation in Vibrating sample magnetometer

A Vibrating sample magnetometer (VSM) is used to measure magnetic behaviour of magnetic materials with the variation of temperature (T) and field (H). VSM operates on Faraday's Law of Induction, according to which a changing magnetic flux can produce an e.m.f or voltage. This voltage can be measured. The sample which is to be studied is kept in an applied magnetic field generated by an electromagnetic pole pieces. The applied magnetic field magnetizes the sample by aligning the magnetic domains, or the individual magnetic spins, along or opposite to the field direction. The stronger the applied magnetic field, the larger the magnetization would be. The magnetic dipole moment of the sample creates a magnetic field around it, known as the magnetic stray field. As the sample is moved vertically up and down (Z direction), this magnetic stray field changes as a function of time and can be sensed by a set of pick-up coils. The alternating magnetic field (changing magnetic flux ϕ) causes an induced voltage in the pick-up coils according to Faraday's Law of Induction i.e $V_{coil} = \frac{d\phi}{dT} = \frac{d\phi}{dZ} \frac{dZ}{dT}$

. This induced voltage is proportional to the magnetization of the sample. If the sample is vibrating sinusoidally then $V_{Coil}=2\pi fKMZ_0\sin(2\pi ft)$, where f is the frequency of oscillation, K is the coupling constant, M is the D.C. magnetic moment of the sample and Z_0 is the amplitude of oscillation. The greater the magnetization, the greater is the induced voltage. The induction voltage is amplified and detected by a lock-in amplifier. As a lock in amplifier can detect an induced voltage as low as few μV , VSM can detect a change in magnetisation as low as few $\mu e.m.u.$ For our measurement, we have used a commercial VSM and a Quantum Design Magnetic Property Measurement System (MPMS) XL-7 magnetometer. The maximum magnetic field generated for experiment was 1.6 T. The field produced had homogeneity of $\pm 0.1\%$ over a circular area of diameter 5cm. The low temperature measurement was performed using a variable temperature cryostat which allows measurements from 80 K to 400 K. The various components are interfaced and automated to a computer. We have done the $M - T$ and $M - H$ curve varying the temperature (80 – 300K) and applied field (10 Oe to 1.6T) in three $LaMnO_3$ single crystals (discuss in detail in chapter 4.)

2.6.2 A.C. susceptibility measurement

In a.c. magnetisation measurement, we apply an oscillating magnetic field to develop a time dependent magnetic moment in the sample. It actually measures the time relaxation of the magnetic spins in a material. The induced magnetization in a material due to an oscillating field $H_{ac}\cos(\omega t)$ superimposed on a d.c. applied field H_0 with frequency ω can be expressed as:

$$M(t) = \sum H_{ac}[\chi'_n \cos(n\omega t) + i\chi''_n \sin(n\omega t)] \quad (2.2)$$

,where χ'_n and χ''_n are the real and imaginary susceptibilities. These two susceptibilities can be directly measured from the $M(t)$ by the following relations:

$$\chi'_n = \frac{1}{\pi H} \int_0^{2\pi} M(t) \sin(n\omega t) d(\omega t) \quad (2.3)$$

$$\chi''_n = \frac{1}{\pi H} \int_0^{2\pi} M(t) \cos(n\omega t) d(\omega t) \quad (2.4)$$

, where $n = 1$ represents the linear susceptibility, and $n = 2, 3, 4$ denotes non-linear susceptibilities with higher order harmonics.

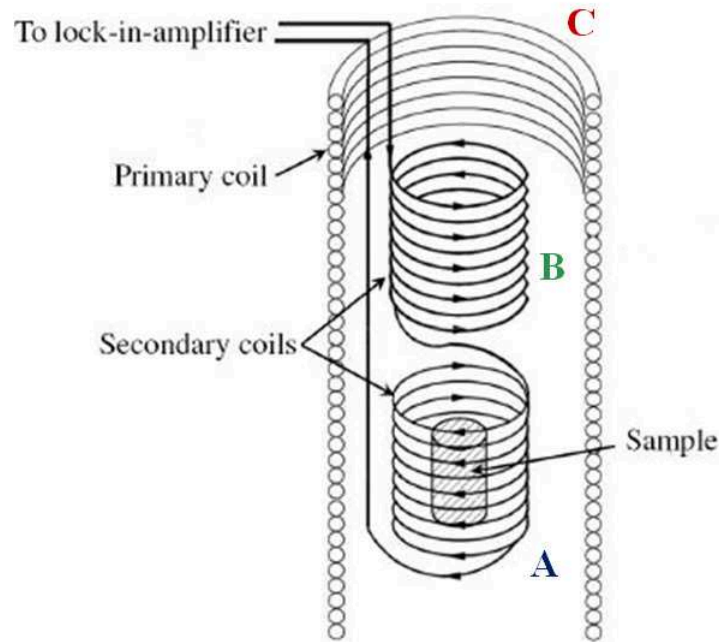


Figure 2.25 Schematic diagram of the set up coils in the a.c. susceptibility measurement. Image from Ref. [120].

We have done A.C. susceptibility measurement in three LaMnO_3 single crystal using a calibrated homemade a.c. susceptibility set up in our centre [120]. A.C. susceptibility was measured using two coil system. The two secondary coils or the detection coils ("A" and "B") are connected in differential mode and balanced in such a way that the signal is minimum when there is no sample. Susceptibility system is shown in Fig. 2.25. The sample is kept inside the one of the secondary coil "A". It gets excited and magnetised by an a.c magnetic field produced by the primary coil "C". Magnetic field is generated by sending current in the primary coil. The change in the magnetic flux in the coil A introduces a voltage drop (δV) between the leads of "A" and "B" which is detected by a lock in amplifier. A homemade cryostat system was used to vary the temperature [120].

2.7 Electrical and magneto transport measurement

We have performed electrical and magneto transport measurements in different single crystals and thin films of parent and hole doped manganites to investigate the effect of various external stimuli like

Table 2.6 Different electrical and magnetotransport measurements. R , ρ , I , V , T , I_{DS} , V_{DS} , I_G and V_G represents resistance, resistivity, current, voltage, temperature, source to drain current, source to drain voltage, gate current and gate voltage respectively.

Sample	Measurements	Phenomena studied	Chapter
LaMnO ₃ -1, LaMnO ₃ -2, and LaMnO ₃ -3	T dependent $I - V$, $\rho - T$, H dependent $\rho - T$, T dependent $R - H$	Resistive switching and Magnetoresistance	3,4
La _{0.9} Sr _{0.1} MnO ₃	T dependent $I - V$	Resistive switching	3
GdMnO ₃	$I - V$ at $T = 300K$	Resistive switching	3
La _{0.85} Ca _{0.15} MnO ₃ film on Si/SiO ₂	V_G dependent $I_{DS} - V_{DS}$, $I - V_G$ at fixed V_{DS} , $I_{DS} - t$ with pulsed V_G , $I_G - t$ with pulsed V_G , $R - T$ with different V_G	Electrostatic EDL gate effect	5
La _{0.85} Ca _{0.15} MnO ₃ film on NGO, LAO and STO	$\rho - T$, local tunneling conductance	Effect of strain and Phase separation	6

electric and magnetic field, electrostatic charge induction by a dielectric and lattice strain and inhomogeneity. In this section, we will discuss about different electrical and magnetotransport measurement techniques (which is tabulated in table 2.6) which are used for different studies. All the measurements were done in high vacuum to avoid any contamination to the sample due to atmospheric effect.

2.7.1 Electrical measurement in constant current and voltage method

We have measured the $\rho - T$ curve of the samples using a very low current of $1\mu A$ in a four probe configuration to avoid unnecessary Joule heating and contact resistance effect in the samples. $\rho -$

T measurement was also done using a different constant voltages (to study the resistive switching behaviour). In Fig. 2.26, we have shown the schematic diagram of the electrical measurement in four probe configuration using a constant current and constant voltage sources. We have used thermally

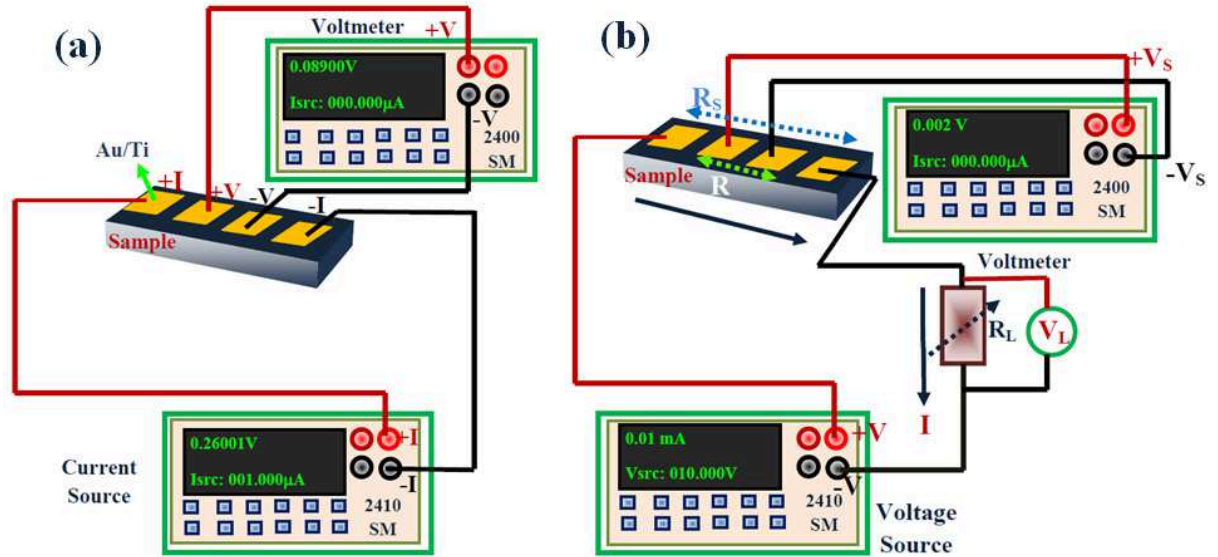


Figure 2.26 Schematic diagram of four probe measurement method for electrical measurement with (a) constant current source and voltmeter and (b) constant voltage source with current-meter and voltmeter

evaporated Au/Cr and Au /Ti pads (thickness of Au, Cr/Ti is $\approx 100\text{nm}$ and 10 nm respectively) for electrical contacts and highly conductive silver paint was used to connect Cu wires to the sample. We have used keithley 2400 surcemeter (SM) for applying constant current and voltage in the electrical circuit. SM can apply a constant current from $1\mu\text{A}$ to maximum 1A and voltage up to 1kV depending on its input power limit 1000W . SM measures a current in the circuit as low as 10nA to as high as 1A . SM is very useful instrument to measure resistive switching with high threshold voltage. Keithley 2400 SM and a Keithley 2000 Digital multimeter (DMM) were used to measure the voltage drop across the sample. The voltage resolution of the voltmeters is $1\mu\text{V}$ and they can measure safely up to 200V depending on the input power of 200W . In constant current method, we apply a constant current (I) in the circuit (shown in Fig. 2.26(a)) and measure the corresponding voltage drop across the sample (V_S) with the varying temperature. This gives us the temperature dependent resistance $R \left(\frac{V_S}{I} \right)$ of the sample.

In constant voltage method, we apply a constant voltage or bias (V) across the sample which is in a series combination with a variable resistor (R_L). We measure the corresponding voltage drops V_S and V_L across the sample and the load resistor respectively (shown in Fig. 2.26(b)). The total voltage drop across the sample is $V - V_L$. The total resistance (between the $+I$ & $-I$ contact pads) of the sample is $\frac{V - V_L}{I}$. This method is very useful when the resistance of the material dependent on applied bias i.e. $R = f(V, T)$ and the material shows high and low resistive states (HRS and LRS) after a switching voltage (V_{th}). The current in the circuit is $I = \frac{V}{R_S(V, T) + R_L}$ (in Fig. 2.26(b)). We have used this method

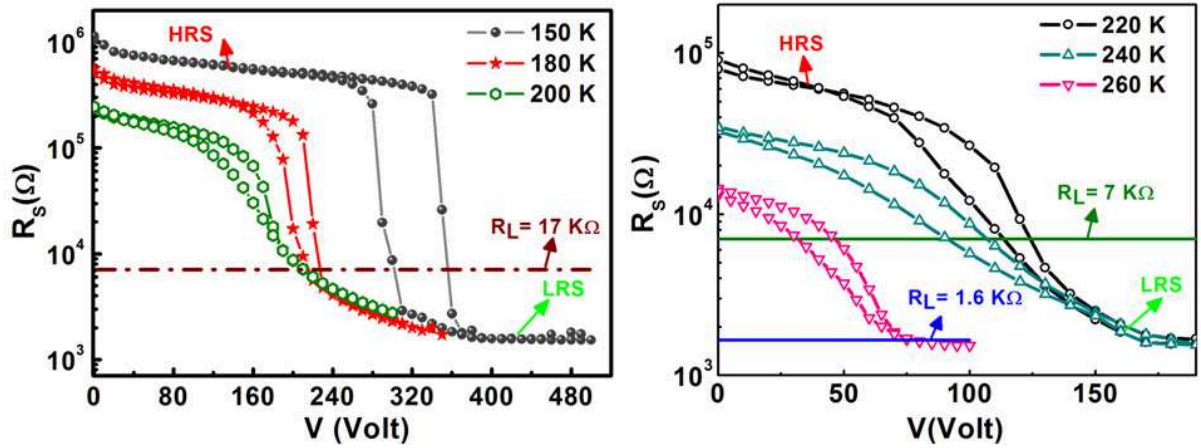


Figure 2.27 Sample Resistance (R) versus applied bias voltage (V) with corresponding values of variable resistor (R_L) in the circuit.

to observe the resistive switching in the three LaMnO_3 single crystals, $\text{La}_{0.9}\text{Sr}_{0.1}\text{MnO}_3$ single crystal (detail discussion in chapter 3).

In Fig. 2.27, we have shown the R_S vs. V curves of a LaMnO_3 single crystal at different temperatures and corresponding values of R_L for the circuit. The value of the series resistor R_L was selected to be much less than the total sample resistance R_S at low bias ($< V_{th}$) to ensure that it did not control the current through the circuit. When the sample goes to the low resistive state after the bias driven transition, the current in the circuit increases and it reaches the compliance limit (after which the instrument cannot measure) of our measuring instrument. However, with the presence of R_L the total resistance of the circuit remains large enough to avoid the compliance limit and we can see the switched state of the sample. From Fig. 2.26(a) and (b), we can see the current in the circuit (in Fig. 2.25(b)) at

low bias ($V < V_{th}$) is controlled by HRS ($\gg R_L$) of the sample but after the switching to LRS, the current in the circuit is control by R_L . In the absence of R_L the current would be ten times higher at low temperature which ($< 220K$) is not possible to measure due to the compliance limit of the instrument and the switched state can not be seen. Depending on the resistance of the different samples, we have varied R_L to see the switched state and limit the current in LRS.

2.7.2 Measurement-set up for transport and magneto transport

The electrical and magneto transport measurement was done in a commercial cryogen free (without liquid N_2 or He) 1.5K Variable temperature insert (VTI) system from Cryogenic limited. It uses a Gifford-McMahon cryo-cooling system in which temperature can be achieved as low as 1.5K. But depending on the purity of the He gas, the normal achievable temperature range is 4K–325K. The magnetic field is applied by a 10T superconducting magnet system attached with the VTI. The magnet is made in a solenoid form made of copper stabilised filamentary superconducting wire of NbTi (outer coil) and Nb_3Sn (inner coil). It can generate magnetic field as high as 10T. The magnetic field decays only very slowly (typically less than 1 part in 10^5 /hour). The direction of the magnetic field is along the axis of the solenoid. the inductance of the magnet coil is 30.8H and the resistance across the terminal at 300K is 4.2 Ω . The image of the set-up is shown in Fig. 2.28(a). The main components of the measurement set up are: (a) cryostat (vacuum insulated chamber whose primary function is to support and thermally shield the superconducting magnet and VTI), (b) superconducting solenoidal magnet (c) cryo-cooler system ,(d) variable temperature insert (VTI) and (e) sample mounting stick with electrical connections.

In Fig. 2.28(b), we have shown the image of the sample stick (made of stainless steel) on which we mount the sample on a sample platform. On the sample platform, there are 10 electrical connections for connecting samples. A calibrated cernoxTM sensor and a 100 Ω heater is kept just beneath the sample inside the sample platform. The wiring from the sample(s), heater and thermometer, is fitted inside the sample rod. The 6 pin Fischer connector provides electrical contact for the thermometer and heater while the 12 pin Fischer connector provides electrical contact to the samples. Heater and sensor

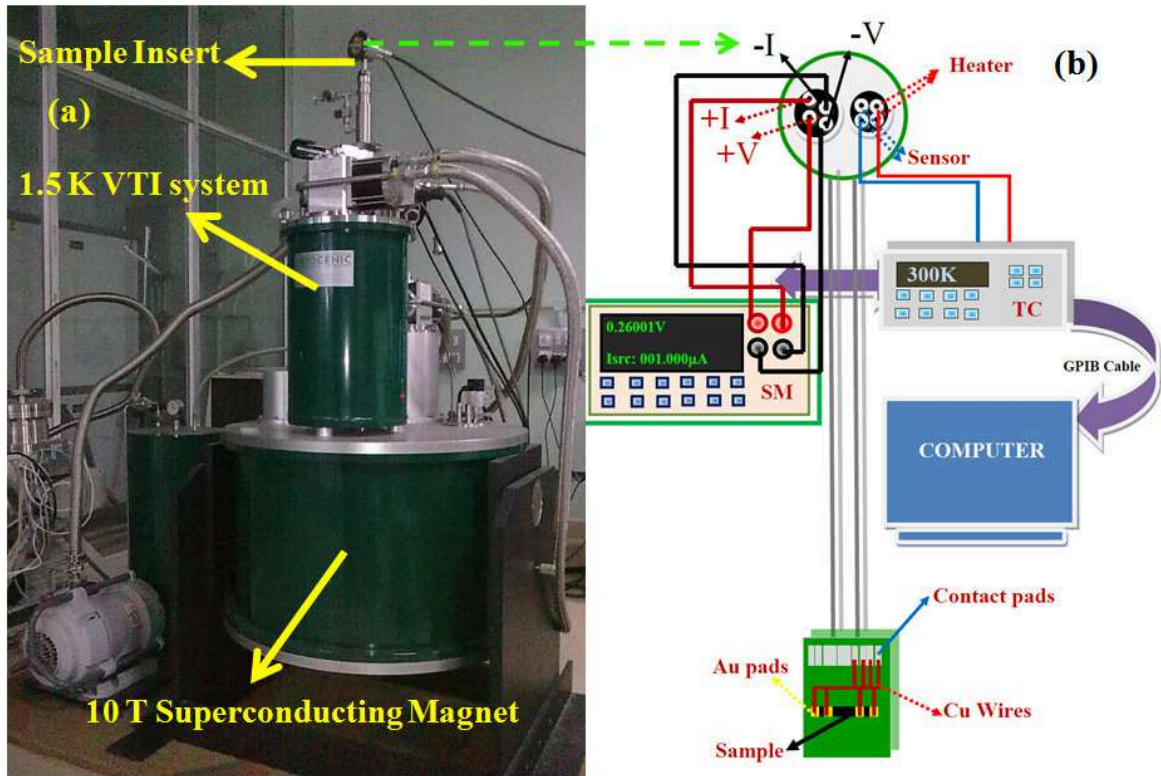


Figure 2.28 (a) Image of the measurement set up. (b) Schematic diagram of the sample stick connected with different measurement set-up. SM: Sourcemeter, TC: Temperature controller.

was connected to a Lakeshore 332 Temperature controller. The length of the stick is such that when it is inserted in the VTI, sample platform is in the centre of the uniform magnetic field. The sample is kept on a mica sheet and then mounted on the sample platform using a thermal grease. The control of the magnet and VTI system is fully automated and run by a Cryogenic labview programme. We have automated the measurement system. Temperature dependent resistivity with and without field was done using a C++ code written by us. For the ρ -T measurement, we have varied the temperature by 1 K/min.

Cooling in the system is done by a standard two-stage cryo-cooler. The main function of the first stage is to cool the radiation shield around the low temperature parts of the system. Cooling for the magnet (to around 4K) and the VTI (below 4K) is provided by the cooler second stage. The cryo-cooler cold head is fitted to the cryostat top plate. The compressor is connected to a dedicated high pressure hoses. The VTI provides the means to vary the sample temperature between 1.6–325K as standard. The VTI is supported in the bore of the magnet. Cooling of the VTI and sample is provided by the sec-

ond stage of the cryo-cooler using circulating helium gas. In Fig. 2.29, we have shown the schematic diagram of the VTI operation. The cooling in the VTI occurs in the following ways:

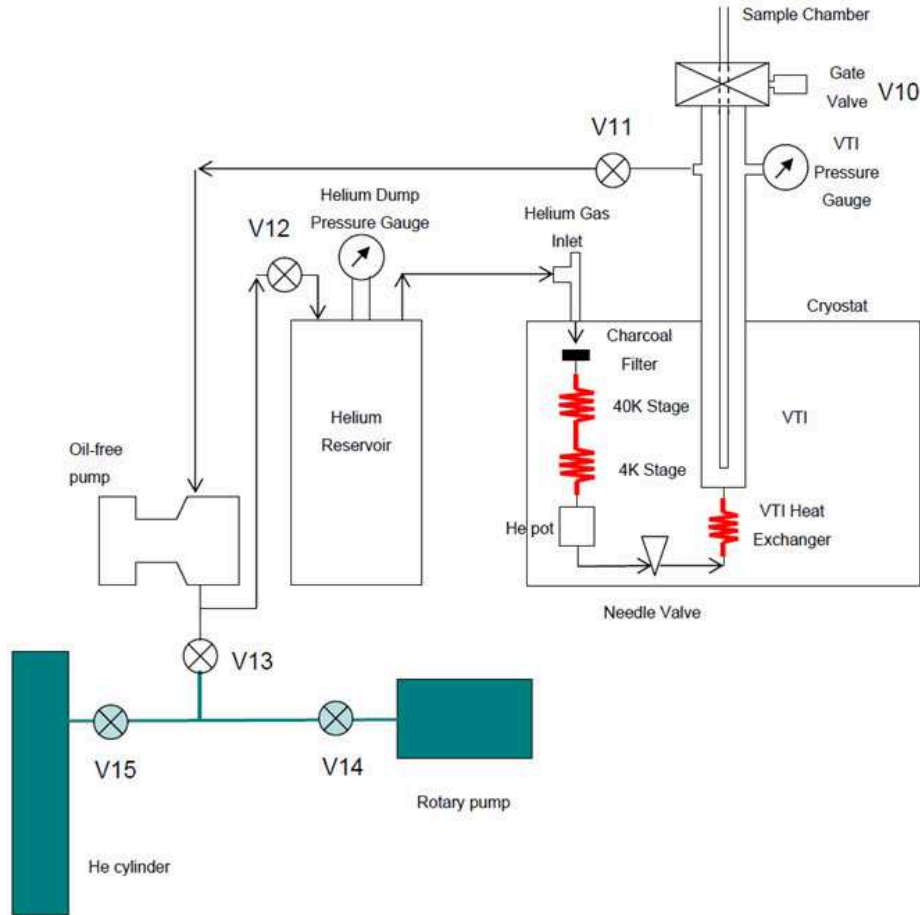


Figure 2.29 Schematic diagram of the VTI operation. Image from Ref. [121].

(a) High purity (99.999%) He gas is stored at room temperature in the reservoir vessel with pressure 0.25 bar,

↓

(b) He gas passes to the second stage of the cryo-cooler via He inlet where it is cooled below 4.2K and condenses in the He pot.

↓

(c) He liquid passes across a needle valve and then enters the main sample space.

↓

(d) This is then driven by a "dry" (oil-free) pump, back to the He gas dump. Needle valve can be controlled manually and it maintain the He gas flow rate. He pressure is monitored via a dial gauge,

↓

(e) The heat exchanger at the bottom of the VTI is fitted with a cernox thermometer and heater controlled from the temperature controller depending on the set point of the measurement,

↓

(f) The sample is inserted through an airlock inside a specially designed vacuum probe. The outside of the probe is in contact with the VTI gas stream and the sample is cooled via a copper link. An airlock is provided to change the sample without contaminating the sample chamber.

Keithley 2700 multimeter is used to scan the temperature of the different stages of the VTI and magnet cooling system. The magnet is fitted with a persistent mode switch that allows it to operate in persistent mode. Under these conditions the superconducting circuit is closed and the current can flow in a continuous loop, as long as the magnet remains superconducting. To set a magnetic field, a power supply ramps the lead current to match the field present in the magnet. Then the Heater is switched ON and the system waits until the temperature of the switch rises and the switch goes into the normal (nonsuperconducting) state. The current from the magnet power supply into the magnet is then increased at the rate specified until the target is reached (ramp rate is 0.1A/sec for 0 to 7T field while it is 0.06A/sec for above 7T filed). The operating current to generate 10T magnetic field is nearly 130A. After that the heater is switched OFF, the switch cools down and becomes superconducting. The lead current is then quickly ramped to zero. The magnet is in persistent mode at the new value of field. For the non persistent mode, the heater is normally ON and the switch is in the normal state. To set the field to a new value, the power supply simply ramps the current through the magnet. For our magneto–transport measurement, we have used magnetic field up to 10T and we have read the magnetic field by measuring the output voltage (by a Keithley 2000 DMM) of the magnetic power supply which is 2.001mV/A and 0.0363T magnetic field produce a 1mV output.

2.8 Local tunneling conductance measurement using UHV-STM

Vacuum tunneling was theoretically predicted by Folwer and Nordheim in 1928. However, the scanning tunneling microscope (STM) appeared in 1981. Gerd Binnig and Heinrich Raohrer of IBM Zaurich constructed a tool for studying/probing the local density of states and to get topographic images down to atomic scale [122]. It's working based on the principle of tunneling through a barrier in high vacuum. In quantum mechanics the electrons exhibit wave like properties and which allow them to penetrate the potential barrier. According to classical physics for an electron of energy $E < V$ (Barrier potential) the electron will not be able to pass through the barrier and it will reflect while quantum mechanically, there is a finite probability that the electron will pass through the barrier. Thus in classical physics the electron flow is not possible without a direct connection by a wire between two surfaces. However quantum mechanically there is a finite probability of tunneling.

In general STM involves a sharp conductive tip made of metals like Pt/Ir which is brought within tunneling distance (sub-nanometre) between the tip and the sample surface, thereby creating a metal-insulator-metal/semiconductor/oxide configuration. In the representation of one-dimensional tunneling (Fig. 2.30), the tunneling wave function of the sample electrons ψ_s and the wave function of a STM tip electrons ψ_t overlap in the insulating gap, allowing a current to flow [123]. From Fig. 2.30, we can

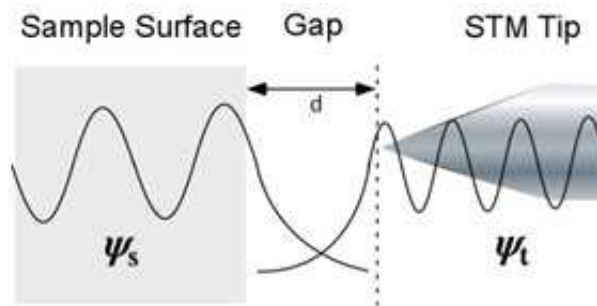


Figure 2.30 Schematic diagram of overlap of electronic wave functions of sample and tip. Image from Ref. [123].

see that the region where wave functions are overlapping allows the current to flow.

In metals, electrons fill the continuous energy levels up to the Fermi level (E_F) which defines an upper boundary to accessible electronic states for conduction. Above E_F we find electrons that are

activated (like thermally). We can raise the Fermi level (e.g., of the sample) in regards to a second material (e.g., tip) by applying a voltage. Even in absence of a bias tunneling occurs. But net current is zero as tunneling from the tip \rightarrow sample and sample \rightarrow tip has same probability. This symmetry is broken by the bias and this give the net current. To observe the tunneling current I_t of electrons through the vacuum gap between the sample and the tip, a bias voltage (V_{bias}) is applied as shown in Fig. 2.31. At $V_{bias} = 0$, the electrons cannot flow in either direction since E_F lies in same level for both the tip and the sample. When $V_{bias} > 0$ (positive bias w.r.t the tip), the E_F of the sample is raised by V_{bias} and the electrons in the occupied state (filled with electrons) of the sample can tunnel into the unoccupied state of the tip. Similarly, when $V_{bias} < 0$ (negative bias), the electrons in the occupied state of the tip and tunnel into the unoccupied state of the sample [122–124]. These conditions are shown in Fig. 2.31. The tunneling current between the sample and the tip (I_t) is directly proportional to the tip sample

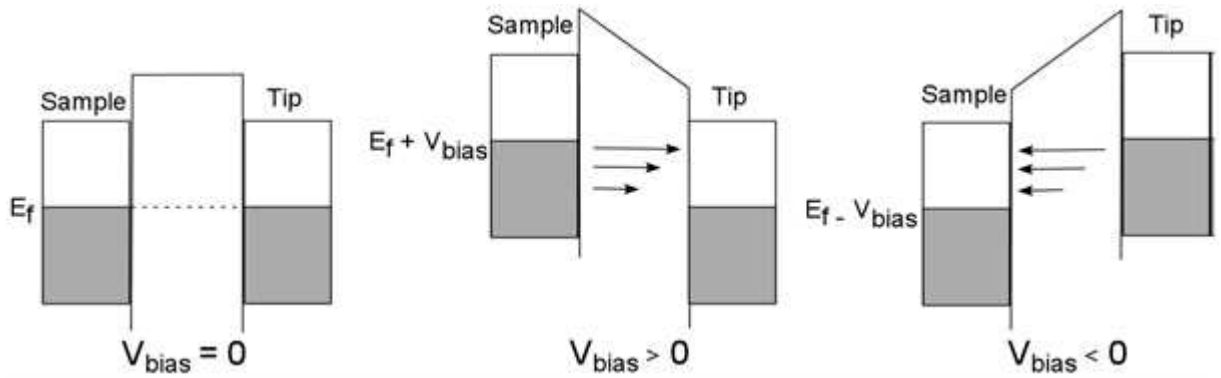


Figure 2.31 Schematic diagram of the tunneling phenomenon in different biasing conditions. Image form Ref. [123].

distance(z), local density of states (N_s) of the sample and applied voltage(V) and can be expressed as

$$I(z, V, W, T) = c \int_{-\infty}^{\infty} N_s \left(E + \frac{eV}{2} \right) N_t \left(E - \frac{eV}{2} \right) \Gamma(z, E, W) \left[f \left(E - \frac{eV}{2} \right) - f \left(E + \frac{eV}{2} \right) \right] dE, \quad (2.5)$$

where E is the energy of the tunneling electron, c is a constant dependent on the tip-sample effective junction area, z is the tip-sample separation, W is the average work function of the tip and sample surface, V is the applied bias between tip and sample, T is the temperature, $N_t(E)$ is the tip DOS, $f(E)$ is the Fermi function at T and τ is the barrier penetration factor [125]. From equation 6.1, it can be

seen that the tunneling current is directly correlated to the local density of states of the localized region.

The STM work described in the thesis (chapter 6) was done using RHK UHV 350 SPM system (shown in Fig. 2.32). The system has two chambers one is main or sample chamber (where imaging and tunneling conductances measurement is done) and the other is sample transfer chamber or load-lock chamber. The main chamber was kept in ultra high vacuum (UHV) level of 10^{-10} mbar by an ion pump and the vacuum in the load lock chamber was maintained at 10^{-8} mbar. The sample is transferred from load lock to the main chamber by a magnetic handle at same pressure (10^{-8} mbar). We have used a Pt-Ir tip and placed a Ni-Al conducting wire on the sample for tunneling measurement. The

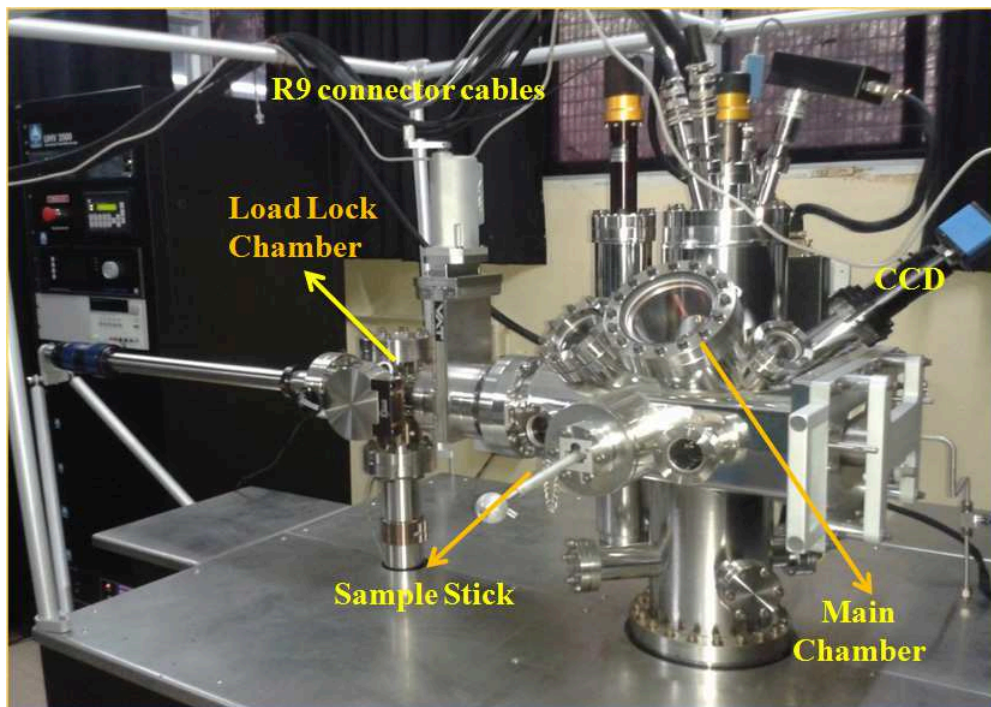


Figure 2.32 Image of the RHK-UHV 350 STM system in our lab.

system consists of different parts like R9 controller, Sample holder, Scan head, Preamplifier, Bias drive amplifier, Lock in amplifier and CCD camera etc. The R9 Controller generates a differential bias signal that is received by the IVP-R9 pre-amplifier and is turned into a single-ended bias signal (0–10V) to be fed into the STM between the tip and sample. The STM preamp signal is fed into the IVP-200 (10^8 Gain, 10nA/V) and is turned into a differential signal that is then sent to the differential input of

the R9. Using differential transmission on the signals between the scan head and the R9 Controller help maintain signal purity and eliminate noise (using a butterworth filter with 2kHz cut off and 48dB roll-off) picked up from the environment. The noise level in the instrument was always maintained below $10\text{-}30 \text{ pA}/\sqrt{\text{Hz}}$. The circuit diagram for measuring the tunnel current is shown in Fig.2.33. The actual image of the surface is obtained by scanning the sample surface in constant current and

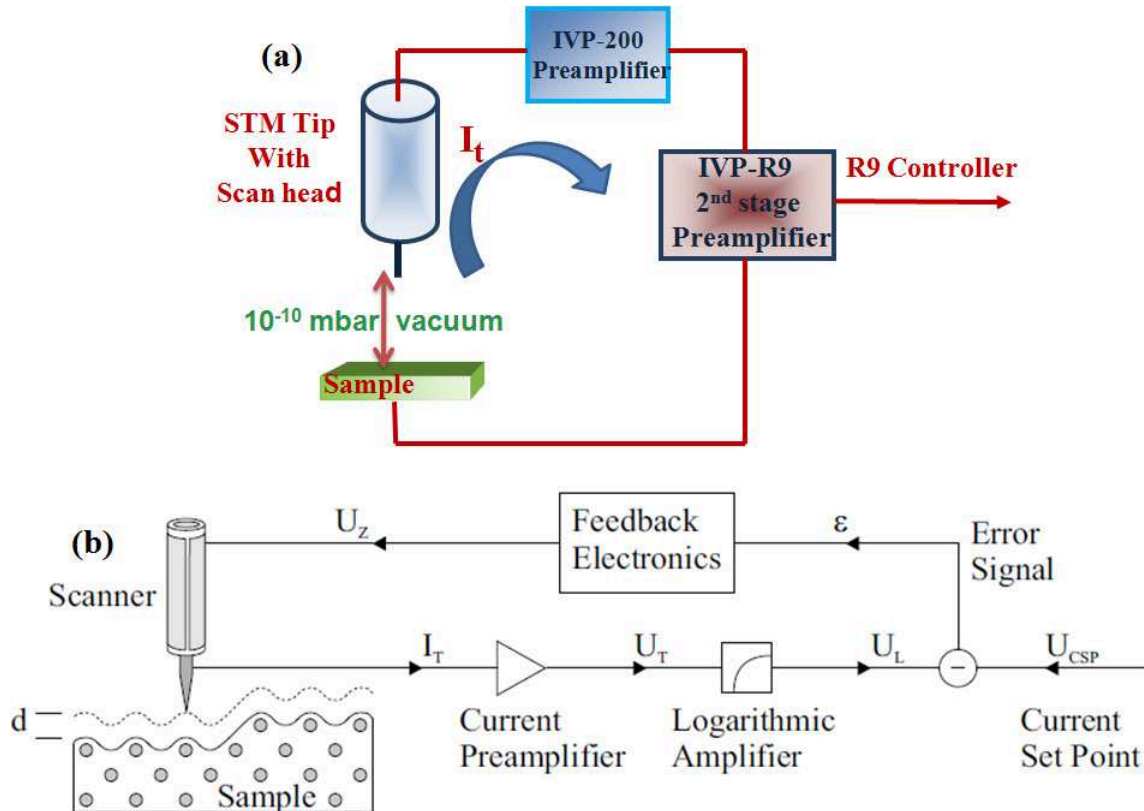


Figure 2.33 (a) Schematic diagram of to detect the tunnel current. (b) Schematic diagram of the electronic circuit for imaging in constant current mode [124].

constant height modes. In constant current mode, a feedback loop keeps the tunneling current constant and the change in the vertical (z) position due to the sample topography is monitored. This mode is more sensitive to the topography of the structure and is, therefore, the preferred mode for imaging. In constant height mode, the tip is kept at a constant height (z feedback is then disabled) over the sample and the change in the tunneling current monitored and it is useful for spectroscopic ($\frac{dI}{dV}$) measurement. For imaging, we have used 400pA to 1nA current depending on the sample surface and bias voltage is

kept from 0.5V to 1V.

It is possible to obtain spectroscopic ($I - V$ curve) information about a sample surface by using modulation techniques in which a constant current topography and the spatially resolved tunneling conductance (dI/dV) can be acquired simultaneously. This method is called local conductance mapping. The local conductance map (LCMAP) is basically a two-dimensional map of the differential tunneling conductance across the surface for a fixed bias and at a fixed average tunnel current. The a.c. modulation bias is chosen to be much smaller than the d.c. bias applied to the sample. The tunnel current has a d.c. as well as an a.c. component. At the a.c. excitation frequency, the AC component of $I(t) = I_{DC} + \left(\frac{dI}{dV}\right) \delta V \cos(\omega t) + \dots$. The AC component of I_t is measured by a lock-in amplifier which gives the in-phase component giving the $\frac{dI}{dV}$ directly [126]. For spectroscopic measurement, we have varied the voltage between $\pm 1V$ and resolution was 1mV. We have applied modulation of amplitude 10mV with 1kHz frequency. There was a stabilisation delay (i.e. a wait time after re-engaging the feedback loop between each spectrum to be sure that the probe Z position is back to where it started before repeating the spectroscopic measurement) of $100\mu s$ to few ms between each spectra and sampling time was kept at few ms.

Another important part is to mount the sample in a sample holder and to approach the probe to the sample properly. The scan head consists of three piezoelectric legs which works on transverse piezoelectric effect (Z piezo sensitivity 1.5 nm/V and Z can vary up to $\pm 225nm$). In Fig. 2.34, we have shown the image of the scan-head with the tip and the sample holder. In order to produce rotation, a sawtooth voltage is applied to each leg. Once approach is completed, the raster scan waveform are applied to piezo-legs to create back and forth motion of the entire scan head which helps in moving the probe (mounted in the centre of scan head). The tip approaches to a distance from the sample surface where it gets the set current. The sample holder is sloped around the outer section of the holder which is necessary to bring the tip and sample close enough for an interaction to take place. To study the temperature dependence of local conductance, the temperature of the sample, and the heating /cooling stage was controlled by the liquid nitrogen and radiative heating. There are three thermocouples in a sample holder which allows us to measure sample temperature, to monitor temperature of the heating/cooling

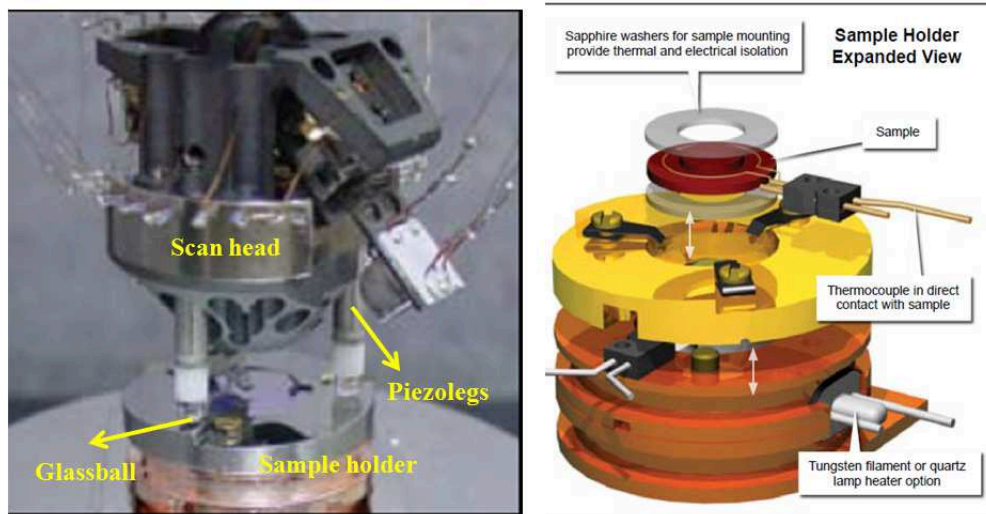


Figure 2.34 Image of the Scan–head of an UHV-STM system with the schematic view of the sample holder [127].

stage and to monitor cryostat temperature respectively.

STM measurements are very sensitive to the vibrations which may arise from buildings, and pumps. Generally, the distance between the sample and tip is very small (\sim few nm). Therefore, a mechanical stability of the order of nm is very important. For this reason, vibration and external noise isolation of the system is necessary for stable functioning of the system. The UHV-STM system was placed on four air/N₂ filled legs to avoid mechanical vibrations.

Chapter 3

Effect of electric field on the insulating state of undoped LaMnO_3 and GdMnO_3

Investigation of nonlinear transport and field driven switching due to externally applied electric field in the adiabatic polaronic insulating state of three nominally pure single crystals of LaMnO_3 and thin film of GdMnO_3 , have been performed. Both LaMnO_3 and GdMnO_3 has highly insulating ground state. We observed reversible destabilization of the highly resistive insulating state to a lower resistance state at low temperature (for LaMnO_3) and at room temperature (for GdMnO_3). The low resistance state is a bad metallic state. The resistive state transition occurs at a particular threshold field (E_{Th}) and it has a memory or hysteresis. This resistive switching is explained by bias driven percolation type transition between two coexisting phases, where the majority phase is a COI polaronic insulating phase and the minority phase is a bad metallic phase. The important physics studied here is that bad metallic minority phase can co-exist with PI state due to charge transfer instability driven charge disproportionation which creates electron hole (E-H) pair ($\text{Mn}^{3+} + \text{Mn}^{3+} \rightarrow \text{Mn}^{2+} + \text{Mn}^{4+}$). These E-H pair is depinned by applied field and shows an activated kinetics. This transition is distinct from the field induced resistance state change (both with memory and without memory) that have been seen in manganites with much higher level of hole doping (typically $x \geq 0.2$).

3.1 Introduction

The localization of electronic states due to strong electron-phonon coupling in strongly co-related oxides like RMnO_3 (R = rare-earths like La, Pr, Nd etc.) and the effect of external stimulations on these states has been an important research interest over the last two decades [1, 2]. In materials like RMnO_3 , the strong coupling between the electrons and phonons mediated by the JT distortion leads to the formation of polarons. Below a certain temperature (T_{JT}) cooperative JT distortions set in and one obtains a polaronic insulating state accompanied by an orthorhombic distortion of the lattice. Depending on the R ion the value of T_{JT} can vary between 750K for $R = \text{La}$ to 1150K for $R = \text{Nd}$. At a much lower temperature AFM order sets in at the Neel temperature $T_N \approx 150\text{K}$ leading to an A-type AFM insulating state. The physical properties, including crystallographic structure and its temperature evolution through T_{JT} of RMnO_3 systems (like LaMnO_3) have been studied in detail using various techniques. Although many important issues still remain unsolved [5–8]. The orthorhombic polaronic insulating state with cooperative JT distortion can be destabilized by hole doping using divalent substitution at the rare-earth site. This leads to insulator-metal transition with long range FM order. In addition to the hole doping, the polaronic insulating state can be destabilized by external stimulants like pressure [9], very high magnetic field [10] and by high electric field close to T_{JT} [11].

In this investigation we find that an applied electric field of moderate magnitude can induce instability at room temperature or below in the resistive state of nominally pure single crystal of LaMnO_3 and thin film of GdMnO_3 . This leads to a reversible destabilization of the highly resistive insulating state to a lower resistance bad metallic state. (Note: The lower resistance state is called a bad metallic because it has a temperature independent resistivity value which though lower than the insulating state, is higher than those seen in metallic states of manganites obtained after substantial hole doping). The observed field induced destabilization can be sharp at lower temperature and it can lead to resistance changes of even few orders of magnitude occurring sharply over a small field range. The destabilization of the insulating state which we have observed in case of nominally pure LaMnO_3 single crystals and GdMnO_3 thin film is distinct from the field induced resistance state change (both with memory and

without memory) that have been seen in manganites with much higher level of hole doping (typically $x \geq 0.2$) [91–94]. In manganites with higher level of hole doping (that show FMI or CO state), the resistive switching has been seen in single crystals [128, 129], in films [130] and also in nanoscopic regions that can be created by local probes [131, 132]. Creation of FM filaments by high electric field in charge ordered manganites have been reported [94]. Resistive state switching in Schottky junctions involving manganites have also been seen [40]. The above list of observation of resistive state switching is not exhaustive and is suggestive of a number of explanations for the resistive state transitions in hole-doped manganites. These explanations are ionic migration near room temperature particularly in junctions [47], electron heating [133], Joule heating [134, 135] and electric field induced structural changes [132, 136]. However, the observed phenomena in nominally pure LaMnO_3 single crystals and GdMnO_3 thin film, reported here, are different from those reported in hole-doped systems. In this case, the starting insulating state is a polaronic insulating state with JT distorted MnO_6 arranged in a cooperative long range ordered state. The observed characteristics in this case have different field and temperature dependences including a sharp field driven transition. The field driven transition appears to change critically for hole doping around $x \approx 0.1$. In earlier reports involving hole-doping with concentration $x \geq 0.15$, the starting insulating state was either a charge ordered state (occurring for hole doping ≈ 0.5) or a FMI state (occurring for hole doping ≈ 0.15 - 0.22).

In this chapter we have studied the effect of external stimuli like electric field on the polaronic insulating high resistive state of parent manganites. The experiments have been carried out on three nominally pure single crystals of LaMnO_3 having different dimensions (LaMnO_3 -1, LaMnO_3 -2 and LaMnO_3 -3), $\text{La}_{0.9}\text{Sr}_{0.1}\text{MnO}_3$ and on GdMnO_3 thin film to establish the generality of the phenomena and the extent of its sample dependence (detail about the samples was discussed in Chapter 2). In the next section (3.2) we will discuss the normal resistivities of these samples.

3.2 Polaronic insulating state in LaMnO_3 , $\text{La}_{0.9}\text{Sr}_{0.1}\text{MnO}_3$ and GdMnO_3

In strongly co-related parent perovskites, electronic states are localized due to strong electron-phonon coupling mediated by JT distortion. This distortion leads to the formation of polarons. Strong JT distortion along with onsite Coulomb repulsion (U) as well as charge transfer energy plays a crucial role to make the system, like LaMnO_3 , insulating. High pressure studies on LaMnO_3 have shown that even if the JT distortion is removed, the insulating phase still does not collapse. Below a certain temperature (T_{JT}), cooperative JT distortions set in and one obtains a polaronic insulating state accompanied by a orthorhombic distortion of the lattice [5–8]. The electronic transport in this state depends on temperature as:

$$\rho = \rho_0 T^n \exp\left(\frac{E_a}{k_B T}\right) \quad (3.1)$$

, where ρ_0 is related to the hopping frequency, length, and dimensionality and E_a is the activation energy. E_a can be expressed as $E_a = \epsilon_0 + W + \lambda^{3-2n}$ where ϵ_0 is the energy required to produce intrinsic carriers, $2W$ is the polaron formation energy and λ is the transfer integral. There are two limits of this polaronic transport; one is adiabatic limit and other is non adiabatic limit. In adiabatic limit, $\kappa_B T$ (characteristic polaron energy scale which gives the polaron tunnelling rate) is greater than polaron formation energy $\hbar W_{ph}$ (where, W_{ph} is the characteristic phonon frequency involved in the polaron formation) and exponent $n = 1$ in equation 3.1. For nonadiabatic limit exponent $n = 3/2$ and electron tunnelling event is not necessarily faster than relevant optical mode lattice vibration.

We have measured the resistivities of LaMnO_3 -1, LaMnO_3 -2, LaMnO_3 -3 and $\text{La}_{0.9}\text{Sr}_{0.1}\text{MnO}_3$ single crystals with a low bias current of $1\mu\text{A}$ in a standard four-probe method (measurement procedure is given in Chapter 2). In Fig. 3.1(a), $\rho - T$ data of three LaMnO_3 single crystals are shown. All the three LaMnO_3 single crystals qualitatively shows similar kind of resistivity (10^2 - $10^6 \Omega\text{cm}$) but the quantitative difference arises due to the slight variation of Mn^{4+} in these samples (sample details and characterisations are discussed in chapter 2 & 4). The divalent atom (Ca, Sr) doping at rare earth site in RMnO_3 creates mix valence Mn (presence with Mn^{4+}) and dilutes the local JT distortion. Presence of Mn^{4+} destabilize the polaronic insulating state and reduce the ρ of the system. In Fig. 3.1(b),

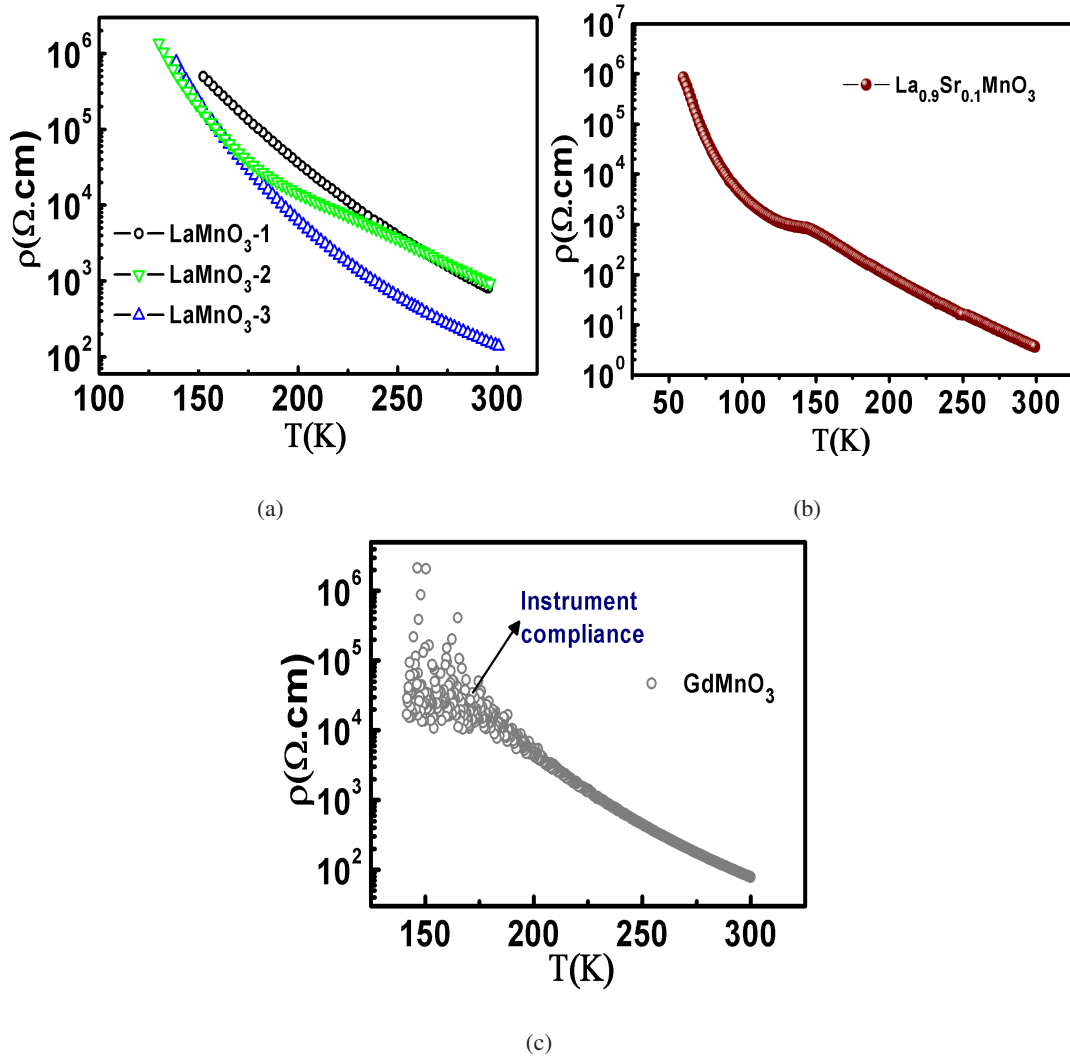


Figure 3.1 Temperature dependent resistivities (ρ) of (a) LaMnO_3 -1, LaMnO_3 -2 and LaMnO_3 -3 single crystals, (b) $\text{La}_{0.9}\text{Sr}_{0.1}\text{MnO}_3$ single crystal and (c) GdMnO_3 thin film.

$\rho - T$ data of $\text{La}_{0.9}\text{Sr}_{0.1}\text{MnO}_3$ is shown which has lower resistivity than the three LaMnO_3 single crystals. This is due to the presence of finite amount of Mn^{4+} for Sr substitution. With the substitution of divalent atom like Ca or Sr in parent LaMnO_3 , a hole is created in the e_g levels of the 3d-orbital of Mn. It leads to the de-localization of carriers and increases the conductivity. The introduction of Mn^{4+} dilutes the cooperative JT distortion and enhances the strength of the FM Double Exchange (DE) interaction. For the Sr doped system, $x = 0.1$ region is the critical region [137]. In this region of hole concentration, slight variation of Mn^{4+} can change the system from highly insulating CAF regime to

ferromagnetic FMI state at low temperatures [1, 2, 137]. As a result, in $\text{La}_{0.9}\text{Sr}_{0.1}\text{MnO}_3$, there are three distinct regions; PI (145-300K), FMI (starts below 120K), and in between there is a small metallic region (120K-145K) where $\frac{d\rho}{dT}$ is positive. This would also imply co-existence of complex phases in this region of hole concentration. This complexity makes the $x = 0.1$ region very sensitive to exact Mn^{4+} concentration. Increasing the Sr concentration to $x > 0.15$ stabilizes the FMM state [138, 139].

Resistivity of the GdMnO_3 thin film is shown in Fig. 3.1(c). $\rho - T$ curve of the GdMnO_3 film is measured with a constant low bias voltage of 1V as the film is very highly resistive at room temperature. For a fixed bias measurement the joule heating is given as $\frac{V^2}{R}$. As a result, when it is cooled, resistance (R) increases which reduces the Joule heating. For constant current measurement, the heating being I^2R , on cooling the joule heating increases. The resistance increases on cooling and reaches a compliance limited range below 180K (The noise in the data is due to the compliance limit).

To find out the nature of the insulating state, we fitted the $\rho - T$ curve of the three LaMnO_3 single crystals and GdMnO_3 thin film with the equation (3.1) considering $n = 1$ for adiabatic polaronic transport. From equation (3.1) with $n = 1$, we can found that the plot of $\ln(\rho T^{-1})$ vs. T^{-1} is a linear curve and the slope of the curve is the activation energy (E_a) for the transport. We have plotted the $\rho - T$ curve as $\ln(\rho T^{-1})$ vs. T^{-1} for all the LaMnO_3 single crystals, $\text{La}_{0.9}\text{Sr}_{0.1}\text{MnO}_3$ single crystal and GdMnO_3 thin film (shown in Fig. 3.2). From the linear fit in Fig. 3.2(a), we found that all three samples of the nominally pure LaMnO_3 have almost the same activation energy, $E_a \sim 217-235\text{meV}$ and this matches well with the previously reported data [140]. The sample LaMnO_3 -2 shows deviation in the $\rho - T$ curve around 180K from the fit following single E_a . This is likely due to the magnetic inhomogeneity caused by local FM moment/cluster formation which is discussed in chapter 4. From Fig. 3.2(b), we found that E_a for $\text{La}_{0.9}\text{Sr}_{0.1}\text{MnO}_3$ is nearly equal to 180meV which is due to the Sr substitution discussed earlier in this section. GdMnO_3 thin film has $E_a \sim 230\text{meV}$ which is comparable to LaMnO_3 single crystals and other parent manganites.

In this section, we discussed about the nature of the insulating state of the parent manganites (LaMnO_3 single crystals and GdMnO_3 thin film) and the effect of divalent atom doping (Sr) on the polaronic insulating state of these oxides. We observed that parent LaMnO_3 single crystals and GdMnO_3

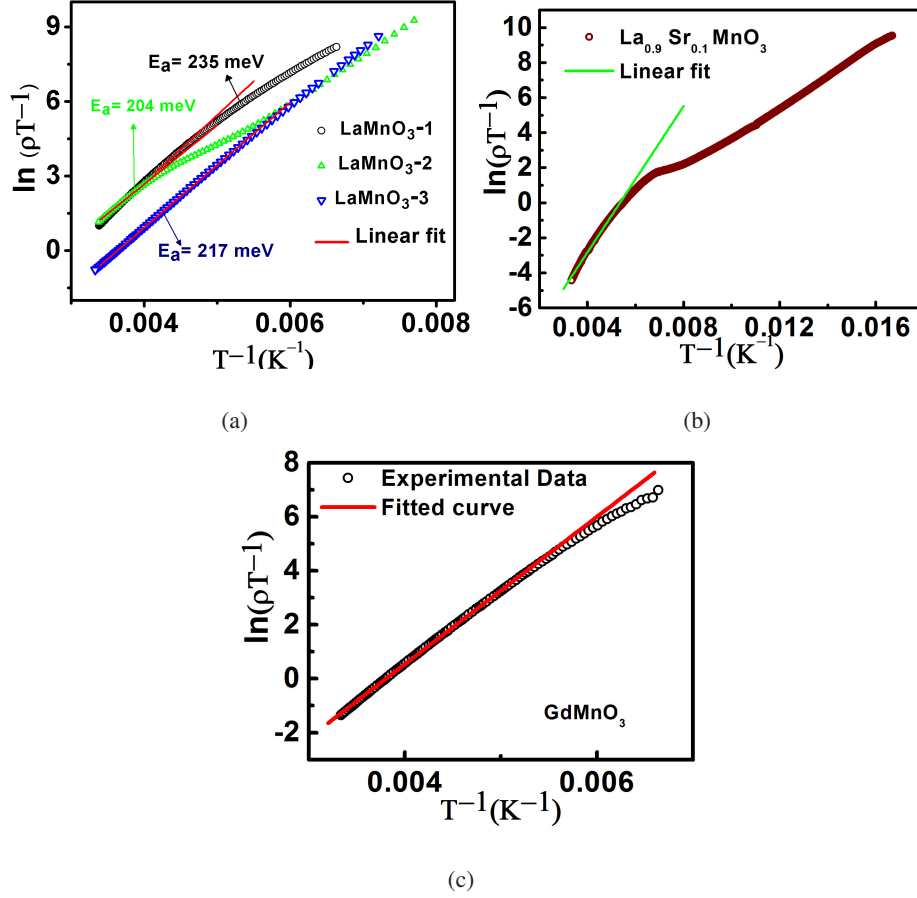


Figure 3.2 Adiabatic polaronic fit of $\rho - T$ for (a) LaMnO_3 -1, LaMnO_3 -2 and LaMnO_3 -3 single crystals, (b) $\text{La}_{0.9}\text{Sr}_{0.1}\text{MnO}_3$ single crystal and (c) GdMnO_3 thin film.

thin film have nearly same E_a while $\text{La}_{0.9}\text{Sr}_{0.1}\text{MnO}_3$ single crystal has lower E_a due to the Sr doping.

3.3 Effect of electric field on the polaronic insulating state of LaMnO_3 single crystals and GdMnO_3 thin film

In this section, we will discuss the effect of electric field on the polaronic insulating state of three nominally pure LaMnO_3 single crystals, $\text{La}_{0.9}\text{Sr}_{0.1}\text{MnO}_3$ single crystal and GdMnO_3 thin film. The experiments were carried out on different single crystals of LaMnO_3 , lightly doped $\text{La}_{0.9}\text{Sr}_{0.1}\text{MnO}_3$ and GdMnO_3 thin film having different dimensions and morphology to establish the generality of the phenomenon and the extent of its sample dependence. Effect of the electric field on the insulating state

was measured by varying the bias (V) across the sample and measuring the corresponding current (I) through it in a four probe configuration (four thermally evaporated Au/Cr and Au/Ti pads were used for metal contacts). To avoid the Joule heating we have used a pulsed voltage with 50% duty cycle for LaMnO_3 and continuous low bias for GdMnO_3 thin film. $I - V$ measurement was done in the three LaMnO_3 single crystals varying the temperature from room temperature to 150K (data are taken up to 150K as below this temperature sample resistance reaches the compliance limit of the instrument) and $I - V$ was measured at room temperature for GdMnO_3 thin film. The electrical circuit configurations for four probe $I - V$ measurement for three LaMnO_3 single crystals, $\text{La}_{0.9}\text{Sr}_{0.1}\text{MnO}_3$ single crystal and GdMnO_3 thin film is shown in Fig. 3.3. LaMnO_3 single crystals and $\text{La}_{0.9}\text{Sr}_{0.1}\text{MnO}_3$ single crystal

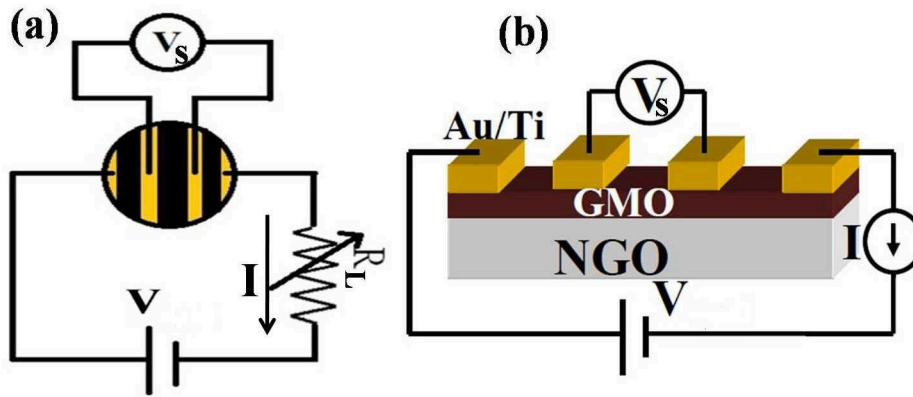


Figure 3.3 Circuit configuration to measure bias voltage (V) versus sample current (I) for (a) LaMnO_3 single crystals and $\text{La}_{0.9}\text{Sr}_{0.1}\text{MnO}_3$ single crystal. R_L is the variable resistor to limit the current through the sample and (b) GdMnO_3 thin film. Due to the high resistance of the film R_L was not used in the circuit.

have low resistance of $\sim 300\Omega$. We used a current limiter resistor R_L series with the sample to make sure that high current (in the compliance limit of the instrument) should not pass through the sample in the switched state (low resistive state). We adjusted R_L (from $\text{K}\Omega$ to $\text{M}\Omega$) with lowering of temperature, depending on the sample resistance and applied magnitude of the bias (V) (discussed in detail in chapter 2). The sample voltage (V_S) was measured across the two middle probe of the sample to get the actual threshold field (which exclude the contact resistance) for switching for LaMnO_3 single crystals and $\text{La}_{0.9}\text{Sr}_{0.1}\text{MnO}_3$ single crystal (it will be discussed in the later section). But R_L was not used in the circuit configuration in 3.3(b) as GdMnO_3 thin film has a very high resistance of few $\text{M}\Omega$ and the

applied bias (V) was low ($< 10\text{V}$). Detail discussion on the circuit configuration is in chapter 2.

3.3.1 Temperature dependent $I - V$ data and bias induced destabilization of the polaronic state in LaMnO_3

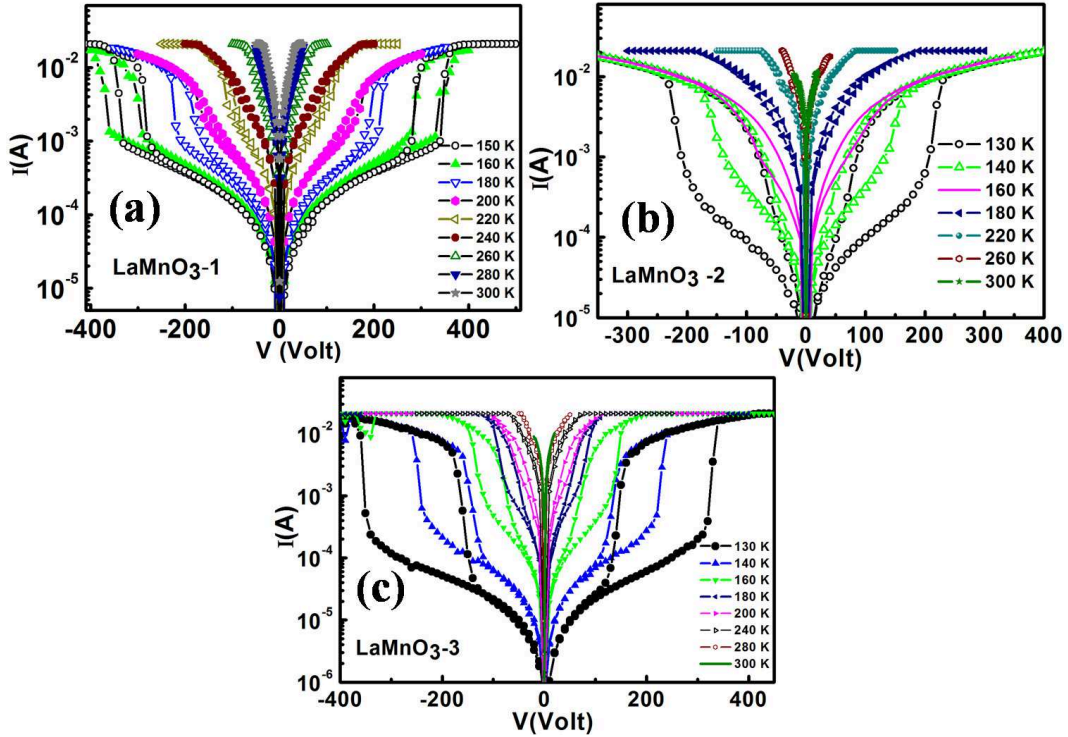


Figure 3.4 Temperature dependent $I - V$ data for (a) LaMnO_3 -1, (b) LaMnO_3 -2 and (c) LaMnO_3 -3 single crystals.

In this subsection, we will discuss the temperature dependent $I - V$ characteristics of three nominally pure LaMnO_3 single crystals (LaMnO_3 -1, LaMnO_3 -2 and LaMnO_3 -3). Details of the three nominally pure (slight variation in Mn^{4+}) LaMnO_3 single crystals is discussed in chapter 2. Here, in Fig. 3.4, we show the $I - V$ data for the three samples. It can be seen from Fig. 3.4 that after a particular voltage (which we call threshold voltage V_{th}) the current through the sample switches to a higher value. This arises because the resistive state makes a transition from a high resistive state (HRS) to a low resistive state (LRS). The current in the LRS shows saturation due to the compliance limit of the source. The LRS prevailed until the voltage was lowered below a threshold value after which it

again returned back to the HRS. This transition region showed a hysteresis and it persisted up to 260–280K (depending on the LaMnO_3 single crystal). We found that both below and above the threshold voltage, the $I - V$ characteristics follow an approximate power law $I \propto V^n$, below V_{th} (in the HRS) $n \sim 1$ and above the threshold (in the LRS) $n > 1$ (see Fig. 3.5). In Fig. 3.6(a), we have plotted the

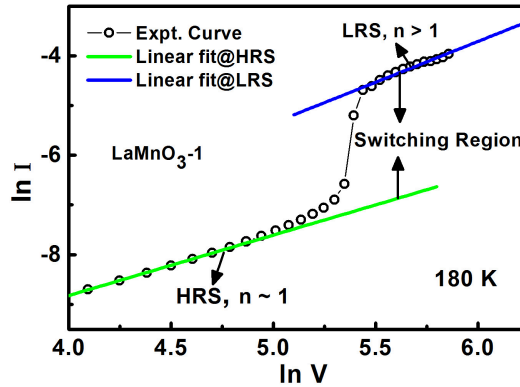


Figure 3.5 Power law dependence of $I - V$ curve before and after switching at 180K for LaMnO_3 -1.

sample voltage (V_S) with the applied bias voltage (V) at different temperatures. This way of plotting the data (V_S as a function V) identify the V_{Th} at which the transition occurs. When the sample is in HRS (high resistance insulating state), the sample voltage follows the applied bias. On reaching the threshold voltage V_{th} , the sample makes transition to the LRS, leading to a fall in the bias across the sample because the bias now drops predominantly across the limiter R_L . The Fig. 3.6(b) shows an example of the field induced transition and the hysteresis at a representative temperature $T = 150\text{K}$ and the threshold voltage V_{th} is marked (direction and colour of the arrow indicating the loop and transition between HRS and LRS respectively). From this value of V_{th} , the field E_{th} is obtained. In the Fig. 3.6(c) we show the temperature variation of E_{th} for all the three samples. All the samples show a steep rise with the decrease in temperature and have values that are similar (within a factor of 2). E_{th} becomes very small ($< 100\text{V/cm}$) for temperatures higher than 290–300K, beyond which there is no resistive state transition. The change in the resistance at the transition as a function of temperature is shown in Fig. 3.7(a). High resistance state is marked as HRS and low resistance state as LRS. As temperature is increased, the decrease in sharpness of the transition can be seen. It can be noted that LRS is nearly independent of temperature. The size of the hysteresis region, as well as the jump in the resistance at

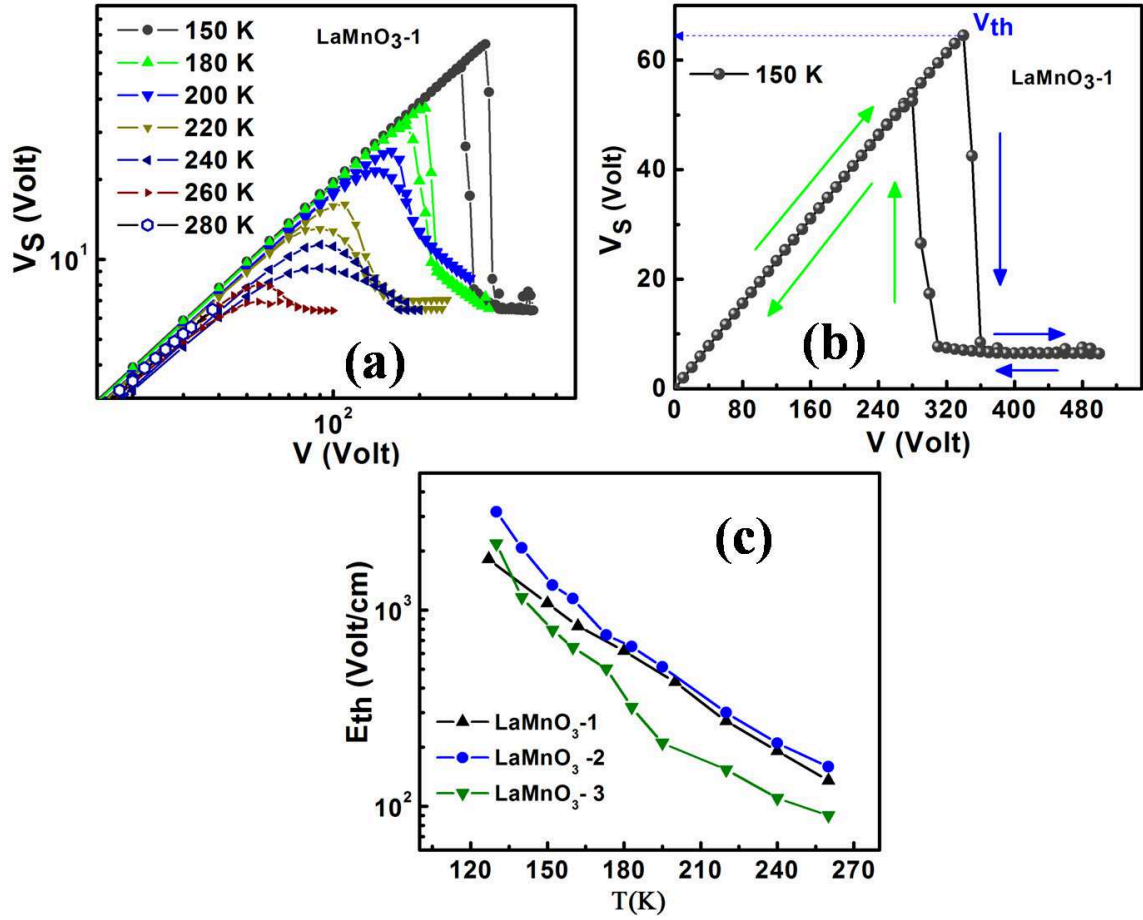


Figure 3.6 (a) Sample voltage (V_S) versus bias voltage (V) at different temperatures, (b) Typical threshold voltage V_{Th} at which the sample voltage jumps to a lower value and (c) Variation of the threshold field E_{th} for the three different LaMnO_3 crystals used.

the transition, reduces with increasing temperature and nearly vanishes after 280-290K. In the HRS, resistivity has strong temperature dependence (see Fig. 3.1). However the LRS has resistance that is nearly temperature independent. In Fig. 3.7(b), we have plotted the percentage of change in resistivity vs. temperature for the three samples. $\frac{\Delta\rho}{\rho}$ is defined as $\frac{\rho_{hrs} - \rho_{lrs}}{\rho_{hrs}}$ (We have used ρ_{hrs} in the denominator and not ρ_{lrs} to avoid unnecessary magnification of the resistance change). It can be seen that the change is nearly 100% below 210K for all the crystals and it approaches small values for $T > 280\text{K}$. While for the other two crystals (LaMnO_3 -2 and LaMnO_3 -3) the data are identical but there is small quantitative difference near the region where $\frac{\Delta\rho}{\rho} \rightarrow 0$ for LaMnO_3 -1. This actually reflects the differences in the exact Mn^{4+} content of the samples.

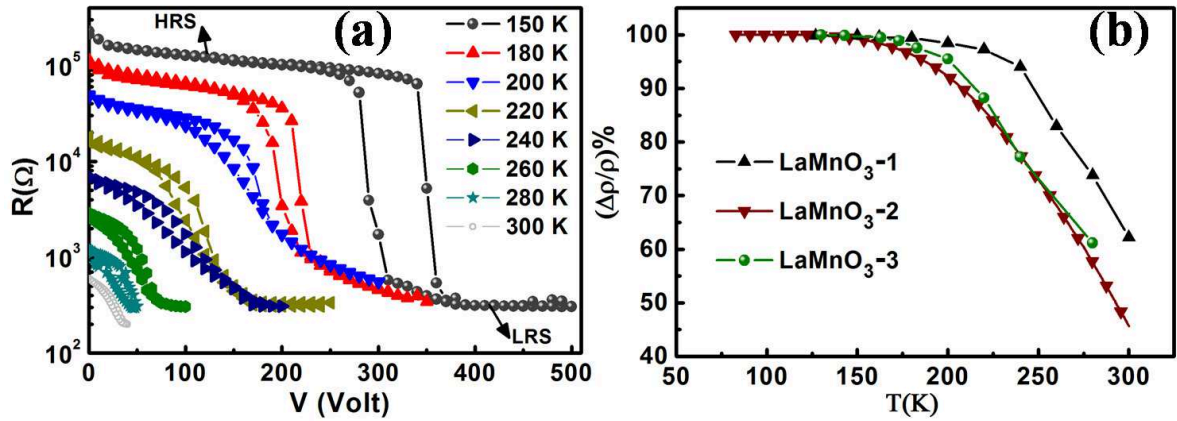


Figure 3.7 (a) Sample resistance (R) vs. applied bias voltage (V) for LaMnO_3 -1 and (b) Percentage of change in resistivity with temperature for the three LaMnO_3 samples used at the resistive state transition.

We have observed two field dependent resistive states (HRS and LRS) from the $I - V$ characteristics of LaMnO_3 . Normal (low field) resistive state is insulating and high field switched state shows a nearly temperature independent low resistive state. In spite of the fact that three LaMnO_3 single crystals have a slight variation in composition (in respect of Mn^{4+}) and as well as in dimension, all the sample shows this field driven resistive switching which shows that this resistive state transition is an intrinsic effect in parent LaMnO_3 . The $I - V$ characteristics of the three LaMnO_3 samples also show that an optimum electric field can destabilize the normal insulating state of LaMnO_3 .

In the next section we will discuss the difference between the field driven resistive state transition in LaMnO_3 with lowering of resistivity due to the increase of Mn^{4+} content due to divalent atom doping (like Sr) in LaMnO_3 (as in Fig. 3.1). This will prove that the observed effect is not due to the presence of Mn^{4+} content in LaMnO_3 rather it has a different origin (which will be discussed in detail in next section.)

3.3.2 $I - V$ data for hole doped $\text{La}_{0.9}\text{Sr}_{0.1}\text{MnO}_3$

To investigate the effect of Mn^{4+} on the field driven transition, we repeated these measurements in $\text{La}_{0.9}\text{Sr}_{0.1}\text{MnO}_3$ single crystal where the Mn^{4+} content is significantly larger than that of a nominally pure LaMnO_3 . Choice of the doping concentration $x = 0.1$ was motivated by the fact that it marks the

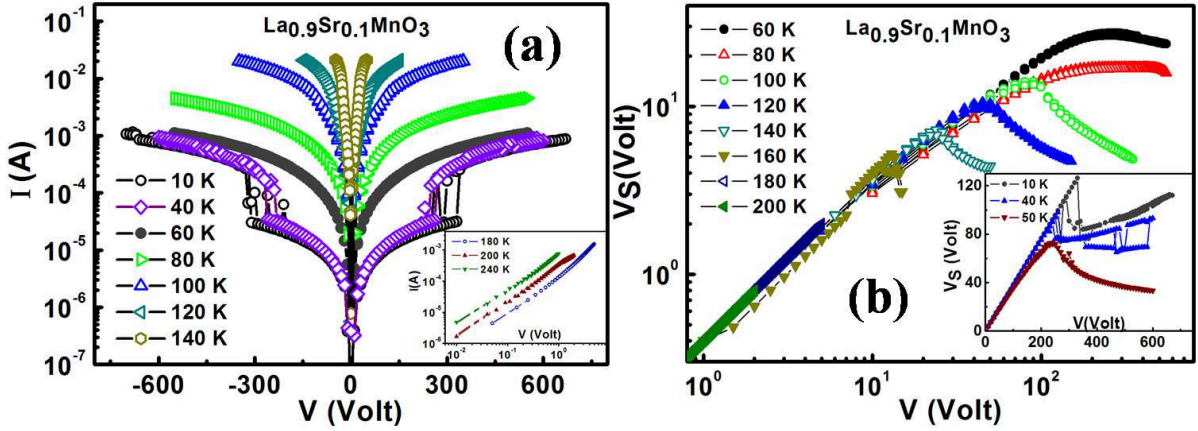


Figure 3.8 (a) $I - V$ characteristics of $\text{La}_{0.9}\text{Sr}_{0.1}\text{MnO}_3$ at different temperatures. Inset shows the data at higher temperatures $T > 160\text{K}$ and (b) Sample voltage versus bias voltage at different temperatures in the range $10\text{K} < T < 240\text{K}$. Inset shows the jump of sample voltage at the resistive state transition below 50K .

boundary between the CAF state and the FMI state, as stated before. The $I - V$ data in $\text{La}_{0.9}\text{Sr}_{0.1}\text{MnO}_3$ (in Fig. 3.8(a)) were taken in the same way as it was done in the other crystals. In $\text{La}_{0.9}\text{Sr}_{0.1}\text{MnO}_3$ the resistive state transition softens compared to that seen in LaMnO_3 . The resistive state transition occurs at low temperatures below 50K , although the $I - V$ data are strongly non-linear for all T below 140K . The minimum field ($\sim 7\text{KV/cm}$) needed to enact the transition is also much larger. In Fig. 3.8(b), we plot V_S vs. V from 10K to 240K . The data at lower temperature $T \leq 50\text{K}$ are shown in the inset. For $T \leq 50\text{K}$, the sample voltage shows similar kind of jump as observed in the three LaMnO_3 samples, showing existence of HRS to LRS transition. At higher temperature there is a strong non-linearity leading to a substantial decrease of the sample resistance showing precursor of a resistive state transition that may occur at higher bias. Our data is qualitatively similar as seen by one of us [137] in $\text{La}_{0.9}\text{Sr}_{0.1}\text{MnO}_3$ single crystal with nominally same composition. However, there are differences in details that will reflect the difference in exact Mn^{4+} content and also the possibility of co-existence of many phases near the critical concentration $x = 0.1$. The data taken by us as well as those reported in Ref. [137] show that introduction of Mn^{4+} gradually changes the nature of the sharp resistive state transition seen in LaMnO_3 .

From the $I - V$ data of $\text{La}_{0.9}\text{Sr}_{0.1}\text{MnO}_3$ we observed that divalent atom doping or introduction of

hole in parent LaMnO_3 noticeably reduces the resistive switching which establish the fact that existence of Mn^{4+} due to chemical doping is not responsible for this kind of switching. The origin of the field driven resistive state transition in LaMnO_3 is rather more intrinsic in nature for LaMnO_3 or parent perovskites. To establish this fact, we have performed same kind of $I - V$ measurement in GdMnO_3 thin film which has different composition and morphology with respect to LaMnO_3 . In the next section, we will discuss the $I - V$ measurement on GdMnO_3 .

3.3.3 $I - V$ data of GdMnO_3 thin film

In this section, we will discuss the bias driven switching of resistive states in a thin film (thickness ≈ 10 nm) of GdMnO_3 at room temperature. $I - V$ data on the film was measured using the circuit configuration as shown in Fig. 3.3(b) with four Au/Ti metal pads of area 1mm^2 with distance between pads $\approx 250 \mu\text{m}$. The switching ($I - V$) data of the GdMnO_3 film at room temperature is shown in Fig. 3.9(a). $I - V$ curves of the sample was taken with the bias from -8V to $+8\text{V}$ at room

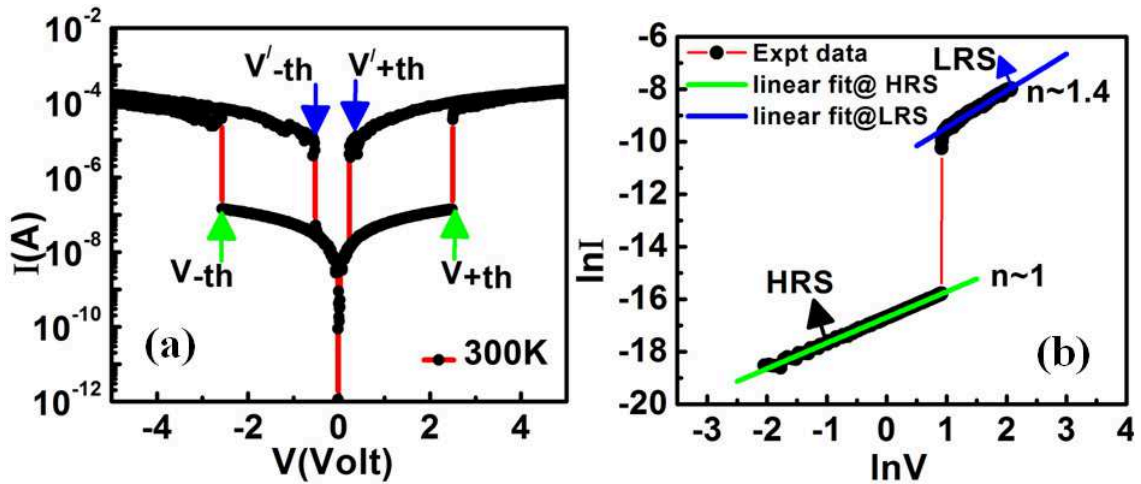


Figure 3.9 (a) $I - V$ curve of the GdMnO_3 film with positive and negative bias; green arrows showing the threshold voltage for switching to LRS and blue arrows showing the threshold voltage for switching to HRS. (b) Power dependence of the $I - V$ curve.

temperature. The applied bias V is varied in steps of 10mV . It can be seen that at a certain bias (V_{th}) the current through the sample switches nearly three orders in magnitude from one tenth of a μA to one tenth of a mA . Before the threshold field, sample resistance is nearly few $\text{M}\Omega$ and due to this high

resistance of the film we didn't use the current limiter R_L in the measurement circuit (in Fig. 3.3(b)). The state having low I (or high R) is the HRS while that has high I (or low R) is the LRS. The observed switching occurs between two stable resistive states are very sharp.

The voltage at which the system switches from the HRS to LRS is represented as V_{+th} for positive cycle and V_{-th} for negative cycle and $V_{+th} \approx 2.5\text{V}$ (shown in Fig. 3.9(a)). The system remains in this state up to the highest bias applied. The switching from HRS to LRS is extremely sharp and occurs within one step of the applied bias (10mV). When the bias is again reduced back to zero, the sample state stays in the LRS state for $V \ll V_{+th}$ and switches back to the HRS state at a much smaller bias of $\approx 0.25\text{V}$ (which we call V'_{+th}). Due to the symmetric nature of the electrodes, the switching is symmetric and similar resistive jump is also observed in the negative bias cycle at a defined bias which we mark as V_{-th} where the absolute values of V_{-th} is close to that of V_{+th} . On reducing the negative bias to zero the LRS state is retained and transition to the HRS occurs at much smaller bias (V'_{-th}) which also has similar absolute value close to V'_{+th} .

It is also unipolar switching as the polarity of the V_{+th} and V'_{+th} biases are same and the resistance jump occurs symmetrically in both positive and negative bias. Importantly, the resistive state switching maintains a substantial hysteresis in the $I - V$ curves between the V_{+th} and V'_{+th} as the two biases are well separated ($V_{th} / V'_{+th} \approx 10$). The large difference between the two resistive states ($R_{HRS}/R_{LRS} \approx 10^3$) is maintained almost over the whole bias window between V_{th} and V'_{+th} . Even at a bias just above V'_{+th} the ratio R_{HRS}/R_{LRS} stays high. We have repeated $I - V$ measurement over many cycles and each time we get the two state transition which establishes the reproducibility of the switching phenomena. Between cycle to cycle there is some wandering of the biases V_{th} and V'_{+th} by $\pm 0.75\text{V}$ and $\pm 0.05\text{V}$ respectively.

The two resistance states have different characteristic dependence on bias (in Fig. 3.9(b)). The HRS state shows an ohmic conduction with negligible non-linearity ($I \propto V$, $n \approx 1$). However, the LRS state has a non-linear characteristics ($I \propto V^n$ with $n \approx 1.4$). This non-linearity does not arise from heating. If heating would have been the cause of non-linearity, n should be < 1 . The issue of joule heating will be discussed in later section. In this section, we found that GdMnO_3 thin film shows

Table 3.1 Comparison of resistive switching in the LaMnO₃ single crystals and GdMnO₃ thin film.

Sample	E_{th} (V/cm)		$-\frac{\Delta\rho}{\rho}$ %	
	150K	300K	150K	300K
LaMnO ₃ -1	~1000	~100	~100	~60
LaMnO ₃ -2	~1000	~100	~100	~45
LaMnO ₃ -3	~1000	~100	~100	~45
GdMnO ₃		~100		~100

similar kind of resistive switching like LaMnO₃ single crystals but for GdMnO₃, switching occurs at room temperature while for LaMnO₃ it occurs around 150K. The threshold voltage for switching is much lower than LaMnO₃. But the qualitative features of the resistive state transition are similar. For both the samples, an optimum field destabilize the polaronic insulating state. The two samples (LaMnO₃ and GdMnO₃) shows ohmic conduction in HRS and non-ohmic behaviour (in LRS) in the switched state. The comparison of the resistive switching in the LaMnO₃ single crystals and GdMnO₃ thin film are tabulated in table 3.1. The reason for different temperature regime for resistive switching in LaMnO₃ single crystals and GdMnO₃ thin film will be discussed in a section where we will explain the microscopic origin of the switching. But interestingly highly insulating parent manganites like LaMnO₃ and GdMnO₃ shows resistive switching on the application of a small critical field.

3.4 Temperature dependence of switched state in LaMnO₃ and GdMnO₃

From the $I - V$ measurement of LaMnO₃ and GdMnO₃, the existence of a low resistive state above a critical field (E_{th}) is confirmed. We also observed that high field resistive state (HRS) in these two samples has adiabatic polaronic transport. In this section, we will explore the temperature dependence of the low resistive states (LRS) in LaMnO₃ and GdMnO₃. The temperature dependences of the HRS and LRS states have been investigated by measuring the resistivities at constant bias voltages $V > V_{th}$ ($V \approx 300V$ for LaMnO₃, $V \approx 6V$ for GdMnO₃) and $V < V_{th}$ ($\approx 1V$ for both LaMnO₃ and GdMnO₃)

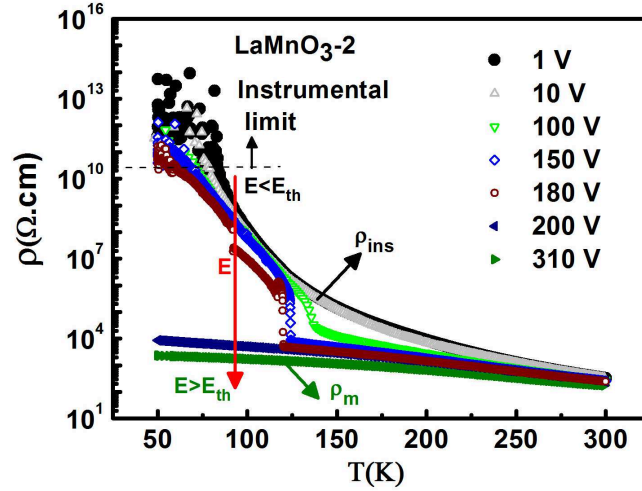


Figure 3.10 $\rho - T$ curves for a LaMnO_3 single crystal measured at different constant bias from 1V to 310V in four probe configuration. The transition in resistivity from LRS to HRS on cooling at different bias can be seen.

in four probe method (as in Fig. 3.3) to compare with the resistive state transition as seen in the $I - V$ data in LaMnO_3 and GdMnO_3 . The variation in ρ with T measured at different biases are shown in Fig. 3.10 for one of the LaMnO_3 samples (LaMnO_3 -2). For lower biases $< 200\text{V}$ (corresponding to $E_{th} < E$), the sample makes transition to the HRS on cooling below a certain temperature and below 100K, we cannot measure the resistivity due to the instrumental measurement limit (marked in the Fig. 3.10). At higher bias ($> 200\text{V}$) the resistivity is in the LRS till the lowest temperature 50K due to the steep rise of E_{th} . This data (along with the data of Fig. 3.6(c)) clearly demonstrates the existence of a threshold field for the transition and its steep temperature dependence. At higher temperatures when E_{th} is small and applied $E > E_{th}$, the sample is in LRS. On cooling in a fixed E , the E_{th} increases sharply and whenever $E_{th} \geq E$, the transition occurs to the HRS. For the sample shown in Fig. 3.10, there is a clear resistivity jump in the range 125K to 150K. It can be seen that while the resistivity in HRS (ρ_{ins}) has a strong temperature dependence (the polaronic insulating state), the resistivity of the LRS, which is stable for $E_{th} < E$, is nearly temperature independent (marked as ρ_m in Fig. 3.10). From Fig. 3.10, it can be seen that ρ_{ins} equal to or comparable to ρ_m above 280K and there is no observable resistivity transition above 280K. The exact value of this will depend on the exact crystal used and the difference between ρ_{ins} and ρ_m will determine the switching.

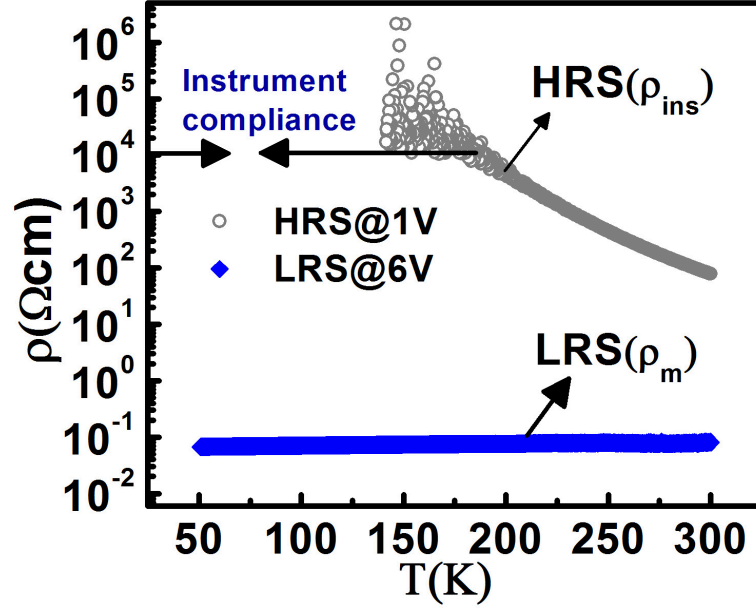


Figure 3.11 $\rho - T$ measurement in GdMnO_3 with different bias showing the temperature dependent resistivities in the two states.

For GdMnO_3 , we have also observed temperature dependent ρ_{ins} and ρ_m as like LaMnO_3 . In Fig. 3.11, we show the resistivity ρ as a function of T measured with $E < E_{th}$ (HRS state) and $E > E_{th}$ (LRS state). The resistance increases on cooling and reaches a compliance limited range below 180K (The noise in the data is due to the compliance limit). The temperature dependence of ρ for the HRS state is activated as discussed in section 3.2. In the same graph we show the temperature dependence of ρ measured down to 40K in the LRS state that has been created at room temperature by applying a bias of $V > V_{+th}$. It can be seen that in the LRS, the ρ - T curve is similar to that of a high resistive metal with $\frac{d\rho}{dT} > 0$. The shallow T dependence of ρ in the LRS is not discernable in Fig. 3.11 that has a log scale for the y-axis. From Fig. 3.12, we show ρ as a function of T in the LRS state which shows a metallic behaviour. Though $\frac{d\rho}{dT}$ is positive but the change in $\Delta\rho$ is not very large in between 300K to 50K which is similar to that found in many highly resistive metallic oxides [141]. We fitted the $\rho - T$ curve with:

$$\rho = \rho_{0L} + AT^m \quad (3.2)$$

Where ρ_{0L} is the residual resistivity. The power m was found to be ≈ 1 from fit to the data, as one would

expect in a metal. $\rho_{0L} \approx 60 \text{ m}\Omega\text{cm}$ in the LRS and is comparable to but greater than that generally found in metallic oxide films [141]. From Fig. 3.2(c) and 3.11, it is clear that the two states between which the

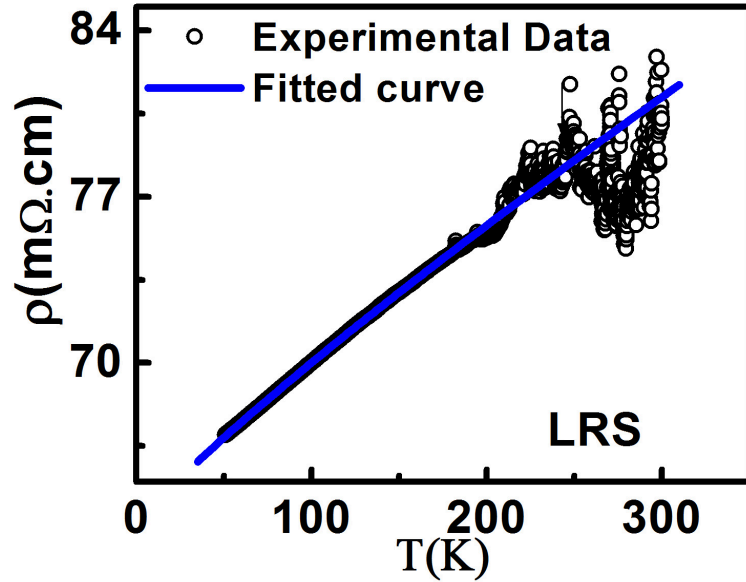


Figure 3.12 Linear fit to $\rho - T$ curve in LRS for GdMnO_3 .

transition occurs are distinct electronically. HRS is a polaronic insulating state (from Fig. 3.2(c)) while LRS is a metallic one. On the application of switching voltage (V_{+th}), there is an insulator to metal transition mediated by the electric field. $\rho - T$ data establishes that two bistable states are qualitatively different; one being a metal (though it is a bad metallic behaviour) while the other is an insulator. From Fig. 3.11, we find that the difference in ρ_{ins} and ρ_m between HRS and LRS is nearly three order at room temperature and it increase to nearly 5 order at low temperature which is extremely large and that is why in GdMnO_3 thin film resistive switching occurs at room temperature. It is noted that GdMnO_3 , even it is substantially hole doped, does not show a metallic state unlike LaMnO_3 , which on optimal hole doping (i.e., creation of adequate Mn^{4+}) leads to a metallic FM state. This is due to the narrow band width in GdMnO_3 that originates from relatively smaller ionic size of Gd ions. Thus the observation of a stable metallic state in pure GdMnO_3 created by a field is truly fascinating and suggest that this resistive state transition has an electronic origin.

The switching in the present investigation on LaMnO_3 single crystals and GdMnO_3 thin film have

been seen in a planar configuration of electrodes where the current is in plane (CIP) of the single crystal pellet or the film and the electrodes play no role in the observed switching phenomena. The measurement of the 4-probe resistivity establishes that the switched states that show insulating/metallic behaviour are in the bulk of the film and are not in electrode region. The observed field driven switched state (LRS) in LaMnO₃ single crystals and in GdMnO₃ film shows nearly temperature independent low resistive state (in LaMnO₃) or bad metallic state (in GdMnO₃) with shallow temperature dependence. The two bi-stable states (ρ_{ins} and ρ_m) are of qualitatively different nature than the switching observed before in oxides including manganites, as discussed before. We also observed that the difference in magnitude between ρ_{ins} and ρ_m plays a crucial role in the resistive switching. For LaMnO₃ the difference in resistivities between HRS and LRS at room temperature is small and there is no resistive state transition. But for GdMnO₃ this difference is large enough to see a field driven resistive switching at room temperature though the switched states are qualitatively similar. Interestingly, the LRS in LaMnO₃ has a much higher ρ ($10^2 - 10^4 \Omega\text{cm}$) compared to that in GdMnO₃ ($\leq 100\text{m}\Omega\text{cm}$). It may arise from the single crystal (LaMnO₃) and thin film (GdMnO₃) nature of the samples. The nature of the switched states will depend on the morphology and composition of the samples used. In the next section, we will argue that switching in LaMnO₃ and GdMnO₃ occur from a similar electronic origin where the bi-stability is ensured by the existence of an inherent electronic phase separation in undoped manganites that may arise due to charge disproportionation.

3.5 A phenomenological model for the transition

In this section we will discuss a phenomenological model for the observed resistive switching in LaMnO₃ and GdMnO₃. The model is based on the basic premises that there is a phase coexistence of two phases in LaMnO₃ and GdMnO₃ below the structural transition temperature ($T > 750\text{K}$). One is the orthorhombic JT distorted polaronic insulating phase with resistivity ρ_{ins} (the majority phase) and other is the bad "marginally" metallic resistance phase (the minority phase) which has nearly temperature independent resistivity ρ_m (note: ρ_m may be high but $\rho_m \ll \rho_{ins}$). The rationale for this

phase co-existence will be discussed in the next section. The volume fraction of the minority phase at room temperature or below is very small in zero applied bias. As a result the observed ρ is determined predominantly by the ρ_{ins} . The volume fraction f can be represented as the "mobile" (or de-pinned) fraction of the phase that will contribute to the transport. We make this distinction, because some part of the minority phase can be pinned and will not contribute to the transport. This issue will be elaborated in next section. The phenomenological model uses the physical scenario that the conducting volume fraction f can be enhanced with an applied field E as well as with increase of temperature T . The field driven transition to the LRS occurs when f , on application of the field E , crosses the volume fraction for percolation threshold. In Fig. 3.13, we have shown the schematic diagram of the above discussed phenomenon. The suggested phenomenological model for the resistive state transition is thus

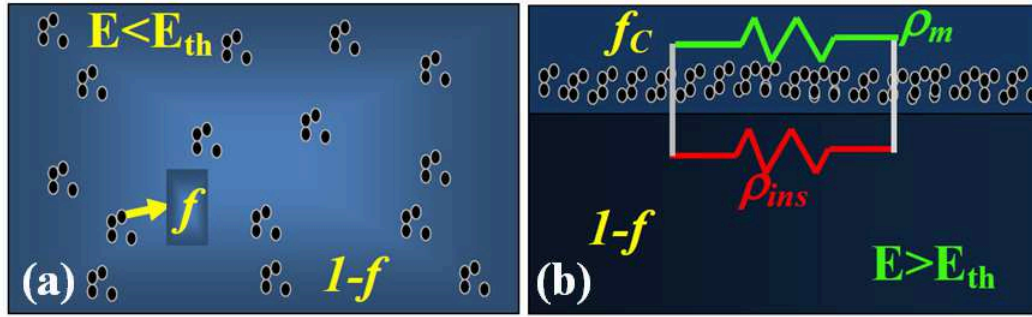


Figure 3.13 (a) Two phase model below $E < E_{th}$; f represents the metallic phase (the black circles) and $(1 - f)$ is the polaronic insulating phase. (b) Formation of the parallel conducting channel (ρ_m) above $E > E_{th}$ when f becomes equal to a critical concentration f_c .

a field induced percolation transition between two phases that coexist at and below 300K. In this model the applied field does not create any new minority phase, but enhances its mobile fraction f . f is also enhanced by the increase of temperature by thermal activation. We evaluated the volume fraction f from the observed data (ρ as a function of E) in the frame work of effective medium theory [142] :

$$\rho_{obs} = \frac{\rho_{ins}\rho_m}{(1-f)\rho_m + f\rho_{ins}} \quad (3.3)$$

$$f = \frac{\rho_m(\rho_{ins} - \rho_{obs})}{\rho_{obs}(\rho_{ins} - \rho_m)} \quad (3.4)$$

$\rho_{ins}(T)$ and ρ_m are marked in Fig. 3.10 and 3.11.

In Fig. 3.14(a) we show the data of the metallic volume fraction f as a function of V or E for different temperatures for one of the LaMnO_3 samples (as resistive switching is more or less similar in nature for all the three LaMnO_3 samples). The f is very small at lower temperatures but it grows very rapidly as the temperature rises. It can be seen that at $E = E_{th}$, f crosses $f_c \approx 0.25$, which is close to the critical value for volume percolation in 3D [142], leading to the resistive state transition. From Fig.

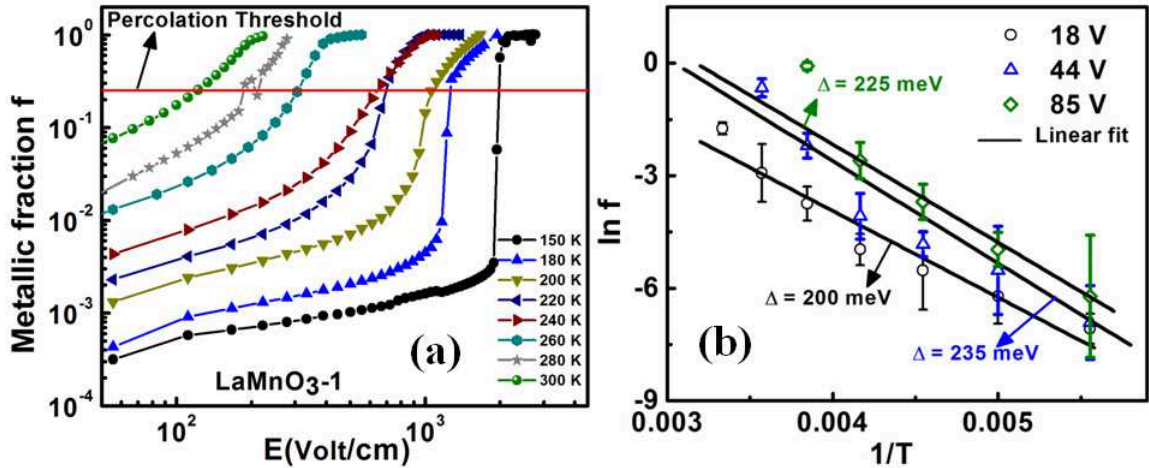


Figure 3.14 (a) Variation of the fraction f with the applied field E for LaMnO_3 -1. (b) Activated temperature variation of the fraction f for LaMnO_3 -1.

3.14(a), we find that the growth of the volume fraction f is strongly enhanced by an applied field. At lower temperatures, for $E \rightarrow 0$, f being very small, the effect of the applied bias is stronger leading to a sharp transition between HRS and LRS. As the temperature approaches to 280K–290K the decrease in the difference between ρ_{ins} and ρ_m (see Fig. 3.10.) softens the transition considerably.

The transition at a given temperature T , in an applied field E , occurs when the fraction $f(E, T) = f_c$. This defines $E_{th}(T)$ at a given temperature T . On application of the field, f grows rapidly. As f also increases with T even in zero field, the threshold f_c is reached at much lower bias for higher temperature. This results in the resistive state transition at smaller bias at higher temperature. The steep dependence of $E_{th}(T)$ on T is thus a reflection of the strong dependence of f on T and E . We will show that the f depends on thermal activation and field induced de-pinning respectively.

The temperature and field dependence of f (determined from the Eqn. 3.4 using the measured

values of ρ_m , ρ_{ins} and ρ_{obs}) was found to be an activated process following the relation:

$$f = f(E) \exp\left(\frac{-\Delta}{\kappa_B T}\right) = C \exp\left(\frac{-E_0}{E}\right) \exp\left(\frac{-\Delta}{\kappa_B T}\right) \quad (3.5)$$

, where C is a constant, E_0 is a scale for de-pinning field for the minority phase and Δ being the activation energy. The temperature dependence of f is shown in Fig. 3.14(b) for three representative biases. Thermal activation energy Δ is found to be in the region of 200–235 meV and largely independent of E . Interestingly the value of Δ is the same as the activation energy (E_a) found in the polaronic state in the three LaMnO₃ crystals. The pre-factor $f(E)$ increases with E . We find that the predominant effect of the electric field E is to change the pre-factor $f(E)$, as discussed below.

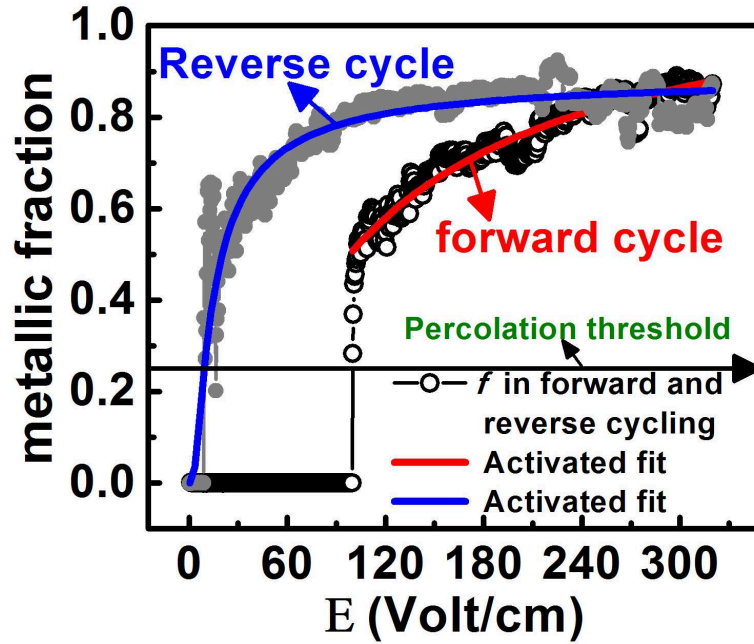


Figure 3.15 Variation of metallic fraction f vs. electric field E in increasing and decreasing field sequence. f vs. E fitted with an activated dependence on E .

In Fig. 3.15, we have shown the variation of f with the electric field (E) in GdMnO₃ which has been obtained by using the $I - V$ curve (Fig. 3.9(a)) and experimentally known ρ_{ins} and ρ_m using equation 3.4. The field dependence of f is also found to be an activated process following the relation: $f(E) \propto \exp\left(\frac{-E_0}{E}\right)$ (as the pre factor in the Eqn. 3.5). This is very similar to the relation found in many field driven de-pinning phenomena including charge density wave de-pinning [143, 144].

To summarize, the observed resistive transition has been described as a bias driven percolation type transition between two states with coexisting phases: the polaronic insulating phase and a "marginally" metallic phase. The transition is controlled by two parameters. The first is the mobile fraction f of the more conducting phase that has a steep E and T dependence that is described by Eqn. 3.5. The second parameter is the relative differences between the two phases ρ_{ins} and ρ_m as shown in Fig. 3.10 and 3.11. This difference determines the magnitude of the resistive jump at the transition. For LaMnO_3 , the transition is not observable near $T \approx 280\text{K} - 290\text{K}$ as $\rho_{ins} \rightarrow \rho_m$. However, as $\rho_{ins} \gg \rho_m$ for GdMnO_3 , a sharp transition is observed near room temperature.

The creation of Mn^{4+} by Sr substitution in LaMnO_3 changes the nature of the transition and can gradually suppress it. The data on the single crystal $\text{La}_{0.9}\text{Sr}_{0.1}\text{MnO}_3$ taken by us show that in most of the temperature range the transport shows strong non-linearity but f may not exceed f_c . The strong non-linearity can also be modelled by the phenomenological model described for the nominally pure LaMnO_3 , where the mobile fraction f gets enhanced by the applied bias leading to the strong non-linearity. In this case the bias dependence of f for most of the temperature range is much less steep compared to the nominally pure systems. From the experimental data using the 2-phase model, we find the resistivities of the two phases ρ_{ins} and ρ_m for $\text{La}_{0.9}\text{Sr}_{0.1}\text{MnO}_3$. In Fig. 3.16, we show the data.

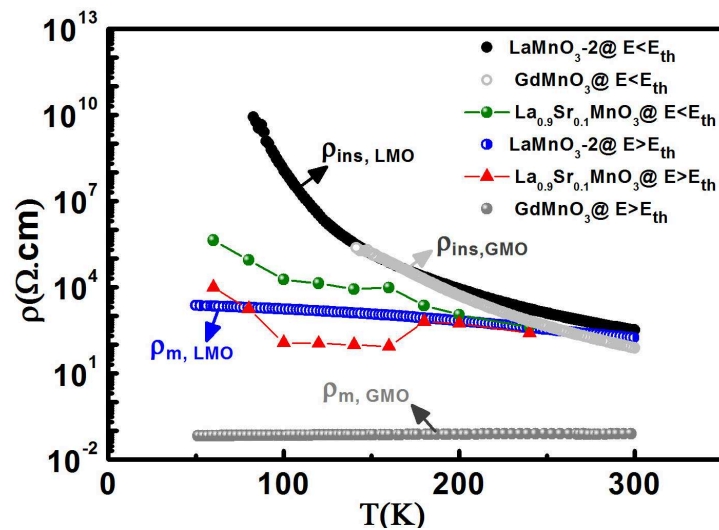


Figure 3.16 Resistivities of LaMnO_3 , GdMnO_3 and $\text{La}_{0.9}\text{Sr}_{0.1}\text{MnO}_3$ in HRS in comparison to the ρ_m of the LRS as deduced from the experiment.

The resistivity ρ_{ins} in the polaronic insulating state is much suppressed by Sr substitution compared to LaMnO_3 and GdMnO_3 . However, for $T \geq 150\text{K}$, the resistivity of the minority phase ρ_m is identical to that of the value of ρ_m that we found for LaMnO_3 . This is an important observation that while the creation of Mn^{4+} suppresses the resistivity of the polaronic insulating state considerably, the resistivity of the minority bad metallic phase is not affected. This suggests that the bad metallic phase that gives ρ_m , is different from the low resistive state due to deliberate hole (Mn^{4+}) doping (Sr substitution). It can be seen that in the temperature range $T \geq 150\text{K}$, the value of ρ_{ins} for the Sr substituted system being lower it is not much different from the ρ_m . As a result the resistive transition becomes soft and loses the sharpness as seen in the case of LaMnO_3 . It shows up as a non-linear $I - V$ curve as f changes with bias (in Fig. 3.8). Below 150K, when the FM state sets in, there is phase co-existence with lower resistance FMM phase (in Fig. 3.1(b)). This brings down ρ_m . However, it recovers below 100K when the FMI state sets in. In this region ρ_{ins} also rises rapidly on cooling. This leads to a sharp transition at lower temperature (in Fig. 3.8). The quantitative details of the transition where one has co-existing phases of different kind would depend on the exact value of the Mn^{4+} . From Fig. 3.16, we can observe the quantitative difference in ρ_m for LaMnO_3 and GdMnO_3 and this difference arises due to the internal chemical structure, morphology and dimensions of the two samples which leads to variation in volume fraction of the minority phase f . We have found that these minority phases can lead to formation of FM clusters which are dispersed in the insulating PM and AFM phases of LaMnO_3 (details in chapter 4). We observed that bias driven percolation type transition occurs in parent manganites due to the coexistence of two phases (polaronic insulating and "marginally" metallic phases) and external applied field can control this percolation driven transition.

3.6 Microscopic scenarios for the phenomenological model

The phenomenological model given above is based on phase co-existence of a relatively low resistance marginally (or bad) metallic phase that has nearly temperature independent resistivity along with the polaronic insulating phase. This was seen to occur in nominally pure LaMnO_3 as well as in GdMnO_3 .

In this subsection, we explore whether there are evidences of such phase coexistence and a microscopic scenario for such a marginally metallic phase.

In nominally pure LaMnO_3 , there exists unintentional (explained in Chapter 2) Mn^{4+} . The dominant phase below the structural transition temperature (T_{JT}) is an orthorhombic polaronic insulating phase which leads to A-type AFM ordering below 150K. However, there are evidences based on Neutron scattering studies [145], Resonant X-Ray scattering [146], and also from optical conductivity experiments [147] that this picture may not be complete and there are evidences of the presence of small concentration of a phase that have similarity in structure and electronic properties with the high temperature phase that is found above T_{JT} . This minority phase can be another orthorhombic and rhombohedral FM phases with a considerably smaller unit-cell volume with a FM transition temperature near T_N . Based on the above experiments, it has been recently suggested [89] that such a minority phase can be a marginally metallic phase. Strong evidence of this comes from pressure induced metallization of LaMnO_3 . It had been observed [9] that the pressure induced destabilization of the insulating state in LaMnO_3 at 300K (at pressure ≥ 32 GPa) leads to an orbital disordered phase that is like a bad metal with temperature independent resistivity. Subsequent X-ray Absorption Spectroscopy in LaMnO_3 under pressure [148] showed that although the insulator-metal transition is completed above 32 GPa, there is co-existing orbital dis-ordered phase that exists in a wide pressure range above 7GPa till the transition is complete. Thus there is evidence that a marginal metallic phase with small volume fraction can co-exist with the insulating phase well below T_{JT} in LaMnO_3 .

It is also experimentally observed that a dilute metallic phase can exist in GdMnO_3 which is the minority phase and it was found in hexagonal GdMnO_3 thin film grown in low O_2 pressure by XPS study [149]. In this case the presence of minority phase is due to the oxygen stoichiometry. In our case GdMnO_3 has an orthorhombic structure and the existence of such marginally metallic phase can be due to the oxygen stoichiometry.

It has been suggested [89] recently that charge transfer (CT) instabilities can lead to dynamic charge disproportionation ($\text{Mn}^{3+} + \text{Mn}^{3+} \rightarrow \text{Mn}^{4+} + \text{Mn}^{2+}$) in nominally pure manganites, which can act as an electron-hole (EH) pair. The presence of this instability leads to phase separation between a JT

distorted polaronic insulator (the conventional phase) and a phase that behaves as a bad (or marginal) metal comprising of EH droplets ($Mn^{4+} - Mn^{2+}$ pairs). There are evidences [150,151] that such a phase is present well below T_{JT} and even at 200K with a finite volume fraction. Increase in temperature leads to enhanced volume fraction of this phase and the phase transition at T_{JT} is envisaged to be facilitated by this phase. It is suggestive that the metallic minority phase, proposed in the phenomenological

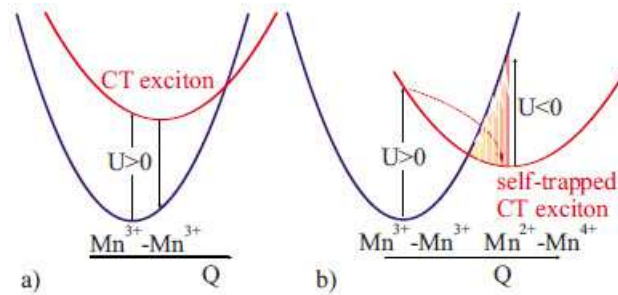


Figure 3.17 Schematic diagram of the adiabatic potentials for (a) without charge transfer and (b) with charge transfer. Q is related to the lattice degrees of freedom and U is the charge disproportion energy. Image is reproduced from [89] with author's permission.

model above, may be related to this CT instability driven EH droplet phase [89, 90, 152]. The full volume of EH droplets that make the minority phase need not be mobile and it can be self-trapped at lattice sites or may also be trapped by local impurity potentials. The schematic diagram of the charge transfer (CT) instability driven charge disproportionation (CD) effect [89] is shown in Fig. 3.17. In Fig. 3.17, we have shown that manganites may have two phases; one is CT stable system with only lower energy minimum (in Fig. 3.17(a)) for a certain charge configuration and other is the bistable, or CT unstable systems with two energy minima for two local charge configurations [89]. One of the bistable states is associated with the self-trapped CT excitons resulting from self-consistent charge transfer and electron-lattice relaxation [89].

The applied electric field in our measurement depinned this self trapped E-H pairs. The volume fraction (f) of the minority metallic phase estimated from the electrical resistance data gives the volume fraction of the mobile phase. The enhancement of f occurs with temperature following an activated process that is very similar to the activation energy seen in transport in the polaronic insulating phase. The applied electric field can lead to de-pinning of the EH droplets from the lattice sites or impurity

pinning sites. The nature of the E dependence of f seen by us suggests that this can indeed be the case. Creation of Mn^{4+} by Sr substitution is likely to be different from the Mn^{4+} in the EH pair. In a very qualitative sense, Mn^{4+} in EH pair is like intrinsic doping while that created by substitution is like extrinsic doping. With creation of more Mn^{4+} due to substitutional doping, they will dominate over the intrinsic EH pair seen in nominally pure $LaMnO_3$ and $GdMnO_3$. The inhibition of the resistive state transition in $La_{0.9}Sr_{0.1}MnO_3$ can be a manifestation of this crossover from a disproportionation (EH pair) controlled region to an intentionally hole doped region where disproportionation created by Mn^{4+} has negligible effect.

3.7 Issue of Joule heating

Joule heating has been suggested as one of the origin of resistive state switching observed in manganites [134, 135]. Here we will discuss that such is not the case for the observed switching in the parent manganite samples. To check the contribution of Joule heating in our observed resistive switching, we have done a current level measurement as a function of time for one of the $LaMnO_3$ samples (at low temperature) and $GdMnO_3$ thin film (at room temperature) with two fixed voltages (in Fig. 3.18(a) and (b)). In $LaMnO_3$, we found nearly a constant sample current level with the time when a bias of 200V

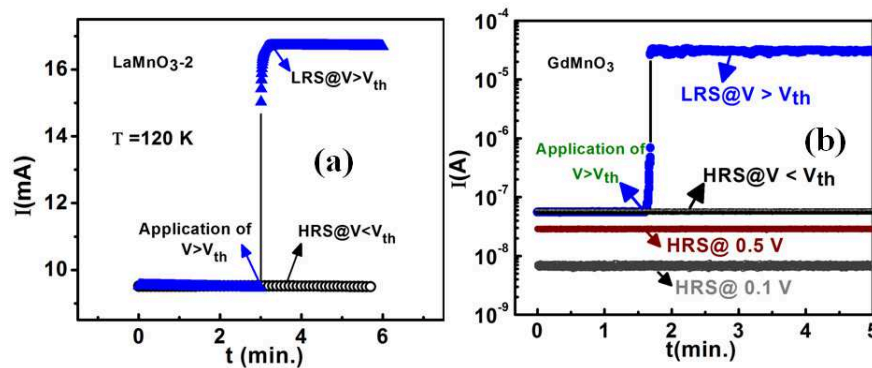


Figure 3.18 Time dependent current measurement on application of a switching voltage for (a) $LaMnO_3$ -2 and (b) $GdMnO_3$ thin film.

is stepped to 305V. These are voltages just before and after the resistive state switching. If there is any substantial Joule heating that has occurred in the sample, sample resistance and hence the current in the

sample would drift with time. We apply 200V in the sample for nearly 3 minutes and then suddenly step the bias to 305V (blue arrow at $t \approx 3$ min.) and we observe that the sample current switches to higher level but stays constant with the time. Secondly to avoid the Joule heating (as we applied high bias in LaMnO₃, we have performed the $I - V$ measurement with pulsed voltage of 50% duty cycle. We have also done a calculation for the maximum temperature rise in the sample (LaMnO₃) due to the Joule heating considering the heat generated in the sample (in ON pulse) and dissipated from the sample (in OFF pulse) through the metal base via the GE-Varnish and thermal grease [90] (for detail calculation see Appendix A). We found that the temperature rise even at the lowest temperature is ≤ 4 K with maximum power applied. These rule out any substantial contribution of the Joule heating to the observed result.

To overrule the effect of Joule heating in GdMnO₃, we have measured the current as a function of time with different applied biases ($V \ll V_{th}$ to $V > V_{th}$) (shown in Fig. 3.18(b)). From Fig. 3.18(b), we see that for biases below V_{th} (e.g, 0.1, 0.5 and 1V), the current remains constant over the duration of measurements and shows no drift or resistive switching. It shows that the HRS is stable as long as $V < V_{th}$. When we apply a bias greater than the switching voltage (V_{th} which is marked by blue arrow in Fig. 3.18(b)) at $t \approx 1.5$ min. (before the bias was at $V < V_{th}$), the current immediately shows a jump by nearly three orders (in LRS state). As long as the bias is not changed back to below V'_{+th} , the LRS state is maintained and it is independent of time. Thus the LRS like the HRS state is also a stable state. The power at the time of switching for GdMnO₃ is $250\mu W$ (see Fig. 3.9(a)). The maximum temperature rise ΔT was estimated to be ≈ 2.5 K, which was calculated using the thermal boundary resistance between the substrate and the thermal bath. The temperature rise ΔT is thus too small to be of any relevance.

From our time dependent current measurement in LaMnO₃ and GdMnO₃, we rule out the effect of joule heating as the resistance in the switched state does not show any drift [90] and the temperature rise at maximum applied power is too small to have any effect. We have also showed (for LaMnO₃-2) that when data are taken with a constant bias the material makes a sharp transition from a lower resistance state to a higher resistance state at low temperature (in Fig. 3.10) which is opposite to what

one expects if the entire effect is due to Joule heating.

3.8 Conclusion

In summary, we observe a sharp transition in the resistive state of nominally pure LaMnO_3 single crystals at temperatures below 300K and in GdMnO_3 thin film at room temperature with a moderate applied bias. The field induced resistive state transition seen in this work is different from those seen in manganites with higher level of Mn^{4+} content. Thus the mechanisms proposed for them are not applicable for the observations made in these parent manganites. In this case the transition occurs between the polaronic insulating state of LaMnO_3 and GdMnO_3 to a bad metallic phase that has a nearly temperature independent resistivity.

All the three crystals and the film, despite differences in absolute values of resistivities, show qualitatively similar bias induced resistive transitions. At lower temperatures change at the transition can be as high as four orders of magnitude and for GdMnO_3 it is nearly three orders in room temperature. The transition becomes softer and eventually is not observed above 280K for LaMnO_3 . Similar experiments were also carried out on single crystal of Sr substituted $\text{La}_{0.9}\text{Sr}_{0.1}\text{MnO}_3$. In this case we find that the increase of Mn^{4+} content on Sr substitution inhibits the resistive state transition.

The observation has been explained as bias driven percolation type transition between the two coexisting phases mentioned above. The applied bias can change the mobile fraction f of the bad metallic phase leading to a percolation type transition to the lower resistive state when the fraction f crosses a critical volume fraction for percolation transition. The mobile fraction f (as estimated from the experimental data) has an activated dependence on temperature with activation energy $\approx 200\text{meV}$. The fraction f has a dependency on the field as $f = C \exp(\frac{-E_0}{E})$. This leads to rapid enhancement of f on application of field leading to a sharp transition in the resistive states. Likely microscopic mechanisms for co-existing phases have been proposed based on recent suggestions for appearance and existence of such phases. It appears that a bad metallic minority phase can co-exist in nominally pure LaMnO_3 and GdMnO_3 or in parent perovskite due to charge transfer instability driven charge disproportionation [89].

Chapter 4

Magnetoresistance of nominally pure LaMnO₃ single crystals.

In this chapter, we investigate MR in nominally pure LaMnO₃. Three single crystals have been used for the investigation and the MR behaviour in the three crystals were found to be different. Structural characterisations and magnetic measurements confirm that three LaMnO₃ single crystals have Orthorhombic crystal structure with orbital ordered ground state with antiferromagnetic insulating (AFI) phase. However, the magnetic measurements also show presence of FM clusters below certain temperature. The magnetic clusters arise from presence of small amount of Mn⁴⁺ ions which induce FM interaction in an otherwise AFI lattice. The presence of Mn⁴⁺ has been detected by XPS and EELS. Samples have low negative MR (~ 10-15%) at room temperature but on cooling below 200K, close to T_N, MR increases and in one of single crystal a large MR (~ 70%) at highest applied magnetic field (14T) has been observed. The observed MR in nominally pure LaMnO₃ is different from the conventional colossal MR found in chemically doped manganites with higher hole concentration.

4.1 Introduction

Magnetotransport in perovskite oxide manganites have been studied extensively as they exhibit colossal magneto-resistance (CMR) i.e. the large change in resistance with the externally applied magnetic field, mainly in the vicinity of insulator-metal transition temperature (T_{MI}) and it is generally observed in single crystals. The highest MR is found at $x \approx 0.33$ doping (x represents atomic fraction of divalent atom) $\text{La}_{1-x}\text{Ca}_x\text{MnO}_3$ and the T_{MI} shifts to higher temperature with the application of magnetic field. A number of theoretical models have been introduced to explain this MR behaviour in manganites but still we do not have full theoretical understanding of this mechanism. Zener double exchange mechanism can explain the FMM ground state in the optimum doping region of $x \approx 0.2 - 0.5$ [153–155] but it cannot explain the MR effect observed in low hole doped (x) manganites and it can not also explain the polaronic insulating state above T_C [156]. Manganites, having very low doping ($x < 0.1$), can also have small negative MR ($\leq 20\%$) due to the small concentration of Mn^{4+} [96, 157].

In this chapter, we have discussed MR in the low temperature insulating phase of parent LaMnO_3 single crystals. The single crystals are nominally pure and do not have any intentional substituted hole doping. The ground state of pure LaMnO_3 single crystals is A type antiferromagnet where the e_g spins are ferromagnetically coupled to each other in the ab plane while in subsequent ab spins are ordered antiferromagnetically (shown in Fig. 4.1) [158, 159]. Room temperature magnetic phases of these

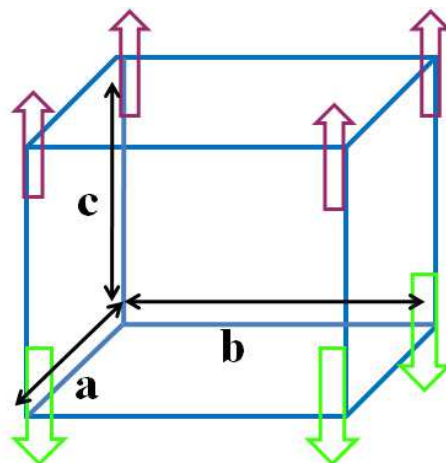


Figure 4.1 "A" type AFM structure of perovskite unit cell. Spins of Mn atoms are represented by upward and downward arrows.

single crystals are paramagnetic (PM). In pure LaMnO_3 , Mn should have a fixed valance of Mn^{3+} . Nominally pure LaMnO_3 (as grown crystal) has often a small amount of Mn^{4+} which can be due to the unintentional metal vacancy that occurs during crystal growth at high temperature ($\geq 2000^\circ\text{C}$) in an image furnace (discussed in detail in chapter 2). The metal vacancy creates Mn^{4+} and makes the oxygen strictly $3+\delta$ with $\delta \ll 1$. Another "natural cause" may be dynamic charge disproportionation which creates E-H pair ($\text{Mn}^{3+} + \text{Mn}^{3+} \rightarrow \text{Mn}^{4+} + \text{Mn}^{2+}$) in parent LaMnO_3 as discussed before. The Presence of Mn^{4+} , that changes effective oxygen stoichiometry, gives rise to FM interactions. Such interactions of very small Mn^{4+} create deviation from perfect AFM order leading to spin canting [159, 160]. As the Mn^{4+} concentration increases, the FM interactions lead to formation of isolated FM clusters, which may be detected by magnetisation and susceptibility studies. Eventually for Mn^{4+} fraction $\geq 12\%$, long range FM order sets in [14, 159].

In this chapter, we investigate MR in nominally pure LaMnO_3 single crystals where FM cluster formation may occur depending on the single crystal growth condition. The MR in hole doped manganites ($x > 0.1$) is adequately investigated (discussed in chapter 1), however there is no investigation in pure (or nominally pure) LaMnO_3 single crystals. One reason may be that nominally pure LaMnO_3 being an insulator, its resistivity can be very high making transport measurements difficult. Other reason may be the expectation that pure AFM order LaMnO_3 will not show any MR. In this chapter our investigation has shown that nominally pure LaMnO_3 has a reasonable MR and which may even be large beyond certain temperature. We have linked the observed MR to the presence of FM cluster in an AFM matrix. We used a phenomenological model to add quantitative value to our analysis.

The magnetotransport measurements were performed on three nominally pure LaMnO_3 single crystals ($\text{LaMnO}_3\text{-1}$, $\text{LaMnO}_3\text{-2}$, $\text{LaMnO}_3\text{-3}$) having slightly different oxygen stoichiometry. All the three single crystals behave as an insulator (at low current or low bias) throughout the whole temperature range (120K-300K) and show AFM ground state. We found that three single crystals have different kind of MR behaviour and one of them ($\text{LaMnO}_3\text{-1}$) has the largest negative MR ($\approx 70\%$) around the Neel temperature (T_N). We established the presence of FM cluster by magnetic susceptibility measurement (in d.c. & a.c. method). The reason of MR behaviour in three single crystals is attributed

to the presence of different volume concentration of FM cluster (and also having different interaction strength) due to the intrinsic stoichiometric imbalance and charge disproportionation (CD) phenomena.

4.2 Investigation of presence of Mn^{4+} in the three $LaMnO_3$ single crystals

In this section we will discuss the process of detection of Mn^{4+} present in the three $LaMnO_3$ single crystal as it plays an important role in the MR behaviour in manganites. To find out the presence of Mn^{4+} in these samples, we have performed several characterisation techniques like high temperature X-ray diffraction (HTXRD), electron energy loss spectroscopy (EELS) and X-ray photoelectrons spectroscopy. HTXRD, EELS and XPS measurements are generally very useful to find out the very small amount of Mn^{4+} ($< 10\%$). In the next subsections, we will discuss about these characterisation measurements on the three $LaMnO_3$ samples. As discussed in chapter 2, we have also done EDAX in three $LaMnO_3$ samples to confirm that no impurity element present except La, Mn and O.

4.2.1 High temperature XRD of $LaMnO_3$ single crystals and variation of structural transition

Parent $LaMnO_3$ has a John-Teller (JT) distorted orthorhombic structure at 300 K. On heating, orthorhombic structure gradually disappears $> 800K$ by transforming to a Rhombohedral (R) structure [6, 161–163]. This structural transition temperature (T_R) decreases with the increase in Mn^{4+} concentration [7, 50, 51, 139, 177]. High temperature XRD (HTXRD) is thus a good check to confirm the presence of Mn^{4+} in parent $LaMnO_3$. The HTXRD curves for all the three single crystals in the temperature range from $25^\circ C$ to $800^\circ C$ are given in Fig. 4.2(a),(b) and (c). In room temperature all the three samples show an Orthorhombic structure with the 100% peak at 32.5° with hkl value (1 1 2) and two nearby low intensity peaks at (0 2 0) and (0 2 1) which are marked as black arrow in the graph (in Fig. 4.2(a),(b) and (c)). Two low intensity orthorhombic peaks gradually vanish at 773K for $LaMnO_3$ -1 (Fig. 4.2(a)), 1050K for $LaMnO_3$ -2 (Fig. 4.2(b)) and 1073K for $LaMnO_3$ -3 (Fig. 4.2(c))

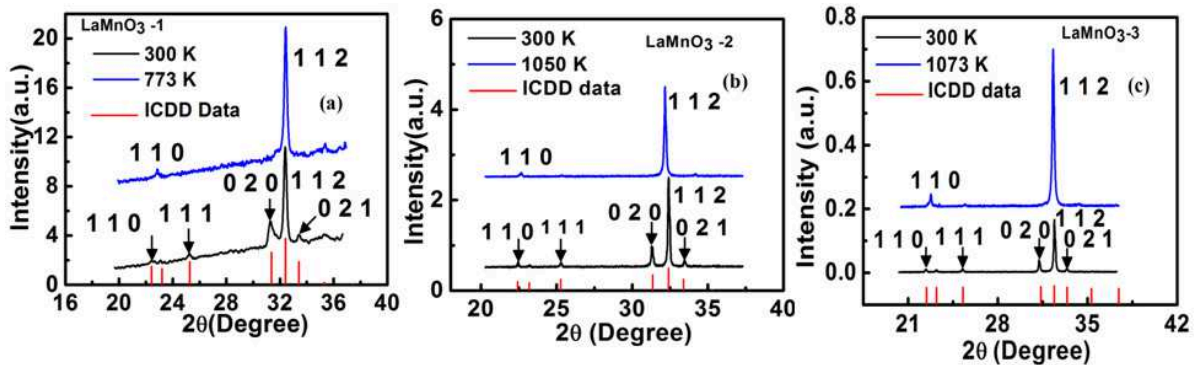


Figure 4.2 (a), (b) and (c) High temperature XRD of three $LaMnO_3$ single crystals.

which is a clear indication of structural transition from orthorhombic to rhombohedral and all the three samples have nearly perfect stoichiometry. As $LaMnO_3$ -1 has lower T_R than other two crystals, it has higher Mn^{4+} content in respect to the other two.

4.2.2 XPS and EELS Analysis to check the mix valency of Mn

As $LaMnO_3$ -1 sample shows lower T_R than the other two samples, it is expected to have more Mn^{4+} concentration. We have done the core level XPS analysis of the sample to check the concentration of Mn^{4+} present in the sample. $Mn\ 2p_{3/2}$ core level XPS spectra of $LaMnO_3$ -1 is shown in Fig. 4.3(a). The Mn -2p XPS spectrum has two broad lines with maxima at 641.9 and 653.5 eV for $Mn\ 2p_{3/2}$ and $Mn\ 2p_{1/2}$ emission respectively and the binding energy of the $Mn\ 2p_{3/2}$ peak is usually used to study the Mn valence state in manganites [164]. The binding energy of Mn^{3+} is close to 641.2 eV and if there is a presence of Mn^{4+} in the system, $2p_{3/2}$ peak shows an asymmetry and Mn^{4+} peak develops at 642.5 eV. The percentage of Mn^{4+} is calculated by the ratio of the area under the curve for the Mn^{3+} and Mn^{4+} peak [119]. We have made the background correction (black line) of the experimental XPS spectra and then fit the spectra with a Gaussian-Lorentzian curve (red line) using the XPSPEAK-4.1 software as shown in the Fig. 4.3(a). The area under the curves of Mn^{3+} and Mn^{4+} shows that the content of Mn^{4+} (<10%) is $\ll Mn^{3+}$.

To find out the actual difference in Mn valence state in three nominally pure $LaMnO_3$ samples, we performed EELS analysis. Mn valence can be determined by the intensity ratio of L_3 and L_2 lines

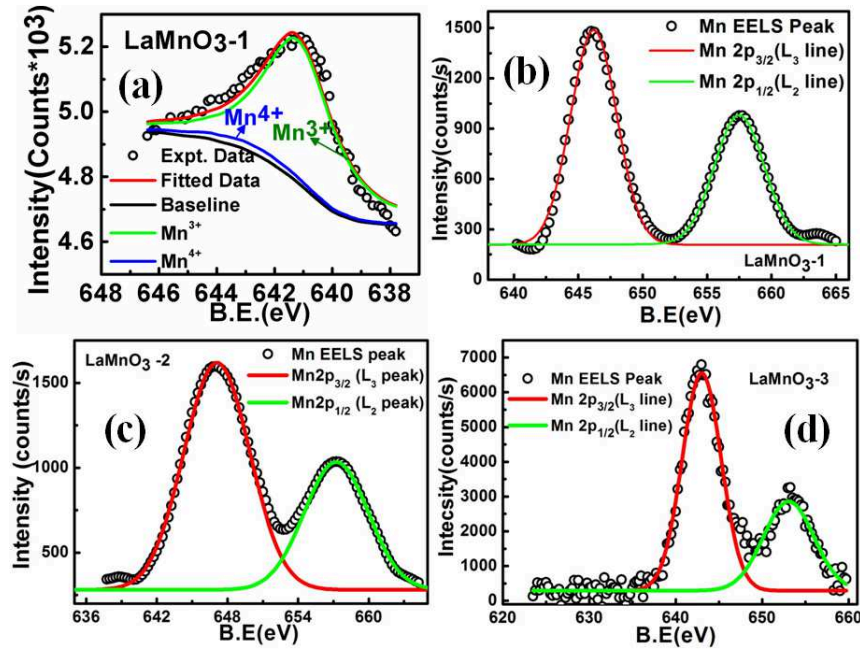


Figure 4.3 (a) XPS spectra of Mn $2p_{3/2}$ peak for LaMnO₃-1. (b) Mn EELS peak for LaMnO₃-1 (c) Mn EELS peak for LaMnO₃-2 and (d) Mn EELS peak for LaMnO₃-3.

originated from electronic transitions in between spin-orbit coupled states of $2p^{3/2}$ to $3d^{3/2}3d^{5/2}$ (L_3 peak) and $2p^{1/2}$ to $3d^{1/2}$ (L_2 peak). L_3 and L_2 peaks appear at the same binding energy for all the three samples shown in Fig. 4.3(b), (c) and (d) but having different intensity ratio. We have fitted each EELS spectra by multiple Gaussian peaks and found the L_3 (Red line) and L_2 (Green line) peaks for the three single crystals (in Fig. 4.3(b), (c) and (d)). We calculate $L_3:L_2$ from the ratio of the heights of the two peaks. L_3/L_2 values for LaMnO₃-1, LaMnO₃-2 and LaMnO₃-3 are ≈ 1.7 , 1.8 and 2.06. We compared these values with the calibrated values of L_3/L_2 for MnO, Mn₂O₃ and MnO₂ with Mn valence state +2, +3 and +4 (shown in Fig. 4.4) [165]. From the calibration curve, we found that Mn valence state in LaMnO₃-1 ≈ 3.1 , for LaMnO₃-2 ≈ 3.04 and it is ≈ 2.82 for LaMnO₃-3. EELS analysis implies that Mn valences in the three LaMnO₃ samples are mix valence which is the reason for existence of tiny volume of Mn⁴⁺. The existence of Mn⁴⁺ is due to the intrinsic doping (vacancy at the metal sites) during the crystal growth and the chemical formula for LaMnO₃ can be expressed as $\text{La}_{(1-x)}^{3+}[\text{Mn}_{(1-3x)}^{3+}\text{Mn}_{3x}^{4+}]\text{O}_3^{2-}$ where x is the fraction of cation vacancy. This type of self doped system is equivalent to $\text{La}\langle\text{Mn}\rangle\text{O}_{3\pm\delta}$ where $\langle\text{Mn}\rangle$ is the mix valence Mn and δ is the oxygen excess or

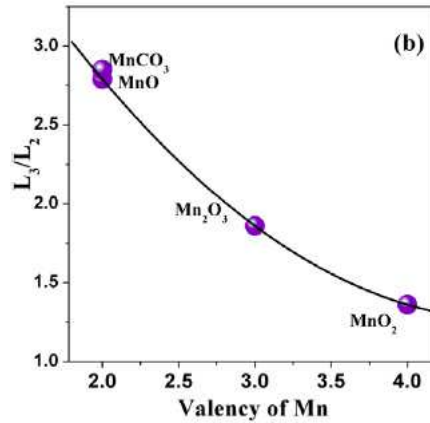


Figure 4.4 Calibration of Mn valence from the intensity ratio of L₃ and L₂ lines of different known Mn valence oxide compounds. Image form [165]

deficient. From the EELS data of the three LaMnO₃ samples, we know the average valence of $\langle \text{Mn} \rangle$ from which we have calculated δ . The δ values of the three LaMnO₃ samples are tabulated in table 4.1.

Table 4.1 Determination of δ in the three LaMnO₃ samples .

Sample	LaMnO ₃ -1	LaMnO ₃ -2	LaMnO ₃ -3
δ	0.05	0.02	-0.09

In this section, we found that three LaMnO₃ samples have a variation in Mn⁴⁺ (from HTXRD, XPS and EELS measurement) due the intrinsic doping. In the next section, we will discuss the magnetic properties of these LaMnO₃ samples due to this variation in Mn valence.

4.3 D.C. Magnetisation in the three LaMnO₃ samples

HTXRD and EELS analysis in the three single crystals confirm the presence of slightly higher Mn⁴⁺ in LaMnO₃-1 than the other two single crystals. It is established that the amount of Mn⁴⁺ is not large enough that one may see onset of FM order. But it is large enough that might lead to formation of isolated FM clusters. Temperature dependent magnetisation ($M - T$) measurements in the three LaMnO₃ samples were done to check the formation of magnetic moments in the PM as well as AFM

phase. $M - T$ measurements were performed both in zero field cooled (ZFC) and in field cooled (FC) modes. In ZFC, the sample is cooled to lowest temperature without applying any external magnetic field then a small field is applied to measure the temperature evolution of the magnetisation of the sample as it is warmed up. The sample is cooled under a finite magnetic field in FC method then warmed up and the magnetisation is measured as function of temperature in the constant applied field. In the ZFC mode, the moment of the clusters will be locked by the random anisotropy field (H_A) if the applied magnetic field at lowest temperature is $< H_A$. Due to this, moment will be low till the temperature is raised enough to unlock the moments from the anisotropy field. In FC mode, since the field is applied

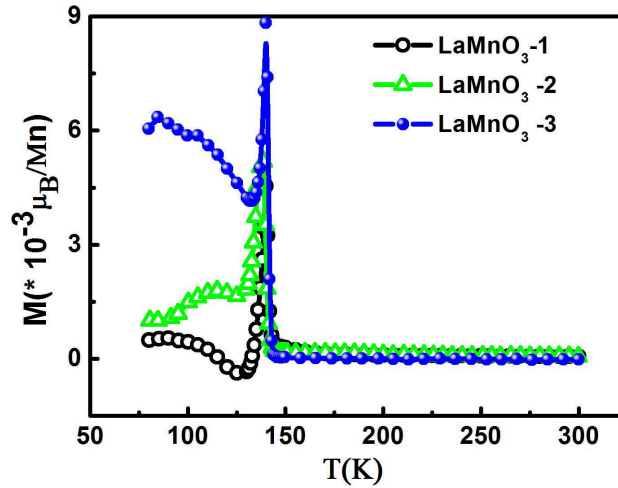


Figure 4.5 Zero field cooled $M - T$ data of the three LaMnO_3 samples with 20 Oersted field.

at higher temperature (above the temperature where cluster form), it will show larger magnetisation. In Fig. 4.5, we have shown the ZFC data with 20 Oe field for the three LaMnO_3 samples. ZFC data in the three LaMnO_3 samples show a peak at temperature $T \approx 143\text{K}$ exhibiting a sharp peak. We assign this peak as a signature of PM to AFM phase transition which is close to the reported value of $T_N = 140\text{K}$ for LaMnO_3 [159]. In Fig. 4.6, we have shown the M-H curve of the three LaMnO_3 samples at $T = 135\text{K}$ which is just below T_N . Data were taken for field up to 1.6T. All the three single crystals show a soft FM hysteresis loop with non saturated magnetic moment even up to highest applied field. All the three LaMnO_3 samples have low and asymmetric coercive field ($\pm H_c$) and exchange field (H_E) which are tabulated in table 4.2.

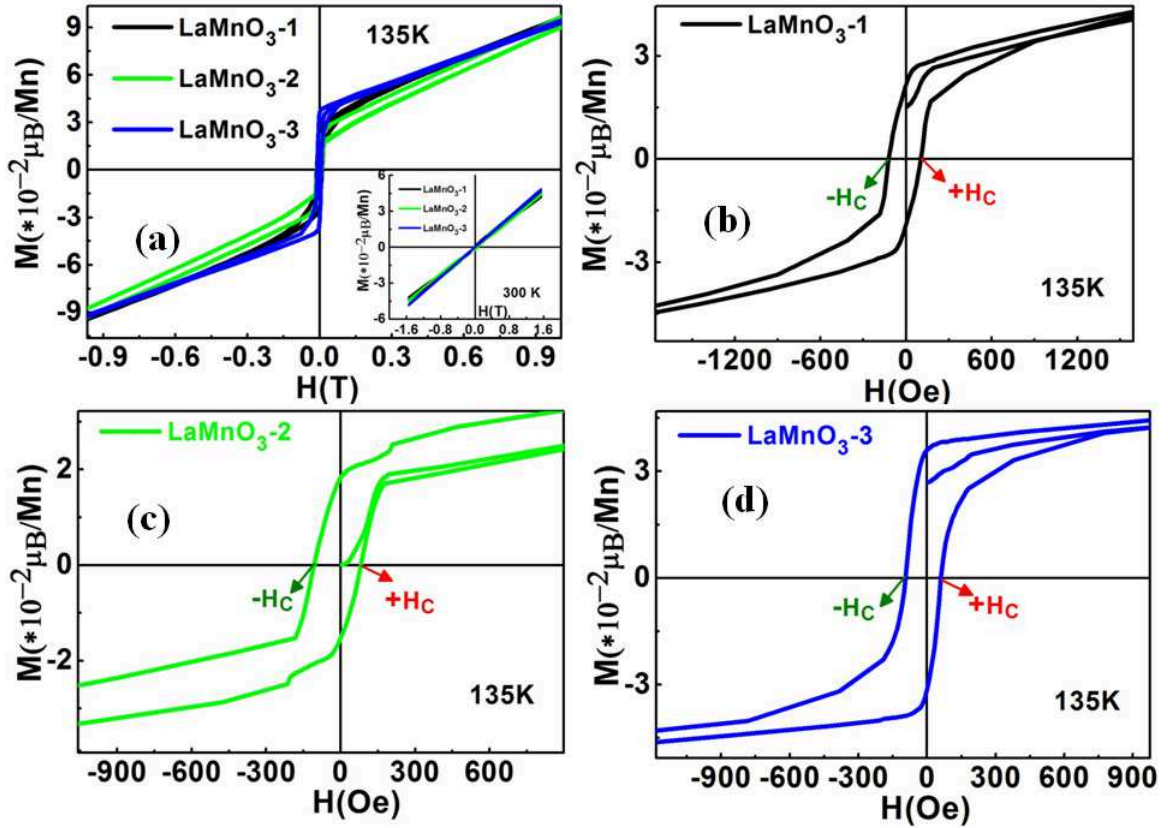


Figure 4.6 (a) $M - H$ curve for all the three LaMnO_3 samples below T_N . Inset shows the $M - H$ curve at 300K. Ferromagnetic hysteresis loop at lower field for (b) LaMnO_3 -1, (c) LaMnO_3 -2 and (d) LaMnO_3 -3.

Table 4.2 Coercive and exchange fields for three LaMnO_3 samples from Fig. 4.6.

Sample	$+H_c$ (Oe)	$-H_c$ (Oe)	$H_E = \Delta H_c$ (Oe)
LaMnO_3 -1	109	121	12
LaMnO_3 -2	84	108	24
LaMnO_3 -3	60	98	38

The asymmetric coercive field generally occurs when materials with FM-AFM interfaces are cooled through the Neel temperature (T_N) leading to an anisotropy (exchange bias) in FM phase [166]. The phenomenon of exchange bias occurs due to exchange anisotropy created at the interface between an AFM and an FM material [166,167]. The hysteresis loop shift is generally known as exchange bias field

H_E . The presence of H_E stabilizing the fact that there is a presence of small FM moment in the AFM phase of the three LaMnO₃ samples. From table 4.2, it is clear that LaMnO₃ -1 has the highest coercive field and lowest exchange field than the other two single crystals which establishes the presence of higher FM moment. Due to the lower amount of Mn⁴⁺ and the FM moment in LaMnO₃ -3, it has low coercive field. However, the exchange bias seen in LaMnO₃ -3 is the largest as it has strongest AFM interaction. M-H curve for all the three samples show PM phase at 300K (in the inset of Fig. 4.6(a)).

To check the evaluation of FM moment with the applied field, we measured the $M - T$ curves of all the three samples with varying the field from 10 Oe to 1.6T. $M - T$ curves with different applied magnetic fields for all the three samples are shown in Fig. 4.7(a), (b) and (c). From Fig. 4.7(a), 4.7(b)

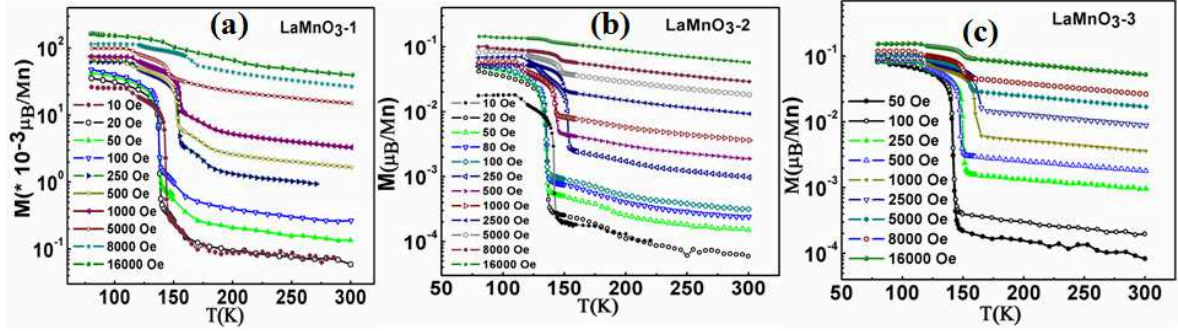


Figure 4.7 $M - T$ curves in the presence of different applied magnetic field (a) for LaMnO₃-1 ,(b) for LaMnO₃-2, and (c) for LaMnO₃-3.

and 4.7(c), we found that $\left[\chi = \frac{dM}{dH} \right]_T$ is larger at higher temperature and get reduced below T_N where the AFM phase develops in the samples. From the $1/\chi - T$ (derived from $M - T$) curve of LaMnO₃-1 for each field, we found a temperature (T_{CL}) where the curve deviates from Curie-Weiss behaviour (shown in Fig. 4.8). This denotes formation of FM clusters in the PM phase of the sample. In a similar way, we have determined T_{CL} in LaMnO₃ -2. In Fig. 4.9, we have shown the variation T_{CL} with different field. But we did not found any clear signature of cluster formation for LaMnO₃-3 (shown in Fig. 4.10) and it may be due to the small volume concentration of cluster (detail discussion in the next section). It is clear from the $\frac{1}{\chi}$ vs. T plot for the three LaMnO₃ samples, there is a presence of FM cluster in LaMnO₃ -1 and to a lesser extent in LaMnO₃ -2. In Fig. 4.11, we have shown the variance of T_{CL} for LaMnO₃ -1 and LaMnO₃ -2 with the applied field H . T_{CL} increases with the applied field and at the

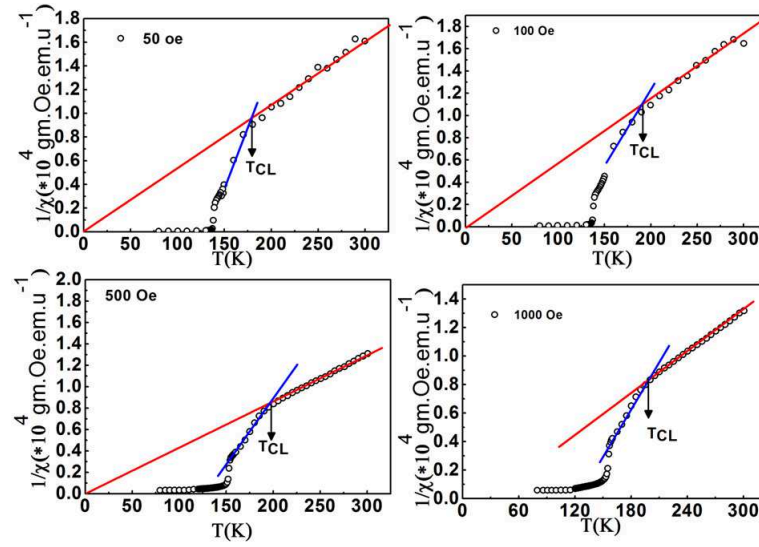


Figure 4.8 Determination of T_{CL} with different applied field (50 Oe, 100 Oe, 500 Oe and 1000 Oe) for LaMnO_3 -1.

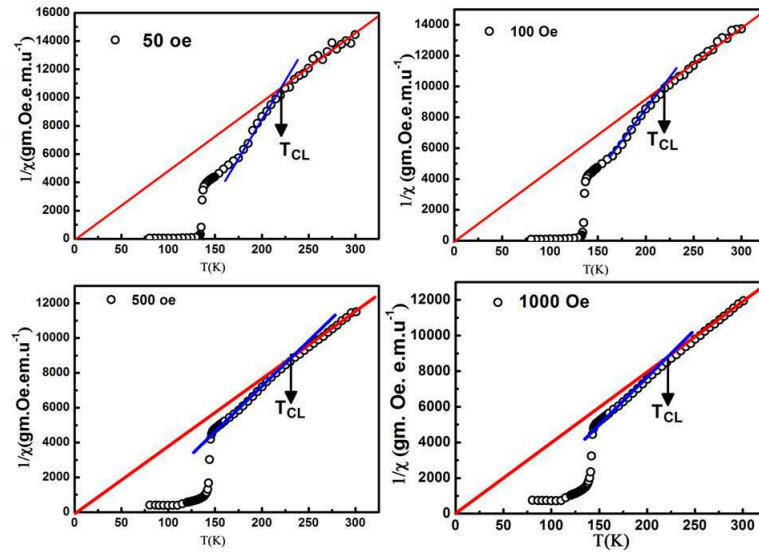


Figure 4.9 Determination of T_{CL} with different applied field (50 Oe, 100 Oe, 500 Oe and 1000 Oe) for LaMnO_3 -2.

highest applied field (1.6T), $\Delta T_{CL} \approx 90\text{K}$ for LaMnO_3 -1 and $\approx 50\text{K}$ for LaMnO_3 -2. The applied magnetic field actually increases the cluster formation temperature (T_{CL}). At lower field (< 500 Oe), there is a sharp rise in T_{CL} for LaMnO_3 -1 but it does not change appreciably for LaMnO_3 -2 up to this field. The change in T_{CL} with the applied field is much higher in case of LaMnO_3 -1. At 1.6 T, the cluster formation temperatures $T_{CL} \approx 230\text{K}$ (for LaMnO_3 -1) and 267K (for LaMnO_3 -2) which are

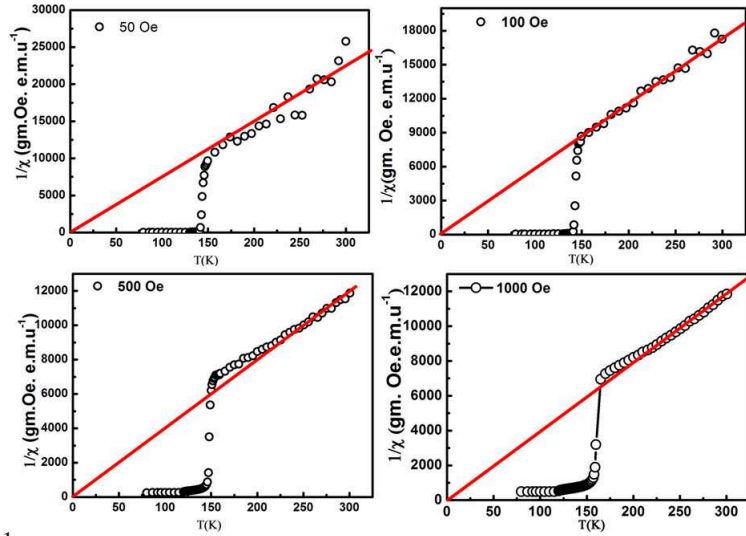


Figure 4.10 $\frac{1}{\chi}$ vs. T plot with different applied field (50 Oe, 100 Oe, 500 Oe and 1000 Oe) for LaMnO_3 -3.

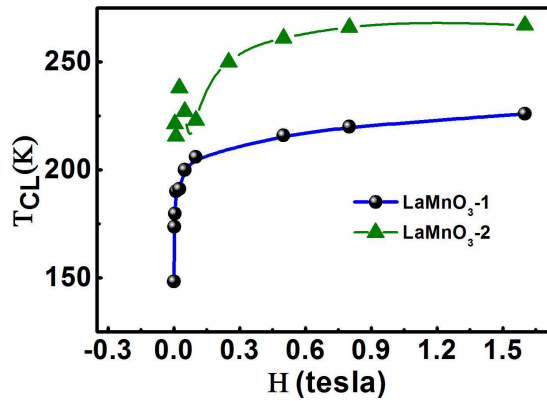


Figure 4.11 Variation of T_{CL} with applied field.

some what lower but close to the FM T_C in optimally doped $\text{La}_{0.67}\text{Ca}_{0.33}\text{MnO}_3$ ($T_C \approx 275\text{K}$).

From the $M - T$ curves (taken at different fields in FC method) of the three samples, it is clear that LaMnO_3 -1 and LaMnO_3 -2 have FM cluster formation at higher temperature or in the PM phase. The field cool $M - T$ data with various magnetic field (10 Oe to 1.6T) show existence of FM cluster formation temperature higher than T_N for LaMnO_3 -1 and LaMnO_3 -2 but it is not found in case of LaMnO_3 -3. M-H curves of the three LaMnO_3 samples show a finite but small FM hysteresis loops with non saturation magnetic moments below T_N even for a field of 1.6T. This shows the dominant contribution of the AFM order in the samples. The FM clusters are embedded in the AFM matrix and

the FM clusters have a short range order. We have tabulated the moment of the three samples at highest (1.6T) and one of the lowest (50 Oe) field in table 4.3.

Table 4.3 M in μ_B/Mn for the three LaMnO₃ samples at $T < T_N$ and $T > T_N$

Sample	M at 1.6T		M at 50 oe	
	135K	300K	135K	300K
LaMnO ₃ -1	0.13	0.04	13×10^{-3}	13×10^{-5}
LaMnO ₃ -2	0.13	0.06	6×10^{-3}	1.5×10^{-4}
LaMnO ₃ -3	0.13	0.05	30×10^{-3}	8×10^{-5}

From the field dependent $M - T$ data (in FC method) and $M - H$ curve, it is evident that size and volume concentration of the FM cluster are different in the three LaMnO₃ samples.

4.4 A.C. susceptibility of the three LaMnO₃ samples

To find out the different volume concentration of FM clusters in the three samples, we performed frequency dependent (11Hz-1kHz) susceptibility measurement around T_N . In general a.c. susceptibility gives us a better understanding of the dynamics of the magnetic system in the time scale defined by the measuring frequencies. The magnetisation (M) of a system can be expressed in terms of applied magnetic field (H) as below:

$$M(H) = M_0 + \chi_1 H + \chi_2 H^2 + \chi_3 H^3 + \dots \quad (4.1)$$

,where M_0 is the spontaneous magnetisation, χ_1 is the linear susceptibility and χ_2, χ_3, \dots are the nonlinear susceptibilities. A.C. susceptibility measurement is very sensitive to the change in slope of $M(H)$ not to the absolute value unlike the case of d.c. magnetisation that measures M . This makes an effective tool to detect small shifts in magnetic order in the system. For very low frequency ($f \rightarrow 0$) of the applied magnetic field, a.c. magnetic measurement has equivalence the $\frac{\partial M}{\partial H}$ form the d.c. magnetisation.

In A.C susceptibility, we measured the real and imaginary parts of the susceptibility. The real and

imaginary susceptibility follow the relation:

$$\chi^{Real} = \chi \cos \phi; \quad \chi^{img} = \chi \sin \phi; \quad \chi = \sqrt{(\chi^{Real})^2 + (\chi^{img})^2} \quad (4.2)$$

, where ϕ is the phase and χ is the magnitude. χ^{img} represents the dissipative process in the sample. In general for conductive sample χ^{img} is due to the eddy current while relaxation of spins, domain wall motion gives rise to nonzero value of χ^{img} in an insulator. χ^{real} and χ^{img} are also very sensitive to thermodynamic phase changes.

For all the three samples, the real part of the linear a.c. susceptibility (χ_1^{Real}) is plotted with temperature at various frequencies (11Hz–1KHz) of a.c magnetic field of amplitude 40 Oe (shown in Fig. 4.12(a), 4.12(b) and 4.12(c)). χ_1^{Real} shows a peak similarly as ZFC magnetisation (at low field) and the

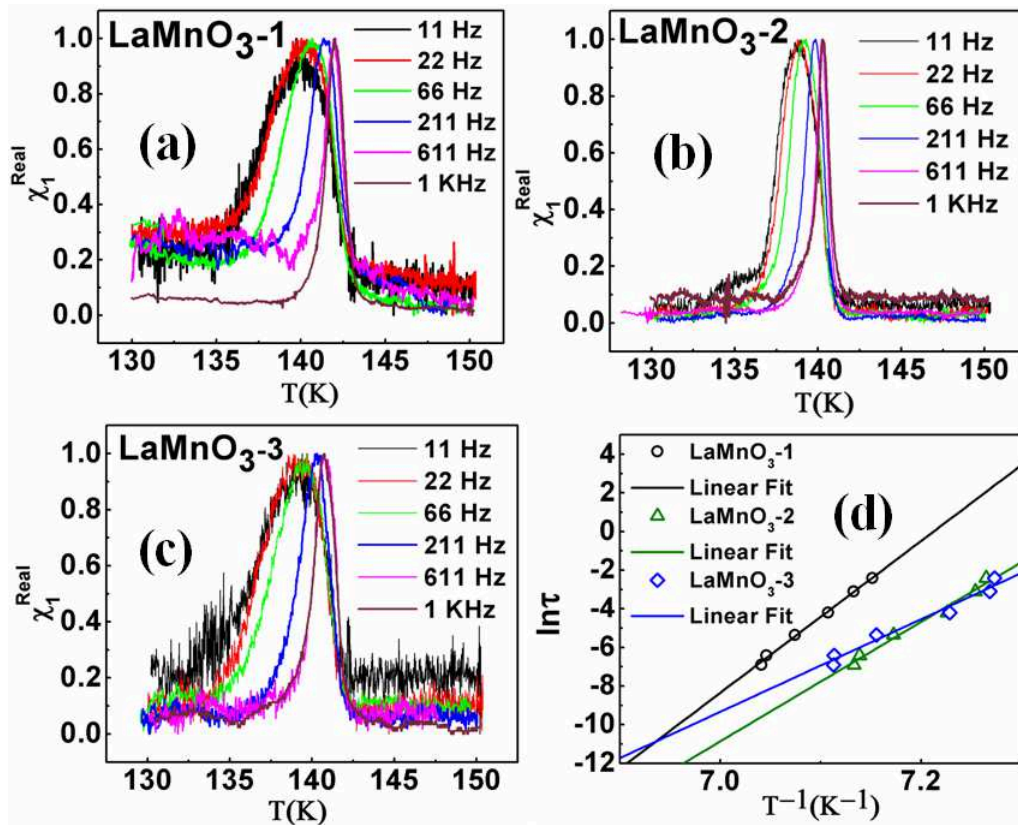


Figure 4.12 Frequency dependent real part of linear a.c. susceptibility (χ_1) (a) for LaMnO₃-1, (b) for LaMnO₃-2, (c) for LaMnO₃-3. (d) Activated fit of relaxation time (τ).

peak position (T_B) shifts with the applied frequency (f) for all the LaMnO₃ samples. T_B is the blocking

temperature. This kind of peak shift with the frequency or f dependence of T_B shows the absence of normal long range FM order [168]. A parameter Φ can be estimated from the f dependence of χ_1^{Real} as the following equation.

$$\Phi = \frac{\Delta T_B}{T_B \Delta \log_{10} f} \quad (4.3)$$

In general, the values of Φ in between 0.02-0.005 found in canonical spin-glasses, cluster-glasses, interacting superparamagnets and the value of ϕ is nearly two orders of magnitude lower than that observed in non-interacting superparamagnets [168–171]. We have fitted all the peaks with Gaussian function and found out the T_B with f . For all the LaMnO₃ samples, peak shift is nearly 2.5K when f is varied by nearly two orders from 11Hz to 1 KHz. Using the equation 4.3, the calculated value of Φ comes out nearly 0.01 which is in good agreement with that expected in samples with cluster. From the corresponding peak shift, we found out the relaxation time ($\tau = 1/f$) of the magnetic cluster in presence of a.c. field for all the three LaMnO₃ samples. τ shows an activated temperature dependence (shown in Fig. 4.12(d) for an ensemble of non-interacting spins and follows the Neel–Arrhenius law [172],

$$\tau = \tau_0 \exp\left(\frac{E_\tau}{k_B T}\right) \quad (4.4)$$

where τ_0 is the time constant corresponding to the characteristic attempt frequency and E_τ is the average anisotropy energy barrier. The calculated τ vs. T data from peak shift of χ_1^{Real} in Fig. 4.12(a), (b) and (c) is fitted with the equation 4.4 and we found the fitting parameters τ_0 (10^{-126} to 10^{-77} s) and E_τ (≈ 3.4 ev to 2eV) have nonphysical value for all the three LaMnO₃ samples. Neel–Arrhenius (NA) law signifies presence of interaction between the FM spin clusters. Absence of physical fitting parameters signifies that the samples may have cluster glass behaviour. We consider the Vogel-Fulcher (VF) law for interacting spin cluster dynamics as given below [168, 172],

$$\tau = \tau_0 \exp\left[\frac{E_\tau}{k_B (T - T_0)}\right] \quad (4.5)$$

where the temperature T_0 corresponds to the strength of inter-cluster interaction. We have fitted τ vs. T_B data by equation 4.5 which is shown in Fig. 4.13(a), (b) and (c).

Though the values of τ_0 improve from that obtained from NA fitting, still it is much lower than the

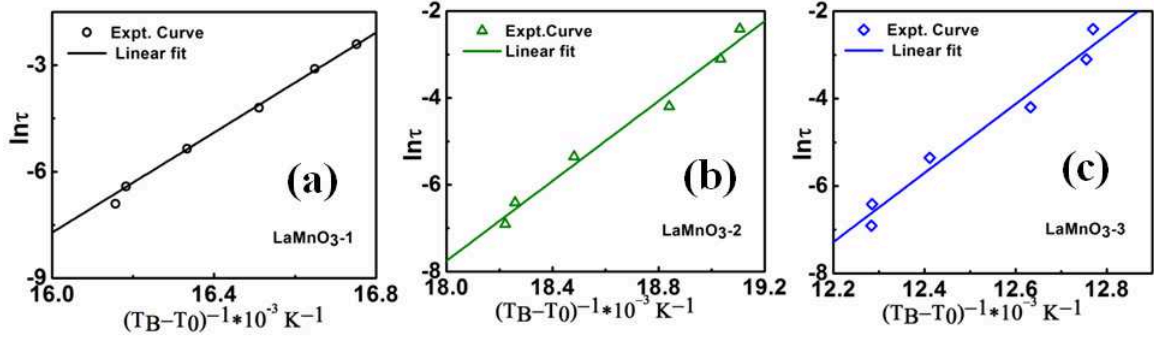


Figure 4.13 Fitting of Vogel-Fulcher equation for (a) LaMnO_3 -1, (b) LaMnO_3 -2 and (c) LaMnO_3 -3.

Table 4.4 Fitting parameters from VogelFulcher equation.

Sample	τ_0 (s)	E_τ (eV)	T_0 (K)
LaMnO_3 -1	4.5×10^{-53}	0.6	80
LaMnO_3 -2	4.2×10^{-40}	0.4	85
LaMnO_3 -3	9×10^{-40}	0.7	59

conventional spin glass system but qualitatively supports the existence of FM cluster with significant interactions. This FM cluster interactions are not strong enough to make it a spin glass and FM moments will not freeze out even at very low temperatures. But analysis of the frequency dependent a.c. χ measurement suggests that there is a formation of FM cluster and there is a variation of FM cluster in the three LaMnO_3 samples. From table 4.4, we can see that inter cluster interaction strength (T_0) is higher in LaMnO_3 -1 and LaMnO_3 -2 but it is lower in LaMnO_3 -3 where cluster formation is less significant. The inter cluster interaction strength will depend on the cluster volume present in the three LaMnO_3 samples. A.C. susceptibility in the three samples clearly indicates the formation of FM cluster with different strength in the three LaMnO_3 single crystals.

4.5 Magneto-transport measurements

In this section, we will discuss the effect of magnetic field on the electronic transport on the three LaMnO_3 single crystal samples. From the magnetisation measurement in the three LaMnO_3 samples,

we found the clear evidence of FM cluster formation with different strength. We will now see that in the presence of applied magnetic field how do they affect the electronic transport. We have performed MR measurements on the three LaMnO_3 samples in four probe configuration (with very low current of $1\mu\text{A}$) with applied magnetic field up to 14T. To find out the dependence of the MR on the applied field, we did the MR vs. H measurement with a fixed bias current at different temperatures varying only the magnetic field from 0T to 8T.

4.5.1 Temperature dependent Magnetoresistance of the three LaMnO_3 single crystals

We have done the temperature dependent resistivity measurement from 1200K to 300K. The $\rho - T$ curves in presence of the applied field for LaMnO_3 -1, LaMnO_3 -2 and LaMnO_3 -3 are shown in Fig. 4.14(a), 4.14(b) and 4.14(c). All the three single crystals show highly insulating behaviour and up to

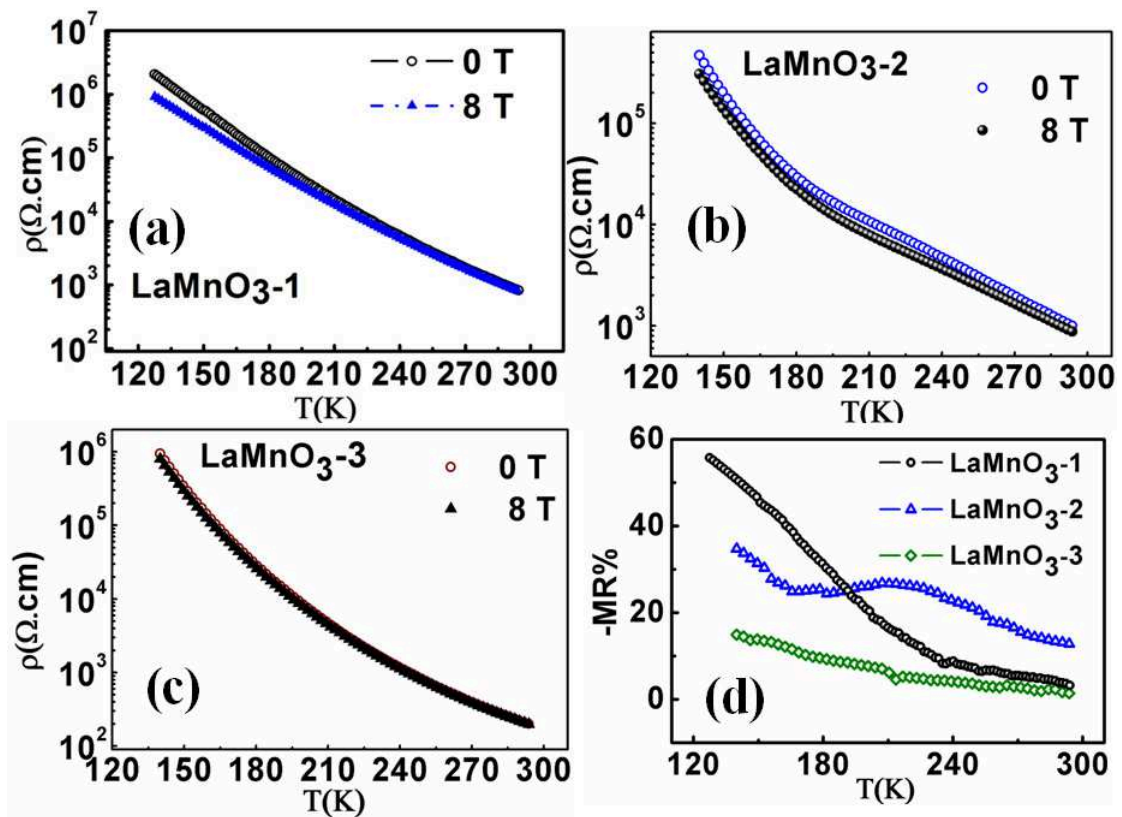


Figure 4.14 $\rho - T$ curve in the presence of magnetic field (a) for LaMnO_3 -1, (b) for LaMnO_3 -2, (c) for LaMnO_3 -3. (d) Temperature dependent MR for the three samples at 8T field.

250K, $\rho - T$ curves at 0T can be fitted with adiabatic polaronic model

$$\rho = \rho_0 T \exp\left(\frac{E_a}{k_B T}\right) \quad (4.6)$$

, where ρ_0 is related to the hopping frequency, length and dimensionality and E_a is the activation energy [90]. All the three samples have high E_a around 210-230meV (discussed in chapter 1) which match well with previously reported data [140].

All three single crystals show negative MR under the applied magnetic field. However, the magnitude of MR and T dependence are distinct in the three single crystals. MR increases for all the three LaMnO_3 single crystals as T decreases (shown in Fig. 4.14(d)). The change (decrease) in resistance due to the applied magnetic field or MR of the samples are defined as $\frac{\Delta\rho}{\rho_0} = \frac{\rho(H) - \rho(0)}{\rho(0)}$, where ρ_H and ρ_0 are the resistivities with and without field respectively. Highest MR of nearly 60% was observed for LaMnO_3 -1 at low temperature while it is $< 5\%$ near room temperature (shown in Fig. 4.14(d)). LaMnO_3 -1 and LaMnO_3 -3 have nearly same MR at 300K. However around T_N , LaMnO_3 -3 has three times less MR. In LaMnO_3 -2, the temperature dependence of MR is different. It shows a shallow peak near 220 K and has MR of 20% at 300K. The temperature variation of MR observed in LaMnO_3 samples is different from that observed in highly ($x \geq 0.2$) doped manganites, where there is well developed long range FM order.

4.5.2 Field dependence of MR

To find out the dependence of MR on the applied field (H), we have measured the R-H curve of the three LaMnO_3 samples sweeping the magnetic field from -8T to +8T at several fixed temperatures (140K-250K). In Fig. 4.15, we have shown the change in the resistance of the three LaMnO_3 samples by plotting $\frac{R}{R(0)}$ vs. H (where $R(0)$ is R for $H = 0\text{T}$) at $T < T_N$ and $T > T_N$ (for LaMnO_3 -1 and LaMnO_3 -2). For LaMnO_3 -3, $R - H$ curve is shown (in Fig. 4.15(c)) only for 140K as at higher temperatures MR is so small that it can not be perfectly measured and will introduce unnecessary error in the data. $R - H$ curve for all the three LaMnO_3 samples are symmetric. The change in the magnitude of resistance as well as the dependence of R on H is different for the three LaMnO_3 samples. The

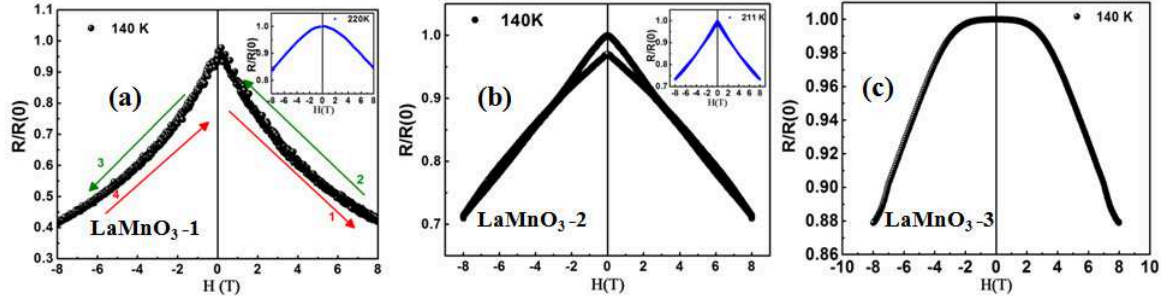


Figure 4.15 (a) $R-H$ curve for $\text{LaMnO}_3\text{-1}$ at $T < T_N$. Inset shows $R-H$ curve at $T > T_N$. (b) $R-H$ curve for $\text{LaMnO}_3\text{-2}$ at $T < T_N$. Inset shows $R-H$ curve at $T > T_N$. (c) $R-H$ curve for $\text{LaMnO}_3\text{-3}$ at $T < T_N$.

nature of the $R-H$ curves also change below and above T_N . Below T_N and at highest applied field (8T), the change in resistance for $\text{LaMnO}_3\text{-1}$ is much higher than the other two crystals. From the measured $R-H$ data at different temperatures (140K-250K), we found out the field dependence of MR (shown in Fig. 4.16). The magnitude of MR has a strong dependence on the applied field H . The nature

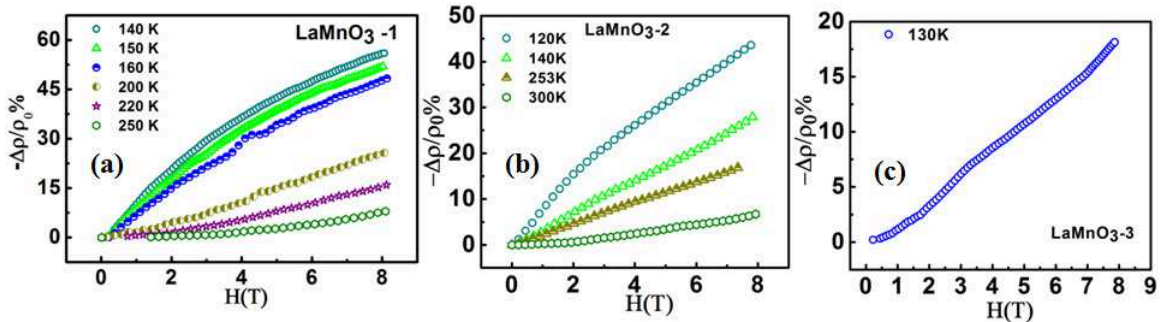


Figure 4.16 Magnetic field dependent MR for (a) $\text{LaMnO}_3\text{-1}$, (b) $\text{LaMnO}_3\text{-2}$ and (c) $\text{LaMnO}_3\text{-3}$.

of the field dependence of MR changes as the temperature changes. For $\text{LaMnO}_3\text{-1}$ and $\text{LaMnO}_3\text{-2}$ where the MR is substantial, the change in field dependence occurs around T_N signifying the effect of AFM order in magnetotransport. In Fig. 4.16(c), the change in MR with H at $T < T_N$ for $\text{LaMnO}_3\text{-3}$ is lower than that seen in the other two crystals as the AFM order in $\text{LaMnO}_3\text{-3}$ is more dominating. Another fact for different MR behaviour in the three samples is the presence of FM cluster in the AFM matrix in different strength which is evident from our magnetisation measurement. In the next section, we will explain the observed H and T dependence of MR considering FM cluster in an AFM matrix. We used a phenomenological model to add quantitative value to our analysis.

4.5.3 Phenomenological model for MR in LaMnO₃

In this subsection, we propose a model to explain the observed T and H dependence of MR in LaMnO₃. In particular, we would like to address the observation that the three crystals show different MR even if they are nominally same. The model we have used is phenomenological and is based on model of FM droplets in AFM matrix. The model was developed for explaining transport in low hole doped manganites [174]. We extend the model with the some modification as explained below. We explained the observed MR arising due to the formation of FM cluster (as it was confirmed by the a.c. and d.c. magnetisation measurement). The difference in MR in the three crystals is proposed to arise from the extent of size and concentration of FM clusters in them. The evolution of these FM clusters, with the applied magnetic field and temperature, determine the observed MR in three LaMnO₃ single crystals. We consider FM clusters of radius " a " in PM ($T > T_N$) and AFM ($T < T_N$) matrix in the three LaMnO₃ samples with the assumption that the concentration (n) of FM droplets is less than a critical volume (n_c) which is the percolation threshold and needed for long range FM order formation. The conduction of electron from one cluster to another will experience on the electrostatic interaction $A \approx \frac{e^2}{\epsilon a}$, and resistivity can be expressed as below [174],

$$\rho = C T \exp\left(\frac{A}{2\kappa_B T}\right) \quad (4.7)$$

, where C is a constant. This is similar to transport in granular composites with coulomb charging of the metal dispersed phase. A has a dependence on the applied magnetic field (H). H increases the cluster size " a " which decreases " A " and in first order it can vary with the field as:

$$A_H = A_0[1 - bH] \quad (4.8)$$

, where A_H is the modified interaction in the presence of field, A_0 is the interaction with zero field and b is a constant depending on the Heisenberg exchange integral $J(0)$, total spin S , gyromagnetic ratio g and Bohr magneton μ_B [174]. The constant b can be expressed as $b \approx \frac{g\mu_B}{5J(0)S}$. Using equations 4.7 and 4.8, we can derive the expression for MR due to the presence of FM clusters. MR can be expressed as

(negative sign represents the negative MR)

$$-MR = - \left[\frac{\rho(H) - \rho(0)}{\rho(0)} \right] = \left[1 - \exp \left(\frac{A_H - A_0}{2\kappa_B T} \right) \right] = 1 - \exp \left[-\frac{bA_0 H}{2\kappa_B T} \right] \quad (4.9)$$

, where $\rho(H)$ and $\rho(0)$ are the resistivities with and without the applied magnetic field. From equation 4.9, it can be seen that at lower T and higher H , the value of MR increases (as seen in Fig. 4.14(d) and 4.16). This model does not include the dependence of MR on the concentration (n) of FM clusters. There will be dependence of n on H and T and this will further affect the MR. To include the effect of FM clusters, we modify the equation 4.9 with two phenomenological parameters as discussed below,

$$-MR = \frac{-\Delta\rho}{\rho_0} = C \left[1 - D(H) \exp \left(\frac{-bA_0 H}{2\kappa_B T} \right) \right] \quad (4.10)$$

.The parameter C is taken as proportional to the maximum value of FM cluster moment present in a sample at $T \rightarrow 0$. This parameter is needed to acknowledge the fact that the highest value of MR occurs at low temperature. $D(H)$ is a parameter related to the cluster orientation at a finite field. We have fitted the equation 4.10 to MR vs. T curve for all the LaMnO_3 single crystals (shown in Fig. 4.17). From

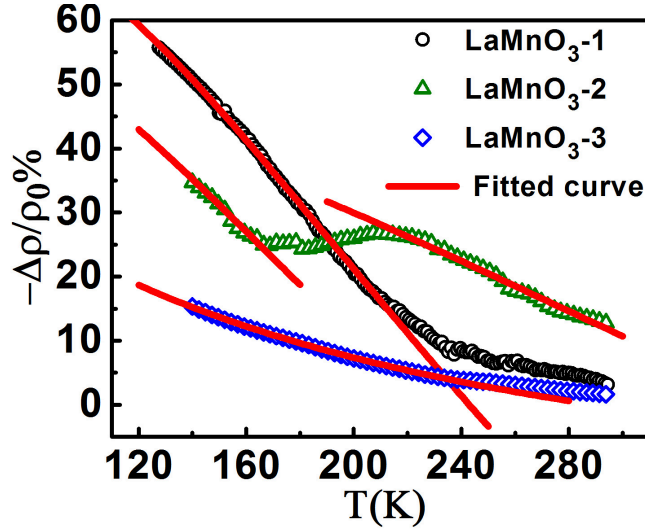


Figure 4.17 Fitting of FM cluster model (Eqn. 4.10) to MR vs. T curve for all the three LaMnO_3 samples at 8T field.

Fig. 4.17, it can be seen that LaMnO_3 -3 shows qualitatively similar MR dependence on T and the low MR in LaMnO_3 -3 reflects much less FM clusters compared to that in LaMnO_3 -1. The nature of the MR for LaMnO_3 -2 is different than the other two single crystals. It can be due to the reason

that LaMnO_3 -2 may have two types of FM clusters and these clusters dominate in different regions. We have fitted our model separately in these two regions. From Fig. 4.17, we can see that after a certain temperature ($T > 200\text{K}$) fitted curves deviate from the experimental curve for LaMnO_3 -1 and LaMnO_3 -3. For $T > 200\text{K}$, FM clusters are not fully formed and we cannot fit this region with our proposed model (which is discussed later). We have tabulated the fitting parameters for all the three samples in table 4.5. From table 4.5, it is clear that fitting parameters C , $D(H)$ and b vary in the three

Table 4.5 Fitting parameters from MR vs T data fitted with equation 4.10 for $H = 8\text{T}$.

Sample	C	$D(H)$	bA_0 (eVT ⁻¹)	A_0 (eV)	b (T ⁻¹)
LaMnO_3 -1	~ 80	~ 3.8	$\sim 7 \times 10^{-3}$	~ 3.5	$\sim 2 \times 10^{-3}$
LaMnO_3 -2	~ 43	~ 4.4	$\sim 1 \times 10^{-2}$	~ 3.5	$\sim 3 \times 10^{-3}$
	($T > 225\text{K}$)	($T > 225\text{K}$)	($T > 225\text{K}$)		($T > 225\text{K}$)
	~ 59	~ 4.4	$\sim 7.2 \times 10^{-3}$	~ 3.5	$\sim 2 \times 10^{-3}$
	($T < 180\text{K}$)	($T < 180\text{K}$)	($T < 180\text{K}$)		($T < 180\text{K}$)
LaMnO_3 -3	~ 37	~ 1.62	$\sim 3 \times 10^{-3}$	~ 3.5	$\sim 1 \times 10^{-3}$

LaMnO_3 samples. This is expected as the three samples show different MR behaviour. The parameters (C , $D(H)$ and b) related to clusters are distinctly higher in LaMnO_3 -1 compared to that in LaMnO_3 -3, reflecting larger contributions from FM clusters, as expected from magnetic measurements. $D(H)$ and b values of LaMnO_3 -2 is similar to LaMnO_3 -1 at $T < 180\text{K}$ but it differs above 225K . This is the reason LaMnO_3 -2 shows different nature of MR at $T > 225\text{K}$ than that seen in the other two single crystals.

As LaMnO_3 -1 has well formed clusters, we have further applied our proposed model (Eqn.4.10) to the MR vs. T data at different fields (8T and 14 T). The data are shown in Fig. 4.18(a). From the fitting of the MR vs. T curve in Fig. 4.18(a) to equation 4.10, we get the corresponding values of the fitting parameters (shown in table 4.6). It can be seen that Eqn. 4.10 fits well for both the data at 8T & 14T below certain temperatures (T_{CL1} & T_{CL2}) where cluster formation occurs.

From table 4.6, bA_0 and C are field independent parameters and D has a field dependence that increases

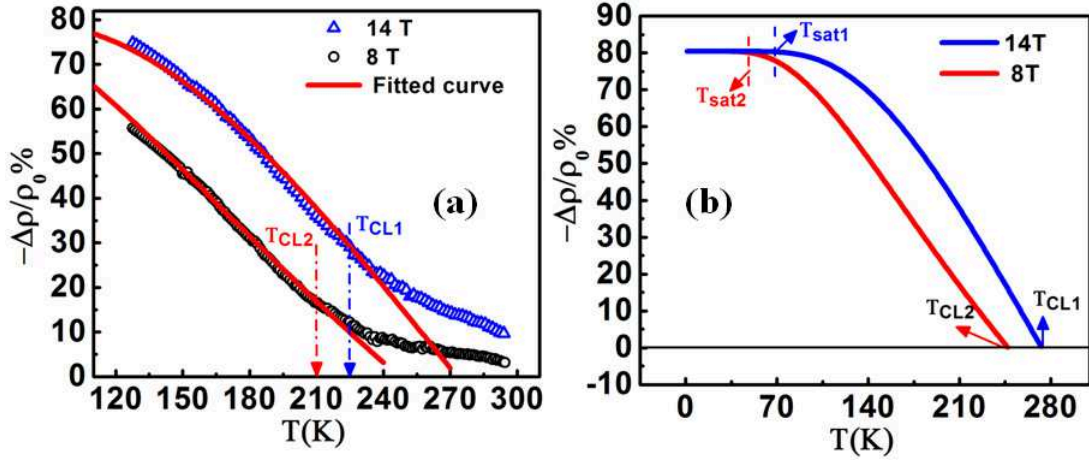


Figure 4.18 (a) MR vs. T data of LaMnO_3 -1 at 8T and 14T. Red curve shows the fitted curve with Eqn. 4.10. (b) Theoretically calculated curve using the Eqn. 4.10 with the fitting parameters from experimental curve.

Table 4.6 Fitting parameters from equation 4.10 for LaMnO_3 -1.

H (T)	C	$D(H)$	bA_0 (eVT $^{-1}$)
14	~ 80	~ 10	$\sim 7 \times 10^{-3}$
8	~ 80	~ 3.8	$\sim 7 \times 10^{-3}$

with H . We have found out that the H dependence of $D(H)$ can be written as $D(H) = 1 + pH + qH^2$ which is shown in Fig. 4.19. In LaMnO_3 , FM cluster formed due to the Mn^{4+} and $b \approx \frac{1g\mu_B}{5J(0)S} \approx$

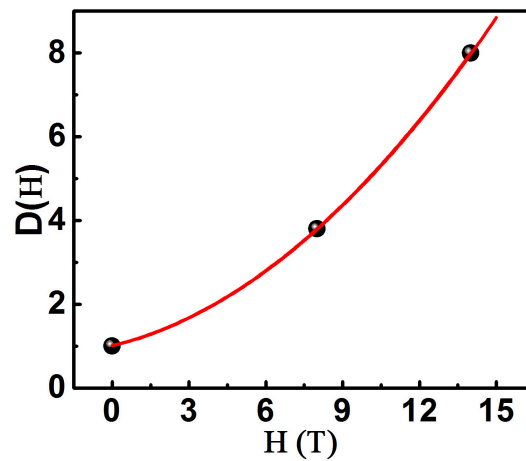


Figure 4.19 Dependence of $D(H)$ on H and fitted with $D(H) = 1 + pH + qH^2$.

$2 \times 10^{-3} \text{T}^{-1}$ can be calculated considering $g = 2$, $\mu_B = 5.8 \times 10^{-5} \text{eV T}^{-1}$, $J(0) \approx 100 \text{K}$ or 8.62meV and $S = 3/2$. Using the value of b , we found out that $A_0 \approx 3.5 \text{eV}$ which is comparable to the onsite electron-electron interaction found in manganites [174].

From Fig. 4.18(a), we can see that after a certain temperature (T_{CL1} , T_{CL2} are the cluster formation temperatures for 8T and 14T respectively) fitted curve deviates from the experimental curve. The signature of the T_{CL} is also found from our field dependent d.c. magnetisation in LaMnO_3 -1 (in Fig. 4.11). For $T > T_{CL}$, FM clusters are not fully formed and we cannot fit this region with our proposed model (Eqn. 4.10). It is also observed that higher applied magnetic field shifts the T_{CL} to higher temperature (and gets saturated at higher field) which is also found from Fig. 4.11. Due to the highly insulating nature of the sample, we could not measure the data below 130K. To find out the behaviour of MR at low temperature, we calculated the MR data from 1K to 280K using equation 4.10 with the fitting parameters tabulated in table 4.6 and the simulated MR vs. T curves are shown in Fig. 4.18(b). From Fig. 4.18(b), it can be seen that MR saturates at low temperature (T_{sat1} & T_{sat2}). This is expected due to the freezing of cluster moment. T_{sat} shifts to higher temperature at high magnetic field as magnetic moments get sufficient energy to overcome the thermal energy at higher temperature. These temperatures are theoretically the cluster formation temperatures (which is also observed in Fig. 4.18(a)). The above discussion shows that Eqn. 4.10 can be used to analyse the MR data in LaMnO_3 -1 which have very well formed FM clusters.

4.5.4 Role of $D(H)$ in the three LaMnO_3 samples

In the previous section, we found that the cluster orientation $D(H) = 1 + pH + qH^2$ in the three samples are different. To understand the role of $D(H)$ in the three samples, we have fitted our model (equation 4.10) to the MR vs. H curves of the three LaMnO_3 samples (shown in Fig. 4.20) below $T < T_{CL}$. We have fitted equation 4.10 to MR curves in LaMnO_3 -2 considering the values of bA_0 at $T < 180 \text{K}$ and $T > 225 \text{K}$ from table 4.5. The $D(H)$, p and q values for LaMnO_3 -1, LaMnO_3 -2 and LaMnO_3 -3 are tabulated below.

From table 4.7, it can be observed that p values for all the three LaMnO_3 samples are nearly similar but

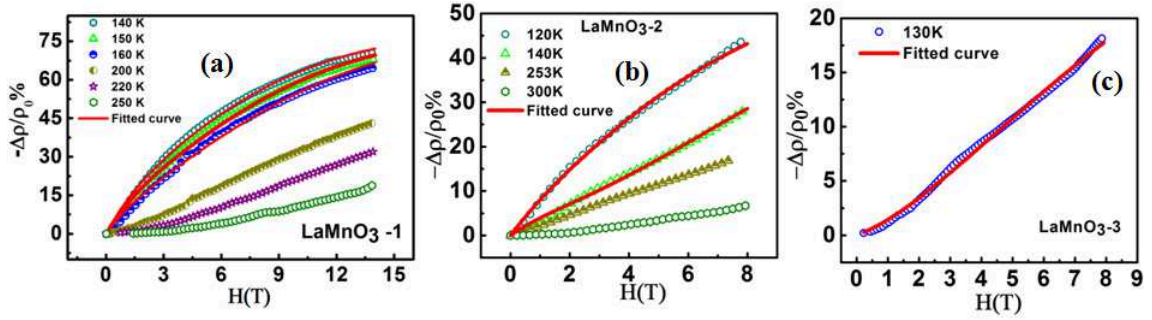


Figure 4.20 Magnetic field dependent MR for (a) LaMnO₃-1, (b) LaMnO₃-2 and (c) LaMnO₃-3. Red curve is the fitted curve with eqn. 4.10.

Table 4.7 Variation of $D(H)$ for three LaMnO₃ single crystals.

Sample	H (T)	$D(H)$	p	q
LaMnO ₃ -1	8	~ 3.8	~ 0.14	~ 0.024
LaMnO ₃ -2	8	~ 4.4 ($T < 180\text{K}$)	~ 0.19	~ 0.03 ($T < 180\text{K}$)
	8	~ 4 ($T > 225\text{K}$)	~ 0.16	~ 0.022 ($T > 225\text{K}$)
LaMnO ₃ -3	8	~ 2	~ 0.15	$\sim 4 \times 10^{-5}$

quadratic coefficient q is much smaller in LaMnO₃-3 than the other two LaMnO₃ single crystals. To understand the difference in $D(H)$ in the three LaMnO₃ samples, we have plotted $\frac{D(H)-1}{H} = p + qH$ vs. H in Fig. 4.21. We found that $\frac{D(H)-1}{H}$ for LaMnO₃-1 and LaMnO₃-2 vary similarly but it is

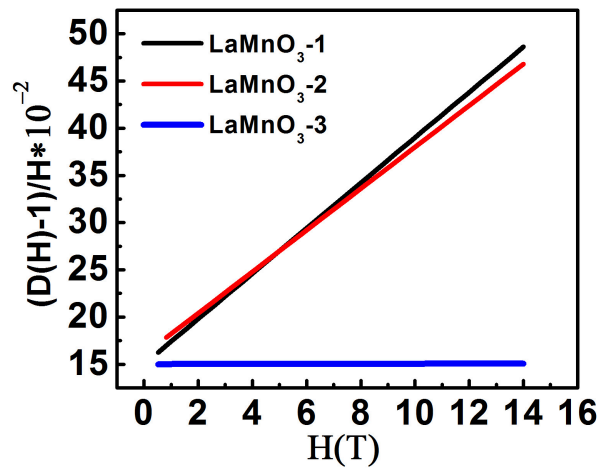


Figure 4.21 Variation of $\frac{D(H)-1}{H}$ vs. H for three LaMnO₃ samples.

nearly constant for LaMnO₃ -3. From Fig. 4.21, it is clear that orientation of FM clusters varies with H in LaMnO₃ -1 and LaMnO₃ -2 while it is nearly independent of field for LaMnO₃ -3. As the parameter $\frac{D(H) - 1}{H}$ is low for LaMnO₃ -3, we get low MR for LaMnO₃ -3 than the other two LaMnO₃ samples. In table 4.8, we have tabulated all the important parameters which actually determine the different MR behaviour observed in the three samples.

Table 4.8 Comparison of C , $\frac{D(H) - 1}{H}$, E_τ (eV), T_0 , T_R and $J(0)$ in the three LaMnO₃ samples.

Sample	C	$\frac{D(H) - 1}{H}$	E_τ (eV)	T_0 (K)	T_R (K)	$J(0)$ (meV)
LaMnO ₃ -1	80	~ 0.35 (8T)	~ 0.6	~ 80	773	~ 8
LaMnO ₃ -2	43	~ 0.42 (8T)	~ 0.4	~ 85	1050	~ 8
LaMnO ₃ -3	8	~ 0.12 (8T)	~ 0.7	~ 53	1073	~ 16

From table 4.8, it is clear that the difference in parameters like $\frac{D(H) - 1}{H}$ (measure of the cluster orientation), E_τ (the energy required to align moments), T_0 (the cluster interaction strength), T_R (structural transition temperature which is related to Mn⁴⁺ content) and exchange interaction energy $J(0)$ is responsible for the observed different MR behaviour.

4.6 Conclusion

Strongly correlated oxides are electronically inhomogeneous and this type of behaviour manifested better in the rare-earth manganites [175]. Thus these materials consist of different spatial regions with different electronic and magnetic orders and the phenomenon that has come to be known as phase separation and this is most clearly found in weakly doped manganites. Generally in parent manganites these special regions can be existed due to intrinsic doping or self doping. In LaMnO₃, intrinsic doping or self doping occurs due to the vacancy at the La site during the crystal growth which creates mix valence Mn (Mn³⁺ – Mn⁴⁺). The other natural cause is charge transfer (CT) instability driven dynamic charge disproportionation (Mn³⁺ + Mn³⁺ → Mn⁴⁺ + Mn²⁺) [89] even in the absence of any chemical doping (x). The presence of this CT instability driven EH pair (minor phase) in the conventional

polaronic insulating phase (major phase) leads to an phase-coexisted regions.

This minority phase (due to intrinsic doping and charge disproportionation effect) can have FM moment and form FM cluster in the PM and AFM phase of the sample and can be detected in magnetisation measurement. These kind of FM clusters have been observed in a complex study (a.c. magnetic susceptibility, magnetization, MR, and neutron diffraction) of slightly nonstoichiometric $\text{LaMnO}_{3+\delta}$ system [177]. The evaluation of these FM clusters with the applied magnetic field and temperature gives rise to MR in nominally pure LaMnO_3 . Depending on the concentration and strength of these FM clusters, MR can be different in the nominally pure LaMnO_3 samples. The FM ordering temperatures of these clusters can be close to T_N . With the application of applied magnetic field, size and concentration of the cluster increases which decrease the electrostatic interaction of the electron hopping from one cluster to another. This leads to increase in the conductivity of the sample under magnetic field or give rise to negative MR. The observed difference in MR behaviour in the three LaMnO_3 single crystals is due to the presence of different volume concentration of FM clusters. The concentration of the FM cluster can vary in the three LaMnO_3 samples for the presence of Mn^{4+} due to the different extent of self doping and charge disproportionation effect. This is also the reason that we observed different $\frac{\Delta\rho}{\rho}$ in case of resistive switching of three LaMnO_3 single crystals under applied electric field (Fig. 3.7(b) in chapter 3).

In conclusion, we have observed different MR behaviour in three LaMnO_3 single crystals and one of the sample (LaMnO_3 -1) shows a large MR ($\sim 60\%$) at low temperature. The MR in the three LaMnO_3 samples increases with the lowering of the temperature and saturates at very low temperature. The observed magneto transport, in the three nominally pure LaMnO_3 single crystals, is explained by the formation of FM clusters in different strength due to the intrinsic doping and CT instability driven dynamic CD effect. We have confirmed the presence of the FM clusters in the three samples by the structural & magnetic characterisation techniques like HTXRD, XPS, EELS, d.c. and a.c. magnetisation. Magnetic measurements show the variation in interaction strength of the FM clusters with the applied magnetic field.

Chapter 5

Electrostatic EDL gate effect on the electrical transport of $\text{La}_{0.85}\text{Ca}_{0.15}\text{MnO}_3$

The effect of electrostatic surface charge induction due to the formation of electrical double layer (EDL) by an electrolyte gate on the transport of hole doped functional perovskites like $\text{La}_{0.85}\text{Ca}_{0.15}\text{MnO}_3$ has been studied. In this work, we have showed that a bipolar control can be obtained on the transport in such an EDL–FET device using a nano-structured hole doped perovskite as a channel at room temperature. We also showed that the modulation of electronic phases can be achieved in such EDL gated device. We observed that the depletion region at the grain boundaries (GB) and the electronic phases of a nano-structured film can be controlled and tuned through electrostatic gate.

5.1 Introduction

In recent years use of ionic liquid (e.g. DEME-TFSI, DEME-BF₄) or solid electrolyte (e.g. PEO-LiClO₄, PEO-KClO₄) as a gate dielectric to control physical properties of functional oxides has become an active field of research [88, 178–180]. Formation of the Electric Double Layer (EDL) at the solid electrolyte surface leads to a large specific capacitance often in excess of $1\mu\text{Fcm}^{-2}$ that can give rise to surface charge density more than $\geq 10^{13}\text{cm}^{-2}$ for moderate gate bias of $\approx 1\text{V}$. The electron density in oxides is orders of magnitude greater than that in conventional semiconductors. As a result, charge induced by conventional gates are much less than the electron density in oxides. Thus conventional dielectric based gate insulators have marginal or no effect in oxide channels. However, induced charge by the electrolyte gate is orders of magnitude higher than that induced by conventional oxide gate insulators like SiO₂, SrTiO₃ for the same bias. Large induced charge by electrolyte gate thus can control the electrical transport of strongly correlated oxides (like transition metal perovskites) which depends strongly on the carrier density and often on the co-existing electronic phases with different electrical resistivities (like hole doped manganites). The modulation of carrier density by electrolytes or ionic liquids (as gate dielectric) give rise to various interesting phenomena like metal-insulator transition [87], superconductivity [83], EDL gate tuned magnetism in nano-particles [181], gate enhanced photo-current and persistent photo-conductivity when an appropriate functional oxide is made a channel in an EDL-Field Effect Transistor (FET) configuration [180]. The oxides studied range from binary oxides like ZnO and VO₂ [83, 180, 182] to strongly correlated perovskite oxides with ABO₃ structure like, SrTiO₃, KTaO₃, La_{0.75}Sr_{0.25}MnO₃, NdNiO₃, Ca_{1-x}R_xMnO₃ etc. [87, 178, 181, 183, 184].

In this chapter we discuss how a bipolar control can be achieved in the non-linear transport of a nano-structured film of functional perovskite oxide like La_{0.85}Ca_{0.15}MnO₃ using an EDL gate. The control has been achieved in two ways. The first effect is to modulate the grain boundary (GB) region with induced surface charge by gate bias which affects the GB controlled conductivity. The Second effect is to tune the carrier concentration (specifically hole concentration) and due to that the conductivity within a grain was modulated. We will also show that the second effect leads to the control of co-existing

phases and through it control of electronic transport can be obtained in such nano-structured films of functional oxides at the level of GB. The work presented here has been divided into two parts. In one part of the work, we have presented the main motivation that is to control the depletion region at the grain boundaries (GB) of a nano-structured film through EDL gate. In the other part we achieve control on coexisting electronic phases.

5.2 Modulation of GB controlled non-linear transport in nano-structured film

The depletion layer in the GB regions controls the current transport through the film and are predominantly responsible for the non-linear transport that is often observed in them [95, 97]. The effect of the gate appears to be the modification of the GB potential barrier ϕ_{GB} and the depletion width t at the GB region. The response of the channel to the applied gate bias is distinct from that seen in an epitaxial film because the change occurs primarily in the non-linear transport that is controlled by tunnelling at the GB region. The nano-structured nature of the film also helps in enhancing the gate effects as the electrolyte (while settling from liquid to the gel state) can flow around the nano-crystallites and creates an all around gate condition.

We show that an effective bipolar control of the transport at room temperature can be obtained in EDL-FET made from a nano-structured film of a manganite where the conductivity at room temperature can be modulated by nearly $\pm 40\%$ with a moderate gate bias of $\pm 5V$. We have also found that application of a gate bias can control the relative fraction of the co-existing electronic phases leading to a large change in the transport properties at low temperature.

For our investigation we have chosen a hole doped manganite $La_{1-x}Ca_xMnO_3$, $x = 0.15$. The hole doped manganite $La_{1-x}Ca_xMnO_3$ evolves from an insulating orbital ordered AFM phase for $x = 0$ to a FMM phase for $x \geq 0.22$ through an intermediate FMI phase that typically occurs in the range $0.13 < x < 0.22$. In our case, sample shows a FMI state at $T \leq 150K$. In this region of composition, the conductance of the material is not too high or too low and also it has a large sensitivity to the degree

of hole doping (x) even at room temperatures. It is expected that such dependence will make it more susceptible to the gate induced carriers in the EDL-FET configuration.

Grain boundary (GB) controlled transport in manganites as distinct from bulk transport has been realized before when enhanced grain boundary contribution to MR was found in manganites $\text{La}_{1-x}\text{Ca}_x\text{MnO}_3$ ($x = 0.33$) with grain size down to 15nm [185]. Subsequent investigations on transport through artificial GB junctions in films of $\text{La}_{1-x}\text{Ca}_x\text{MnO}_3$ and $\text{La}_{1-x}\text{Sr}_x\text{MnO}_3$ at $x = 0.3-0.33$ showed that the grain boundary regions in manganites act like hole depleted region with low conductance [95, 97, 186] and give rise to non-linear transport. The hole-depleted region in the GB region is not sharp and is generally diffused. The non-linear transport through grain boundary regions in polycrystalline manganites in the FMM state of $\text{La}_{1-x}\text{Ca}_x\text{MnO}_3$ at $x = 0.30-0.33$ have been investigated. At temperatures $> 10\text{K}$, the transport through the grain boundary is governed by tunnelling (elastic process) as well as multi-step inelastic tunnelling which gives rise to non-linear conductivity [187, 188]. At much lower temperatures ($T < 10\text{K}$) elastic tunnelling through the barrier becomes the dominant mode of conduction [189]. In spite of extensive investigations on GB transport in manganites, it has never been investigated that whether the GB transport can be modulated by a gate, particularly at room temperature. The observation discussed in this chapter thus allows a voltage controlled nanoscopic control of the GB transport in such materials.

5.2.1 Making of EDL-FET device and formation of electric double layer

EDL-FET with effective channel length of 1mm with Au/Ti contact pads as Source (s) and Drain (d) was fabricated on $\text{La}_{0.85}\text{Ca}_{0.15}\text{MnO}_3$ (LCMO) thin film grown on a SiO_2/Si substrate. The thin film channel of thickness $\approx 10\text{nm}$ and width $300\mu\text{m}$ was grown by pulsed laser deposition (PLD) method with a fluence of 1 J/cm^2 using a Si hard mask for patterning (detail in chapter 2). Atomic force microscopy (AFM) image of the nano-structured film (see Fig. 5.1(a)) shows island type growth pattern with bimodal distribution of grain size. One distribution is narrow with an average size of $\approx 3\text{nm}$ and the other is a broad distribution with average grain size $\approx 22\text{nm}$ (see Fig. 5.1(b)). The film has a low surface roughness of 0.5nm. The composition of the film was checked with Energy Dispersive X-ray

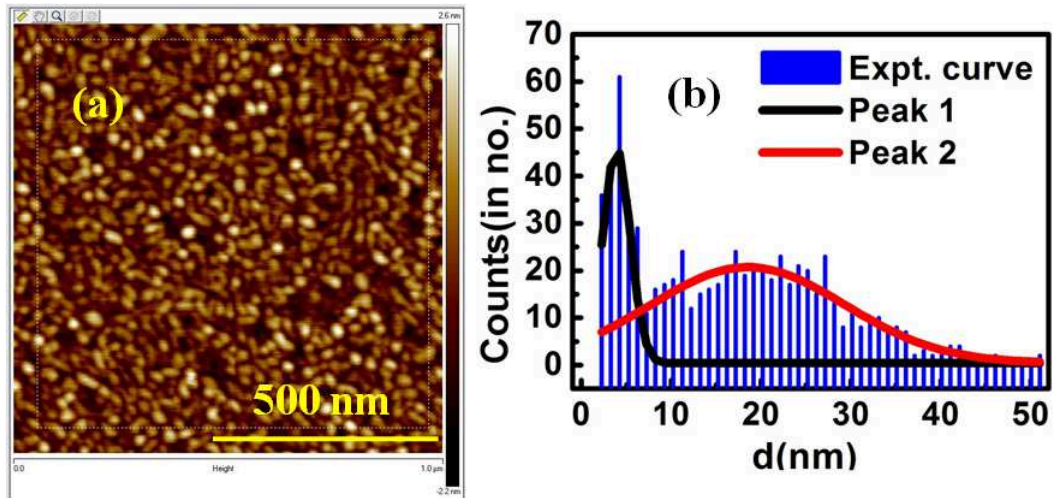


Figure 5.1 (a) Surface topography of the $\text{La}_{0.85}\text{Ca}_{0.15}\text{MnO}_3$ film taken by AFM. (b) Grain size distribution of the film.

Analysis (EDAX). The film has the desired composition that is close to the bulk pellet from which it was grown (see chapter 2).

The FET device was fabricated with LiClO_4 as gate material. The d and s pads were protected from the polymer electrolyte by a thick layer of e-beam resist (PMMA) which is baked for 3 min at 180°C . A window was opened in the resist layer on the channel for applying the gate. PEO/ LiClO_4 polymer-electrolyte made of 10:1 ratio of $(-\text{CH}_2\text{CH}_2\text{O}-)_n$ and LiClO_4 was used as gate dielectric which was applied to the exposed region of the channel. A thin metal wire was used as the gate contact. Schematic of the EDL-FET and the biasing arrangements are shown in Fig. 5.2. Here I_{DS} represents the source to drain current or the current through the channel, V_{DS} is the applied bias between the source and drain and V_G is the applied gate bias in the polymer electrolyte through the channel. Generally it has been observed that the applied negative bias to the gate dielectric with respect to drain creates charge separation in the electrolyte (see Fig. 5.2(a)). Positive ions move towards the gate electrode and negative ions accumulate near the channel electrolyte interface and correspondingly attract holes or positive charge near the interface. The accumulated ions in electrolyte forms charge layer near the interface and it is known as electric double layer (EDL). EDL formation works as a gate dielectric and that is why electrolyte gated FET device is referred to as EDL-FET. For negative V_G , one can see the

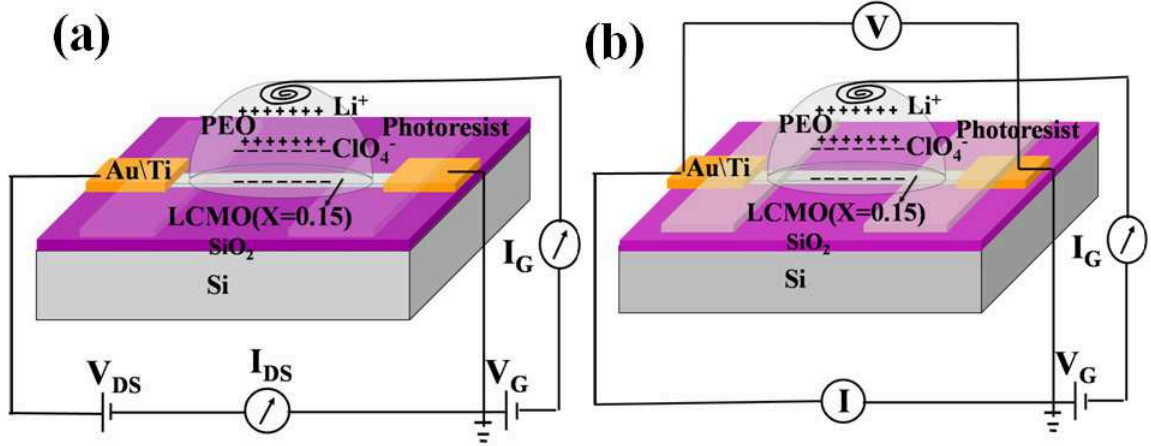


Figure 5.2 Schematic diagram of the EDL-FET device for measuring gate bias (V_G) dependent $I_{DS} - V_{DS}$ curves. (b) Biasing arrangement of the EDL-FET device for measuring $\rho - T$ curves with different V_G .

reverse effect i.e. the electrons in the channel will accumulate near the channel-electrolyte interface. Applied gate bias ($\pm V_G$) can electrostatically dope electrons or holes in the channel provided there is no charge transfer occurs between the channel and electrolyte i.e. electrochemical reaction occurs.

Now the EDL capacitance can be described by the following equation

$$\frac{1}{C} = \frac{1}{C_{Helmholtz}} + \frac{1}{C_{Gouy-Chapman}} \quad (5.1)$$

, where $C_{Helmholtz}$ is the capacitance due to the charge separation at the electrolyte/electrode interface (charged electrodes attracts opposite polarity ions and repels similar ions) proposed by Helmholtz and $C_{Gouy-Chapman}$ is the capacitance of the diffuse layer in the electrolyte solution due to the combined effects of diffusion and electrostatic forces on the mobile ions in the electrolyte which is proposed by Gouy-Chapman [190]. The two capacitances can be expressed as

$$C_{Helmholtz} = \frac{\epsilon_0 \epsilon_r}{H}; C_{Gouy-Chapman} = \frac{\epsilon_0 \epsilon_r}{\lambda_D} \quad (5.2)$$

, where ϵ_0 is the free space permittivity, ϵ_r is the relative permittivity of the electrolyte solutions, d is the thickness of the Helmholtz double layer and λ_D is the Debye length of the electrolyte with the assumption that electrode radius is much greater than d and λ_D [88, 190]. The estimated capacitance can be about few $\mu F/cm^2$ due to the very small d and λ_D (in nm) and such large capacitance would

enable large carrier accumulations at moderate bias. Due to this large modulation in carrier by the EDL, one can achieve similar carrier concentration as chemical doping in strongly correlated electron systems like perovskites.

5.2.2 Static and dynamic characteristics of the channel

The static characteristic of a FET device is the measure of I_{DS} with varying V_{DS} keeping V_G constant. Measurements of the I_{DS} - V_{DS} curves with different applied V_G was done using Sourcemeters at room temperatures by the circuit diagram shown in Fig. 5.2(a). A typical $I-V$ curve with no gate bias taken on the device is shown in Fig. 5.3. The $I-V$ curve is non-linear but symmetric. The symmetric nature is expected because of the identical electrodes at the s and d . The effect of the gate bias V_G on the device

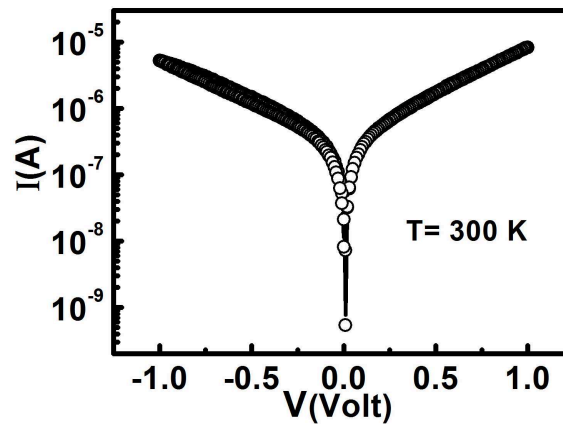


Figure 5.3 $I-V$ curve of the device with $\text{La}_{0.85}\text{Ca}_{0.15}\text{MnO}_3$ channel without any gate bias.

current has been demonstrated through the static characteristic curve (I_{DS} - V_{DS}) taken with different gate biases. The data are shown in Fig. 5.4. We have scanned V_{DS} from 0 to 1 V with different V_G (+5 V to -5 V). We have applied V_G with an interval of few minutes then measured the $I-V$ so that the channel stabilizes with each gate voltage (reason for this will be discussed in section 5.4). A negative gate bias (that induces more holes) enhances the current I_{DS} , while the positive bias (that compensates holes in the channel) reduces I_{DS} for the same V_{DS} . The change in I_{DS} with gate has a bipolar effect. For both maximum negative and positive V_G , the change in I_{DS} at $V_{DS} = 1\text{V}$ is nearly 40% , which is quite large compared to reported gate effects in manganite based EDL-FET at room temperature.

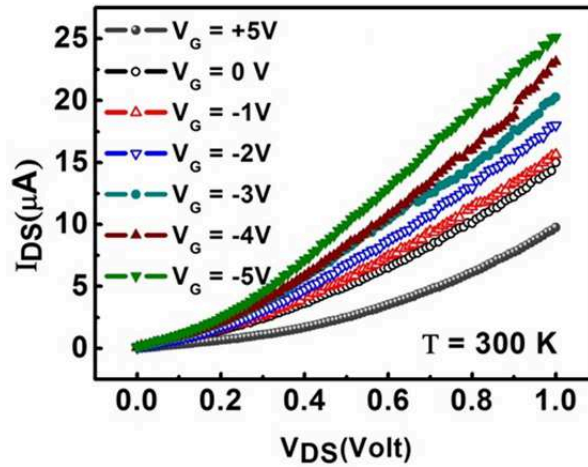


Figure 5.4 Static Characteristic of the EDL-FET device with nano-structured $\text{La}_{0.85}\text{Ca}_{0.15}\text{MnO}_3$ channel.

To ensure that the observed effect is electrostatic, we have also measured dynamic characteristic of the device i.e. the change in gate current I_G by varying the gate bias V_G keeping V_{DS} constant. The leakage current I_G is measured at fixed V_{DS} of 0.6V by varying V_G from +4 to -10V. The dynamic characteristic of the device is shown in Fig.5.5. We varied the gate bias slowly at a rate of 6 mV/s so that

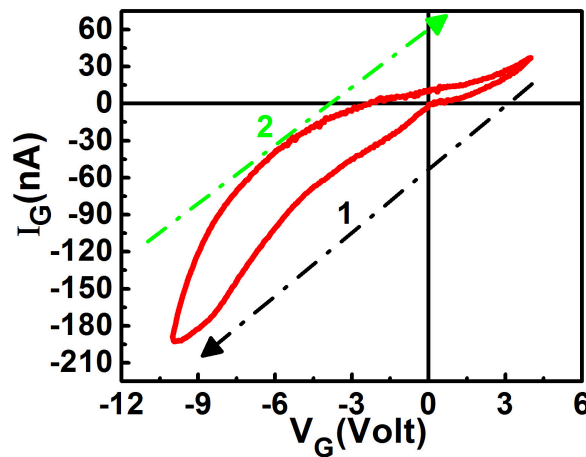


Figure 5.5 Dynamic Characteristic of the EDL-FET device with nano-structured $\text{La}_{0.85}\text{Ca}_{0.15}\text{MnO}_3$ channel. Black arrow is showing gate current I_G from $V_G = +4\text{V}$ to -10V and green arrow is showing I_G from $V_G = -10\text{V}$ to $+4\text{V}$.

the effect of gate bias stabilizes within the time interval of two subsequently applied gate biases. I_G vs. V_G curve shows hysteresis which is a characteristic signature of polymeric gate due to the involvement

of ionic motion in the leakage current. From Fig. 5.5, we found that the leakage current at $V_G = -5V$ and $V_{DS} = 0.6V$ is $\approx -25nA$ where $I_{DS} \approx$ tens of μA (in Fig. 5.4) for same V_G and V_{DS} . So the gate current I_G is nearly three order less than the channel current I_{DS} for all the gate voltages ($-5V < 0 < +5V$). But after $V_G > -6V$, I_G increases rapidly and at $V_G = 10V$, I_G becomes one tenth of I_{DS} . That is why we have restricted our measurement at $V_G = \pm 6V$ in which we have a proper FET operation. This is the reason, we cannot apply very large gate bias in an electrolyte gate (as we discussed in section 5.2.1).

In this section we observe that the channel conductance of the hole doped perovskite FET device can be modulated bipolarly at room temperature using an EDL gate dielectric applying moderate gate bias. In the next section we will discuss how does charges induced by applied gate bias modulate the conductance of the GB region in the $La_{0.85}Ca_{0.15}MnO_3$ channel of the FET device at room temperature and the basic physics behind the observed effect.

5.2.3 Modulation of the Grain boundary conductance by the EDL gate dielectric

From Fig. 5.3 and 5.4, we observed that the transport through the channel region is strongly non-linear. We express the conductance as a bias (V_{DS}) dependent differential conductance $G(V_{DS})(= dI_{DS}/dV_{DS})$. To show the nature of non-linear conduction, $G(V_{DS})$ is plotted vs. V_{DS} in Fig. 5.6. The data also show

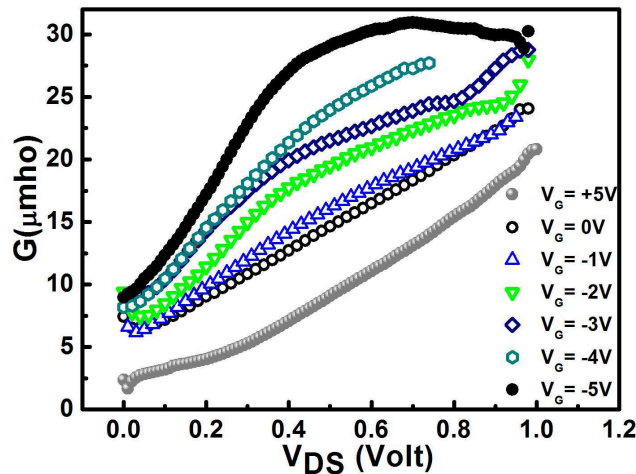


Figure 5.6 The conductance $G(V_{DS}) = dI_{DS}/dV_{DS}$ of the channel as a function of V_{DS} for different applied gate bias.

how the bias dependent $G(V_{DS})$ depends strongly on the applied gate bias V_G . For $-5V \leq V_G \leq +5V$,

$G(V_{DS})$ increases monotonously with V_{DS} . For $V_G \leq -5V$, when the conductance $G(V_{DS})$ becomes larger the bias dependence of the channel conductance saturates. This generally occurs for $V_{DS} > 0.5V$. The important observation is that the non-linear component of the transport is strongly affected by the gate bias. Grain boundaries in most oxides are strongly depleted by carriers making the transport through them controlled by barrier depletion. Application of the gate bias modulates the potential barrier in the depletion region leading to a large effect on the current through the channel. Analysis of the effect, as done below, will show that the non-linear component of the transport which is related to the tunnelling in the grain boundary of the nano-structured film, is enhanced/reduced significantly with the applied V_G .

The observed data have been quantitatively analysed based on the nature of the GB controlled transport and its modification by the applied gate bias has been obtained. In our case at room temperature where the barrier has a width that is much larger than the elastic tunnelling length, multi-step inelastic tunnelling is the dominant mode of transport [95, 98]. In this case, the conductance G as a function of source-drain bias $V = V_{DS}$ is given as:

$$G = G_{0d} + \sum_{n=1} G_n V^{n - \frac{2}{n+1}} = G_0 + G_2 V^{4/3} + G_3 V^{5/2} + \dots \quad (5.3)$$

,where the direct tunnelling term G_{0d} and the first term in the summation ($n = 1$) are both bias independent. They are taken together in the term $G_0 = G_{0d} + G_1$. The term with coefficient G_2 is for multi-step tunnelling with $n = 2$ and that with coefficient G_3 is for multi-step tunnelling with $n = 3$. The coefficients G_n 's become smaller as the value of n increases. They are related to the depletion width t and the inverse tunnelling length χ by the relation:

$$G_n = A_n \exp\left(\frac{-2\chi t}{n+1}\right) \quad (5.4)$$

where the depletion width $t = \sqrt{\frac{2\epsilon_0\epsilon_r\phi_{GB}}{e^2 n_{3D}}}$ and inverse tunnelling length $\chi = \sqrt{\frac{2m\phi_{GB}}{h^2}}$. ϕ_{GB} is the GB potential barrier, n_h is the hole density in the bulk of the grain and ϵ_r is the dielectric constant [191, 192]. A_n is a constant independent of χ and t . The observed $G(V_{DS})$ was fitted to Eqn. 5.2 as shown in Fig. 5.7. In the region of low bias where the conductance variation does not saturate, we could fit the data

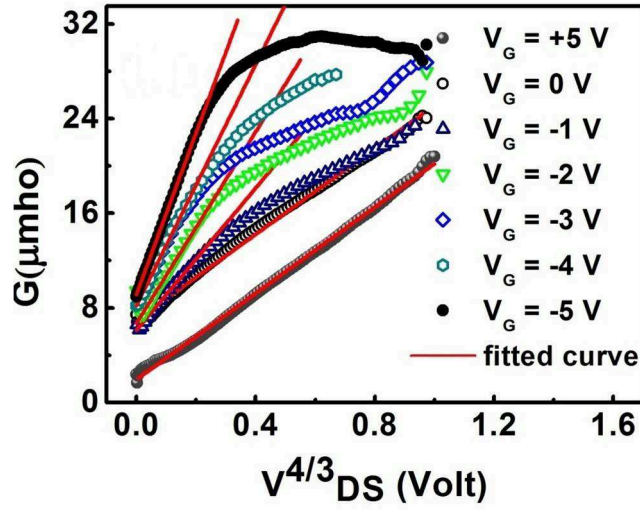


Figure 5.7 The conductance $G(V_{DS}) = dI_{DS}/dV_{DS}$ of the channel as a function of V_{DS} for different applied gate bias. The lines through the data are fit to the equation $G = G_0 + G_2V^{4/3}$.

using the relation $G(V_{DS}) = G_0 + G_2V^{4/3}$, which is Eqn. 5.2 for $n \leq 2$ (reason for x-axis in Fig. 5.7 being plotted as $V_{DS}^{4/3}$). The higher order terms make very small contributions and are not considered. The values of the terms G_0 and G_2 are obtained from the fit. In Fig. 5.8(a) and 5.8(b), we show the dependence of G_0 and G_2 on V_G as obtained from the analysis of the data. These leading terms G_0 and G_2 have dependence on V_G and this leads to the gate bias dependence of the conductance. For the most part, the change occurs due to the change of the term G_2 when V_G is applied, establishing that the gate effect is large on the non-linear conductivity. (Note: The gate induced effect occurs within a layer of thickness \sim Debye-length. The film thickness is more than that. It thus may happen that there will be a parallel layer that is not affected by the gate. Such a layer can lead to the saturation in I_{DS} at higher V_{DS}). The term G_0 , which is independent of V_{DS} and leads to linear $I_{DS} - V_{DS}$ enhances linearly with V_G . However, the coefficient G_2 enhances exponentially with the gate bias V_G , contributing most to the gate induced effect. The exponential dependence on the gate bias is an important observation which we explained below.

The coefficients of the multi-step tunnelling term G_n has an exponential dependence on the χt product, $\chi t = \sqrt{\frac{4m\epsilon_0\epsilon_r}{e^2h^2n_{3D}}} \phi_{GB}$. Thus a change in ϕ_{GB} and n_h on application of the gate bias can substantially change G_2 (Note: the change in G_0 is much more suppressed compared to that in G_2 because of the

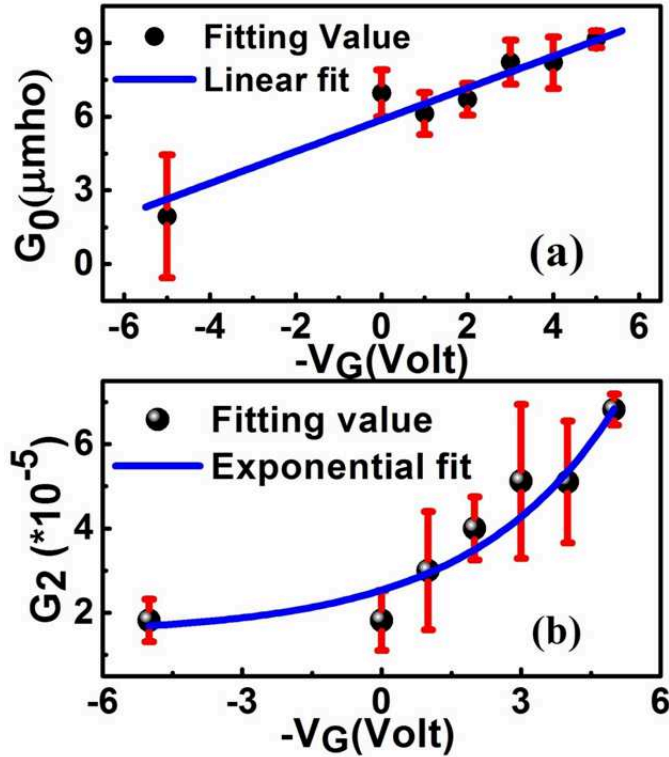


Figure 5.8 Dependence of (a) G_0 and (b) G_2 on gate bias V_G .

likely contribution of the parallel layer that is unchanged by the gate bias). Application of the gate bias will change the carrier concentration of the channel. The hole concentration of the $\text{La}_{0.85}\text{Ca}_{0.15}\text{MnO}_3$ film is in a region where its conductivity is susceptible even to a small change in the hole concentration that can be brought about by the gate. Application of negative gate bias induces more holes in the channel which leads to the enhancement of its conductivity. The enhancement in the conductivity in the neighbouring grains leads to reduction of the barrier potential (ϕ_{GB}) at the grain boundary. This reduces the χt product and enhancement of the term G_2 . This enhancement will be further strengthened by the enhancement of n_h which occurs due the negative bias in the GB region. Positive gate bias that reduces the hole concentration has an opposite effect.

5.2.4 Transient response of the EDL-FET device and characteristics of the gate dielectric

The response of the I_{DS} and I_G (at a given source-drain bias V_{DS}) for a step change in the gate bias V_G has been investigated to correlate the time response of the EDL gate and the response in the nano-structured channel. It is noted that analysis of the transient response has not been done in such EDL-FET devices before. The data are shown in Fig. 5.9. The top panel shows the step change in the applied gate bias

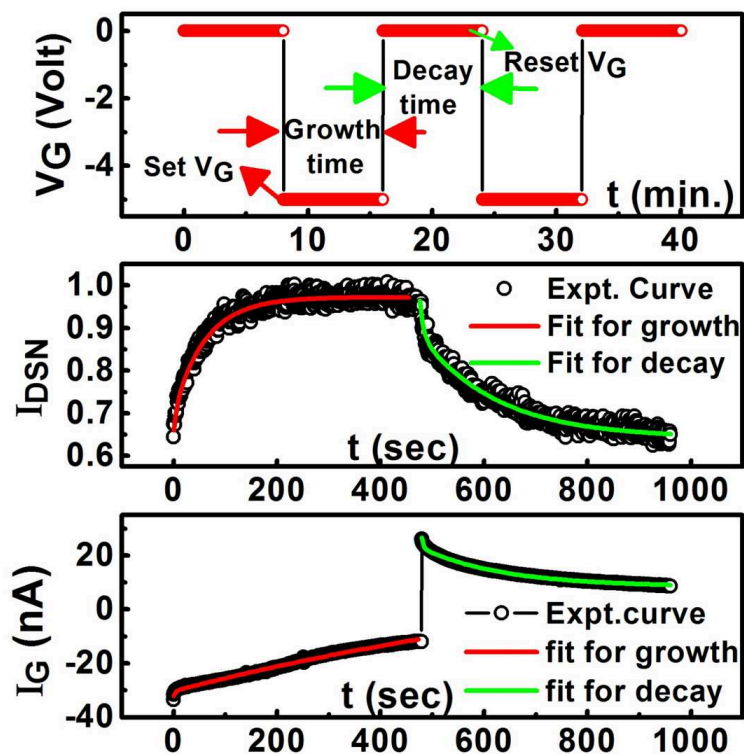


Figure 5.9 Top panel shows the step change in the voltage V_G . Middle panel shows the transient response of the normalised (I_{DS}/I_{max}) drain current I_{DS} at fixed $V_{DS} = 0.4V$ and bottom panel shows the transient response of gate current I_G .

from 0V to -5V to 0V with a 50% duty cycle. The gate current in response to the step change to the gate bias (the charging and discharging current of the gate capacitor) are shown in the bottom panel of the Fig.5.9. The magnitude of I_G is \ll than that of I_{DS} for the range of applied V_G showing a proper FET operation. The transient response of the I_G shows the process of charging the electrolyte as well as the EDL capacitor (discussed in subsection 5.2.1). We have fitted the growth and decay curves of

I_{DS} and I_G using the bi-exponential equations,

$$I = I_0 + (I_{max} - I_0)[1 - ((1 - c)\exp\left(-\frac{t}{\tau_1}\right) + c\exp\left(-\frac{t}{\tau_2}\right))]; \quad (5.5)$$

$$I = I_0 + (I_{max} - I_0)[(1 - c)\exp\left(-\frac{t}{\tau_1}\right) + c\exp\left(-\frac{t}{\tau_2}\right)]; \quad (5.6)$$

where I_0 , I_{max} are the currents at $t = 0$ and $t = \infty$, τ_1 , τ_2 are the time constants associated with charging and discharging of the EDL capacitor as well as electrolyte capacitor and "c" ($0 < c < 1$) is the weightage factor of τ_1 and τ_2 . From Fig. 5.9, we found that the growth and decay curves of I_G follow two time scales. The fast time scale τ_{g1} (~ 1 sec) is the same for both the growth and decay curves of I_G . This part of the transient response of the gate current is most likely the charging and discharging of the EDL capacitor. From the maximum gate charging and discharging current we found that the gate charging occurs through an equivalent resistance of $R_G (= \frac{V_G}{I_G}) \approx 200$ MOhm. From the fast time constant of the charging and discharging current we find an equivalent specific gate capacitance $C_G \approx 2\mu\text{F}/\text{cm}^2$.

The slow component of the charging part of I_G has two time scales, one exponential component with $\tau_{g2} \approx 200$ sec and a creep like behaviour over a longer time scale. The longer time scale occurs only when V_G is ON and it can arise from the movement of ions in the gate electrolyte under the applied bias. In case of the discharging part, that occurs with $V_G = 0$ V, τ_{g2} is nearly same order ≈ 150 sec but there is no creep like behaviour in the absence of a gate bias.

The response of the channel I_{DS} current to the gate bias at $V_{DS} = 0.4$ V is shown in the middle panel. In the figure I_{DS} has been normalized by dividing it to the maximum channel current. The growth and decay curves of I_{DS} mirror (qualitatively) the time response of I_G and also follow two characteristic time scales τ_1 and τ_2 . The fast time constant τ_1 is same for both the growth and decay curves (~ 6 s) and is similar to the fast time scale τ_{g1} for the I_G . I_{DS} also has a slow component τ_2 which is qualitatively similar to τ_{g2} of I_G and in this time scale I_{DS} saturates to its maximum value. The slow component τ_2 is about an order larger than τ_1 for the growth curve (~ 60 s) and even larger for the decay curve (~ 150 s) which exactly follow the slow component of I_G . The initial response of the channel current is thus a reflection of the charging/discharging of the capacitor. This confirms that the changes occurring in the

gate region control the transport in the channel region.

5.3 Control of Electronic phases in manganites using EDL-FET

In section 5.2, we observed that electrostatic gate can bipolarly modulate the GB conductance at room temperature tuning the depletion width t by changing the GB potential ϕ_{GB} . We discussed earlier that the composition of our sample falls in the region where different electronic phases coexist together depending on the temperature. In this section, we will discuss the effect of electrostatic gate on these coexisting electronic phases. Here, we used low bias for the measurement so that the non-linear conduction arising from GB region does not contribute appreciably.

5.3.1 Gate bias modulated temperature dependent channel resistance with coexisting electronic phases

We have measured the temperature dependent conduction of the nanostructured $\text{La}_{0.85}\text{Ca}_{0.15}\text{MnO}_3$ channel with different V_G in EDL-FET configuration (Shown in Fig. 5.2(b)). The resistance of the channel was measured using a low constant current of $1\mu\text{A}$ so that the voltage across the s-d i.e. V_{DS} is less than 0.4V where the non-linear conductance due to GB effects do not occur. As it is discussed in section 5.2, at higher bias, non-linear conduction sets in due to the tunnelling type grain boundaries where one can tune the GB barrier heights and GB depletion layer by an EDL gate [193]. For $R-T$ measurement, we used a low bias between the drain and source in the channel so that non-linear effects do not come into play (Note: the gate current I_G is found to be much lower than the channel current (I_{DS}) in the presence of V_G confirming a proper FET operation).

The $R-T$ curves with different gate biases (+4V to -6V) are shown in Fig. 5.10. The relative change in the resistance of the channel at room temperature due to the highest applied $\pm V_G$ is nearly $\pm 40\%$ (which is also observed in the static characteristics of the FET device in Fig. 5.4). The change in R gets enhanced at low temperatures. For instance, at $T = 100\text{K}$, a change of V_G from +4V to -6V makes the channel resistance R change from nearly 3Mohm to 0.2Mohm . The evolution of the resistance of

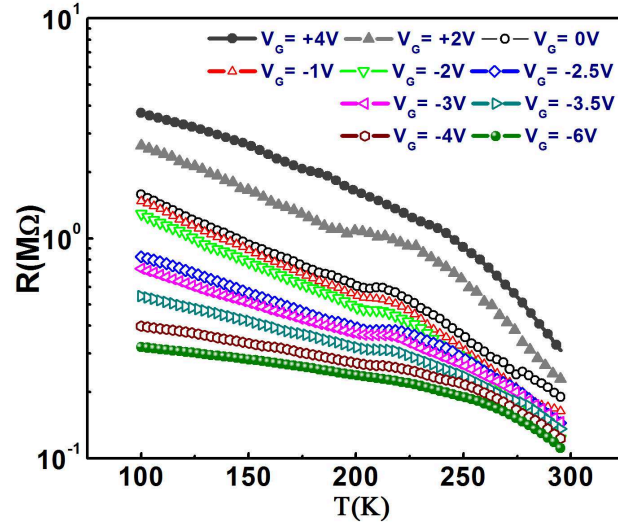


Figure 5.10 $R - T$ curves of the channel with different gate bias.

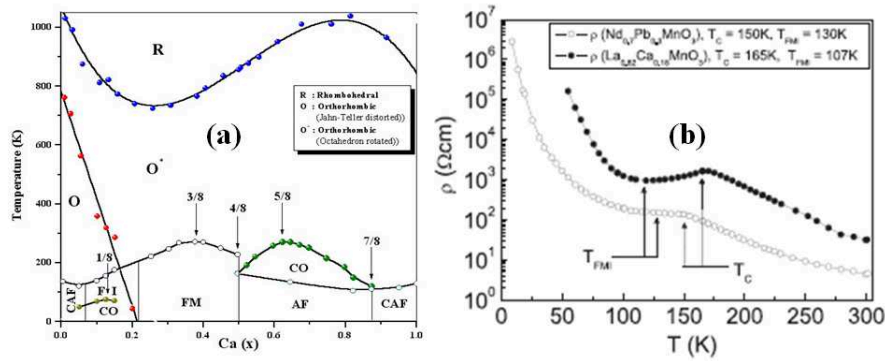


Figure 5.11 (a) $\text{La}_{1-x}\text{Ca}_x\text{MnO}_3$ phase diagram for chemical doping (x) vs. temperature (T) plane. Different phases are PI: Paramagnetic Insulator, FM: Ferromagnetic Metal, FI: Ferromagnetic Insulator, AF: Antiferromagnetic Insulator, CAF: Canted AF and CO: Charge/Orbital Ordering. "O" represents the Jahn-Teller distorted orthorhombic structure and O^* represents octahedra rotated structure. Image from [1, 2, 7, 50, 51, 139]. (b) $\rho - T$ data of $\text{La}_{0.82}\text{Ca}_{0.18}\text{MnO}_3$ (LCMO18) and $\text{Nd}_{0.7}\text{Pb}_{0.3}\text{MnO}_3$ (NPMO30) single crystals showing existence of different electronic phases. T_C is the onset of PI to FM transition and T_{FMI} is the onset of FI state. Image is adopted from [194].

the channel as a function of gate bias V_G shows shift in some of the characteristic temperatures which mark the transformation between different electronic transport regimes in the film. These regions can be clearly identified in $R - T$ data of a low doped manganite single crystal and in the $\text{La}_{1-x}\text{Ca}_x\text{MnO}_3$ phase diagram (shown in Fig. 5.11(a) and (b)). To identify these temperatures and the regimes clearly, we have taken the derivative of the $R - T$ curve (shown in Fig. 5.12) where we plot $\frac{d(\ln RT^{-1})}{d(T^{-1})}$ as

a function of T at $V_G = 0V$ and at few representative V_G . The derivative curve accentuates the three

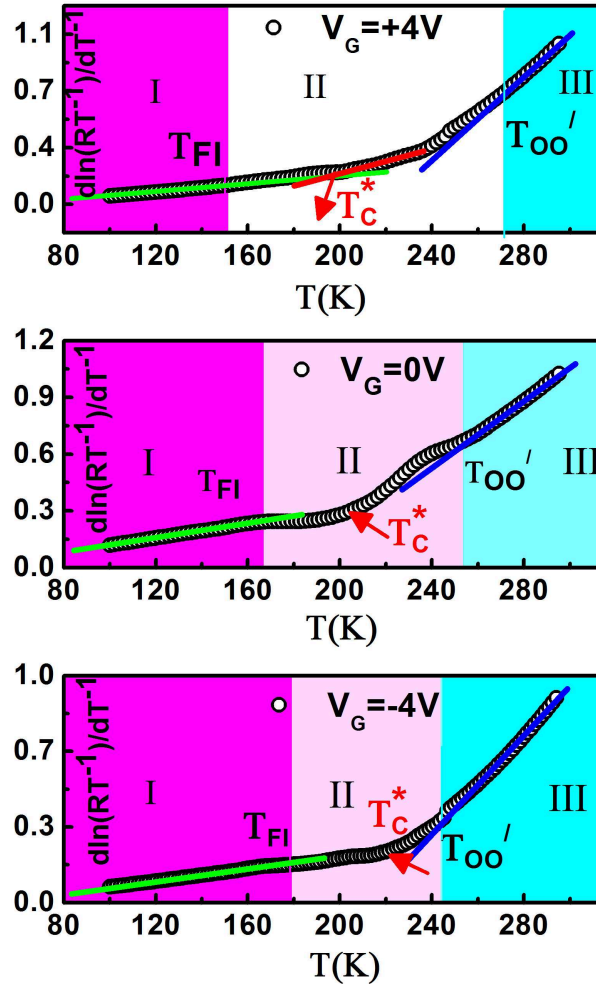


Figure 5.12 The characteristics temperature regions (I, II and III) of the LCMO channel as determined from transport data by plotting normalized $\frac{d(\ln RT^{-1})}{dT^{-1}}$ vs. T at $V_G = +4V$, $0V$ and $-4V$. Colour boundaries indicate different characteristic transition temperatures. Red arrow shows the position of T_C^* .

regions clearly as a deviation from a smooth variation. These temperatures are marked in our sample at $V_G = +4V$, $0V$ and $-4V$. We track from evolution of the derivative curves how these temperatures change with V_G . In our sample, we have identified three distinct regions (region I, II and III). In region III, the system is in Paramagnetic insulating (PI) state with orthorhombic phase with JT distortions (O phase), in region I it is in a low temperature FMI state and in region II it is a predominantly mixed phase region with co-existing low resistance FM phase (which may be metallic) and an high resistance

insulating phase with different crystallographic structures like "O" and O' phases (orthorhombic phase with rotated regular octahedra). We have marked $T_{OO'}$ in Fig. 5.12 where the experimental curve deviates from linear region of $\frac{d(\ln RT^{-1})}{d(T^{-1})}$ vs. T curve at the OO' structural transition (Note: Resistivity data taken on single crystals also show this transition as a change in slope [140]). In region II, the paramagnetic to FM transition that shows up as a change in the slope of the $R-T$ curve. This we mark as the temperature T_C^* (Note: We do not call it a FM transition temperature T_C as it is not determined by a magnetic transition in our experiment). In region I, the onset of the FMI state is marked by the temperature T_{FI} . The characteristics temperatures obtained from the $\frac{d(\ln RT^{-1})}{d(T^{-1})}$ vs. T curve as shown in Fig. 5.12 at $V_G = 0V$ matches well with the $\text{La}_{1-x}\text{Ca}_x\text{MnO}_3$ phase diagram in $x = 0.15$ region. Application of V_G of either signs shifts these temperatures.

In Fig. 5.13, we show the evolution of the three characteristic temperatures ($T_{OO'}$, T_C^* and T_{FI}) as a function of gate bias. The change in these temperatures are similar to what one would expect

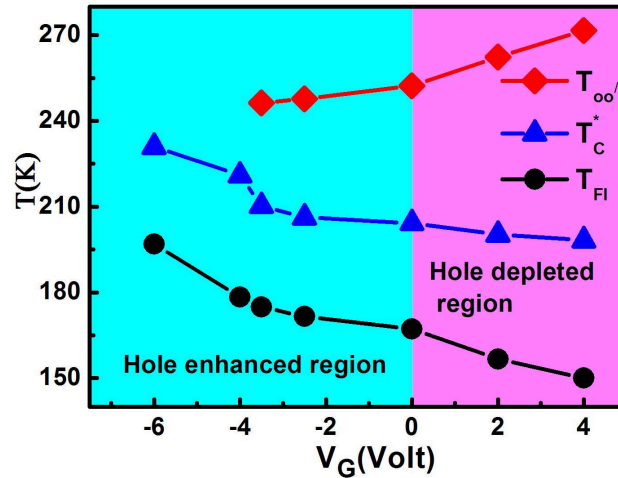


Figure 5.13 Variation of $T_{OO'}$, T_C^* and T_{FI} as a function of gate bias.

from the variation in hole concentration introduced by divalent metal substitution. The variation of the temperatures arise from the change in the relative fraction of the two co-existing phases which can be brought forward by the applied V_G (discussed later). All the three temperatures show substantial change on application of moderate gate bias which closely resemble the evolution of electronic phase in $\text{La}_{1-x}\text{Ca}_x\text{MnO}_3$ on hole doping for low value of x [50,51,139], establishing that the changes ushered

by the gate induced charges (Field effect induced charges) mimics the change that one would expect by change of hole concentration (δx) in $\text{La}_{1-x}\text{Ca}_x\text{MnO}_3$ brought about by chemical substitution. Importantly, the change is bipolar with a positive (negative) V_G that leads to hole depletion (or enhancement) depressing (or raising) T_C^* , T_{FI} and raising (depressing) $T_{OO'}$. Increasing hole concentration suppress the OO' transition, which in turn enhances FM interaction by increasing electron itinerancy. This leads to enhancement of T_C^* . As the phase diagram suggests that the two temperatures approach each other at $x \simeq 0.25$, the induced charge creates an effect which very close to chemical doping. The observation that one can tune the temperature T_C^* , T_{FI} and $T_{OO'}$ by an applied gate bias is new and is a direct manifestation that the field induced charges can change the hole concentration similar to that could be achieved by chemical substitution.

5.3.2 The Field effect and induced charge in channel

The observed bipolar modulation of the resistance of the channel due to the formation of EDL near the electrolyte–channel interface arises from the modulation of carrier density due to application of finite gate bias. The electric field due to the formation of EDL near the electrolyte–channel interface will affect the carrier concentration in the channel mostly over a length scale from the surface that is of the order of Debye length [88, 195]. We have calculated the Debye length (λ_D) of the sample using equation $\lambda_D = \sqrt{\frac{\epsilon_r \epsilon_0 \kappa_B T}{n_{3D} e^2}}$, where ϵ_0 is the permittivity of free space, ϵ_r is the dielectric constant of the material, κ_B is the Boltzmann constant, e is the electronic charge and n_{3D} is the volume carrier density in the channel. We obtain $\lambda_D \approx 4$ nm at $T = 300\text{K}$ using the value of ϵ_0 , $n_{3D} \approx 10^{21}/\text{cm}^3$ and $\epsilon_r \approx 100$ (for LCMO) [196]. The estimated λ_D is comparable to the average grain size ($\approx 3\text{nm}$) of the film and the film thickness though somewhat larger but also comparable ($\approx 2.5\lambda_D$). Since the electrolyte flows around the grains during its solidification, we may assume that the whole thickness of the channel is affected more or less uniformly by the field induced charge and an effective carrier density modulation can be achieved by applied gate bias V_G (Note: This may not be a rigorously correct assumption but it makes the analysis simpler). Without the application of any gate bias, the channel has both positive (holes) and localized negative (electrons) carriers due to the substitution of Ca at La site which creates

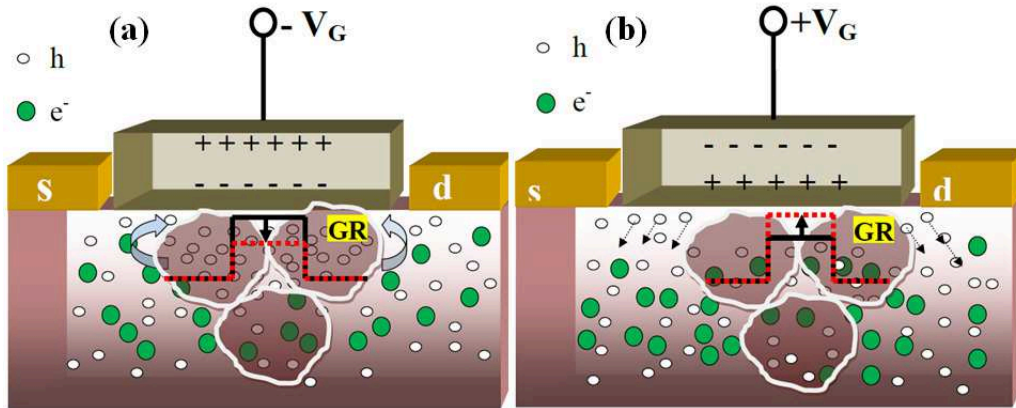


Figure 5.14 Schematic diagram of (a) the effect of $-V_G$ within the channel; s and d are source and drain electrodes. h, e, and GR represents holes, electrons and grains. Black and Red (lower) potential wells represent the GB barrier potential at $V_G = 0V$ & at $-V_G$, and (b) the effect of $+V_G$ within the channel. Black and Red (higher) potential wells represent the GB barrier potential at $V_G = 0V$ and at $+V_G$.

mix valence $Mn^{3+} - Mn^{4+}$. The electron at Mn^{3+} site is localized while Mn^{4+} has a hole in its e_g orbital. For negative V_G the electrolyte gets ionized and negative charge accumulates near the interface (shown in Fig. 5.14(a)). These negative charges now attract positive holes in the channel leading to the enhancement of the hole density (n_h) that enhances the carrier transport. The enhanced hole density consequently can enhance the conduction within the body of the grain and a part of the field induced holes will act to reduce the depletion region that forms at the GB region. Positive gate bias depletes the holes from the channel (shown in Fig. 5.14(b)) and increase the GB potential barrier ϕ_{GB} which reduces the carrier transport in the grains.

5.3.3 Quantitative comparison of gate dielectric induced carrier modulation with that achieved by chemical doping(x)

In the subsection 5.3.1, we observed that a moderate gate bias can tune the R , its temperature dependence and also the characteristic temperatures ($T_{OO'}$, T_C^* and T_{FI}) substantially. In this section, we will quantitatively compare the changes brought about by the gate induced carriers with that expected from chemical doping (δx). The strategy that we follow is to estimate the change in hole concentration from the induced charge which can be found from the measured gate capacitance for a given gate bias and

compare that with change in x as one would expect from the bias induced change in $T_{OO'}$. Enhanced hole concentration suppresses the $T_{OO'}$ [50, 139, 177, 197]. Since the change in $T_{OO'}$ as a function of x (brought about by chemical substitution) is well established, its change by the gate bias thus can be used as measure of the effective change of hole concentration δx due to V_G .

In our experiment we measured the transient gate current $I_G(t)$ in response to a step change in the gate bias V_G . Analysis of the transient gate current has been used to obtain the gate capacitance (C_g) from the charging time constant ($R_g C_g$), where R_g is the gate resistance through which the gate capacitance charges. From the measured C_g and the specific gate capacitance $\approx 1.6 \mu\text{F}/\text{cm}^2$, we can estimate an induced surface charge density of $1 \times 10^{13}/\text{cm}^2$ for a gate bias of 1V. Using the value $\lambda_D \approx 4$ nm at $T = 300\text{K}$ and the assumption that induced carriers can affect the carrier density in the channel over a depth from the surface $\approx \lambda_D$, we find a volume charge density of $\approx 0.5 \times 10^{19}/\text{cm}^3$ for a gate bias change of 1V. From the formula unit volume of $\approx 60 \text{ \AA}^3$, we find the induced carrier density causes a change of $\delta x \approx \pm 0.0013$ /formula unit for $V_G = \pm 1\text{V}$. To distinguish this δx , obtained from electrostatic method, from that obtained by chemical substitution, we call it δx_e to mean that this has been brought forward by electrostatic effect. In Fig.5.15, we show δx_e as a function of V_G . This shows the expected change in hole concentration that one would expect from the gate induced field effect.

We have calculated the modulation of δx from the variation of $T_{OO'}$ by V_G from the known linear variation of $T_{OO'}$ with x in $\text{La}_{1-x}\text{Ca}_x\text{MnO}_3$ when x is change by chemical substitution as documented in the phase diagram of $\text{La}_{1-x}\text{Ca}_x\text{MnO}_3$ [50, 139, 197]. From the data we find that a lowering of 1K in $T_{OO'}$ occurs due to an enhancement of $\delta x \approx 3 \times 10^{-4}$. From Fig. 5.13, we could thus calculate the variation of δx as a function of $\pm V_G$. In Fig. 5.15, we have shown the variation of δx with V_G along with δx_e . From Fig. 5.15, it can be seen that the estimated value of δx from $T_{OO'}$ and δx_e derived from the field effect induced charge are nearly same in the positive gate voltage region ($+V_G$). It is of similar order but somewhat different in the $-V_G$ region. It is indeed gratifying that δx and δx_e , though estimated from two independent methods, give nearly same (or similar) values. It establishes that the change in hole concentration by the field effect (using the EDL dielectric) is predominantly an electrostatic effect. There is a difference in the negative gate bias region, where we find that $\delta x < \delta x_e$. This implies that the

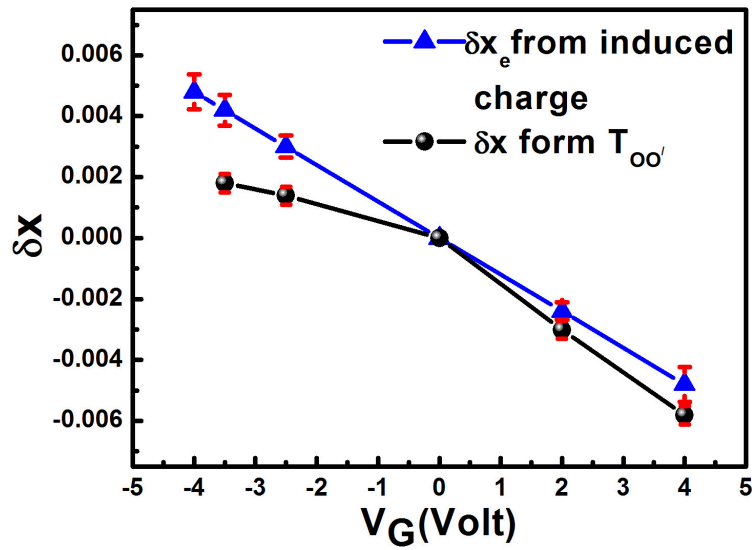


Figure 5.15 Variation of δx and δx_e with different V_G calculated from induced charge due to field effect (δx_e) and from the change in $T_{OO'}$ (δx).

hole accumulation within a grain due to the field effect is less than that what is expected from simple electrostatic effect. This difference likely arises from the fact that part of the induced holes (being majority carriers) compensates the heavily depleted GB region. In such nanostructured film, the GB region being strongly depleted of majority carriers, makes a depletion region. A part of the field effect induced charge leads to the lowering of the GB potential barrier and narrowing of the depletion layer. For the positive gate bias, where the hole concentration is reduced by the gate bias, the GB region gets further depleted. This makes the value of δx closer to that of δx_e .

5.3.4 Dependence of the activation energy of transport on the gate bias.

In the temperature range $T > T_C^*$, the charge transport is strongly activated with an activation energy E_a . The charge transport within a grain is polaronic in nature and the activation of transport has a polaronic origin. The presence of the GB potential barrier further modulates this activation energy (calculated from the polaronic fit to $R - T$ data for different V_G). We observed that the field effect induced charges change E_a (shown in Fig. 5.16). The change in E_a due to the gate bias V_G can be compared qualitatively to the change in E_a that can arise from hole doping by substitution (change in x) [140]. The applied

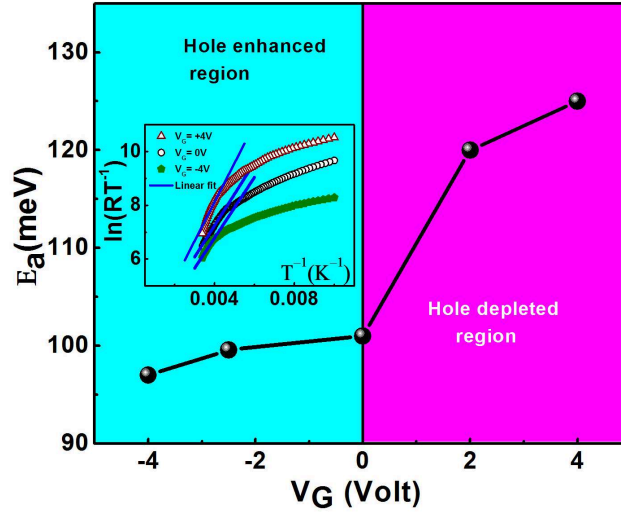


Figure 5.16 Variation of E_a with V_G . Inset shows the polaronic fit to $R-T$ data for $V_G = +4V$, $0V$ and $-4V$.

gate bias can lead to the modulation of both the polaronic contribution to E_a as well as that arising from the GB barrier. In the temperature region of interest ($T > T_C^*$) at $V_G = 0V$ and negative V_G , due to lowering of the barrier at the GB by the induced hole, it is expected that the activation energy E_a will arise predominantly from the polaronic origin. It has been known from past studies done on single crystals [140] that the activation energy E_a is suppressed by the enhancement of x (enhancement of hole doping). Thus the reduction in E_a due to applied negative gate bias can be understood. For positive gate bias where the hole density is depleted one would expect E_a to go up. The scale of change of E_a in this region, however, is very steep and is more than what one would expect from change in hole density alone [140]. It is likely that the steep change in E_a is a reflection of the enhancement of the GB barrier that arises due to strongly depleted region.

5.3.5 Control of coexisting electronic phases by the electrostatic gate

In the previous subsections, we have observed that there is a bipolar modulation of the conductance of the channel by V_G . The change in the conductance of the channel occurs due to the modulation of carrier density and GB potential barrier by the applied gate bias. In this subsection, we explore whether a two phase model can explain the resistivity data, where relative fraction of the two phases is changed

by the gate bias.

The evolution of the resistance R as a function of temperature T as well as the gate bias V_G can be phenomenologically explained from the evolution of the relative fraction (f) of the two co-existing phases in the channel. The transport in the region I and II take place through predominantly two co-existing phases: one high resistance insulating phase (resistance denoted by R_{ins}) and other a low resistance "marginally" metallic phase whose resistance is denoted by R_m (Note: We call it metallic only for referral purpose. It can be bad metallic phase with relatively lower resistance). Changes in T and V_G change the relative fraction f of the two phases. Thus the change in f can describe phenomenologically the change in R as a function of T and V_G . The presence of such co-existing phases, as stated before, have been invoked to explain the transport and magnetic properties in manganites in the low doped region ($x \approx 0.22$) [139, 197].

The change in the hole concentration within a grain will change the relative fraction of the coexisting phases, however, the observed effective f will also depend on the conductivity of the GB region. For negative gate bias that reduce the GB potential barrier due to the hole enhancement, one would see an enhancement of the effective f over that expected from the contributions arising from changes within a grain alone. Similarly a gate bias induced enhancement of GB potential, that occurs at positive V_G will contribute to the reduction of the effective f . Thus in the nanostructured film, the potential barrier at the GB will affect the effective f .

We obtain an estimate of f from a simple 2-phase model for conduction. In presence of two such phases, the channel resistance (R) can be expressed as

$$\frac{1}{R} = \frac{(1-f)}{R_{ins}} + \frac{f}{R_m}, 0 \leq f \leq 1, \quad (5.7)$$

We have assumed $R_{ins}(T)$ as the resistance of the channel at $V_G = +4V$. The rationale for this assumption is that the hole depletion has converted the channel into the high resistance insulating phase with a metallic fraction $f \rightarrow 0$ along with the highly depleted GB region with enhanced GB barrier. $R_m(T)$ is taken as the resistance of the channel at $V_G = -6V$, where we assume that the full channel, by enhancement of hole concentration, has only the "metallic" phase ($f \rightarrow 1$) with reduction of depletion

region and the grain boundary barrier potential. From equation 5.7, we obtained f as a function of T for different gate bias (V_G). We have limited our analysis for $T < T_{OO'}$ where we have the mixed phase region. In Fig. 5.17, we have plotted metallic fraction (f) vs. T curve for different V_G . The fraction f can be written as $f(T, V_G)$ since it is a function of both T and V_G as seen in Fig. 5.17. For $T \leq$

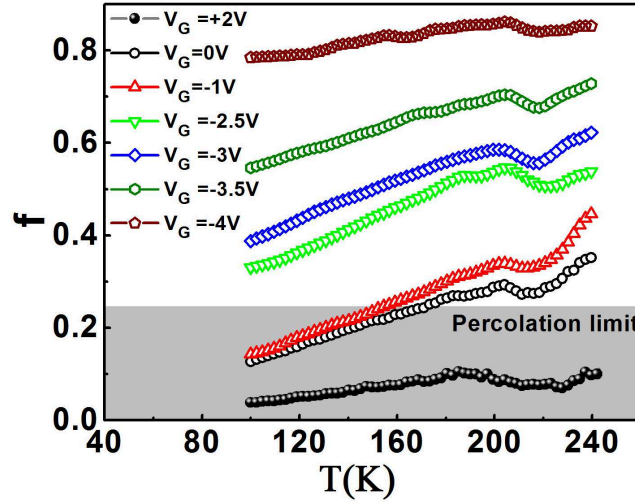


Figure 5.17 Temperature dependence of f with different V_G .

240K and for all gate bias, $f(T, V_G)$ decreases on cooling due to the activated nature of the transport in the channel as well as due to the barrier in the GB region. The temperature dependence is more steep when $V_G > 0$ that depletes hole density in the channel thus enhancing the insulating fraction of the co-existing phases. A negative V_G that leads to the accumulation of more holes in the channel in turn leads to larger $f(T, V_G)$ ($\rightarrow 1$) and the temperature dependence of $f(T, V_G)$ also becomes less steep due to the predominance of the metallic fraction. For $V_G \approx -3V$ and beyond, it is more or less T independent. For positive $V_G (\geq 2V)$, the metallic fraction $f(T, V_G)$ is below the percolation limit for volume percolation ($f_c = 0.25$) [142] and the insulating phase makes predominant contribution to the transport as $f(T, V_G)$ is $< f_c$.

$f(T, V_G)$ has dependence on both T and the gate bias V_G . The explicit dependence of $f(T, V_G)$ on T is given by $f_0(T)$ which gives the temperature variation for zero bias. The scaled quantity $f(T, V_G)/f_0$ would thus show the explicit dependence of the fraction f on the applied gate bias. If we consider the scenario that the gate bias control of f predominantly occurs due to the control of the GB conductivity

by V_G , then one would expect that $f(T, V_G)/f_0$ is directly proportional to the GB conductance G_{GB} . It has been established through experiments on GB conductance that it is controlled by tunneling at the GB [95, 97, 198]. The tunneling takes place through the depletion width of thickness t , which is given by $t = \sqrt{\frac{2\epsilon_0\epsilon_r\phi_{GB}}{e^2n_{3D}}}$, where ϕ_{GB} is the GB potential barrier. G_{GB} is $\propto \exp(-\chi.t)$, where the inverse tunneling length $\chi = \sqrt{\frac{2m\phi_{GB}}{\hbar^2}}$. Thus G_{GB} will be determined by the product χt , where $\chi t = \sqrt{\frac{4m\epsilon_0\epsilon_r}{e^2\hbar^2n_{3D}}}\phi_{GB}$. The application of the gate bias will change both the barrier ϕ_{GB} and n_{3D} leading to a change in G_{GB} and thus $f(T, V_G)/f_0$. The GB barrier ϕ_{GB} has an inverse dependence on the gate bias V_{GB} as established through such studies done in polycrystalline semiconductors [191, 192]. Using

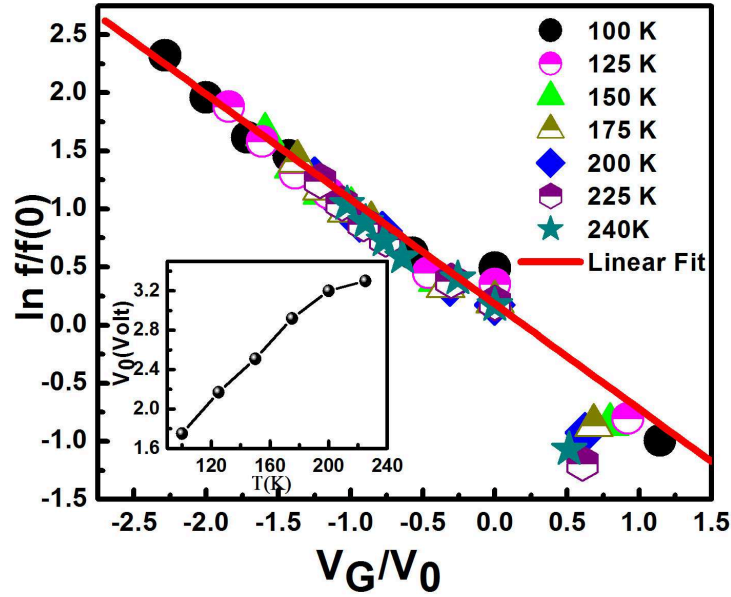


Figure 5.18 The field dependence of the scaled $f(V, T)/f_0$ with V_G/V_0 . The inset shows the T dependence of $V_0(T)$.

the above discussion we argue that $f(T, V_G)/f_0$ will have an exponential dependence on V_G and we can write the dependence of $f(T, V_G)$ on T and V_G as :

$$f = f_0(T)\exp\left(-\frac{V_G}{V_0}\right) \quad (5.8)$$

, where $f_0(T)$ describes the T dependent evaluation of f at $V_G = 0$ as stated before. The scaling voltage V_0 it self may have a T dependence because it can have dependence on ϵ_r as well as n_{3D} both of which have a T dependence. To check the above relation we plot the scaled graph where $\ln(f(T, V_G)/f_0)$ is

plotted vs. V_G/V_0 . We find that all the data for f can be merged on to the scaled curve that has a single parameter V_0 (shown in Fig. 5.18). The values of V_0 at each T needed to merge all the data on to a single curve is shown in the inset. Fig. 5.18 establishes the exponential dependence of the fraction f on the gate bias and it shows that the phase control is predominantly brought about by the control of the potential barrier ϕ_{GB} . The parameter $V_0(T)$ has a linear dependence on T .

5.4 Conclusion

We have shown that non-linear transport of a nano-structured perovskite manganite film can be substantially modulated at room temperature by applying a moderate gate bias using an EDL gate. The EDL gate has two effects. Firstly, it can control the depletion layer in GB transport and secondly it can control the relative ratio of the electronic phases within a grain. The non-linear transport in such films can occur due to the tunnelling through the barrier in the depletion layer in the GB region. Application of gate bias in the EDL layer leads to the change in hole concentration in the channel which increases its conductance and decreases potential ϕ_{GB} in the depletion layer of the grain boundary. This leads to the modulation in the non-linear conduction. A change in the channel conductance by nearly $\pm 40\%$ can be achieved at room temperature with a gate bias of $V_G = \pm 5V$.

To make a correlation of the gate modulation with the drain-source response, we also studied the time responses of the drain current as well as the gate current when there is a step change in the gate bias. The two responses were found to be correlated. The low leakage current in our EDL-FET device ensure the electrostatic carrier modulation. The observation reported in this work has implication in such devices that using nano-structured films as a channel, where nanoscopic control of the grain boundary transport can be achieved by moderate gate bias using such EDL gate.

Finally, we have shown that using a gate with EDL dielectric, it is possible to control the co-existing phases in film of a low hole doped $\text{La}_{1-x}\text{Ca}_x\text{MnO}_3$ for $x = 0.15$. The field effect induced charges not only change the resistance of the film (channel in the FET device) but also changes the relative fraction f of the co-existing phases as well as the characteristics temperatures $T_{OO'}$, T_C^* and

T_{FI} . The change brought about by the field effect closely mimics (quantitatively) the change that can be obtained by chemical substitution. One of the important observation in this study is that the field effect can change the temperature associated with the $O - O'$ transition that shows a characteristic feature at $T_{OO'}$ identifiable from the resistance data. While $T_{OO'}$ gets suppressed on hole accumulation, the transition temperature to FM order T_C^* is enhanced. These two appear to converge to a common value $\approx 240\text{K}$, for a negative gate bias more than 6V. This value is very close to the highest value of T_C observed in $\text{La}_{1-x}\text{Ca}_x\text{MnO}_3$ system for $x \approx 0.33$. Though we could not establish the enhancement of T_C by the applied gate bias through direct magnetic measurements, it is intriguing that such a moderate gate bias (with EDL dielectric) can lead to enough hole density enhancement that the onset of the FM transition can be so much enhanced. This behaviour compares very well to the phase-diagram of $\text{La}_{1-x}\text{Ca}_x\text{MnO}_3$ when x is changed by substitution.

The film used in this work is a nano-structured film as opposed to epitaxial film used in past such studies. The nano-structured film has the additional factor of transport through the GB region that is controlled by ϕ_{GB} . The substantial control of the gate bias on the co-existing phases as well as on the charge transport in such film has been enabled by the effect of the gate bias on ϕ_{GB} which in effect controls the GB transport. We have shown that the exponential control of the gate bias V_G on f originates from the predominant control of ϕ_{GB} by V_G .

Chapter 6

Strain and Phase separation effect on the transport in ferromagnetic insulating manganite

The low hole doped manganites exhibit extensive phase separation and phase coexistence. We have studied the effect of strain (biaxial) as well as local strain inhomogeneity on phase separation and its effect on the electrical transport of $\text{La}_{0.85}\text{Ca}_{0.15}\text{MnO}_3$. In this composition range, one observes FMI state. The FM state in manganites is generally associated with electron itinerancy. DE mechanism, which is generally used to explain FM state in manganites, can not be used to explain the FMI state. Recent theories consider the FMI state as an inhomogeneous state that can be controlled by strain. In this chapter, we investigate the FMI state using strain as a variable. The effect of local electronic phase inhomogeneity on the conduction and its evolution with temperature is studied by local tunnelling conduction measurements using UHV STM. The investigations show that there are inhomogeneities in local tunnelling conductance in macroscopic length scales (sub 100 nm) which also change as the temperature changes. The growth of these nanoscopic inhomogeneities have strong dependence on the lattice mismatch. Tunnelling conductance measurement confirms that modulation of the density of states near the Fermi level is due to the strain and inhomogeneity which directly affect the electrical transport in these phase separated perovskites.

6.1 Introduction

Manganites with chemical composition $\text{La}_{1-x}\text{Ca}_x\text{MnO}_3$ have different kind of electronic phases depending on the degree of hole doping x [1, 2, 7, 50, 51, 139]. These complex electronic phases can have nearly similar energy and one can switch between different phases by means of external perturbations. Generally, these perturbations are electric & magnetic field, pressure or strain and size reduction to nanoregime. Due to this electronic phase coexistence, manganites shows some fascinating range of electronic and magnetotransport behaviour and it allows us to control different electronic properties by using suitable control parameters [1, 2]. There is also another important aspect that the scale of phase separation in these materials can indeed be on a wide length scale from a scale of few unit cells to mesoscopic scales extending over hundreds of nm [55, 59, 199]. Many properties of manganites are closely related to such intrinsic phase separation. The occurrence of phase inhomogeneity has been proposed to be related to CMR effect observed in manganites [65, 200, 201]. The presence of these phase separated regions in manganites can be probed experimentally by measuring the local conductance of the material in UHV-STM [58, 59]. There are also studies using TEM [132]. The tunneling current between the sample and the STM tip is directly correlated to the local density of states (DOS) of the material [122–124] which can be used to measure the spatial variation of the DOS near the fermi level. This helps us to measure the local conductance of the material belonging to certain electronic phase. It has been known that the DOS in manganites have a strong temperature dependence even when the manganite is in FMM state. A gap opens up in DOS at the onset of insulating state (as in COI state). The DOS thus will be a sensitive probe to investigate phase separation in FMI.

Phase separation has a special significance in the context of the FMI state. Here, we will briefly elaborate this particular issue. The coexistence of ferromagnetism and insulating behaviour contradicts the conventional DE model in manganites. The FMI state is also distinct from the COI state. This may be appreciated from the fact that the COI state can be destabilized by magnetic field [35] while MR collapses in FMI state. The FMI state can be perturbed by external pressure due to its relation to the orbital order [202]. The origin of the phase coexistence is not clear. However, it is believed that it arises

from a balance between orbital ordering (leads to charge localisation) and FM interactions [203]. The orbital order (or disorder) originates from the JT distortion of the MnO_6 octahedra. Therefore, local strain, in particular, anisotropic strain can affect the orbital order. The variation of local strain can affect the balance between the charge localisation and delocalisation (due to FM interaction). This leads to phase separation between phases of different electrical conductivities [7, 204, 205]. Recent theoretical investigation [206] showed that coexisting phases can have length scales in nanoscopic domain. These coexisting phases are amenable to strain inhomogeneities that occurs even in films grown on single crystalline substrates.

It is now established that the phenomena of phase separation depends on strain (biaxial) as well as local strain inhomogeneity that can act as nucleating site for the phase separation [55, 65, 199, 207, 208]. The effects of epitaxial strain are different from the changes induced by external parameters like hydrostatic or chemical pressure. Hydrostatic pressure and chemical pressure are generally isotropic in nature. However, the substrate induced strain is intrinsically anisotropic because the in-plane strain leads to an out-of-plane strain with different sign due to Poisson ratio. The lattice-substrate mismatch induces phase separation and inhomogeneities in films and thus causes electronic behaviour which was not found in bulk materials of same composition [55, 65, 199, 207, 208]. The hole doped manganite $\text{La}_{1-x}\text{Ca}_x\text{MnO}_3$ with $x = 0.15$ is sandwiched between insulating orbitally ordered AFM phase for $x = 0$ and FMM phase for $x \geq 0.22$. An intermediate FMI phase occurs for $0.13 < x < 0.22$ at low temperature. The FMI state (having a low carrier density) is susceptible to orbital disorder. The orbital ordering (which controls the hole mobility) in presence of long range coulomb interaction (that occurs in a low carrier density system due to lack of shielding) can lead to open a soft gap in the DOS. This is the coulomb gap [204, 206, 209]. Hopping conductance in presence of such a gap has observable consequence. A consequence of such a scenario is the emergence of electronic glassy state leading to slow charge relaxation [210]. Existence of such a glassy region in the FMI state has been observed through non-Gaussian resistance fluctuation [211].

Lattice distortion due to strain plays a crucial role in the phase separation scenario in managinites [212, 213]. Lattice distortion modifies (increase or decrease) the JT distortion around e_g localized

electrons in MnO_6 octahedra [208,214]. These distorted octahedra may arrange themselves differently in various crystallographic planes giving rise to short and long wave length lattice distortions. These lattice distortions have been proposed to be at the origin of the energy landscape responsible of the inhomogeneous ground state [212,215]. Although the issue of strain has been discussed in context of nanoscopic phase separation in hole doped manganites, there has been no detailed experimental investigation on the effect of biaxial strain in the phase separation. In particular, local probes like STM has not been used for the measurement of electronic phase inhomogeneities. STM is particularly suitable for this kind of investigation because of its nanoscopic spatial resolution and its capability to probe the local DOS.

In this work, we investigated the effect of substrate induced biaxial strain and the local phase separation effect on the electric transport of a FMI thin film of $\text{La}_{0.85}\text{Ca}_{0.15}\text{MnO}_3$ (thickness ≈ 10 nm) grown epitaxially on single crystal substrates of NdGaO_3 (NGO), SrTiO_3 (STO) and LaAlO_3 (LAO). Films were grown on different substrates to tune the strain in the FMI state. Though, it is an interesting way to control the biaxial strain in the film, there are complexities to estimate the strain. This is due to the extent of strain relaxation in the films. Here, we will discuss this issue. We have also studied these local electronic inhomogeneities by tunnelling conductance measurement. We observed that the temperature dependent electronic transport in the three films are different having coexisted electronic phases (PI, FM and FMI) in a specific temperature range. To explain the observed difference in the electronic transport, we have measured the local conductance variation on these films (film on NGO and STO) at different temperatures in UHV-STM. We found that the scale of inhomogeneity is markedly different in the two films. The magnitude and nature of the local conductance in two films varies with the temperature. We found that the substrate induced strain and local inhomogeneity plays a crucial role to govern the electronic transport in low hole doped manganite. The "local" STM investigation was supplemented with "bulk" measurements like resistivity.

6.2 Substrate induced strain in the film of $\text{La}_{0.85}\text{Ca}_{0.15}\text{MnO}_3$

In this section, we will discuss how the strain varies in a film when deposited on different substrates with different lattice constants. For our investigation, we have used films of $\text{La}_{0.85}\text{Ca}_{0.15}\text{MnO}_3$ epitaxially grown on single crystal substrates of NGO (2 0 0), STO(2 0 0) and LAO (1 0 0) (discussed in chapter 2). To calculate the nature of the strain, we have done the rocking curve measurement of the film (detail procedure in chapter 2). We have varied the angle 2θ between the incident x-rays ($\text{CuK}\alpha$) and the detector keeping the angle between the incident x-rays and sample surface ω fixed (generally, ω is fixed at the half of the value of peak position (2θ) of the substrate.) Rocking curve of the films on LAO (1 0 0), NGO (2 0 0) and STO (2 0 0) are shown in Fig. 6.1. To determine the sample and substrate peak

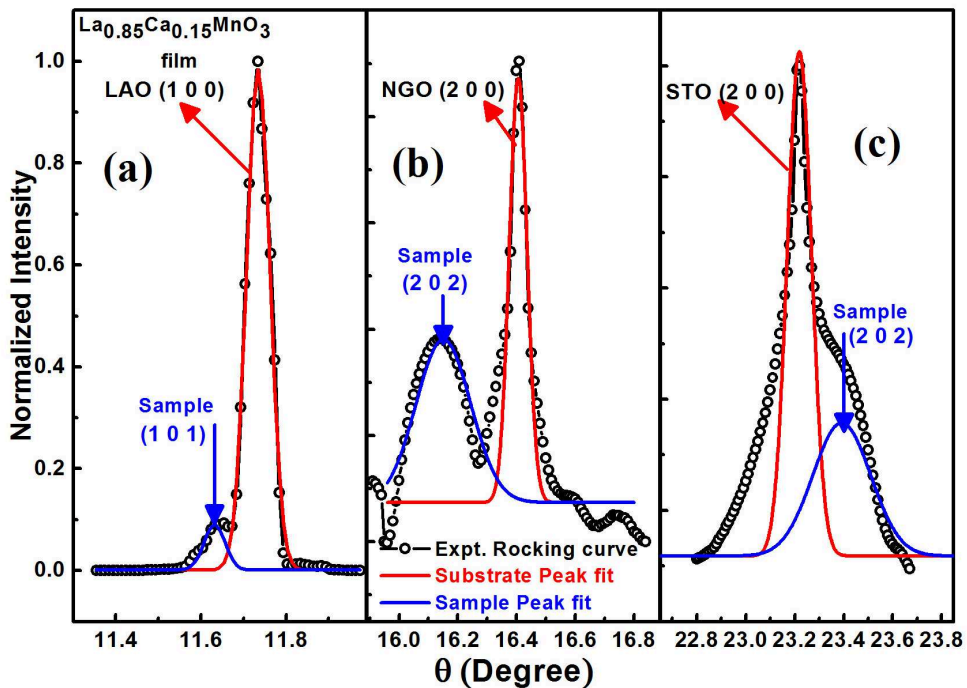


Figure 6.1 Rocking curve of the $\text{La}_{0.85}\text{Ca}_{0.15}\text{MnO}_3$ film on (a) LAO (1 0 0) (b) NGO (2 0 0) and (c) STO (2 0 0). Films were grown in the same deposition process using same deposition condition.

positions, we have fitted the experimental curve by Gaussian multiple peaks (shown in Red and blue curve in Fig. 6.1). From Fig. 6.1, it can be seen that sample peak (θ_{film}) appears very close ($< 0.4^\circ$) to the substrate peaks (θ_{sub}) which signifies that the deposited film tried to follow the lattice direction of the substrate. The major substrate peaks at $2\theta \approx 23.46^\circ$, 32.9° and 46.4° matches with the standard (1 0

0), (2 0 0) and (2 0 0) peaks of LAO, NGO and STO substrates. The sample peak appears at lower angle of 23.12° and 32.3° than the substrate peak for the film on LAO (1 0 0) and NGO (2 0 0) substrates while it appears (46.78°) at higher angle for STO(2 0 0). The 2θ values for $\text{La}_{0.85}\text{Ca}_{0.15}\text{MnO}_3$ film on LAO, NGO and STO nearly matches with the crystallographic orientations (1 0 1), (2 0 0) and (2 0 2) having values 22.89° , 32.50° , 46.76° respectively. The 2θ values of the films slightly differs from the 2θ values of the bulk $\text{La}_{0.85}\text{Ca}_{0.15}\text{MnO}_3$ with the above mentioned crystallographic orientations. This indicates that the lattice spacing (d) of the film is different (as $2d\sin\theta = n\lambda$) for the three substrates. This is due to the substrate induced strain. The bulk $\text{La}_{0.85}\text{Ca}_{0.15}\text{MnO}_3$ and NGO (2 0 0) single crystal substrate have orthorhombic structure ($a_{or} \neq b_{or} \neq c_{or}$) and can be represented with pseudocubic lattice constants $a = c = \frac{1}{2}\sqrt{(a_{or})^2 + (b_{or})^2}$ & $b = \frac{c_{or}}{2}$. The LAO (1 0 0) single crystal substrate has Rhombohedral crystal structure ($a = b = c$, $\alpha = \beta = \gamma \neq 90^\circ$) and STO (2 0 0) single crystal substrate has cubic structure ($a = b = c$, $\alpha = \beta = \gamma = 90^\circ$). The lattice constants of bulk $\text{La}_{0.85}\text{Ca}_{0.15}\text{MnO}_3$, LAO, NGO and STO are tabulated in table 6.1. Due to the mismatch of the lattice parameters (a , b & c) between

Table 6.1 Orthorhombic and pseudocubic lattice constants and lattice spacing of bulk $\text{La}_{0.85}\text{Ca}_{0.15}\text{MnO}_3$ and NGO, LAO and STO substrates from ICDD data base and MTI corporation.

Sample	a (in Å)	b (in Å)	c (in Å)	a_{cubic} (in Å)	d (in Å)
$\text{La}_{0.85}\text{Ca}_{0.15}\text{MnO}_3$	5.50	5.48	7.74	3.88	2.75 (for 2 0 0)
					5.52 (for 1 0 0)
LAO	3.79	3.79	3.79	3.79	3.79
NGO	5.44	5.50	7.71	3.86	2.72
STO	3.90	3.90	3.90	3.90	1.95

the substrate and the $\text{La}_{0.85}\text{Ca}_{0.15}\text{MnO}_3$, the deposited film will be strained. We have calculated the in-plane (e_{\parallel}) and out of plane (e_{\perp}) strains in the $\text{La}_{0.85}\text{Ca}_{0.15}\text{MnO}_3$ films considering the pseudocubic (a_{cubic}) values of $\text{La}_{0.85}\text{Ca}_{0.15}\text{MnO}_3$ bulk and the substrates as the bulk and substrates have different crystallographic structures [216]. The out of plane and in plane strain have the relation $e_{\perp} = -4 \nu e_{\parallel}$ with $\nu=0.3$ for managanites [208,217]. Negative and positive sign indicates the compressive and tensile

nature of the strain. The in-plane and out of plane strains are schematically shown in Fig. 6.2. . In

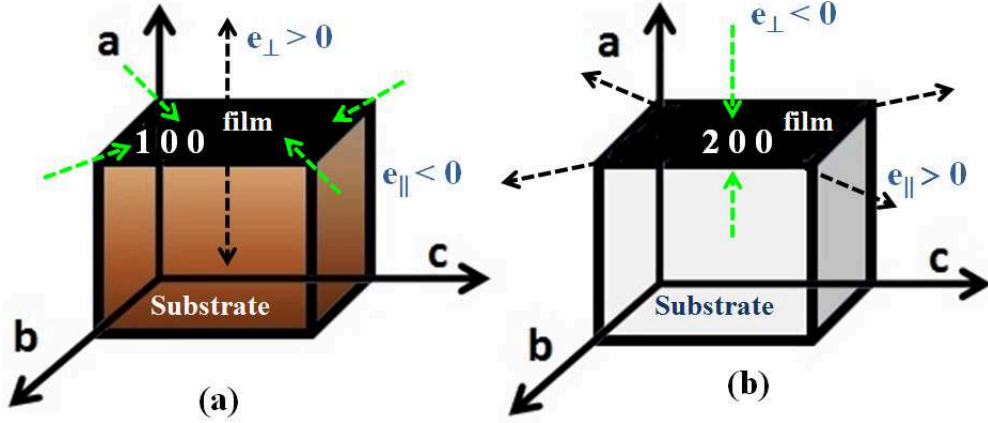


Figure 6.2 Schematic diagram of the nature of substrate induced strain due to lattice mismatch when (a) $a_{Sub} < a_{bulk}$ and (b) $a_{Sub} > a_{bulk}$.

table 6.2, we have tabulated e_{\parallel} & e_{\perp} acting in the $\text{La}_{0.85}\text{Ca}_{0.15}\text{MnO}_3$ films along in-plane and out of plane directions. We have calculated the strain as $e = \frac{(A_{Sub} - A_{bulk})}{A_{bulk}}$, where A is the a_{cubic} values of the bulk $\text{La}_{0.85}\text{Ca}_{0.15}\text{MnO}_3$ and the three substrates. However, the strain generated due to lattice mismatch will act on few atomic layers of the film and after that the film can be strain relaxed. The extent of this strain relaxation will depend on nature of growth of the deposited film on different substrates. We have

Table 6.2 Values of e_{\parallel} , e_{\perp} along in plane and out of plane directions in the $\text{La}_{0.85}\text{Ca}_{0.15}\text{MnO}_3$ film and the effective strain in the film.

Film	Substrate induced strain		Effective strain (e_{Eff})
	e_{\parallel}	e_{\perp}	
Film on LAO	-2.3%	2.76%	2.6%
Film on NGO	-0.5%	0.6%	-0.5%
Film on STO	0.5%	-0.6%	0.04%

also calculated the effective strain in the $\text{La}_{0.85}\text{Ca}_{0.15}\text{MnO}_3$ film comparing the slight mismatch of the 2θ values between the film and bulk $\text{La}_{0.85}\text{Ca}_{0.15}\text{MnO}_3$ with same crystallographic orientations as it is appeared in the rocking curve. The effective strain is calculated as $e_{eff} = \frac{\Delta d}{d} = \frac{\sin\theta_{film} - \sin\theta_{bulk}}{\sin\theta_{film}}$, where we have considered the 2θ value for $\text{La}_{0.85}\text{Ca}_{0.15}\text{MnO}_3$ film and bulk $\text{La}_{0.85}\text{Ca}_{0.15}\text{MnO}_3$ for same

crystallographic orientations. From the table 6.2, it can be seen that $\text{La}_{0.85}\text{Ca}_{0.15}\text{MnO}_3$ film on LAO, NGO & STO suffers different kind of strains in different crystallographic directions. Interestingly, the e_{Eff} for the film on STO is nearly zero or the film is strain relaxed. e_{Eff} for the films on the three substrates differs in nature and magnitude. Out of the three films, film on LAO suffers the highest e_{Eff} . e_{Eff} in the film actually gives us the total strain which the film is actually suffered. The difference in the e_{Eff} for the three films also visible in their topographic images (shown in Fig. 6.3). From. Fig. 6.3,

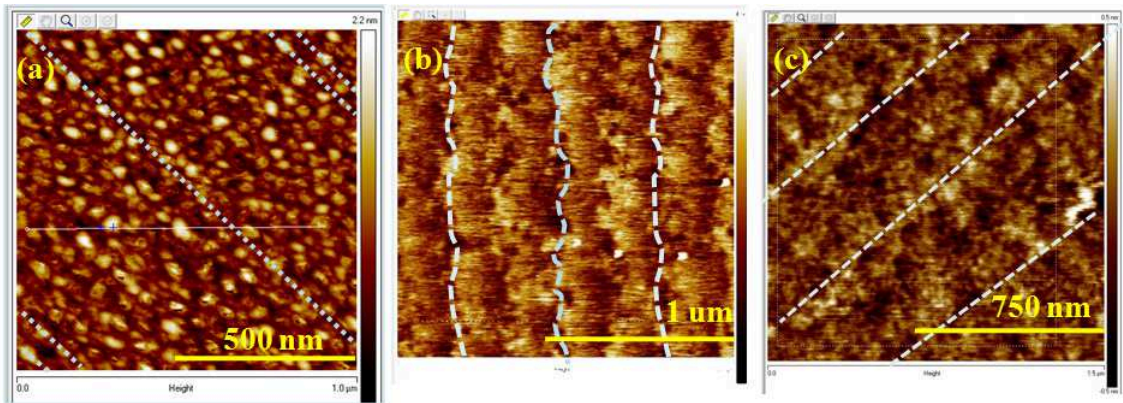


Figure 6.3 AFM image of the $\text{La}_{0.85}\text{Ca}_{0.15}\text{MnO}_3$ thin film deposited with 1000 laser shots in PLD on (a) NGO, (b) LAO and (c) STO substrates. Dotted lines are showing the preferred pattern of the films.

It can be seen that as the film on LAO suffered highest e_{Eff} , it has layered growth pattern with very low surface roughness of few unit cells. On the other hand, as the films on STO and NGO are more or less strain relaxed, they have island type grain growth with surface roughness of 1-2nm.

It can be observed that the difference in e_{Eff} in the films leads to electronic phases inhomogeneity. This will in turn affect the conduction process [208] (discussed in later section).

6.3 Determination of the Scale of inhomogeneity present in the three thin films by local conduction mapping

In the previous section we have found that $\text{La}_{0.85}\text{Ca}_{0.15}\text{MnO}_3$ film suffers different e_{Eff} when grown on various substrates. In this section, we will investigate the extent of inhomogeneity and nanoscale phase separation present in the three thin films as the growth of these nanoscopic inhomogeneities have

strong dependence on the built in strain that arises due to lattice mismatch. These local inhomogeneities and nanoscale phase separations can be probed well by using a scanning tunnelling microscope (STM) [58,59]. In particular, the length scale of the phase separation is expected to be nanoscopic/mesoscopic and more than an unit cell. As a result mapping of local tunneling conductance by STM, that gives information on the local DOS will be a useful tool.

In scanning tunnelling microscope, generally a metal tip is used to measure the tunnelling current between the sample surface and tip through a barrier (ultra high vacuum) for a given applied bias. The tunnelling current between the sample and the tip (I_t) is directly proportional to the tip sample distance(z), local density of states (N_s) of the sample and applied voltage (V) and can be expressed as

$$I(z, V, W, T) = c \int_{-\infty}^{\infty} N_s \left(E + \frac{eV}{2} \right) N_t \left(E - \frac{eV}{2} \right) \Gamma(z, E, W) \left[f \left(E - \frac{eV}{2} \right) - f \left(E + \frac{eV}{2} \right) \right] dE, \quad (6.1)$$

where E is the energy of the tunnelling electron, c is a constant which depends on the tip-sample effective junction area, z is the tip-sample separation, W is the average work function of the tip and sample surface, V is the applied bias between tip and sample, T is the temperature, $N_t(E)$ is the tip DOS, $f(E)$ is the Fermi function at temperature T and Γ is the barrier penetration factor [125]. From equation 6.1, it can be seen that the tunnelling current is directly correlated to the local DOS ($N_s(E)$) of the localized region. For a fixed applied bias between the STM tip and the sample surface, the tunnel current can vary spatially over a nanoscale region due to the spatial variation of local DOS. The spatial variation of DOS will arise from the coexistence of different phases which are likely to have different DOS. The spatial variation will capture how the fraction of the coexisting phases changes over a length scale. High tunnelling current between the STM tip and sample surface signifies a region with large DOS while low tunnelling current represents an insulating region due to the existence of a gap in the DOS. Thus one can map these localised conductive and insulating regimes over a nanoscale area and correlated them to the direct measure of the nanoscale electronic phase separation in the sample.

For our investigation, we have measured the local conductance map (LCMAP) of the $\text{La}_{0.85}\text{Ca}_{0.15}\text{MnO}_3$ film on NGO and STO substrates over a localised area of $500\text{nm} \times 500\text{nm}$. Our lower limit for current detection (above noise floor) is 10pA. This corresponds to a tunneling resistance $\approx \text{G}\Omega$. We were not

able to do LCMAP on film on LAO due to undetectable tunnelling current for the high resistance of the sample (which can be seen in the $\rho - T$ data in later section). We have also studied the temperature evaluation of these nanoscopic electronic phases from room temperature to low temperature ($\approx 100\text{K}$). Below 100K , $\rho \geq 10 \text{ }\Omega\text{cm}$ (sheet resistance $\geq 10 \text{ M}\Omega$) which makes the STM measurement difficult due to low tunneling current. The LCMAP technique generates a two-dimensional map of the tunnelling conductance across the surface for a fixed bias and at a constant height (here height is the tunnelling barrier between STM tip and the sample) where the distance between the STM tip and sample is much higher than the height variation in different spots. This is achieved by applying a small a.c. bias modulation over the d.c. sample bias and using a lock-in amplifier to measure $\frac{dI}{dV}$ directly (detail procedure in chapter 2). Before capturing the LCMAP, we have selected an area of $500\text{nm} \times 500\text{nm}$. The topographic image of the specified area was taken by applying a 500mV bias and constant 1nA current between the sample surface and the STM tip (detail procedure in chapter 2). To take topographic image, a feedback loop is generally used to take care of the height variation in the sample surface so that the tunnel current remain constant. The movement of the piezo (attached with the STM tip) from the set reference level generates a topographic image of the sample surface. After taking the image, we took 256 points on this specified area in a form of a 16×16 matrix. In Fig. 6.4, we have shown the topographic image of the $\text{La}_{0.85}\text{Ca}_{0.15}\text{MnO}_3$ film on NGO substrate with 256 points in matrix form. The brighter regions in the image corresponds to higher z value (vertical distance or the height of the surface) and darker regions represent lower Z value. To generate the LCMAP in the specified area, we raster scan the STM tip (green arrow in Fig. 6.4) and took the $\frac{dI}{dV}$ spectra. In similar way, we have taken the LCMAP in the $\text{La}_{0.85}\text{Ca}_{0.15}\text{MnO}_3$ film on STO. We varied the applied bias between the tip and the sample surface from -1V to $+1\text{V}$. To generate the LCMAP over the specified region, we took the $\frac{dI}{dV}$ spectra at 256 points and generate a data set of conductance value for these points at specific voltage (0.5V). We have plotted the conductance $\frac{G}{G_{rms}}$ where G_{rms} is the root mean square conductance. This way of plotting help us to understand the variation of conductance from its rms value and we can compare the LCMAP at different temperatures which take care of the other effects that can perturb the tunnelling current between the STM tip and the sample surface. In Fig. 6.5(a),

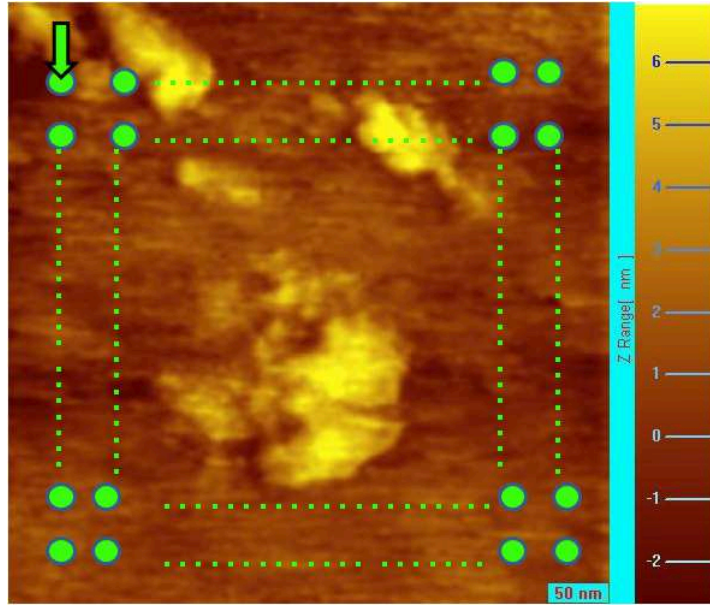


Figure 6.4 Topographic image of the $\text{La}_{0.85}\text{Ca}_{0.15}\text{MnO}_3$ film on NGO substrate in $500\text{nm} \times 500\text{nm}$ area. Green dots represents the points in a matrix from where $\frac{dI}{dV}$ spectra were taken and green arrow represents the position of the STM tip.

we have shown the variation of conductance ($\frac{G}{G_{rms}}$) over a specified area at room temperature. Here X and Y axis denote the coordinates of the 256 points. The colour bar from blue to red is representing the variation in local conductance in a scale of 0 to $4 \frac{G}{G_{rms}}$. It can be clearly seen from Fig. 6.5(a) that there is a existence of mixed conductive regions in the $\text{La}_{0.85}\text{Ca}_{0.15}\text{MnO}_3$ film on NGO. The presence of higher conductive ($\frac{G}{G_{rms}}$ is higher) regions (yellow to red) is very less in the specified region. The region is full of lower conductive regions (blue colour, $< 0.8 G_{rms}$) and mid conductive regions (green band or 1.2 to $2.0 G_{rms}$). In Fig. 6.5(a), we have marked one of the lower conductive regions of the value $0.28 G_{rms}$ with the boundary in black. Though these regions are not too many, their number is finite. To investigate how does these electronic inhomogeneities evolve with temperature, we have cooled down the sample to 110K and LCMAP was done at that temperature. In Fig. 6.5(b), we have shown the LCMAP at 110K. At 110K, the film grown on NGO is at the threshold of entering into the FMI state or has just entered the state. It is found that that there is a presence of inhomogeneity in the $\text{La}_{0.85}\text{Ca}_{0.15}\text{MnO}_3$ film on NGO. The LCMAP at 110K is clearly different from that at 300K. We can see that the contributions of lower conductive regions 0.28 (marked as black boundary) increases from

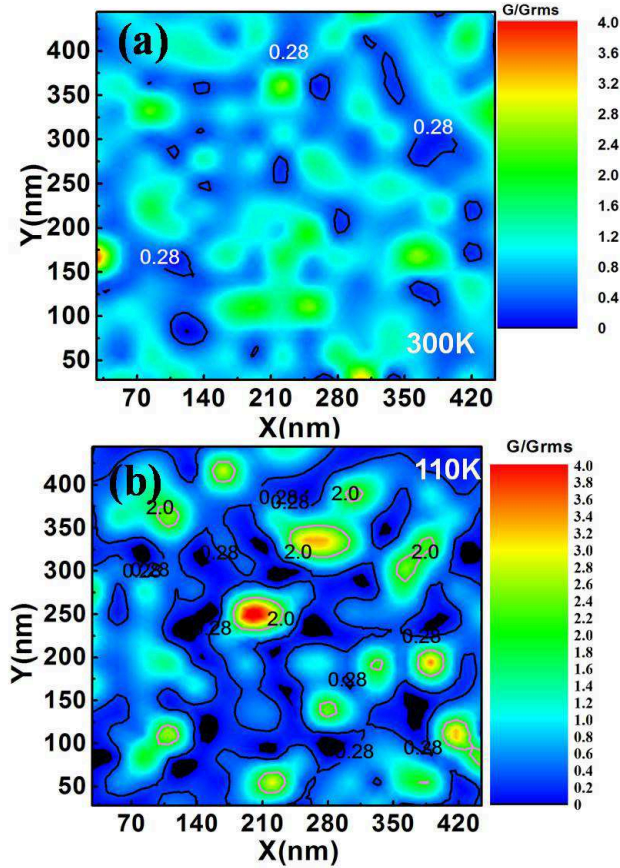


Figure 6.5 Local conduction mapping (LCMAP) in a $500\text{nm} \times 500\text{nm}$ area for $\text{La}_{0.85}\text{Ca}_{0.15}\text{MnO}_3$ film on NGO at (a) 300K and (b) 110K at 0.5V. Colour code (from blue to red) represents lower conductive region to higher conductive regions.

300K and nearly continuous except in few regions. The inhomogeneity is distinctly enhanced. Some high conductive regions (yellow to red) can be noticed in specified areas in the sample which was not observed in case of LCMAP at 300K. There are also some mid conductive regions which has value between 1.2 to $2.0 G_{rms}$ and we marked one of these regions in Fig. 6.5(b) with value $2.0 G_{rms}$ (having boundary in magenta colour). We have also found some regions which are black, from which actually there is no tunnel current between STM tip and the sample surface. These black regions are highly insulating regions where the $\text{DOS} \rightarrow 0$ near the Fermi level. From Fig. 6.5(a) and (b), It is clear that the temperature has a strong effect and on cooling the sample down to the onset of FMI phase, it becomes more inhomogeneous with insulating phase becoming a dominant phase.

We have done similar LCMAP in the $\text{La}_{0.85}\text{Ca}_{0.15}\text{MnO}_3$ film on STO for 0.5V at 110K and 300K (data

are shown in Fig. 6.6). These local conduction maps give us a clear insight how does the electronic inhomogeneities vary in the $\text{La}_{0.85}\text{Ca}_{0.15}\text{MnO}_3$ film grown on two different lattice match substrates. From Fig. 6.6(a), it can be seen that at room temperature the $\text{La}_{0.85}\text{Ca}_{0.15}\text{MnO}_3$ film on STO is more

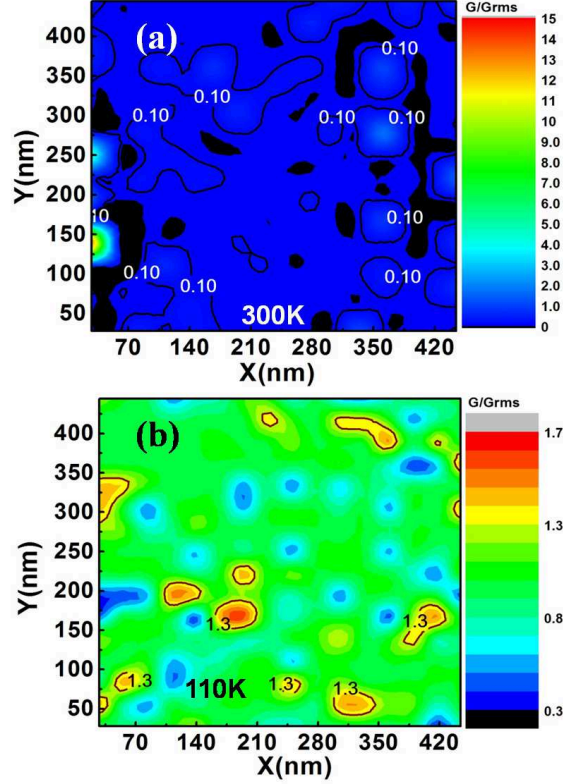


Figure 6.6 Local conduction mapping(LCMAP) in a $500\text{nm} \times 500\text{nm}$ area for $\text{La}_{0.85}\text{Ca}_{0.15}\text{MnO}_3$ film on STO at (a) 300K and (b)110K. Colour code (from blue to red) represents lower conductive region to higher conductive regions.

homogeneous than the film on NGO (in Fig. 6.5(a)). The specified area is almost covered with similar conductive regions (coloured blue). We have marked one of the conductive region having value $0.1 G_{rms}$ (with boundary in black) in Fig. 6.6(a). There also exists some regions which are highly insulating and appears as black. When the sample was cooled down to 110K, electronic inhomogeneity (having conductive regions of lower to higher value) in the specified area increases. However, the inhomogeneity is distinctly less with most regions having $\frac{G}{G_{rms}}$ values form 0.8-1.2. We have marked one of the higher conductive regions having value $1.3 G_{rms}$ (boundary in wine colour) in Fig. 6.6(b). LCMAP in the $\text{La}_{0.85}\text{Ca}_{0.15}\text{MnO}_3$ films on NGO and STO over a specified area establishes the existence of local

inhomogeneity in the two samples. The scale of electronic inhomogeneity or the phase separation is different in the two samples. It appears that the film on STO is more homogeneous in terms of fluctuations of local conductance and thus in DOS. It may be due to the fact that the film on STO is nearly strain relaxed. We have observed some black regions in both films form where we have get very little tunnel current. If the concentrations of these regions become very high in a specified area, it would be difficult to image as well as took $\frac{dI}{dV}$ spectra from that region. As the $\text{La}_{0.85}\text{Ca}_{0.15}\text{MnO}_3$ film on LAO is highly insulating, we were unable to generate a local conduction map on this film.

6.4 Differences in tunnelling conductivities in $\text{La}_{0.85}\text{Ca}_{0.15}\text{MnO}_3$ films grown on NGO and STO substrates

In section 6.3, we observed that the scale of local electronic inhomogeneity or phase separation present in the $\text{La}_{0.85}\text{Ca}_{0.15}\text{MnO}_3$ film on NGO and STO substrates are different. In this section, we will find out the nature of the conductance (G) curve with applied STM bias (V) for the film on NGO and STO. It was found that the tunneling $G - V$ curves for metal, semiconductor and insulator are different as the tunnelling current between the sample and tip (I_t) is directly proportional to the tip sample distance (z), local density of states (N_S) of the sample and applied voltage (V) (as shown in eqn. 6.1). For most of the cases we used a metal tip and consider N_t as a constant. So the tunnelling conductance $G (\approx \frac{dI}{dV})$ is directly proportional to the DOS of the sample N_S keeping the other parameters constant. As the DOS near Fermi level is different for metal, semiconductor and insulator, the nature of the $G - V$ curve also changes from sample to sample.

From the LCMAP of the $\text{La}_{0.85}\text{Ca}_{0.15}\text{MnO}_3$ film on NGO at 110K (in Fig. 6.5(b)), we found some nanoscopic regions of lower and higher conductivities having size $\approx 50\text{nm}$. Here, we represent low conductive regions as phase-I and high conductive regions as phase-II. In Fig. 6.7, we have shown the $G - V$ curve in the phase-I & phase-II regions at 110K. From Fig. 6.6, we can see that G in phase-II region steeply increases with V and $G(V)$ is higher than the phase I region. In tunnelling conductance measurement, the Fermi level (E_F) situated at $V = 0$. As the presence of phase-II regions (red colour)

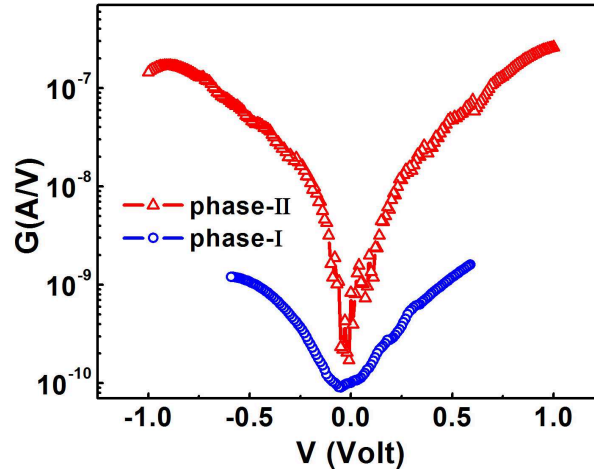


Figure 6.7 $G - V$ curve in the phase-I & phase-II (blue and red coloured regions in LCMAP) in $\text{La}_{0.85}\text{Ca}_{0.15}\text{MnO}_3$ film on NGO at 110K .

is less than the phase I regions (blue colour), G falls sharply in the voltage range $-0.125 \leq 0 \leq 0.125$. It is clear from Fig. 6.7 that the phase-I & II regions have distinct features in LCMAP for $\text{La}_{0.85}\text{Ca}_{0.15}\text{MnO}_3$ film on NGO at lower temperature. The sharp bias dependence of the $G - V$ curve on V at low bias for the phase II region is reminiscent of a Coulomb glass or that expected in a system with a Coulomb gap. It is quite likely that the phase-II regions are insulating due to the presence of a Coulomb gap and is distinct from the phase-I regions where there may actually be a gap (though small) at Fermi level.

Similarly we have taken the $G - V$ curve in phase-I & phase-II regions in LCMAP in the $\text{La}_{0.85}\text{Ca}_{0.15}\text{MnO}_3$ film on STO. In Fig. 6.8, we have shown the $G - V$ curve for $\text{La}_{0.85}\text{Ca}_{0.15}\text{MnO}_3$ film on STO at phase-I & phase-II regions at 110K. From Fig. 6.8, it can be seen that $G - V$ curves for phase-I and phase-II regions markedly differs from $\text{La}_{0.85}\text{Ca}_{0.15}\text{MnO}_3$ film on NGO (in Fig. 6.7). Here, we observe that G in phase-I region steeply decreases near the Fermi level E_F . But G in phase-II regions has not fallen sharply in the vicinity of $V = 0$ or near E_F having a finite conductance. This would imply that the phase-II regions are actually metal like with extended states. The value of G at $V = 0$ for these regions is also larger than that seen for phase-II region for the film on NGO. The phase-I regions that show deep in $G - V$ curve near $V = 0$ can also arise from a coulomb gap. The insulating region in this film thus can be an electron glass.

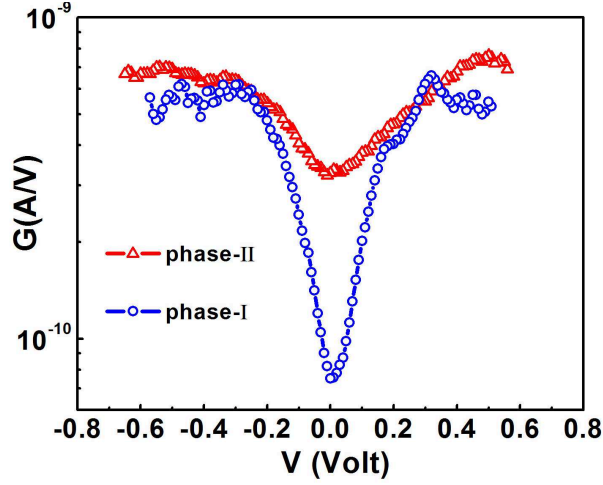


Figure 6.8 $G - V$ curve in the phase-I & phase-II regions (blue and red coloured regions in LCMAP) in $\text{La}_{0.85}\text{Ca}_{0.15}\text{MnO}_3$ film on STO at 110K .

6.5 Effect of strain and inhomogeneity on the electronic transport of the $\text{La}_{0.85}\text{Ca}_{0.15}\text{MnO}_3$ film grown on different substrates

From sections 6.2 and 6.3, it is clear that the films of $\text{La}_{0.85}\text{Ca}_{0.15}\text{MnO}_3$ grown on NGO, LAO, STO substrates have not only different e_{Eff} but also have electronic phase inhomogeneity evolving with temperature. In this section, we will explore the effect of strain and inhomogeneity on the electrical transport of $\text{La}_{0.85}\text{Ca}_{0.15}\text{MnO}_3$ films grown on different substrates. To investigate the electronic transport properties of the film, temperature dependence of resistivity (ρ) were measured on the $\text{La}_{0.85}\text{Ca}_{0.15}\text{MnO}_3$ films grown on NGO, STO and LAO substrates. $\rho - T$ measurements of the films were done from room temperature to low temperature (up to 50K) using a low constant current of $1\mu\text{A}$ in four probe (thermally evaporated Au/Ti pads) method (we stopped our measurement at 50K as the sample resistance was so high below 50K that it reach the compliance limit of the measuring instrument). $\rho - T$ curves of the films on the different substrates are shown in Fig. 6.9(a). From Fig. 6.9(a), it can be seen that substrate induced strain and inhomogeneity significantly changes the $\rho - T$ curves of the $\text{La}_{0.85}\text{Ca}_{0.15}\text{MnO}_3$ film on the three substrates. At low temperature (below 150K), ρ of the film on LAO is slightly higher than the other two films. The ρ of the film on LAO and NGO are nearly similar in magnitude having different T dependence. The film on STO shows lower resistivity than the other

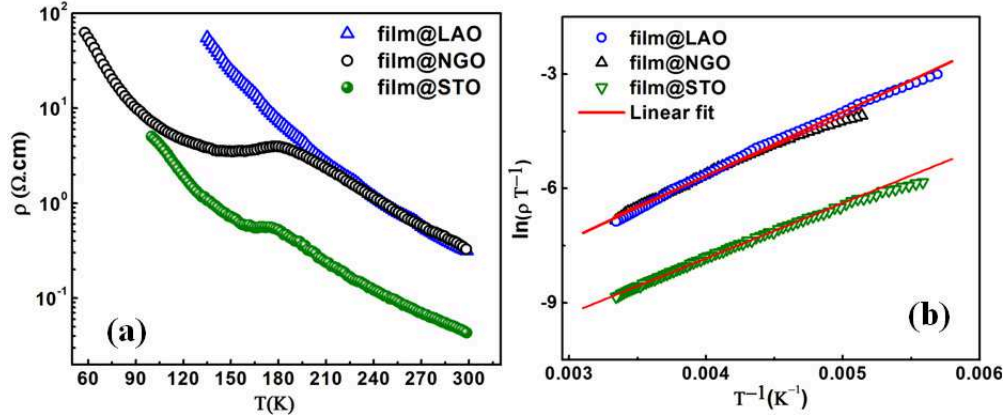


Figure 6.9 (a) $\rho - T$ curves of the film on LAO, NGO and STO (b) Adiabatic polaronic fit to the $\rho - T$ curves.

two films up to 100K but after that the ρ increases steeply and becomes comparable to the ρ of the film on NGO.

The high temperature ($> 200\text{K}$) electrical transport of manganites can be well described by the adiabatic polaronic model (see equation 3.1). In Fig. 6.9(b), we have plotted $\ln(\rho T^{-1})$ vs. T for all the films and the slope of the curve gives us the activation energy E_a (see section 3.2 ,chapter 1). The values of E_a for the films on LAO, NGO and STO are tabulated in table 6.3. The activation energy E_a for the

Table 6.3 Values of E_a for $\text{La}_{0.85}\text{Ca}_{0.15}\text{MnO}_3$ film on LAO, NGO and STO.

Energy	film on LAO	film on NGO	film on STO
E_a (in meV)	161	134	125

films grown on NGO and STO are closer but that in the film grown on LAO is much larger leading to a high resistance in the film. We found that the three films not only differ by ρ and E_a , they show dissimilar existence of electronic phases as discussed below. To clearly mark the different electronic phases present in the three samples, we have taken the derivative of the $\rho - T$ curve (shown in Fig. 6.10) where we plot, $\frac{d(\ln\rho T^{-1})}{d(T^{-1})}$ as a function of T for the $\text{La}_{0.85}\text{Ca}_{0.15}\text{MnO}_3$ film on the three substrates. From Fig. 6.10, it can be seen that the derivative curve accentuates the three regions (regions I, II, and III) clearly as a deviation from a smooth variation for the $\text{La}_{0.85}\text{Ca}_{0.15}\text{MnO}_3$ films on NGO and STO. We marked these temperatures for the $\text{La}_{0.85}\text{Ca}_{0.15}\text{MnO}_3$ films on NGO, STO and LAO substrates. In

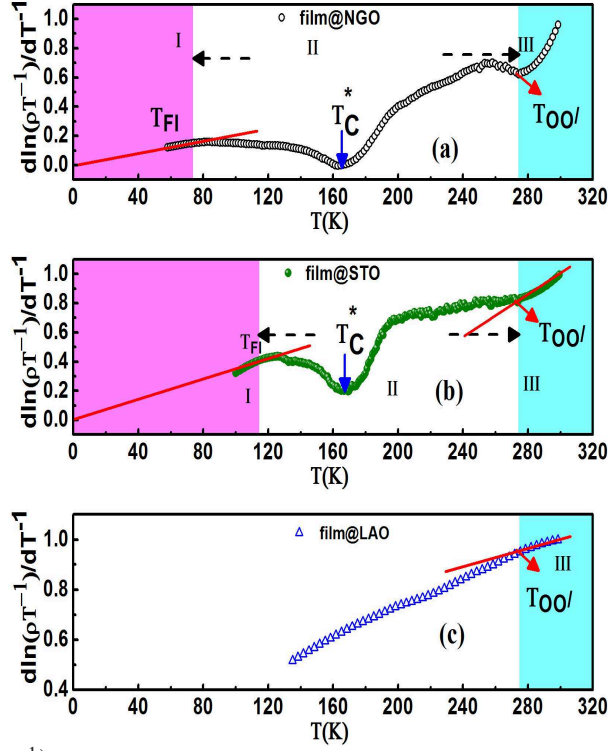


Figure 6.10 $\frac{d(\ln\rho T^{-1})}{d(T^{-1})}$ vs. T for film on LAO, STO and NGO. Region I, II and III represents different coexisting electronic phases.

region III, the system is in PI state with orthorhombic phase with JT distortions (O phase), in region I it is in a low temperature FMI state, and in region II it is a predominantly mixed phase region with co-existing low resistance FM phase (which may be metallic) and an high resistance insulating phase with different crystallographic structures like "O" and O' phases (orthorhombic phase with rotated regular octahedra) [1, 2, 7, 50, 51, 139]. We have marked $T_{OO'}$ in Fig. 6.10 where the $\frac{d(\ln\rho T^{-1})}{d(T^{-1})}$ vs T curve change its slope at the OO' structural transition. In region II, the PM to FM transition shows a change in the slope of the $\rho - T$ curve. This we mark as the temperature T_C^* (Note: We do not call it a FM transition temperature T_C as it is not determined by a magnetic transition in our experiment). In region I, the onset of the FMI state is marked by the temperature T_{FI} . From Fig. 6.10, we found that for all the $\text{La}_{0.85}\text{Ca}_{0.15}\text{MnO}_3$ films $T_{OO'}$ occurs around the same temperature ($\approx 270\text{K}$) and T_C^* ($\approx 170\text{K}$) for the $\text{La}_{0.85}\text{Ca}_{0.15}\text{MnO}_3$ film on NGO and STO are also same. But the PI to FM transition does not appear for the film on LAO. The width (ΔT) of the mixed phase region (II) is different for the $\text{La}_{0.85}\text{Ca}_{0.15}\text{MnO}_3$

film on NGO and STO while it is not evident for the film on LAO. This extended mixed phase region for the film on NGO makes it more inhomogeneous than the other two films which is also evident from our LCMAP mapping in section 6.3. T_{FI} shifts to higher temperature for the film on STO compared to that seen on the film on NGO.

The change in ρ in the three films on three different single crystal substrates can be linked to the nature of the lattice induced strain and extent of nanoscale inhomogeneities present in the films. In the next section we will discuss how strain and inhomogeneity can play a role to determine the electronic transport in manganite.

6.6 Discussion

In this section, we will discuss the effect of substrate induced strain and nanoscopic phase separation in electronic transport of the $\text{La}_{0.85}\text{Ca}_{0.15}\text{MnO}_3$ film when grown on three slightly different lattice matched substrates. In section 6.2, we have found that the three films suffer dissimilar strain (in nature and magnitude) due to the lattice mismatch between the substrate and the film and the effective strain determines the scale of inhomogeneity. The $\text{La}_{0.85}\text{Ca}_{0.15}\text{MnO}_3$ film on LAO suffers an effective out of plane tensile (in plane compressive) strain while $\text{La}_{0.85}\text{Ca}_{0.15}\text{MnO}_3$ film on NGO suffers a small out of plane compressive strain. The film on STO is nearly strain relaxed. In manganites, eight MnO_6 octahedra situated at the corners of a cube with rare earth element (in this case La) at the body centred position. Due to the crystal field symmetry, the five degenerate "d" levels in Mn^{3+} splits into e_g and t_{2g} levels where e_g levels are higher in energy than the t_{2g} levels. If there is one electron at e_g site, e_g level splits up into $d_{x^2-y^2}$ and $d_{3z^2-r^2}$ levels. Due to this a structural orthorhombic distortion occurs which is called JT distortion and the electron become localized at lower energy ($d_{3z^2-r^2}$) level. Now in-plane compressive strain and out of plane tensile strain elongated the MnO_6 octahedra in crystallographic "c" direction which in turn increase the orthorhombic distortion in the perovskite unit cell making the system more insulating. On the other hand in- plane tensile and out of plane compressive strain reduce the orthorhombic distortion and this enhances the hopping rate of e_g electrons, which in turn

make the system less insulating. Thus out of plane tensile strain (or in plane compressive strain) enhances the orthorhombicity and favours the insulating behaviour. As the out of plane tensile strain is higher for LAO, it shows highly insulating behaviour in the electronic transport (in Fig. 6.9(a)). The $\text{La}_{0.85}\text{Ca}_{0.15}\text{MnO}_3$ film on the other substrates is more or less strain (effective) relaxed which actually leads to electronic phase inhomogeneity (for example phase-I & phase II regions in LCMAP). The variation of local strain in these two films (on NGO & STO) can affect the balance between charge localisation and delocalisation (due to FM interaction). This leads to phase separation between phases with different electrical conductivities. So the $\rho - T$ curve for $\text{La}_{0.85}\text{Ca}_{0.15}\text{MnO}_3$ film on NGO and STO shows low resistive behaviour than the film on LAO.

We have also found the evidence of phase coexisted regions (region I, II and III in Fig.6.9) in the three films from the derivative of the $\rho - T$ curve and the extent of these regions differ in the three films. The mixed phase region (region II) is more extended in case of the film on NGO than other two films. In Fig. 6.5(b) & 6.6(b), we have observed the presence of higher conductive regions at 110K and the scale of inhomogeneity is different in the film on NGO and STO. This can explain the existence of extended mixed phase region (region II) in the $\rho - T$ data of $\text{La}_{0.85}\text{Ca}_{0.15}\text{MnO}_3$ film on NGO. This leads to vary the scale of inhomogeneity in the three films which is also evident from the LCMAP of the $\text{La}_{0.85}\text{Ca}_{0.15}\text{MnO}_3$ films on NGO and STO (in section 6.3). From the LCMAP of the films (on NGO & STO) at 110K & 300K, it turns out that the film on STO is more homogeneous than the film on NGO. This is the reason that the film on STO shows higher conductivity than the film on NGO. It is also found that at low temperature lower end conductive regions (phase-I) dominates for the film on NGO (Fig. 6.5(b)) but for the film on STO, higher end conductive regions (phase-II) populate the area (in Fig. 6.6(b)).

Due to the combined effect of substrate induced strain/strain inhomogeneity and having different nanoscale electronic phase separation, the $\text{La}_{0.85}\text{Ca}_{0.15}\text{MnO}_3$ film shows dissimilar electronic transport behaviour. It is observed that the substrate induced strain and local inhomogeneity plays an important role in the electronic transport in hole doped manganites.

6.7 Conclusion

In conclusion, we have studied the effect of biaxial strain and inhomogeneity on the electrical transport of PLD grown $\text{La}_{0.85}\text{Ca}_{0.15}\text{MnO}_3$ film on three different substrates (NGO, STO and LAO). We have found that the effective strain in the three film is dissimilar in magnitude and nature. The three films shows different kind of electronic transport depending on the effective strain generated in the films. Local conduction mapping is done in the films using an UHV-STM to find out the scale of local inhomogeneities. We have also studied the temperature evaluation of these local inhomogeneities. We found that the scale of inhomogeneity differs in the two films on NGO and STO which in turn affects the electronic transport in them. The rocking curve analysis and LCMAP confirms that the strain and inhomogeneity can change the electronic transport in phase separated manganites considerably.

Chapter 7

Conclusion and future outlook

7.1 Conclusion

In this thesis, we have studied and investigated novel electrical and magnetic properties of perovskites, mainly manganites. The novel and interesting electronic and magnetic transport properties, like resistive switching, MR, modulation of GB conductance & tuning of electronic phases EDL-FET, effect of lattice strain and electronic inhomogeneity in the transport has been studied in detail. These effects are measured using external stimuli like electric field, magnetic field, electrostatic carrier induction by EDL gate and substrate induce strain. For these investigations, most of the experiments in this thesis has been carried out on good quality single crystals and nanostructured and epitaxial thin films. We have mainly focussed in the parent manganites like LaMnO_3 & GdMnO_3 and in the hole doped manganites like $\text{La}_{0.9}\text{Sr}_{0.1}\text{MnO}_3$ & $\text{La}_{0.85}\text{Ca}_{0.15}\text{MnO}_3$. The main out comes of this thesis are given below:

(a) In chapter 3, we discussed destabilisation of the polaronic insulating state in nominally pure LaMnO_3 single crystals and GdMnO_3 thin film at temperatures $\leq 300\text{K}$ by externally applied electric field. The resistive state transitions observed in these parent magnetites are different from those seen in manganites with higher level of hole doping. We found a very interesting mechanism which is responsible for this kind of resistive switching in the parent perovskites. In this case the transition occurs from the polaronic insulating state (HRS) of LaMnO_3 and GdMnO_3 to a bad metallic phase (LRS). The obser-

vation has been explained as bias driven percolation type transition between the two coexisting phases mentioned above. The applied bias can change the mobile fraction f of the bad metallic phase leading to a percolation type transition to the LRS state when the fraction f crosses f_c for percolation transition. The mobile fraction f has an activated T and E dependence. This leads to rapid enhancement of f on application of field leading to a sharp resistive transition. The microscopic mechanisms responsible for these co-existing phases in parent perovskite is the charge transfer instability driven charge disproportionation.

(b) In chapter 4, we investigated magnetotransport behaviour in nominally pure LaMnO_3 . We found that the origin of MR is due to the formation of FM clusters of different strength (depending on the samples) due to the charge transfer instability driven dynamic charge disproportionation effect and self doping effect during the crystal growth. The formation of FM clusters is confirmed by the structural and magnetic characterisations of the samples. We observed that MR in parent manganites can be as large as $\sim 70\%$ at low temperature. The observed MR behaviour is different from the conventional CMR effect in hole (x) doped manganites.

(c) In chapter 5, investigation has been done to show the effect of carrier modulation by electrostatic gate in a phase coexisted low hole (x) doped manganites like $\text{La}_{0.85}\text{Ca}_{0.15}\text{MnO}_3$. The study has been made by making an EDL-FET device using a nano structured $\text{La}_{0.85}\text{Ca}_{0.15}\text{MnO}_3$ film as a channel. The EDL gate controls the depletion layer in the grain boundary (GB) region, leading to a control of the tunnelling process. A gate bias ($V_G \approx \pm 5\text{V}$) modulates the channel current I_{DS} at room temperature by nearly $\pm 40\%$. Correlation of the transient response of the gate and channel currents on application of a step-change in V_G , establishes the role of the gate capacitor in the observed phenomena. Gate bias dependent electrical transport shows electronic phase control driven bi-polar modulation of electrical resistance. In addition to the change in R , the gate also substantially changes the activation energy (E_a) of conduction in the PM state of the film. The gate bias also changes the characteristic temperatures of the film like the onset of the FMI state (T_{FI}), PM to FMI transition temperature T_C^* and structural transition temperature $T_{OO'}$ as like chemical doping. The observation has been explained by a field effect induced modification/control of the relative fraction of the co-existing phases that is a characteristic of

the low-hole doped manganites particularly the FMI state. The study thus leads to a field effect induced modification of co-existing phases in complex electronic systems such as manganites.

(d) In chapter 6, we discussed the effect of biaxial strain (due to lattice mismatch) and electronic phase inhomogeneity on the electrical transport of $\text{La}_{0.85}\text{Ca}_{0.15}\text{MnO}_3$ film on different single crystal substrates. It was observed that the effective strain in the three films are dissimilar in magnitude and nature which leads to electronic phase inhomogeneities in different length scale. Local conduction mapping is done in the films to find out the local electronic phase inhomogeneity. LCAMP in the $\text{La}_{0.85}\text{Ca}_{0.15}\text{MnO}_3$ films supports the existence of these electronic phase inhomogeneities. The electronic transport in the three films are affected by the effective strain generated in these films as well as the extent of local phase separation present in these samples. The temperature evaluation of these local inhomogeneities correlates with the temperature dependent electric transport.

7.2 Future outlook

In this thesis, we have done detail investigation on novel electric and magnetic properties of perovskite manganites. However, there are still some basic physics issues which could be addressed.

In chapter 3, we have done the resistive switching measurement in bulk single crystals and in thin film. The study can be further extended to other perovskite samples in bulk & nanostructured forms in which the concentration (f) of the minority phase (E-H pair) may vary due to the charge disproportionation. The variation in f can change the threshold voltage of switching. One could check the existence of these minority phases in parent manganites through Raman spectroscopy in presence of electric field as the vibrational energy of $\text{Mn}^{3+} - \text{O} - \text{Mn}^{3+}$ is different from the E-H pair ($\text{Mn}^{4+} - \text{O} - \text{Mn}^{2+}$). It would be also interesting to study how does the carrier modulation by the electrostatic gate can affect the resistive switching due to this charge disproportionation phenomena.

In chapter 5, we have modulated the x of $\text{La}_{1-x}\text{Ca}_x\text{MnO}_3$ nanostructured film by electric double layer gate and studied its electric transport. It could also be studied how does the electrostatic gate affects the MR behaviour of hole doped manganites.

The effect of strain inhomogeneity on phase separation can be studied in more controlled way on growing the $\text{La}_{0.85}\text{Ca}_{0.15}\text{MnO}_3$ film on Piezoelectric substrate and mapping different conductive regions by measuring local tunneling conductance using STM at different strain values and at different temperatures (mainly in the different characteristic electronic phases like PI, FMM and FMI regions). It would be also interesting to see the modification (due to the strain) of the crystal lattice of the $\text{La}_{0.85}\text{Ca}_{0.15}\text{MnO}_3$ films on the three different substrates by using cross-sectional TEM which gives us the exact length scale over which the strain exist or the length scale of strain inhomogeneity.

Appendix A

Appendix

A.1 Increase of temperature due to applied bias in LaMnO₃

The calculation for the maximum temperature rise in LaMnO₃ due to the Joule heating is done considering the heat generated in the sample (for ON pulse) and dissipated from the sample (for OFF pulse) through the metal base via the GE-Varnish and thermal grease.

The heat balance equation in the sample is given as:

$$C_P \frac{dT}{dt} = \frac{d}{dt}(Q_{in} + Q_{out}) \quad (A.1)$$

$$C_P \frac{dT}{dt} = IV - C_P \left(\frac{T - T_S}{\tau} \right) \quad (A.2)$$

Where T_S is the base temperature,

τ = Thermal relaxation time between the sample and the base,

$\tau = C_P R_{Th}$; C_P is the heat capacity and R_{Th} is the thermal boundary resistance,

and $P = IV$.

$$\frac{dT}{dt} = \frac{P}{C_P} - \frac{T}{\tau} + \frac{T_S}{\tau}; \quad (A.3)$$

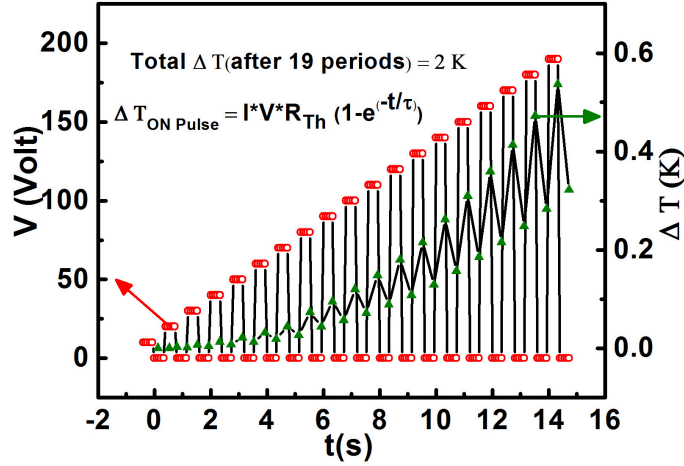
$$\frac{dT}{dt} + bT = \left(\frac{P}{C_P} + bT_S \right); \quad (A.4)$$

Solution to this equation is given as

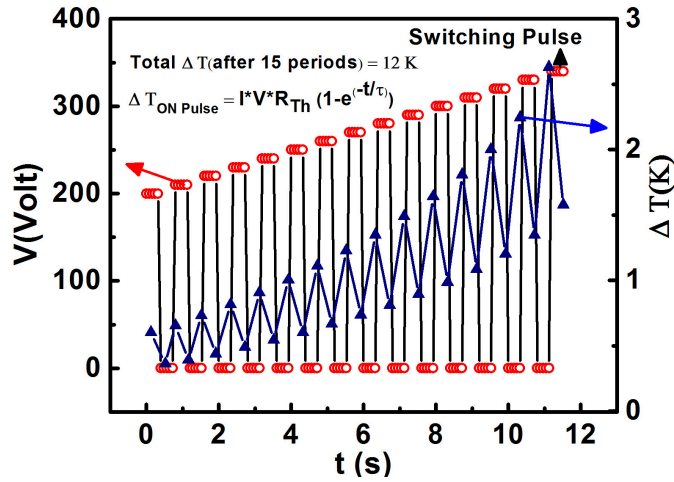
$$T(t) = T_S + \frac{P \times \tau}{C_P} (1 - \exp(-\frac{t}{\tau})) \quad (A.5)$$

Using measured value of C_P and R_{Th} , we evaluate the evolution of $T(t)$ on application of the pulsed power [194, 218]. A typical result of temperature rise $\Delta T = T(t) - T_S$ as function of time is shown in Fig. A.1 at $T_S = 150\text{K}$ for LaMnO₃-1.

The highest temperature rise at the maximum power pulse of nearly 300mW is $< 3\text{K}$ (switching pulse



(a)



(b)

Figure A.1 (a) Temperature rise and fall (ΔT) for each ON and OFF pulses from 10 to 190 V and (b) from 200 to 340V. Total increment in temperature is calculated by adding the ΔT for each ON and OFF pulses .

in Figure A.1(b). In a similar way calculating the ΔT for each pulses from 10V to 340V, we find that the

total temperature rise is $\sim 14\text{K}$ (from Fig. A.1(a) & (b)). This temperature rise (maximum estimated) is not sufficient to generate such kind of resistive transition which we have observed at 150K for LaMnO_3 single crystal.

A.2 Magnetoresistance of the $\text{La}_{0.85}\text{Ca}_{0.15}\text{MnO}_3$ film grown on single crystal substrates of NGO, LAO and STO

We have investigated the effect of substrate induced biaxial strain and the phase separation effect on the magnetic transport of $\text{La}_{0.85}\text{Ca}_{0.15}\text{MnO}_3$ thin films grown on three different single crystal substrates of NGO (200), STO (200) and LAO (100) by PLD. We have done $\rho - T$ measurements at different magnetic fields (0-8T). The data are shown in Fig. A.2.

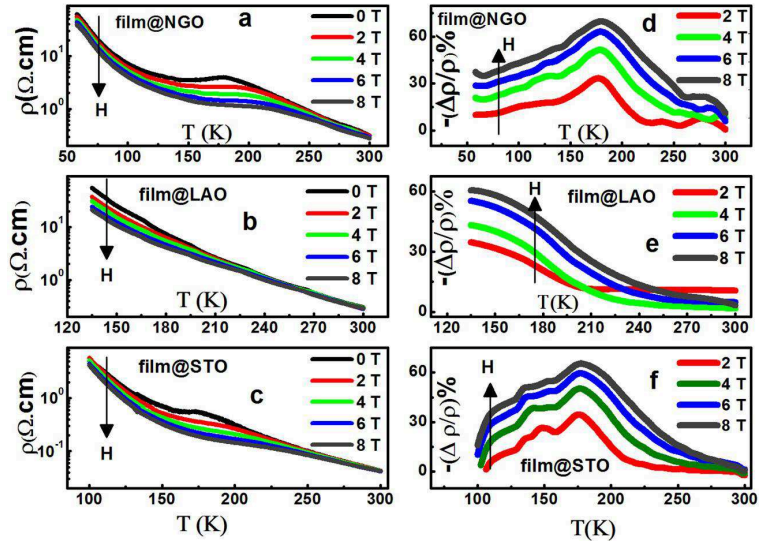


Figure A.2 $\rho - T$ curve of the $\text{La}_{0.85}\text{Ca}_{0.15}\text{MnO}_3$ films at different applied magnetic field H are shown in a, b and c. In d, e, and f, we have shown the variation of MR with T at different H .

All the three samples have $\text{MR} \approx 60\%$ at 8T. However, MR is qualitatively different in the three $\text{La}_{0.85}\text{Ca}_{0.15}\text{MnO}_3$ films. The variation in MR in the three films may be arise due to the different nature of the effective strain (induced by the substrates) which leads to electronic phase separation in these films.

A.3 The C++ code for pulse voltage measurement in LaMnO₃

we have written a c++ code to generate a pulse voltage train for the $I - V$ measurement in LaMnO₃.

The pulsed voltage has 50% duty cycle with 400 msec ON time. The code is given below.

```
#include<stdio.h>
#include<conio.h>
#include<iostream.h>
#include <fstream.h>
#include<string.h>
#include<stdlib.h>
#include<math.h>
#include<time.h>
#include<windows.h>
#include<IEEE-C.h>
#define TC 12
# define SM2 25
int main()
{
double mv,iv,ev,ev1,step1,curr,cur1,wait,del,loop,T=150,Temp,volt, volt1;
char filename[20];
char file[20];
time_t start,end;
int i,l,k,j1,kl,len,status,datano=0,SM;
char V[20],I[80],r[20], vp[20];
cout << "Enter the file name for the V-I measurement" << endl;
cin >> filename;
ofstream f(filename);

cout << "Enter the file name for the V-I measurement" << endl;
cin >> file;

ofstream f1(file);

cout << "Enter the maximum Voltage " << endl;
cin>>mv;
cout << "Enter voltage interval" << endl;
cin>>iv;
```

```

cout << "Enter the no. loop" << endl;
cin>>loop;
cout << "2400(24) and 2410 (25)" << endl;
cin>>SM;
f <<"Volt(V)" <<" " <<"T(K)" <<" " <<"I(A)" <<" " << "SVolt" <<endl;
cout <<"Volt(V)" <<" " <<"T(K)" <<" " <<"I(A)" <<" " << "SVolt" <<endl;
step1=mv/iv;
send (SM,":SOUR:FUNC VOLT",& status);
send (SM,":OUTP ON",& status);
for(i=0;i<=step1;++i)
{
kl=1;
while(kl<=1)
{
cur1=0.0;
volt1=0.0;
for(int j1=1;j1<=5;++j1)
{
ev=i*iv;
sprintf(V,":SOUR:VOLT:LEV %f",ev);
send (SM,V,&status);
Sleep(500);
send (SM,":FORM:ELEM CURR",&status);
send (SM,":READ?",&status);
enter (I,20,&len,SM,&status); curr=atof(I);
cur1=cur1+curr/5;
send (SM2,":READ?",&status);
enter (vp,20,&len,SM2,&status);
volt=atof(vp);
volt1=volt1+volt/5;
T=150;
cout<<ev<<" " <<T<<" " <<curr<<" " <<volt<<endl;

        f1<<ev<<" " <<T<<" " <<curr<<" " <<volt<<endl;

kl=3;
} f<<ev<<" " <<T<<" " <<cur1<<" " <<volt1<<endl;

```

```

}
for(int j1=1;j1≤5;++j1)
{
ev=0.0;
sprintf(V,":SOUR:VOLT:LEV %f",ev1);
send (SM,V,&status);
send (SM,":FORM:ELEM CURR",&status);
send (SM,":READ?",&status);
enter (I,20,&len,SM,&status); curr=atof(I);
send (SM2,":READ?",&status);
enter (vp,20,&len,SM2,&status); volt=atof(vp);
cout<<ev<<" "<<T<<" "<<curr<<" "<<volt<<endl;
f1<<ev<<" "<<T<<" "<<curr<<" "<<volt<<endl;
Sleep(100);
}
}
for(int j=1;j≤loop;++j)
{ for(i=1;i≤2*step1;++i)
{
kl=1;
while(kl≤1)
{
cur1=0.0;

volt1=0.0;
for(int j1=1;j1≤5;++j1)
{
ev=mV-i*iv;

sprintf(V,":SOUR:VOLT:LEV %f",ev);
send (SM,V,&status);
Sleep(500);
send (SM,":FORM:ELEM CURR",&status);
send (SM,":READ?",&status);
enter (I,20,&len,SM,&status);
curr=atof(I);
send (SM2,":READ?",&status);

```

```

enter (vp,20,&len,SM2,&status);
volt=atof(vp);
volt1=volt1+volt/5;
cout<<ev<<" "<<T<<" "<<curr<<" "<<volt<<endl;
cur1=cur1+curr/5;
f1<<ev<<" "<<T<<" "<<curr<<" "<<volt<<endl;
kl=3;
} f<<ev<<" "<<T<<" "<<cur1<<" "<<volt1<<endl; } for(int j1=1;j1<=5;++j1)
} ev=0.0;
sprintf(V,":SOUR:VOLT:LEV %f",ev1);
send (SM,V,&status);
send (SM,":FORM:ELEM CURR",&status);
send (SM,":READ?",&status);
enter (I,20,&len,SM,&status); curr=atof(I);
send (SM2,":READ?",&status);
enter (vp,20,&len,SM2,&status); volt=atof(vp);
cout<<ev<<" "<<T<<" "<<curr<<" "<<volt<<endl;
f1<<ev<<" "<<T<<" "<<curr<<" "<<volt<<endl;
Sleep(100);
}
}
for(i=1;i<=2*step1;++i) {
kl=1;
while(kl<=1)
{
cur1=0.0;
volt1=0.0;
for(int j1=1;j1<=5;++j1)
{
ev=i*iv-mv;

sprintf(V,":SOUR:VOLT:LEV %f",ev);
send (SM,V,&status);
Sleep(500);
send (SM,":FORM:ELEM CURR",&status);
send (SM,":READ?",&status);

```

```

enter (I,20,&len,SM,&status);
curr=atof(I);
send (SM2,":READ?",&status);
enter (vp,20,&len,SM2,&status);
volt=atof(vp);
volt1=volt1+volt/5;
cout<<ev<<" "<<T<<" "<<curr<<" "<<volt<<endl;
cur1=cur1+curr/5;
f1<<ev<<" "<<T<<" "<<curr<<" "<<volt<<endl;
kl=3;

} f<<ev<<" "<<T<<" "<<cur1<<" "<< volt1<<endl;
}
for(int j1=1;j1≤5;++j1)
{
ev=0.0;
sprintf(V,":SOUR:VOLT:LEV %f",ev1);
send (SM,V,&status);
send (SM,":FORM:ELEM CURR",&status);
send (SM,":READ?",&status);
enter (I,20,&len,SM,&status);
curr=atof(I);
send (SM2,":READ?",&status);
enter (vp,20,&len,SM2,&status);
volt=atof(vp);
cout<<ev<<" "<<T<<" "<<curr<<" "<<volt<<endl;
f1<<ev<<" "<<T<<" "<<curr<<" "<<volt<<endl;
Sleep(100);
} } } for(i=1;i≤step1;++i)
{ kl=1;
while(kl≤1)
{ cur1=0.0;
volt1=0.0;
for(int j1=1;j1≤5;++j1)
{ ev=mv-i*iv;
sprintf(V,":SOUR:VOLT:LEV %f",ev);

```

```

send (SM,V,&status);
Sleep(500);
send (SM,":FORM:ELEM CURR",&status);
send (SM,":READ?",&status);
enter (I,20,&len,SM,&status);
curr=atof(I);
cur1=cur1+curr/5;
send (SM2,":READ?",&status);
enter (vp,20,&len,SM2,&status);
volt=atof(vp);
volt1=volt1+volt/5;
cout<<ev<<" "<<T<<" "<<curr<<" "<<volt<<endl;
f1<<ev<<" "<<T<<" "<<curr<<" "<<volt<<endl;
kl=3; }
f1<<ev<<" "<<T<<" "<<cur1<<" "<<volt<<endl;
}
for(int j1=1;j1<=5;++j1)
{
ev=0.0;
sprintf(V,":SOUR:VOLT:LEV %f",ev1);
send (SM,V,&status);
send (SM,":FORM:ELEM CURR",&status);
send (SM,":READ?",&status);
enter (I,20,&len,SM,&status);
curr=atof(I);
send (SM2,":READ?",&status);
enter (vp,20,&len,DMM,&status);
volt=atof(vp);
cout<<ev<<" "<<T<<" "<<curr<<" "<<volt<<endl;
f1<<ev<<" "<<T<<" "<<curr<<" "<<volt<<endl;
Sleep(100);
}
}
send (SM,":OUTP OFF",&status);
return 0;
}

```

A.4 The C++ code for $\rho - T$ measurement in cryogen free VTI system

The programming code for $\rho - T$ measurement in cryogen free VTI system is given below. #include<stdio.h>

```
#include<conio.h>
#include<iostream.h>
#include <fstream.h>
#include<string.h>
#include<stdlib.h>
#include<math.h>
#include<time.h>
#include<windows.h>
#include<IEEE-C.h>
#define TC 16
int main()
{ char m[80];
char n[80];
int k1, SM, status, len;
float r,Tm,Tb,Ta,R,I, i1,r1, tm1,ta1,lowT,highT,Tmax,I2,t1,t2,del ;
char vp[100];
char ve[100];
char vb[100];
char vm[100];
char ip[100];
char T[100];
char t[100];
cout<<"Type a file name for cooling cycle"<<endl;
cin>>m;
ofstream f1(m);
cout<<"Type a file name for heating cycle"<<endl;
cin>>n;
ofstream f2(n);
cout<<"Bias current value"<<endl;
cin>>I2;
cout<<"Enter the lowest temperature"<<endl;
cin>>t1;
cout<<"Enter the highest temperature"<<endl;
```

```

cin>>t2;
cout<<"Enter the room temperature"<<endl;
cin>>Tm;
cout << "2400(24) and 2410 (25)" << endl;
cin>>SM;
cout << "Enter the delay in msec" << endl;
cin>>del;
cout<<"Wait 1 sec for another command...Temperature CoNT is setting now "<<endl<<endl;
Sleep(1000);
cout<<"Wait 1 sec for another command...SM is setting now "<<endl<<endl;
Sleep(1000);
send (TC,"KRDG?B",&status);
enter (ve,80,&len,TC,&status);
Tm=atof(ve);
cout<<"TEMPA"<<" "<<"TEMPB"<<" "<<" SampVolt"<<" "<<"RES"<<" "<<"Bias Curr"<<endl;
f1<<"TEMPA"<<" "<<"TEMPB"<<" "<<" SampVolt"<<" "<<"RES"<<" "<<"Bias Curr"<<endl;

    if(Tm≥t1)
    {
    sprintf(t,"SETP 1 %t1",t1);
    send (TC,t,&status);
    r1=0.0;
    tm1=0.0;
    ta1=0.0;
    for(int j=1; j≤10; j++)
    {
    send (SM,":READ?",&status);
    enter (vp,80,&SM,&status);
    r=atof(vp);
    r1= r1+r/10.0;
    send (TC,"KRDG?B",&status);
    enter (ve,80,&len,TC,&status);
    Tm=atof(ve);
    tm1=tm1+Tm/10.0;
    send (TC,"KRDG? A",&status);

```

```

enter (vm,80,&,TC,&status); Ta=atof(vm);
ta1=ta1+Ta/10.0;
}
R= r1/I2;
cout<<ta1<<" "<<tm1<<" "<<r1<<" "<<R<<" "<<I2<<endl;
f1<<ta1<<" "<<tm1<<" "<<r1<<" "<<R<<" "<<I2<<endl;
Sleep(del);
}
else
}
sprintf(T,"SETP 1 %t1",t2);
send (TC,T,&status);
f2<<"TEMPA"<<" "<<"TEMPB"<<" "<<" SampVolt"<<" "<<"RES"<<" "<<"Bias Curr"<<endl;
while(Tm<=t2)
{
r1=0.0;
tm1=0.0;
ta1=0.0;
for(int j=1; j<=10; j++)
{
send (SM,":READ?",&status);
enter (vp,80,&,SM,&status);
r=atof(vp);
r1= r1+r/10.0;
send (TC,"KRDG?B",&status);
enter (ve,80,&len,TC,&status);
Tm=atof(ve);
tm1=tm1+Tm/10.0;
send (TC,"KRDG? A",&status);
enter (vm,80,&,TC,&status); Ta=atof(vm);
ta1=ta1+Ta/10.0;
}
R= r1/I2;

cout<<ta1<<" "<<tm1<<" "<<r1<<" "<<R<<" "<<I2<<endl;
f2<<ta1<<" "<<tm1<<" "<<r1<<" "<<R<<" "<<I2<<endl;

```

```
Sleep(del);  
}  
}  
getch();  
send (SM,":OUTP OFF",&status);  
return 0;  
}
```

Bibliography

- [1] C. N. R. Rao and B. Raveau, *Colossal Magnetoresistance, Charge Ordering and Related Properties of Manganese Oxides*, World Scientific, (1998).
- [2] Y. Tokura, *Colossal Magnetoresistive Oxides*, Gordon and Breach Science Publishers, New York, (1999).
- [3] Henry J. Snaith, *J. Phys. Chem. Lett.* **4**, 3623 (2013).
- [4] J. G. Bednorz, K. A. Muller, *Phys. B: Condens. Matter* **64**, 189 (1986).
- [5] John B. Goodenough and J.-S. Zhou, *J. Mater. Chem.* **17**, 2394 (2007).
- [6] J. Rodriguez Carvajal, M. Hennion, F. Moussa, A. H. Moudden, L. Pinsard and A. Revcolevschi, *Phys. Rev. B* **57**, 3189 (1998).
- [7] B. B. van Aken, A. Meetsma, Y. Tomioka, T. Tokura, and T. T. M. Palstra, *Phys. Rev. Lett.* **90**, 066403 (2003).
- [8] T. Chatterji, B. Ouladdiaf, P. Mandal, B. Bandyopadhyay, and B. Ghosh, *Phys. Rev. B* **66**, 054403 (2002).
- [9] I. Loa, P. Adler, A. Grzechnik, K. Syassen, U. Schwarz, M. Hanfland, G. Kh. Rozenberg, P. Gorodetsky, and M. P. Pasternak, *Phys. Rev. Lett.* **87**, 125501 (2001).
- [10] S. de Brion, F. Ciorcas, and G. Chouteau, P. Lejay, P. Radaelli, C. Chaillout, *Phys. Rev. B* **59**, 1304 (1999).

- [11] Parthasarathi Mondal and Dipten Bhattacharya, P. Mandal, Phys. Rev. B **84**, 075111 (2011).
- [12] James Loudon, *An investigation of the unconventional phases in $La_{1-x}Ca_xMnO_3$ system*, thesis submitted to University of Cambridge (2003).
- [13] J. M. D. Coey, M. Viret, and S. von Molnar. Adv. Phys. **48**, 167 (1999).
- [14] L.M. Rodriguez-Martinez and J.P. Attfield, Phys. Rev. B. **63**, 024424 (2000).
- [15] T. Kubo, A. Hirai and H. Abe, J. Phys. Soc. Japan **26**, 1094 (1969).
- [16] Sigrun Antje KÖster *Magnetic field effects on the local tunnelling conductivity of $La_{0.75}Ca_{0.25}MnO_3/MgO$ thin films* (2007).
- [17] A. J. Millis, Nature (London) **392**, 147 (1998).
- [18] J. B. Goodenough. Phys. Rev. B **100**, 564 (1955).
- [19] Sudeshna Samanta, *Study Of Low Frequency Conduction Fluctuations In Perovskite Manganites*, thesis submitted to Jadavpur University (2009).
- [20] C. Zener, Phys. Rev. B **82**, 403 (1951).
- [21] P.W.Anderson and H. Hasegawa, Phys. Rev. B **100**, 675 (1955).
- [22] N. D. Mathur and P. B. Littlewood, Solid State Commun. **119**, 271 (2001).
- [23] A. J. Millis, R. Mueller, and B. I. Shraiman, Phys. Rev. B **54**, 5405 (1996).
- [24] T. V. Ramakrishnan, H R Krishnamurthy, S R Hassan and G Venketeswara Pai, Proc. Indian Acad. Sci. (Chem. Sci.) **115**, 767 (2003).
- [25] H R Krishnamurthy, PRAMANA **64**, 1063 (2005).
- [26] N. D. Mathur and P. B. Littlewood, Solid State Commun. **119**, 271 (2001).
- [27] J. B. Goodenough, *Magnetism and Chemical Bonds* Inter science Publishing, New York, (1963).

- [28] M. Colle, M. Buchel, and D. M. de Leeuw, *Organic Electronics*, **7**, 305-312 (2006).
- [29] D. S. Shang, Q. Wang, L. D. Chen, R. Dong, X. M. Li, and W. Q. Zhang, *Phys. Rev. B* **73**, 245427 (2006).
- [30] R. Oligschlaeger, R. Waser, R. Meyer, S. Karthäuser, and R. Dittmann, *Appl. Phys. Lett.* **88**, 042901 (2006).
- [31] S. Q. Liu, N. J. Wu, and A. Ignatiev, *Appl. Phys. Lett.* **76**, 2749 (2000).
- [32] S. Tsui, *Appl. Phys. Lett.* **85**, 317 (2004).
- [33] T. Kenta, O. Isao, K. Hiroshi, O. Masaharu, K. I. Yuji Matsumoto, O. Tsuyoshi, L. Mikk, and K. Hideomi, *Advanced Materials* **19**, 1711 (2007).
- [34] A. Baikalov, *Appl. Phys. Lett.* **83**, 957 (2003).
- [35] A. Asamitsu, Y. Tomioka, H. Kuwahara, and Y. Tokura, *Letters to Nature* **388**, 50 (1997).
- [36] A. Beck et al., *Appl. Phys. Lett.* **77**, 139 (2000).
- [37] Y. Watanabe, et al., *Appl. Phys. Lett.* **78**, 3738 (2001).
- [38] L. Huang, B. Qu, L. Liu, and L. Zhang, *Solid State Communications* **143**, 382 (2007).
- [39] G. S. Park et al., *Appl. Phys. Lett.* **91**, 222103 (2007).
- [40] Akihito Sawa, *materialstoday* **11**, 28 (2008).
- [41] J. P. Shi, Y. G. Zhao, H. J. Zhang, H. F. Tian, and X. P. Zhang, *Appl. Phys. Lett.* **94**, 192103 (2009).
- [42] C.N.R Rao, A. R. Raju, V. Ponnambalam, S. Parashar and N. Kumar, *Phys. Rev. B.* **61**, 594 (2000).
- [43] A. Guha, A. Ghosh, A.K.Raychaudhuri, S. Parashar, A.R.Raju, and C.N.R Rao, *Appl. Phys. Lett.* **75**, 3381 (1999).

- [44] A. Guha, A. K. Raychaudhuri, A. R. Raju, and C.N.R Rao, Phys. Rev. B. **62**, 5320 (2000).
- [45] A. Sawa, et al., Appl. Phys. Lett. **85**, 4073 (2004).
- [46] T. Fujii, et al., Appl. Phys. Lett. **86**, 012107 (2005).
- [47] Y. B. Nian, J. Strozier, N. J. Wu, X. Chen, and A. Ignatiev, Phys. Rev. Lett. **98**, 146403 (2007).
- [48] R. Dong, W. F. Xiang, D. S. Lee, S. J. Oh, D. J. Seong, S. H. Heo, H. J. Choi, M. J. Kwon, M. Chang, M. Jo, M. Hasan, and Hyunsang Hwangb, Appl. Phys. Lett. **90**, 182118 (2007).
- [49] Barnali Ghosh, K.Das, and A. K. Raychaudhuri, J. Appl. Phys. **109**, 083934 (2011).
- [50] P. Schiffer, A. P. Ramirez, W. Bao and S-W. Cheong, Phys. Rev. Lett. **75**, 3336 (1995).
- [51] S.W. Cheong, H.Y. Hwang, Y. Tokura (Ed.), *Contribution to Colossal Magnetoresistance Oxides, Monographs in Condensed Matter Science, Gordon and Breach, London, 1999.*
- [52] Anthony Arulraj, Amlan Biswas, A. K. Raychaudhuri, and C. N. R. Rao, P. M. Woodward, T. Vogt, and D. E. Cox, A. K. Cheetham, Phys. Rev. B **57**, R8115 (1998).
- [53] D. Kim, B. Revaz, B. L. Zink, F. Hellman, J.J. Rhyne and J. F. Mitchell, Phys. Rev. Lett. **89**, 227202 (2002).
- [54] R.I. Zainullina, N.G. Bebnin, V.V. Ustinov, Ya. M. Mukovskii and D. A. Shulyatev, Phys. Rev. B **76**, 014408 (2007).
- [55] E. Dagotto, H. Takashi and A. Moreo, Phys. Rep. **344**, 1153 (2001).
- [56] L.M. Rodriguez Martinez and J.P. Attfield, Phys. Rev. B. **54**, 1562215625 (1996).
- [57] E. Dagotto, J. Burgy and A. Moreo, Solid State Comm. **126**, 9 (2003).
- [58] Ch. Renner, G. Aeppli, B. G. Kim, Yeong Ah Soh and S. W. Cheong, Nature **416**, 518 (2002).
- [59] M. FAath, S. Freisem, A. A. Menovsky, Y. Tomioka, J. Aarts and J. A. Mydosh, Science **285**, 1540 (1999).

- [60] A. P. Ramirez, *J. Phys.: Condens. Matter* **9**, 8171 (1997).
- [61] M. B. Salamon and M. Jaime, *Rev. Mod. Phys.* **73**, 583 (2001).
- [62] C. W. Searle and S. T. Wang, *Can. J. Phys.* **47**, 2023 (1969).
- [63] S. Jin, T. H. Tiefel, M. McCormack, R. A. Fastnacht, R. Ramesh and L. H. Chen, *Science* **264**, 413 (1994).
- [64] M. McCormack, S. Jin, T. H. Tiefel, R. M. Fleming, J. M. Phillips and R. Ramesh, *Appl. Phys. Lett.* **64**, 3045 (1994).
- [65] M. Uehara, S. Mori, C. H. Chen and S. W. Cheong, *Nature* **399**, 560 (1999).
- [66] J. M. DeTeresa, M.R. Ibarra, P. A. Algarabel, C. Ritter, C. Marquina, J. Blasco, J. Garcia, A. delMoral and Z. Arnold, *Nature* **386**, 256 (1997).
- [67] J. M. Zuo and J. Tao, *Phys. Rev. B* **63**, 060407 (2001).
- [68] A. La. Spina, P. Paolicchi, A. Kryszyńska and P. Pravec, *Nature* **428**, 400 (2004).
- [69] G. C. Milward, M. J. C. Calderon and P. B. Littlewood, *Nature* **433**, 607 (2005).
- [70] C. Sen, G. Alvarez and E. Dagotto, *Phys. Rev. Lett.* **98**, 127202 (2007).
- [71] G. Li, H. D. Zhou, S. J. Feng, X. J. Fan, X. G. Li and Z. D. Wang, *J. Appl. Phys.* **92**, 1406 (2002).
- [72] S. L. Yuan, Z. Y. Li, W.Y. Zhao, G. Li, Y. Jiang, X. Y. Zeng, Y. P. Yang, G. Q. Zhang, F. Tu, C. Q. Tang and S. Z. Jin, *Phys. Rev. B* **63**, 172415 (2001).
- [73] Liu Yu-Kuai, Yin Yue-Wei, and Li Xiao-Guang, *Chin. Phys. B* **22**, 087502 (2013).
- [74] M. Jaime, A. Lin, M. B. Salamon and P. D. Han, *Phys. Rev. B* **58** R5901 (1998).
- [75] G M Zhao, V. Smolyaninova, W. Prellier and H. Keller, *Phys. Rev. Lett.* **84**, 6086 (2000).

- [76] Y. X. Jia, L. Lu, K. Khazeni, V. H. Crespi, A. Zettl and M. L. Cohen, *Phys. Rev. B* **52**, 9147 (1995).
- [77] Y. K. Liu, Y. P. Yao, S. N. Dong, S. W. Yang and X. G. Li, *Phys. Rev. B* **86**, 075113 (2012).
- [78] Y. Tokura, *Rep. Prog. Phys.* **69**, 797 (2006).
- [79] X. G. Li, R. K. Zheng, G. Li, H. D. Zhou and R. X. Huang, *Europhys. Lett.* **60**, 670 (2002).
- [80] C. H. Ahn, J. M. Triscone and J. Mannhart, *Nature* **424**, 1015 (2003).
- [81] K. Ueno et al., *Nature Mater.* **7**, 855858 (2008).
- [82] H. Y. Hwang, Y. Iwasa, M. Kawasaki, B. Keimer, N. Nagaosa and Y. Tokura, *Nature Materials* **11**, 103 (2012).
- [83] H. Shimotani, H. Asanuma, A. Tsukazaki, A. Ohtomo, M. Kawasaki, and Y. Iwasa, *Appl. Phys. Lett.* **91**, 082106 (2007).
- [84] H. T. Yuan et al., *Adv. Funct. Mater.* **19**, 10461053 (2009).
- [85] T. Hatano, Y. Ogimoto, N. Ogawa, M. Nakano, S. Ono, Y. Tomioka, K. Miyano, Y. Iwasa, and Y. Tokura, *Sci. Rep.* **3**, 2904(2013).
- [86] S. Asanuma et. al., *Appl. Phys. Lett.* **97**, 142110 (2010).
- [87] K. Ueno, S. Nakamura, H. Shimotani, H. T. Yuan, N. Kimura, T. Nojima, H. Aoki, Y. Iwasa, and M. Kawasaki, *Nature Nanotech.* **6**, 408 (2011).
- [88] You Zhou and Shriram Ramanathan, *Critical Reviews in Solid State and Materials Sciences* **38**, 286 (2013).
- [89] A. S. Moskvina, *Phys. Rev. B* **79**, 115102 (2009).
- [90] R. Nath, A. K. Raychaudhuri, Ya M Mukovskii, P.S. Mondal, D. Bhattacharya and P. Mandal, *J. Phys.: Condens. Matter.* **25**, 155605 (2013).

- [91] C. N. R. Rao, A. R. Raju, V. Ponnambalam, and Sachin Parashar, N. Kumar, *Phys. Rev. B* **61**, 594 (2000).
- [92] A. Asamitsu, Y. Tomioka, H. Kuwahara and Y. Tokura, *Nature* **388**, 50 (1997).
- [93] Ayan Guha, Arindam Ghosh and A. K. Raychaudhuri, S. Parashar, A. R. Raju, and C. N. R. Rao, *App. Phys. Lett.* **75**, 3381 (1999).
- [94] Ayan Guha and A. K. Raychaudhuri, A. R. Raju and C. N. R. Rao, *Phys. Rev. B* **62** 5320 (2000).
- [95] J. Klein, C. HAofener, S. Uhlenbruck, L. Alff, B. BAuchner and R. Gross, *Europhys. Lett.* **47**, 371 (1999).
- [96] R. Mahendiran, R Mahesh, A. K. Raychaudhuri and C. N. R. Rao, *Pramana* **44**, 393 (1995).
- [97] Mandar Paranjape, J. Mitra, and A. K. Raychaudhuri, N. K. Todd, N. D. Mathur, and M. G. Blamire, *Phys.Rev.B* **68**, 144409 (2003).
- [98] L. I. Glazrnan and K. A. Matveev, *Zh. Eksp. Teor. Fiz.* **94**, 332 (1988).
- [99] D. Shulyatev, S. Karabashev, A. Arsenov, Ya. Mukovskii, *Journal of Crystal Growth* **198/199**, 511–515 (1999).
- [100] D. Shulyatev, S. Karabashev, A. Arsenov, Ya. Mukovskii, S. Zverkov, *Journal of Crystal Growth* **237239**, 810814 (2002).
- [101] A.M. Balbashov and S.K. Egorov, *Journal of Crystal Growth* **52**, 498504 (1981).
- [102] J. A. M. van Roosmalen, P. V. Vlaanderen, E. H. P. Cordfunke, W. L. Ijdo, and D. L. W. Ijdo, *J. Solid State Chem.* **114**, 516 (1995).
- [103] A. M. Balbashov, S. G. Karabashev, Y. M. Mukovskii, and S. A. Zverkov, *J. Crystal Growth* **167**, 365 (1996).
- [104] T. Venakatesan, X. D. Wu, A. Inam, and J. B. Wachtman, *Appl. Phys. Lett.* **52**, 1193 (1988).

- [105] T J Jackson and S B Palmer, *J. Phys. D: Appl. Phys.* **27**, 1581-1594 (1994).
- [106] Y. Hiroshima, T. Ishiguro, I. Urata, H. Makita, H. Ohta, M. Tohogi, Y. Ichinose, *J. Appl. Phys.* **79**(7), 3572(1996).
- [107] R. Bachelet, D. Pesquera, G. Herranz, F. SÁnchez, and J. Fontcuberta, *Appl. Phys. Lett.* **97**, 121904 (2010).
- [108] Mandar A Paranjape, K Shantha Shankar and A K Raychaudhuri, *J. Phys. D: Appl. Phys.* **38**, 3674 (2005).
- [109] J.-L. Maurice, R. Lyonnet, J.-P. Contour, *Journal of Magnetism and Magnetic Materials* **211**, 91-96 (2000).
- [110] www.micromagnetic.com
- [111] Milton Ohring, *The Material Science of Thin Films, Academic Press*, (1992).
- [112] N. Andreev, V. Chichkov, T. Sviridova, N. Tabachkova, A. Volodin, C. Van Haesendonck, and Ya. Mukovskii, *EPJ Web of Conferences* **40**, 15014 (2013).
- [113] Y. Leng, *Materials Characterization: Introduction to Microscopy and Spectroscopic Methods*, John Wiley and Sons (Asia) Pvt Ltd, Singapore (2008).
- [114] <http://www.purdue.edu/ehps/rem/rs/sem.html>.
- [115] <http://www.vcbio.science.ru.nl/en/feem/eds>.
- [116] R.F. Egerton, *Electron Energy-Loss Spectroscopy in the Electron Microscope, Third Edition*, Springer (1996).
- [117] R F Egerton, *Rep. Prog. Phys.* **72**, 016502 (2009).
- [118] Z.L. Wang, J.S. Yin, Y.D. Jiang, *Micron* **31**, 571-580 (2000).

-
- [119] Xianfeng Zhou, Jiang Xue, Defeng Zhou, Zhongli Wang, Yijia Bai, Xiaojie Wu, Xiaojuan Liu, and Jian Meng, *Appl. Mat. Interface* **2**, 2689 (2010).
- [120] Sandeep Agarwal, *Study of Relaxation Phenomenon and functional properties in some ferro-magnetic shape memory alloys*, thesis submitted to university of calcutta, 2014.
- [121] Cryogenic 1.5K VTI system manual.
- [122] G. Binning and H. Rohrer, *Surface Science* **126**, 236 (1983).
- [123] Scanning Tunnelling Microscopy, laboratory programme, Nue Unique (2009).
- [124] Diplomarbeit von Antje Lucas, *Design and Commissioning of a UHV-STM: Simplified Besocke Design for the Study of Nanowires*, dissertation, submitted to Physikalisches Institut Universität Stuttgart (March 2000).
- [125] V. A. Ukraintsev, *Phys. Rev. B* **53**, 11176 (1996).
- [126] Sohini Kar Narayanan, thesis submitted to IISC Bangalore, India, (2008).
- [127] rhk-uhv-Beetle-spm. brochure.pdf, www. rhk tech. com.
- [128] Himanshu Jain, A. K. Raychaudhuri, Ya. M. Mukovskii and D. Shulyatev, *App. Phys. Lett.* **89**, 152116 (2006).
- [129] Aveek Bid, Ayan Guha and A. K. Raychaudhuri, *Phys. Rev. B* **67**, 174415 (2003).
- [130] Rickard Fors, Sergey I. Khartsev, and Alexander M. Grishin, *Phys. Rev. B* **71**, 045305 (2005).
- [131] Sohini Kar and A. K. Raychaudhuri, *App.Phys.Lett.* **91**, 143124 (2007).
- [132] Jon-Olaf Krispeneit, Christin Kalkert, Bernd Damaschke, Vasily Moshnyaga, and Konrad Samwer, *Phys. Rev. B* **82**, 144440 (2010).
- [133] Himanshu Jain and A. K. Raychaudhuri, *App. Phys. Lett.* **93**, 182110 (2008).

- [134] M. Tokunaga, Y. Tokunaga, and T. Tamegai, *Phys. Rev. Lett.* **93**, 037203 (2004).
- [135] A. S. Carneiro, R. F. Jardim, and F. C. Fonseca, *Phys. Rev. B* **73**, 012410 (2006).
- [136] Ch. Jooss, L. Wu, T. Beetz, R. F. Klie, M. Beleggia, M. A. Schofield, S. Schramm, J. Hoffmann, and Y. Zhu, *PNAS* **104**, 13601 (2007).
- [137] A. de Andres, N. Biskup, M. Garcia Hernandez, and Y. M. Mukovskii, *Phys. Rev. B* **79**, 014437 (2009).
- [138] A-M Haghiri-Gosnet and J-P Renard, *J. Phys. D: Appl. Phys.* **36**, R127-R150 (2003).
- [139] E. Dagotto, T. Hotta, and A. Moreo, *Phys. Rep.* **344**, 1 (2001).
- [140] Himanshu Jain, A.K. Raychaudhuri, Ya.M. Mukovskii, D. Shulyatev, *Solid State Communications* **138**, 318 (2006).
- [141] A. K. Raychaudhuri, *Advances in Physics* **44**, 21 (1995).
- [142] Qingzhong Xue, *Physica B* **325**, 195 (2003).
- [143] John Bardeen, *Phys. Rev. Lett.* **45**, 1978 (1980).
- [144] J. P. Farges, *Organic Conductors, Marcel Dekker, Inc. New York* (1994).
- [145] Q. Huang, A. Santoro, J. W. Lynn, R. W. Erwin, J. A. Borchers, J. L. Peng, and R. L. Greene, *Phys. Rev. B* **55**, 14987 (1997).
- [146] F. Prado, R. Zysler, L. Morales, A. Caneiro, M. Tovar, and M. T. Causa, *J. Magn. Magn. Mater.* **196**, 481 (1999).
- [147] N. N. Kovaleva, A. V. Boris, C. Bernhard, A. Kulakov, A. Pimenov, A. M. Balbashov, G. Khaliullin and B. Keimer, *Phys. Rev. Lett.* **93**, 147204 (2004).
- [148] A. Y. Ramos, N. M. Souza-Neto, H. C. N. Tolentino, O. Bunau, Y. Joly, S. Grenier, J.-P. Itie, A.-M. Flank, P. Lagarde and A. Caneiro, *EPL* **96**, 36002 (2011).

- [149] D. Lee, J.-H. Lee, P. Murugavel, S. Y. Jang, and T. W. Noh, Y. Jo and M.-H. Jung, Y. D. Ko and J.-S. Chung, *Appl. Phys. Lett* **90**, 182504 (2007).
- [150] Y. Murakami, J. P. Hill, D. Gibbs, M. Blume, I. Koyama, M. Tanaka, H. Kawata, T. Arima, Y. Tokura, K. Hirota and Y. Endoh, *Phys. Rev. Lett.* **81**, 582 (1998).
- [151] M. V. Zimmermann, C. S. Nelson, Y. J. Kim, J. P. Hill, D. Gibbs, H. Nakao, Y. Wakabayashi, Y. Murakami, Y. Tokura, Y. Tomioka, T. Arima, C.-C. Kao, D. Casa, C. Venkataraman, and Th. Gog, *Phys. Rev. B* **64**, 064411 (2001).
- [152] R. Nath, A. K. Raychaudhuri, Ya. M. Mukovskii, N. Andreev, and V. Chichkov, *Appl. Phys. Lett.* **104**, 183508 (2014).
- [153] C. Zener, *Phys. Rev. B* **81**, 440 (1951).
- [154] P.G. De Gennes, *Phys. Rev. B* **118**, 141 (1960).
- [155] T V Ramakrishnan, *J. Phys.: Condens. Matter.* **19**, 125211 (2007).
- [156] A.J. Millis, P. B. Littlewood and B.I. Shraiman, *Phys. Rev. Lett.* **74**, 5144 (1955).
- [157] N.I.Solin, V.V.Mashkaustan, A.V.Korolev, N.N.Ioshkareva, and L.Pinsard, *JETP letters* **77**, 5 (2003).
- [158] E. O. Wollan and W. C. Koehler, *Phys. Rev.* **100**, 545 (1955).
- [159] C. Ritter, M. R. Ibarra, J. M. De Teresa, P. A. Algarabel, C. Marquina, J. Blasco, J. Garcia, S. Oseroff and S. W. Cheong, *Phys. Rev. B* **56**, 8902 (1997).
- [160] T. Chatterji, B. Ouladdiaf, P. Mandal, B. Bandyopadhyay and B. Ghosh, *Phys. Rev. B* **66**, 054403 (2002).
- [161] P. Norby, I. G. Krogh Andersen, and E. Krogh Andersen, *J. Solid State Chem.* **119**, 191 (1995).
- [162] B. B. van Aken, A. Meetsma, Y. Tomioka, T. Tokura, and T. T. M. Palstra, *Phys. Rev. Lett.* **90**, 66403 (2003).

- [163] T. Chaterji, B. Ouladdiaf, P. Mandal, B. Bandyopadhyay, and B. Ghosh, *Phys. Rev. B* **66**, 054403 (2002).
- [164] S. H. Estemirova, A. V. Fetisov and V. B. Fetisov *Journal of Applied Spectroscopy*, **76**, 3 (2009).
- [165] B. Ghosh, V. Siruguri, A. K. Raychaudhuri and T. Chatterji, *J. Phys.: Condens. Matter.* **26**, 025603 (2014).
- [166] J. Nogues, Ivan K. Schuller, *Journal of Magnetism and Magnetic Materials* **192**, 203 (1999).
- [167] W.H. Meiklejohn, C.P. Bean, *Phys. Rev.* **102**, 1413 (1956).
- [168] Devendra Kumar and A Banerjee, *J. Phys.: Condens. Matter.* **25**, 216005 (2013).
- [169] G. F. Goya and V. Sagredo, *Phys. Rev. B* **64**, 235208 (2001).
- [170] D. Y. Cong , S. Roth, J. Liu, Q. Luo, M. Potschke, C. Hurrich and L. Schultz, *Appl. Phys. Lett.* **96**, 112504 (2010).
- [171] M. Thakur, M. Patra, S. Majumdar and S. Giri *J. Appl. Phys.* **105**, 073905 (2009).
- [172] K. Binder and A. P. Young, *Rev. Mod. Phys.* **58**, 801 (1986).
- [173] A. S. Alexandrov and A. M .Bratkovsky, *J. Phys.: Condens. Matter.* **11**, 1989 (1999).
- [174] A. L. Rakhmanova, K. I. Kugel, Ya. M. Blanter, and M. Yu. Kagan, arxiv:cond-mat/0006142v2 [cond-mat.str-el].
- [175] Vijay B Shenoy and C.N.R Rao, *Phil. Trans. R. Soc. A* **366**, 63 (2008).
- [176] A.S. Moskvin, arxiv:1008.2132v1 [cond-mat.str-el].
- [177] C. Ritter, M.R. Ibarra, J.M. De Teresa, P.A. Algarabel, C. Marquina, J. Blasco, J. Garcia, S. Oseroff, and S-W. Cheong, *Phys. Rev. B* **56**, 8902(1997) .
- [178] Menyoungh Lee, J. R. Williams, Sipei Zhang, C. Daniel Frisbie, and D. Goldhaber-Gordon, *Phys.Rev.Lett.* **107**, 256601 (2011).

- [179] Yeonbae Lee, Colin Clement, Jack Hellerstedt, Joseph Kinney, Laura Kinnischtzke, Xiang Leng, S. D. Snyder, and A. M. Goldman, *Phys. Rev. Lett* **106**, 136809 (2011).
- [180] Shahnewaz Mondal, Rishi Ram Ghimire, and A. K. Raychaudhuri, *Appl.Phys.Lett.* **103**, 231105 (2013).
- [181] A. K. Mishra, Azad J. Darbandi, Philipp M. Leufke, Robert Kruk, and Horst Hahn¹, *J.App.Phys.* **113**, 033913 (2013).
- [182] Zheng Yang, You Zhou, and Shriram Ramanathan, *J.Appl.Phys.* **111**, 014506 (2012).
- [183] S. Asanuma, P.-H. Xiang, H. Yamada, I. H. Inoue, H. Akoh, A. Sawa, K. Ueno, H. Shimotani, H. Yuan, M. Kawasaki, and Y. Iwasa, *Appl.Phys.Lett.* **97**, 142110 (2010).
- [184] Ping-Hua Xiang, Shutaro Asanuma, Hiroyuki Yamada , Isao H. Inoue, Hiroshi Sato, Hiroshi Akoh , Akihito Sawa, Kazunori Ueno, Hongtao Yuan, Hidekazu Shimotani , Masashi Kawasaki, and Yoshihiro Iwasa, *Adv. Mater.* **23**, 5822 (2011).
- [185] R Mahesh, R Mahendiran, AK Raychaudhuri, and CNR Rao, *Appl.Phys.Lett.* **68**, 2291 (1996).
- [186] Sohini Kar, Jayanta Sarkar, Barnali Ghosh and A. K. Raychaudhuri¹, *Phys.Rev.B.* **74**, 085412 (2006).
- [187] Barnali Ghosh, Sohini Kar, Loveleen K. Brar, and A. K. Raychaudhuri, *J. App. Phys.*, **98**, 094302 (2005).
- [188] Mandar A Paranjape, K. Shantha Shankar and A. K. Raychaudhuri, *J. Phys. D.* **38**, 3674 (2005).
- [189] Tapati Sarkar, M Venkata Kamalakar and A K Raychaudhuri, *New. J. Phys* **14**, 033026 (2012).
- [190] Hainan Wang and Laurent Pilon, *J. Phys. Chem. C* **115**, 1671116719 (2011).
- [191] T. Serikawa, S. Shirai, A. Okamoto, S. Suyama, *IEEE Trans ED* **34**, 321 (1984).
- [192] I. Shalish, L. Kronik, G. Segal, and Yoram Shapira, S. Zamir, B. Meyler, and J. Salzman, *Phys. Rev. B.* **61**, 15573 (2000).

- [193] Rajib Nath and A. K. Raychaudhuri, *Appl. Phys. Lett.* **104**, 083515 (2014).
- [194] Himanshu Jain, *An investigation of the ferromagnetic insulating state of manganites*, thesis submitted to IISC, India (2008).
- [195] C. H. Ahn, J.-M. Triscone and J. Mannhart, *Nature* **424**, 1015 (2003).
- [196] J. L. Cohn, M. Peterca, and J. J. Neumeier, *Phys. Rev. B* **70**, 214433 (2004).
- [197] R Mahendiran, SK Tiwary, AK Raychaudhuri, TV Ramakrishnan, R Mahesh, N Rangavittal, CNR Rao, *Phys. Rev. B* **53**, 3348 (1996).
- [198] Neeraj Khare, UP Moharil, AK Gupta, AK Raychaudhuri, SP Pai, R Pinto, *Appl. Phys. Lett.* **81**, 325 (2002).
- [199] D. Kim, B. Revaz, B. L. Zink, F. Hellman, J.J. Rhyne and J. F. Mitchell, *Phys. Rev. Lett.* **89**, 227202 (2002).
- [200] E. Dagotto, *Science* **309**, 257 (2005).
- [201] D. Louca, T. Egami, E. L. Brosha, H. Roder and A. R. Bishop, *Phys. Rev. B.* **56**, R8475 (1997).
- [202] S. Arumugam, Barnali Ghosh, A.K. Raychaudhuri, N.R. Tamil Selvan, T.Nakanishi, H.Yoshino, K.Murata and Ya. M. Mukovskii, *J. Appl. Phys* **106**, 023905 (2009).
- [203] G. Papavassiliou, M. Pissas, M. Belesi, M. Fardis, J. Dolinsek, C. Dimitropoulos, and J. P. Ansermet, *Phys. Rev. Lett.* **91**, 147205 (2003).
- [204] Y. Yamada, O. Hino, S. Nohdo, R. Kanao, T. Inami, and S. Katano, *Phys. Rev. Lett.* **77**, 904 (1996).
- [205] V. Markovich, I. Fita, R. Puzniak, M. I. Tsindlekht, A. Wisniewski, and G. Gorodetsky, *Phys. Rev. B.* **66**, 094409 (2002).
- [206] Vijay B. Shenoy, Tribikram Gupta, H. R. Krishnamurthy, and T. V. Ramakrishnan, *Phys. Rev. Lett.* **98**, 097201 (2007).

-
- [207] Y. M. Xiong, G. Y. Wang, X. G. Luo, and C. H. Wang, X. H. Chen, X. Chen and C. L. Chen J. Appl. Phys. **97**, 083909 (2005).
- [208] Anamitra Mukherjee, William S. Cole, Patrick Woodward, Mohit Randeria, and Nandini Trivedi, Phys. Rev. Lett **110**, 157201 (2013).
- [209] A. L. Efros, N. Van Lien, and B. I. Shklovskii, J. Phys. C **12**, 1869, (1979).
- [210] J. H. Davies, P. A. Lee, and T. M. Rice, Phys. Rev. Lett. **49**, 758 (1982).
- [211] Sudeshna Samanta and A. K. Raychaudhuri, Phys. Rev. B **85**, 045127 (2012). (2003).
- [212] K.H. Ahn, T. Lookman, A.R. Bishop, Nature **428**, 401 (2004).
- [213] J. Burgy, A. Moreo, E. Dagotto, Phys. Rev. Lett. **92**, 97202 (2004).
- [214] A.J. Millis, Nature **392**, 147 (1998).
- [215] V. Pena, Z. Sefrioui, D. Arias, C. Leon, J. Santamaria, M. Varela, S.J. Pennycook, M. Garcia-Hernandez, J.L. Martinez, Journal of Physics and Chemistry of Solids **67**, 472 (2006).
- [216] Guanyin Gao, Zhizhen Yin, Zhen Huang, Shaowei Jin and Wenbin Wu, J. Phys. D: Appl. Phys. **41**, 152001 (2008).
- [217] Y. Konishi, Z. Fang, M. Izumi, T. Manako, M. Kasai, H. Kuwahara, M. Kawasaki, K. Terakura, and Y. Tokura, J. Phys. Soc. Jpn. **68**, 3790 (1999).
- [218] Lakeshore Accesories www.lakeshore.com